

University of Southampton Research Repository

Copyright © and Moral Rights for this thesis and, where applicable, any accompanying data are retained by the author and/or other copyright owners. A copy can be downloaded for personal non-commercial research or study, without prior permission or charge. This thesis and the accompanying data cannot be reproduced or quoted extensively from without first obtaining permission in writing from the copyright holder/s. The content of the thesis and accompanying research data (where applicable) must not be changed in any way or sold commercially in any format or medium without the formal permission of the copyright holder/s.

When referring to this thesis and any accompanying data, full bibliographic details must be given, e.g.

Thesis: Author (Year of Submission) "Full thesis title", University of Southampton, name of the University Faculty or School or Department, PhD Thesis, pagination.

Data: Author (Year) Title. URI [dataset]

University of Southampton

Faculty of Engineering and Physical Sciences

School of Engineering
Astronautics Research Group

**The Development of a Miniaturized Raman Instrument for the Detection of
Biosignatures on Europa**

by

Aria Vitkova

Thesis for the degree of Doctor of Philosophy

ORCID ID: 0000-0001-9872-7811

DOI 10.5258/SOTON/T0054

May 2023

University of Southampton

Abstract

Faculty of Engineering and Physical Sciences

School of Engineering

Doctor of Philosophy

The Development of a Miniaturized Raman Instrument for the Detection of Biosignatures

on Europa

by

Aria Vitkova

Raman spectroscopy has gained popularity in planetary exploration over the last decade as an exceptionally versatile non-destructive compositional analysis technique that can identify a vast spectrum of molecules including both minerals and biomolecules, and provide information on the molecular structure, material phase as well as atom arrangements. For its many merits, Raman spectroscopy was proposed as one of the model instruments for the Europa Lander mission currently under development at NASA. For their vast oceans possibly harbouring extraterrestrial life, Europa and other Icy Worlds were identified as high priority planetary targets in both ESA's and NASA's plans for future planetary exploration. However, contemporary state-of-the-art Raman instruments for planetary exploration were designed for bulk mineral detection on Mars, the most imminent planetary target, and are not compatible with life detection on Europa.

This research evaluates the capabilities and limitations of Raman spectroscopy for in-situ detection of biosignatures on Europa in order to identify critical instrument design requirements and enabling technology necessary for the development of a Raman instrument compatible with a landed mission to Europa and its scientific goals. High confidence and high priority biosignatures for the search for life on Europa are identified and a selection of the target molecules is used to study the effects of laser induced damage, fluorescence interference, cryogenically induced spectral changes and the ability of available Raman technology to detect molecules at extremely low concentrations. The research shows that cryogenically induced changes can severely impact the detectability and identifiability of molecules due to Raman shift changes of up to 25 cm^{-1} , as well as the cryogenically induced increase in the fluorescence noise. On the other hand, the significant narrowing of Raman bands as well as the decrease in the variability of the measurements at low temperatures lead to higher precision and accuracy. Cryogenic temperatures also mitigate the effects of laser damage, increase the SNR in the spectra of some molecules and even allow the detection of highly photosensitive molecules that are unresolvable

at higher temperatures. The results also indicate that the spectral resolution necessary for successful detection of biosignatures on Europa could be as high as 2 cm^{-1} , which is much higher than the resolution of contemporary state-of-the-art Raman instruments for planetary exploration and is particularly problematic for miniaturized instruments. Additionally, detection at extremely low concentrations, as required on Europa, is not achievable using traditional Raman spectroscopy.

Based on the identified requirements, two Raman instrument designs compatible with a mission to Europa are proposed. Key enabling technology and future directions for the development of these instruments are identified and discussed. Most notably, Surface Enhanced Raman spectroscopy (SERS) is identified as a critical component of future Raman instruments for planetary exploration. Recent advances in the SERS technology are discussed and a SERS technique compatible with planetary exploration that could allow biosignature detection on Icy Worlds is proposed and described.

Table of Contents

Table of Contents	i
List of Tables	v
List of Figures	ix
List of Accompanying Materials	xix
Research Thesis: Declaration of Authorship	xxi
Acknowledgements	xxiii
Nomenclature and Abbreviations	xxv
Chapter 1 Introduction	1
Chapter 2 Background	7
2.1 Life Detection on Europa.....	8
2.2 Mission Constraints and Environmental Limitations	10
2.2.1 Mass and Size	10
2.2.2 Target Molecule Concentration	11
2.2.3 Cryogenic Temperatures	13
2.2.4 Interference.....	15
2.2.5 High Radiation Environment	15
2.2.6 Transfer Time & Distance	16
2.3 Raman spectroscopy	16
2.3.1 Challenges: Mass and Size.....	19
2.3.2 Challenges: Fluorescence	20
2.3.3 Challenges: Trace Detection.....	25
2.3.4 State-of-the-Art Instruments	29
2.3.5 Raman spectroscopy for Europa	32
Chapter 3 Scope and Overall Methodology	35
3.1 Aims and Objectives	35
3.2 Methodology	36
Chapter 4 Detection Target Molecules	39
4.1 Selection of the Detection Target Molecules.....	39

Table of Contents

4.2	Methodology.....	40
4.3	Results and Discussion	42
4.3.1	Amino Acids	47
4.3.2	Carboxylic Acids	48
4.3.3	Isoprenoids.....	49
4.3.4	Pigments	52
4.3.5	Nucleic Acids & Nucleobases	52
4.3.6	Proteins.....	53
4.3.7	Carbohydrates.....	54
4.3.8	Coenzymes	55
4.3.9	Metabolic Products.....	56
4.3.10	Porphyrins.....	57
4.3.11	Phosphate Biomolecules.....	58
4.3.12	Biominerals	58
4.3.13	Cell Colonies.....	60
Chapter 5	Experimental Methodology.....	61
5.1	Methodology.....	61
5.1.1	Samples.....	61
5.1.2	Measurements and Experimental Set Up.....	63
5.1.2.1	Detection Limit 1: Fluorescence	64
5.1.2.2	Detection Limit 2: Laser Damage	66
5.1.2.3	Detection Limit 3: Effects of Extreme Low Temperatures.....	67
5.1.2.4	Detection Limit 4: Minimum and Maximum Laser Fluence and Total Energy Dose	74
5.1.2.5	Detection Limit 5: Sensitivity	76
5.1.2.6	Overall Detectability and Instrument Design Considerations	77
Chapter 6	Detection Limits: Fluorescence and Laser Damage	78
6.1	Fluorescence	78
6.2	Laser Damage.....	86
Chapter 7	Detection Limits: Effects of Extreme Low Temperatures	98

7.1	Amino Acids.....	98
7.1.1	Glycine.....	99
7.1.2	Alanine.....	104
7.1.3	Histidine.....	109
7.1.4	Tryptophan.....	113
7.1.5	Fluorescence at 532 nm.....	118
7.1.6	Overview & Discussion.....	121
7.2	Porphyryns.....	132
7.3	Carotenoids.....	140
7.4	Pigments.....	149
7.5	Natural Mixtures.....	151
7.6	Nucleic Acids.....	153
7.7	Carboxylic Acids.....	155
7.8	Carbohydrates.....	158
7.9	Isoprenoids.....	160
7.10	Steranes.....	164
7.11	Nucleobases.....	166
7.11.1	Adenine.....	172
7.11.2	Guanine.....	173
7.11.3	Cytosine.....	175
7.11.4	Thymine.....	176
7.11.5	Uracil.....	177
7.12	Coenzymes.....	179
7.13	Inorganics.....	183
Chapter 8	Detection Limits: Sensitivity.....	185
8.1.1	Minimum and Maximum Laser Fluence and Total Energy Dose.....	185
8.1.2	Sensitivity.....	190
Chapter 9	Detection Limits: Overall Detectability and Instrument Design Considerations.....	195
Chapter 10	Instrument Design and Requirements.....	205
10.1	Requirements.....	205

Table of Contents

10.1.1 Detectable Molecules	206
10.1.2 Mass & Size	206
10.1.3 Sensitivity (Limit of Detection)	207
10.1.4 Spectral Resolution	207
10.1.5 Spectral Range	209
10.2 Key Design Parameters	209
10.2.1 Wavelengths Selection.....	209
10.2.2 Sensitivity (Limit of Detection)	212
10.2.3 Fluorescence Mitigation	215
10.2.4 Miniaturization	217
10.3 Design.....	219
10.4 Measurement Method.....	224
10.5 Future Directions	225
Chapter 11 Conclusions & Future Work.....	229
11.1 Future Work.....	235
List of References	237

List of Tables

Table 2-1 Comparison of payload mass between a mission to Europa and a few notable missions to Mars flown to date (based on publicly available data from NASA and [19], [22], [26])	11
Table 2-2 Comparison of radiation dose experienced during various missions [21].....	16
Table 4-1 Key considerations for the selection of high priority biosignatures for the search for life on Europa.....	42
Table 4-2 Selected molecular targets: amino acids and organic metabolic products, note that the list of amino acids is not exhaustive, only a sample of some important amino acids has been selected (T – trace, R – rare, VR – very rare, NP – non-proteinogenic, h – not uniquely biogenic but unlikely to be abiotic at high levels, l – limited occurrence, vl – very limited occurrence, mg – methanogenic)	44
Table 4-3 Selected molecular targets: lipids (r – recent, u – not uniquely biogenic but abiotic formation unlikely or abiotic sources very rare, l – limited occurrence, vl – very limited occurrence, m – main source, mg – methanogenic)	45
Table 4-4 Selected molecular targets: biomolecules (r – recent, u – not uniquely biogenic but abiotic formation unlikely or abiotic sources very rare)	46
Table 4-5 Selected molecular targets: inorganic biosignatures and other targets (u – not uniquely biogenic but abiotic formation unlikely or abiotic sources very rare, h – not uniquely biogenic but unlikely to be abiotic at high levels)	47
Table 5-1 Selected samples for testing, their priority, purity, form and the supplier (*complementary samples)	62
Table 5-2 Raman instrumentation set up and specification	64
Table 5-3 A representative selection of samples tested at the 325 nm excitation	65
Table 5-4 Measurement laser power, laser fluence and total energy dose for experiments exploring the effects of cryogenic temperatures on the Raman spectra (U denotes samples and/or excitations that did not allow investigations of the cryogenically induced changes due to laser damage or excessive fluorescence	

List of Tables

impeding any further characterisation and that were excluded from these experiments)	70
Table 6-1 Fluorescence interference across various excitation wavelengths and different target molecules for the exploration of Europa, 1 = no fluorescence and fully detectable, 2 = mild fluorescence but fully detectable at all laser power settings, 3 = moderate to severe fluorescence depending on the laser power, detectable at high laser power, 4 = severe fluorescence with some Raman bands still visible but not enough for full identification, 5 = very severe fluorescence, no Raman signal visible (*complementary sample, ^undetectable due to laser damage despite relatively low fluorescence noise, ^^critical level of fluorescence noise most likely associated with laser damage).....	79
Table 6-2 Laser damage thresholds of selected target molecules at UV, visible and NIR excitation, the lowest laser damage thresholds at each wavelength are highlighted in red88	
Table 6-3 Laser damage detectability thresholds of selected target molecules at UV, visible and NIR excitation, U = molecules for which laser damage detectability thresholds could not be identified as they were undetectable regardless of the laser damage	89
Table 7-1 Glycine Raman bands at 22 °C, -100 °C and -196 °C (*temperature at which the new band is first detectable in the brackets) [310]	100
Table 7-2 Minimum peak-to-peak distance between adjacent Raman bands and Raman band width in the spectra of Glycine, Alanine, Histidine and Tryptophan at room temperature, -100 °C and -196 °C [310].....	125
Table 7-3 The number of adjacent bands within potential mixtures of Glycine, Alanine, Histidine and Tryptophan with a suggested minimum spectral resolution necessary for full identification of these amino acids at room temperature and at -196 °C [310]	126
Table 7-4 Raman band assignments for hemin and protoporphyrin IX based on DFT calculation using SVP and polarizability functions for the calculation of Raman vibrational frequencies and Raman activity [311].....	136
Table 7-5 Comparison of the Raman shift change from room temperature to -196 °C in the spectra of β -carotene and astaxanthin at 532 nm and 785 nm.....	143

Table 8-1 The number of molecules detectable at each excitation wavelength and each laser power setting (L = limited detectability, D = fully detectable, I = fully detectable with all minor features, i.e. measurement yielding an optimal spectrum)...	190
Table 8-2 Theoretical and experimental LODs of the control molecules	191
Table 8-3 Estimated lowest detectable concentration of target biosignatures for the exploration of Europa at 532 nm and 785 nm (U = molecule undetectable)	193
Table 9-1 The maximum change in the Raman shift observed in the spectra of the examined target molecules from room temperature to -196 °C ranked in descending order and including the molecular structure	201
Table 9-2 Minimum peak-to-peak distance in the spectra of the examined biosignatures at various temperatures. The values are similar for 532 nm and 785 nm and the lower value was chosen in this table. U denotes molecules that were undetectable and the minimum peak-to-peak distance could not be determined. * denotes molecules where high fluorescence may have restricted the number of visible peaks and the shown value is only based on the detectable bands in the spectra.	202
Table 9-3 Spectral range required for the identification of the examined target molecules, * denotes molecules where the required spectral range could not be determined from the experimentally obtained spectra and literature available to date was used instead.....	203
Table 10-1 A description of two promising Raman instrument designs for the detection of biosignatures on Europa including the main design features, techniques, limitations as well as the advantages and areas for further development...	224

List of Figures

Figure 1-1 Jupiter’s moon Europa [373]	3
Figure 1-2 The surface of Europa as captured by Galileo [37].....	4
Figure 2-1 Europa lander mission concept science goals and objectives, searching for the evidence of life being the highest priority goal, followed by assessing the habitability and then supporting future exploration [19]	8
Figure 2-2 Geochemical processes on Europa delivering material from the ocean to the surface are likely to have a major impact on the distribution of any possible biosignatures on Europa. Potential habitable zones include extensional features, plumes, diapirs, sills and perched lakes [19].....	12
Figure 2-3 The temperature profile of the Europan ice crust (based on data from [71] and [73])	14
Figure 2-4 Jablonski energy level diagram showing the electronic and vibrational transitions in a molecule including absorption, fluorescence, elastic scattering and Raman scattering [87], $E = \text{energy}$; $h = \text{Planck’s constant}$; $c = \text{speed of light}$; $\lambda = \text{wavelength}$)	18
Figure 2-5 Raman spectra of water in liquid and ice form and dry ice [88]	18
Figure 2-6 A comparison of the SSE method and other common fluorescence mitigation methods using 4-bromo-N, N-dimethyl-aniline. (A) Fourier-Transform (FT) Raman spectrum acquired using 1064 nm laser. (B) Unprocessed dispersive Raman spectrum at 785 nm laser. (C) Raman spectra processed using SSE. (D) Standard deviation (SD) Raman spectrum. (E) SERDS spectrum (using 2 spectra acquisitions). (F) Principal Component Analysis (PCA) Raman spectrum [111].	21
Figure 2-7 The fluorescence emission region of a number of different materials compared to the emission range of a DUV Raman system at 224 nm, 248 nm and 266 nm [119]	23
Figure 2-8 (a) SERS signal enhancement of otherwise undetectable Rh6G molecules using in-situ activated AgCl SERS at a varying number of submersion cycles during manufacture [158]. (b) A SEM scan of the AgCl non-activated (left) and activated nanoparticles (right) [158]. (c) An AFM scan of AgCl precursor non-activated nanoparticles deposited onto a quartz substrate as a part of this research at the University of Southampton to confirm the method.....	29

List of Figures

Figure 2-9 The optical path (top) and prototype 2 (PT2, bottom) of SHERLOC and a 3D model (right), A DUV Raman instrument for the Mars 2020 mission [89] [161]. Mx: mirrors, OL: objective lens, AF: autofocus, SCNR: scanning mirror, BS: beam splitter, BE: beam expander, IO: imaging optics, CC: context camera, LR: laser rejection filter, P: pinhole, M: convex mirror, S: spherical reflector, G: grating. DUV laser radiation is represented by purple and the fluorescence/Raman emission from the target are represented by blue [89]..... 30

Figure 2-10 SuperCam’s transmission spectrometer cutaway rendering, the transmission spectrometer includes Raman and TRL spectroscopy, while providing enhanced capabilities for LIBS and passive VIS reflectance spectra [163] 31

Figure 2-11 Raman spectra of water/ice (top) and saturated brine, NaCl in water, (bottom) excited with 488 nm [171] 33

Figure 3-1 Aims and objectives with the applied method of research outlined below 36

Figure 3-2 Key milestones to achieve for the development of an optimal miniaturized Raman instrument for the detection of biosignatures on Europa 37

Figure 4-1 Biogenicity of some important amino acids (redrawn based on data from [19], [189]), Gly – Glycine, Ala – Alanine, GluA – Glutamic Acid, AspA – Aspartic Acid, Leu – Leucine, Ser – Serine, Val – Valine, His - Histidine, AIB - α -Aminoisobutyric, iVal – Isovaline, GABA - γ -Aminobutyric Acid, BAla – β -Alanine 48

Figure 5-1 An open Linkam THMS600 cooling stage showing the cooling block used for the experiments. The stage is closed and purged with liquid nitrogen via the liquid nitrogen tubes on the left-hand side. A temperature controller is connected to the stage and a PC interface software, which is used to set the temperature profile. 68

Figure 6-1 Comparison of glycine Raman spectra at 532 nm (class 3), 785 nm (class 1), 633 nm (class 2) and 325 nm (class 1) 80

Figure 6-2 Raman spectra of ectoine collected at 785 nm excitation (class 2) and at various laser power 80

Figure 6-3 Comparison of glycine Raman spectra at 532 nm at two different laser power settings (class 3), most Raman bands are lost in the spectra at a lower laser fluence 81

Figure 6-4 Raman spectra of ectoine at 532 nm excitation (class 4) compared to 633 nm excitation (class 3)	82
Figure 6-5 Full range Raman spectra of Protoporphyrin IX at 532 nm	83
Figure 6-6 Histidine laser damage at UV excitation (325 nm) compared to 325 nm spectra below the laser damage threshold	90
Figure 6-7 Histidine laser damage progression at UV excitation (325 nm) at a high laser fluence	90
Figure 6-8 Physical signs of laser damage of cytosine at 325 nm, top left - 1093 kJ/cm ⁻² (5.4 mJ), top right - 2187 kJ/cm ⁻² (10.8 mJ), bottom left - 10.9 MJ/cm ⁻² (54 mJ), bottom right - 21.9 MJ/cm ⁻² (108 mJ)	91
Figure 6-9 Cytosine laser damage at UV excitation (325 nm).....	91
Figure 6-10 Raman spectra of hemin (a) and protoporphyrin IX (b) at 532 nm excitation across different laser power settings at room temperature (22 °C) showing low signal strength even at the optimal power density of 9.77 kW/cm ² for hemin and 195 W/cm ² for protoporphyrin [311]	94
Figure 6-11 Comparison of the Raman spectra of pure chlorophyll and spinach obtained at 785 nm	95
Figure 6-12 Raman spectra of RNA at 785 nm and various total energy dose	96
Figure 7-1 Raman spectra of Glycine at various temperatures in the range of 22 °C to -196 °C, where ν = stretching, ω = wagging, ρ = rocking, β = bending, τ = torsion, sc = scissoring, as = asymmetric. Assignments are based on an optimized Density Functional Theory (DFT) vibrational frequency calculation using Split Valence Polarization (SVP) and polarizability calculations for Raman vibrational frequencies and Raman activity together with a review of previously published assignments [312]–[314]. A vertical arrow highlights the split of the 497 cm ⁻¹ band, diagonal arrows highlight bands detailed in Figure 7-2 [310]	99
Figure 7-2 The profile of the changes in the Raman band shift and width of the Glycine asymmetrical stretching of CCO Raman band at 1331 cm ⁻¹ (a and c respectively) and NH ₂ wagging at 895 cm ⁻¹ (b and d respectively). These bands are highlighted with arrows in the spectra in Figure 7-1. A general trend of the change is highlighted using a 3 rd order polynomial curve. 2 σ error bars calculated for these peaks at each temperature over 3 measurements at 3 different power settings	

List of Figures

- are included in (a), (c) and (d) to indicate the relative significance of the changes. 3σ error bars are displayed in (b) as the change was too great for 2σ error bars to be visible [310] 101
- Figure 7-3 Variance of Raman band shift (a) and width (b) across individual Glycine spectra as a function of temperature [310] 103
- Figure 7-4 Intensity increase of Glycine Raman spectra at 196 °C compared to room temperature measurements [310] 104
- Figure 7-5 Raman spectra of Alanine at 22 °C, -100 °C and -196 °C, where ν = stretching, β = bending, τ = torsion, sc = scissoring. Assignments are based on an optimized DFT vibrational frequency calculation using SVP and polarizability calculations for Raman vibrational frequencies and Raman activity together with a review of previously published assignments [314]–[320]. Arrows highlight bands detailed in Figure 7-6 [310] 105
- Figure 7-6 Alanine profile of Raman band shift and width change as a function of temperature for the C-CH₃ stretching band at 854 cm⁻¹ (a and c) and NH₂ and CH₃ rocking band at 283 cm⁻¹ (b and d). A general trend of the change, similar to Glycine Raman shift and width change profile, is highlighted in a and c. These bands are highlighted with arrows in the spectra in Figure 7-5. 3σ error bars calculated for these peaks at each temperature over 3 measurements at 3 different power settings are included to indicate the relative significance of the changes [310]..... 106
- Figure 7-7 Variance of Raman band shift (a) and width (b) across individual Alanine spectra as a function of temperature [310] 108
- Figure 7-8 Intensity decrease of Alanine Raman spectra at 196 °C compared to room temperature measurements [310] 109
- Figure 7-9 Raman spectra of Histidine at 22 °C, -100 °C and -196 °C, where R = ring (i.e. imidazole ring), ν = stretching, ω = wagging, ρ = rocking, β = bending, τ = torsion, b = breathing (i.e. in phase stretching of the ring), def = deformation (i.e. out of phase stretching of the ring), sc = scissoring, as = asymmetric, s = symmetric, o.p = out of plane, i.p. = in plane, brackets denote the location of the vibration. Assignments are based on an optimized DFT vibrational frequency calculation using SVP and polarizability calculations for Raman vibrational frequencies and Raman activity together with a review of previously published assignments

[321]–[325]. A diagonal arrow highlights the band detailed in Figure 7-10 [310]	110
Figure 7-10 Histidine profile of Raman band shift and width change as a function of temperature for the 1323 cm^{-1} band (a and b respectively) assigned to mixed vibrations of CH_2 wagging and ring breathing. A general trend of the change is highlighted. This band is highlighted with an arrow in the spectra in Figure 7-9. 2σ error bars calculated for this Raman band at each temperature over 3 measurements at 3 different power settings are included to indicate the relative significance of the changes [310].	111
Figure 7-11 Variance of Raman band shift (a) and width (b) across individual Histidine spectra as a function of temperature [310]	112
Figure 7-12 Intensity increase of Histidine Raman spectra at $-196\text{ }^\circ\text{C}$ compared to room temperature measurements [310]	113
Figure 7-13 Raman spectra of Tryptophan at $22\text{ }^\circ\text{C}$, $-100\text{ }^\circ\text{C}$ and $-196\text{ }^\circ\text{C}$, where R_B = benzene ring, R_P = pyrrole ring, I = indole group (i.e. benzene and pyrrole ring), ν = stretching, ω = wagging, ρ = rocking, β = bending, τ = torsion, b = breathing (i.e. in phase stretching of a ring), def = deformation (i.e. out of phase stretching of a ring), sc = scissoring, o.p = out of plane, i.p. = in plane, brackets denote the location of the vibration. Assignments are based on an optimized DFT vibrational frequency calculation using SVP and polarizability calculations for Raman vibrational frequencies and Raman activity together with a review of previously published assignments [318], [326]. Diagonal arrows highlight the bands detailed in Figure 7-15 [310]	114
Figure 7-14 Average S/N ratio of Tryptophan fluorescence as a function of temperature [310]	116
Figure 7-15 Tryptophan profile of Raman band shift and width change as a function of temperature for the benzene and pyrrole ring breathing band at 757 cm^{-1} (a and c) and the indole out of plane deformation band at 164 cm^{-1} (b and d). A general trend of the change is highlighted. These bands are highlighted with arrows in the spectra in Figure 7-13. 2σ error bars calculated for these Raman bands at each temperature over 3 measurements at 3 different power settings are included to indicate the relative significance of the changes [310]	116

List of Figures

Figure 7-16 Variance of Raman band shift (a) and width (b) across individual Tryptophan spectra as a function of temperature [310]	117
Figure 7-17 Intensity increase of Tryptophan Raman spectra at -196 °C compared to room temperature measurements [310].....	118
Figure 7-18 Raman spectra of amino acids fluorescent at 532 nm excitation collected at room temperature, -100 °C and -196 °C showing a visible increase in the fluorescence noise	119
Figure 7-19 Comparison of the SNR change across varying temperatures for amino acids that are fluorescent at 532 nm and Alanine, which is not fluorescent at this excitation	120
Figure 7-20 (a) The profile of the Raman shift change of Glycine band 895 cm^{-1} as a function of temperature and (b) the profile of the Raman band width change of Glycine 1331 cm^{-1} band as a function of temperature. A theoretical prediction corresponding to the general trend characterized by a 3 rd order polynomial relationship for temperatures approaching 0 K is highlighted [310]	122
Figure 7-21 The comparison of hemin (a) and protoporphyrin IX (b) Raman spectra at cryogenic temperatures (-100 °C and -196 °C) and room temperature using 532 nm excitation and the same laser power density of 9.77 kW/cm^2 for hemin and 195 W/cm^2 for protoporphyrin [311].....	133
Figure 7-22 Molecular structure of hemin (a) and protoporphyrin IX (b) [311]	134
Figure 7-23 Relative SNR increase across all fully resolvable bands in the Raman spectra of hemin (a) and protoporphyrin IX (b) at cryogenic temperatures (-100 °C and -196 °C) compared to room temperature measurements. The SNR enhancement is quantified in percentage of the nominal room temperature signal strength including 2σ error bars (532 nm excitation at 9.77 kW/cm^2 laser power density for hemin and 195 W/cm^2 for protoporphyrin) [311].....	138
Figure 7-24 SNR enhancement across all fully resolvable bands in the Raman spectra of hemin (a) and protoporphyrin IX (b) at cryogenic temperatures (-100 °C and -196 °C) compared to room temperature measurements using 532 nm excitation and the same laser power density of 9.77 kW/cm^2 for hemin and 195 W/cm^2 for protoporphyrin [311]	138

Figure 7-25 Raman spectra of β -carotene and astaxanthin at 22 °C, -100 °C and -196 °C at 785 nm excitation	141
Figure 7-26 Raman spectra of β -carotene and astaxanthin at 22 °C, -100 °C and -196 °C at 532 nm excitation	142
Figure 7-27 Raman shift and band width change of the 1007 cm^{-1} Raman band (methyl rocking) in the spectra of β -carotene and astaxanthin across 22 °C, -100 °C and -196 °C at 785 nm and 532 nm excitation including 2σ error bars (except for Raman shift change in astaxanthin at 532 nm, which is shown with 1σ error bars).....	144
Figure 7-28 Molecular structure of β -carotene and astaxanthin	146
Figure 7-29 Average Raman shift and band width variance across all bands in the spectra of β -carotene and astaxanthin across 22 °C, -100 °C and -196 °C at 785 nm and 532 nm excitation	147
Figure 7-30 SNR change observed at the 3 most dominant carotenoid Raman bands in the spectra of β -carotene and astaxanthin across 22 °C, -100 °C and -196 °C at 785 nm and 532 nm excitation	148
Figure 7-31 Raman spectra of c-phycoyanin at 22 °C, -100 °C and -196 °C at 785 nm excitation	149
Figure 7-32 SNR of the c-phycoyanin spectra across 22 °C, -100 °C and -196 °C at 785 nm excitation	150
Figure 7-33 Molecular structure of c-phycoyanin.....	150
Figure 7-34 Raman spectra of spinach (naturally occurring chlorophyll) and a carrot root (naturally occurring β -carotene) at 22 °C, -100 °C and -196 °C at 532 nm excitation ...	151
Figure 7-35 SNR change observed at the most dominant Raman bands in the spectra of spinach and carrot (1523 cm^{-1} and 1519 cm^{-1} respectively) across 22 °C, -100 °C and -196 °C at 532 nm excitation.....	152
Figure 7-36 Raman spectra of RNA at 22 °C, -100 °C and -196 °C at 785 nm excitation	154
Figure 7-37 SNR change observed in the spectra of RNA across 22 °C, -100 °C and -196 °C at 785 nm.....	155
Figure 7-38 Raman spectra of ectoine at 22 °C, -100 °C and -196 °C at 785 nm excitation (6.9 kJ total energy dose and the fluence of 13.79 MJ/cm^2)	156

List of Figures

Figure 7-39 Raman shift variance (left) and SNR change (right) recorded in the spectra of ectoine across 22 °C, -100 °C and -196 °C at 785 nm excitation	156
Figure 7-40 Raman spectra of palmitic acid at 22 °C, -100 °C and -196 °C at 785 nm excitation (6.9 kJ total energy dose and the fluence of 13.79 MJ/cm ²).....	157
Figure 7-41 Raman shift variance (left) and SNR change (right) recorded in the spectra of palmitic acid across 22 °C, -100 °C and -196 °C at 785 nm excitation.....	158
Figure 7-42 Raman spectra of trehalose at 22 °C, -100 °C and -196 °C at 532 nm excitation (538.8 mJ total energy dose and the fluence of 2.35 MJ/cm ²)	159
Figure 7-43 Raman shift variance (left) and SNR change (right) recorded in the spectra of trehalose across 22 °C, -100 °C and -196 °C at 532 nm excitation	160
Figure 7-44 Raman spectra of pristane at 22 °C, -100 °C and -196 °C at 785 nm excitation.....	161
Figure 7-45 Raman spectra of squalane at 22 °C, -100 °C and -196 °C at 785 nm excitation ...	162
Figure 7-46 SNR change recorded in the spectra of pristane (left) and squalane (right) across 22 °C, -100 °C and -196 °C at 785 nm excitation	163
Figure 7-47 Raman shift variance recorded in the spectra of pristane (left) and squalane (right) across 22 °C, -100 °C and -196 °C at 785 nm excitation	163
Figure 7-48 Raman spectra of 5 α cholestane at 22 °C, -100 °C and -196 °C at 785 nm excitation, note that there are no Raman bands between 1600 cm ⁻¹ and 2750 cm ⁻¹ and this region was excluded for clarity	165
Figure 7-49 Raman shift variance (left) and SNR change (right) recorded in the spectra of 5 α cholestane across 22 °C, -100 °C and -196 °C at 785 nm excitation	166
Figure 7-50 Raman spectra of adenine and cytosine at 22 °C, -100 °C and -196 °C at 532 nm excitation.....	167
Figure 7-51 Raman spectra of thymine and uracil at 22 °C, -100 °C and -196 °C at 532 nm excitation.....	167
Figure 7-52 SNR change recorded in the spectra of nucleobases across 22 °C, -100 °C and -196 °C at 532 nm excitation.....	168

Figure 7-53 Raman shift change from room temperature to -196 °C in the spectra of nucleobases. The trend observed at the most dominant Raman band in the spectra is shown together with 2 σ error bars.....	169
Figure 7-54 Raman shift variance recorded in the spectra of nucleobases across 22 °C, -100 °C and -196 °C at 785 nm excitation	170
Figure 7-55 SNR change recorded in the spectra of nucleobases across 22 °C, -100 °C and -196 °C at 785 nm excitation	171
Figure 7-56 Raman spectra of adenine at 22 °C, -100 °C and -196 °C at 785 nm excitation	172
Figure 7-57 Raman spectra of guanine at 22 °C, -100 °C and -196 °C at 785 nm excitation	174
Figure 7-58 Raman spectra of cytosine at 22 °C, -100 °C and -196 °C at 785 nm excitation.....	175
Figure 7-59 Raman spectra of thymine at 22 °C, -100 °C and -196 °C at 785 nm excitation.....	177
Figure 7-60 Raman spectra of uracil at 22 °C, -100 °C and -196 °C at 785 nm excitation	178
Figure 7-61 Raman spectra of nicotinamide at 22 °C, -100 °C and -196 °C at 785 nm excitation.....	179
Figure 7-62 Raman shift change from room temperature to -196 °C observed at the most dominant band in the spectra of nicotinamide (1046 cm ⁻¹) including 2 σ error bars	180
Figure 7-63 Raman shift variance (left) and band width variance (right) recorded in the spectra of nicotinamide across 22 °C, -100 °C and -196 °C at 785 nm excitation	181
Figure 7-64 SNR change recorded in the spectra of nicotinamide across 22 °C, -100 °C and -196 °C at 785 nm excitation.....	181
Figure 7-65 Raman spectra of nicotinamide at 22 °C, -100 °C and -196 °C at 532 nm excitation.....	181
Figure 7-66 SNR change recorded in the spectra of nicotinamide across 22 °C, -100 °C and -196 °C at 532 nm excitation.....	182
Figure 7-67 Raman shift variance (left) and band width variance (right) recorded in the spectra of nicotinamide across 22 °C, -100 °C and -196 °C at 532 nm excitation	182
Figure 7-68 Raman spectra of Hawaiian palagonite (HWMK101) at 22 °C, -100 °C and -196 °C at 785 nm excitation	183

List of Figures

Figure 8-1 Detectability of target molecules at 532 nm at various laser power (O = detector oversaturated due to high intensity signal, U = undetectable, L = limited detectability, D = fully detectable, I = fully detectable with all minor features, i.e. measurement yielding an optimal spectrum)	186
Figure 8-2 Detectability of target molecules at 633 nm at various laser power (O = detector oversaturated due to high intensity signal, U = undetectable, L = limited detectability, D = fully detectable, I = fully detectable with all minor features, i.e. measurement yielding an optimal spectrum)	187
Figure 8-3 Detectability of target molecules at 785 nm at various laser power (O = detector oversaturated due to high intensity signal, U = undetectable, L = limited detectability, D = fully detectable, I = fully detectable with all minor features, i.e. measurement yielding an optimal spectrum)	188
Figure 8-4 Raman spectra of a pure glycine sample compared to a 5 wt% solution in water at 532 nm.....	191
Figure 10-1 Instrument volume example allocation according to the Europa lander concept study [22]	206
Figure 10-2 Lithography process for high aspect ratio nanostructuring of glassy substrate material [362]. (b), (c) and (d) show cross section of the three proposed methods of combining AgCl in-situ activated SERS with a nanostructured substrate surface	214
Figure 10-3 Working principle of a Spatial Heterodyne Raman Spectrometer [366]	219

List of Accompanying Materials

Research Data (DOI: 10.5258/SOTON/D2371):

- All spectral data collected for this research work including Raman spectra of all molecules examined in this study and band frequency assignments obtained using an automatic peak-pick function.

Research Thesis: Declaration of Authorship

Print name: Aria Vitkova

Title of thesis: The Development of a Miniaturized Raman Instrument for the Detection of Biosignatures on Europa

I declare that this thesis and the work presented in it are my own and has been generated by me as the result of my own original research.

I confirm that:

1. This work was done wholly or mainly while in candidature for a research degree at this University;
2. Where any part of this thesis has previously been submitted for a degree or any other qualification at this University or any other institution, this has been clearly stated;
3. Where I have consulted the published work of others, this is always clearly attributed;
4. Where I have quoted from the work of others, the source is always given. With the exception of such quotations, this thesis is entirely my own work;
5. I have acknowledged all main sources of help;
6. Where the thesis is based on work done by myself jointly with others, I have made clear exactly what was done by others and what I have contributed myself;
7. Parts of this work have been published as:

[1] A. Vitkova, S. J. I. Walker, and H. Sykulska-Lawrence, "The Impact of Extreme Low Temperatures on Raman Spectra of Amino Acids Relevant," *Astrobiology*, vol. 22, no. 11, 2022, doi: 10.1089/ast.2021.0136.

[2] A. Vitkova, S. J. I. Walker, and H. Sykulska-Lawrence, "Cryogenically induced signal enhancement of Raman spectra of porphyrin molecules," *Anal. Methods*, vol. 14, no. 34, pp. 3307–3314, 2022, doi: 10.1039/d2ay00538g.

[3] A. Vitkova, H. Sykulska-Lawrence, and S. Walker, "The Impact of Extreme Low Temperatures Analogous to Europa's Surface and Sub-surface on Raman Spectra of Amino Acids," presented at AGU Fall Meeting 2021: 13-17 December, 2021, pp. P22A-06.

Signature: Date:.... 17/09/2022

Acknowledgements

Firstly, I would like to thank the **University of Southampton** and the **Aeronautics Department** for providing the resources to carry out this research. Most notably, I would like to thank my supervisors, **Hanna Sykulska-Lawrence** and **Scott Walker**, for their guidance and helpful comments. I would also like to highlight all the support I received from the head of the Aeronautics Research Group, **Hugh Lewis**, who was most helpful and forthcoming. Special thanks also belongs to laboratory technicians, **Mike Bartlett** and **Jon Kerly**, for assisting with the supply of liquid nitrogen for the experiments. I would also like to thank the **ECS department**, namely **Kees van Groot**, **Russel Torah**, **Monika Glanc-Gostkiewicz** and **SweZin Oo**, for letting me use their facilities and equipment and for providing the appropriate training. Additionally, I would like to thank my progression review examiners, **Blair Thornton** and **Andrea Da Ronch**, for their helpful feedback and for guiding me in the right direction. Further, I would like to acknowledge the contribution of **Sumeet Mahajan**, **Russell Minns** and other academic staff at the University of Southampton for sharing their knowledge and experience. I would also like to thank the **Cambridge Graphene Centre** and its staff for letting me use their facilities. Lastly, I would like to extend my thanks to **James Lambert** at JPL for sharing his knowledge and helpful insights.

Nomenclature and Abbreviations

@	at
AFM	Atomic Force Microscopy
Ag	silver
AgCl	silver chloride
AGU	American Geophysical Union
as	asymmetric
ATP	adenosine triphosphate
C	speed of light
CCD	Charged-Coupled Device
CH ₃	methane
cm ⁻¹	wavenumber; unit of frequency
CO ₂	carbon dioxide
CspA	cold shock protein A
CW	Continuous Wave
def	deformation
DFT	Density Functional Theory
DMDS	dimethyl disulfide
DMS	dimethyl sulfide
DNA	deoxyribonucleic acid
DUV	Deep Ultraviolet; electromagnetic radiation with wavelength from 200 nm to 280 nm
E	energy, [J]
ESA	European Space Agency
eV	electronvolt; unit of energy
FAD	flavin adenine dinucleotide
f-number	f/#; focal ratio

Chapter 1

FT	Fourier Transform
FT-R	Fourier Transform Raman Spectroscopy
FWHM	full width at half maximum
H	Planck's constant
H ₂ O	water
HSP70	heat shock protein of the 70 family
HSP90	heat shock protein of the 90 family
HWMK101	Hawaii Mauna Kea palagonite sample
i.p.	in plane
iCCD	Intensified Charged-Coupled Device
I _N	noise intensity
IR	Infrared
I _s	signal intensity
JPL	Jet Propulsion Laboratory
JSC	Johnson Space Center
JUICE	JUperiter ICy moons Explorer; mission to the moons of Jupiter
KBr	potassium bromide
LIBS	Laser Induced Breakdown Spectroscopy
LOD	Limit of Detection, i.e. lowest detectable concentration
M	molar; unit of concentration
N ₂ O	nitrous oxide
NA	numerical aperture
NaCl	sodium chloride
NAD	nicotinamide adenine dinucleotide
NADP	nicotinamide adenine dinucleotide phosphate
NASA	National Aeronautics and Space Administration
NH ₃	ammonia

NIR.....	Near Infrared; electromagnetic radiation with wavelength from 780 nm to 2500 nm
nM.....	nanomolar; unit of concentration
NSPIRES.....	NASA Solicitation and Proposal Integrated Review and Evaluation System
o.p.....	out of plane
O ₂	oxygen
O ₃	ozone
PAH.....	polyaromatic hydrocarbons
PCA.....	Principal Component Analysis
ppb.....	part per billion; unit of concentration
ppm.....	part per million; unit of concentration
ppth.....	part per thousand; unit of concentration
PVA.....	polyvinyl acetate
R.....	ring, i.e. aromatic ring
rad.....	unit of absorbed dose of ionizing radiation
Rh6G.....	Rhodamine 6G; highly fluorescent dye
RLS.....	Raman Laser Spectrometer; Raman instrument for the ExoMars mission
RNA.....	ribonucleic acid
Roscosmos.....	State Space Corporation; Russian national space agency
RRS.....	Resonance Raman Spectroscopy
rruff.....	database of Raman spectra of minerals
s.....	symmetric
S/N.....	Signal to Noise
sc.....	scissoring
SD.....	Standard Deviation
SEM.....	Scanning Electron Microscopy

Chapter 1

SERDS.....	Shifted Excitation Raman Difference Spectroscopy
SERS	Surface Enhanced Raman spectroscopy
SHERLOC	Scanning Habitable Environments with Raman & Luminescence for Organics & Chemicals; Raman instrument for the Mars 2020 mission
SHRS.....	Spatial Heterodyne Raman Spectrometer
SHS.....	Spatial Heterodyne Spectrometer
SNR.....	Signal to Noise Ratio
SO ₂	suplur dioxide
SPAD	Single Photon Avalanche Diode Array
SSE	Serially Shifted Excitation
SuperCam	instrument suite for the Mars 2020 mission including a Raman spectrometer
SVP.....	Split Valence Polarization
TRL	Technology Readiness Level
UV	Ultraviolet; electromagnetic radiation with wavelength from 10 nm to 380 nm
VIS.....	visible; electromagnetic radiation with wavelength from 380 nm to 700 nm
wt%.....	weight percent; unit of concentration
β.....	bending
λ	wavelength, [nm]
ν	stretching
ρ.....	rocking
τ.....	torsion
ω	wagging

Chapter 1 Introduction

The quest for finding life beyond the planet Earth is almost as old as the space industry itself. The life sciences department at NASA (National Aeronautics and Space Administration) was founded nearly immediately after its establishment in 1958 and has been one of the highest priorities of the organisation ever since [1]. Soon after, the search for life became an international effort as other space agencies adopted astrobiology as one of their major interests [1]. The search for life in the universe does not only seek the answer to the ever present question of whether humankind and terrestrial life are the only existing life forms, but it also aims to unravel some of the most fundamental questions regarding the origin of life in the universe [2], [3]. These questions are impossible to answer while stuck to the surface of the Earth and therefore space missions to other planets, moons and comets are especially crucial.

Orbiter missions, starting with Mariner 4 as early as 1964, which established Mars as a high priority target for astrobiology, helped to collect the data necessary to enable Mars lander missions [4]. As soon as the 1970s, the Viking missions landed on Mars in order to determine whether the planet harbours life [4]–[6]. Since then, the Martian surface has been extensively explored in the search for extraterrestrial life by multiple other missions such as the Mars Exploration Rovers, Spirit and Opportunity (launched in 2003), Phoenix Mars Mission (2007), Mars Science Laboratory rover Curiosity (2011), and most recently, the InSight lander mission (2018), and the Mars 2020 mission with the Perseverance rover launched in 2020. The interpretation of the results of some of the experiments performed by these missions has been heavily disputed, however, none of the astrobiology missions launched to date has managed to fully confirm the presence of life as of yet [5]–[7]. In addition to the recently launched Mars 2020 Perseverance rover, another rover mission seeking to find life on Mars, ESA's ExoMars, is bound to launch in late 2020s.

Despite Mars being the primary target for space exploration in the search for extraterrestrial life, other corners of the Solar System have also been reached in the pursuit of life detection. The Apollo programme performed in-situ astrobiology experiments on the Moon as early as 1969 and asteroids Vesta and Ceres were studied by the fly-by mission Dawn from 2011 till 2017. The Deep Impact mission, launched in 2005, was the first attempt to land on a comet and analyse its interior. The Messenger probe, launched in 2005, aimed to explore Mercury and Pioneer Venus project launched two spacecraft to investigate Venus in 1978. Most notably, Cassini-Huygens and Galileo, launched in 1997 and 1989 respectively, explored the giant planets in the outer Solar System and their moons and provided evidence that there are other potential life harbouring sites in the Solar System besides Mars [8]–[13]. Saturn's moons Titan and Enceladus or Jupiter's moon

Chapter 1

Europa could even provide a more convenient environment for the presence of past or present life due to their large deposits of water, both in a liquid and in an ice form [8]–[13]. These Icy Worlds are particularly relevant for future planetary exploration as they are cited in the ESA's Voyage 2050 plan as the target of ESA's next large class mission and they are also identified as a high priority planetary target in the latest NASA's Decadal Survey [14]–[17]. Advances in space science and technology have also been making these distant targets become increasingly more reachable.

Among the Icy Worlds, Jupiter's moon Europa is one of the main focus points for astrobiology and the exploration of potentially habitable worlds and has been specifically named in the most recent Planetary Science Decadal Survey as one of the highest priority targets for space exploration in 2013-2022 [14] as well as in the ESA's Voyage 2050 plan [18]. This is due to its sub-surface saline ocean strongly believed to be in contact with a rocky silicate ocean floor. Such an environment, not unlike the Earth's ocean floor, could potentially provide an ideal chemistry and energy balance to harbour life [19].

Europa is the sixth closest moon orbiting Jupiter out of a total of 79 moons. With a diameter of 3138 km, it is Jupiter's fourth largest moon and comparable in size to the Earth's Moon. Even at the closest point, the distance between Jupiter and Earth is approximately 588 million km, more than 10 times the minimum distance between Earth and Mars. Thus, while the transfer time from Earth to Mars could take between 150 to 300 days, the journey to Europa would take at least 6 years [20]. Apart from the extreme transfer time, a mission to Europa would also be exposed to an extremely harsh environment. While the total radiation dose of a 3-year mission to Mars measures in the order of rads, the total radiation dose for a mission landing on Europa is in the order of Mrads over its lifetime of approximately one month [21], [22]. This makes the radiation on the surface of Europa a thousandfold more severe than on Mars, even over a significantly shorter period. Likewise, Europa receives less than 5% of the solar radiation received by Earth [23] and the temperature on the surface of Europa never reaches higher than $-168\text{ }^{\circ}\text{C}$ [24]. At the polar region, the surface temperature could be as low as $-233\text{ }^{\circ}\text{C}$ [24].

The moon is globally covered by a thick layer of ice, estimated to be up to 35 km thick [25] but could vary depending on location (Figure 1-1). This is approximately 7 times as thick as the thickest ice sheet on Earth. However, it is the deep saline ocean underneath the icy crust that is the most interesting site to astrobiologists as the hydrothermal and geochemical processes at the surface of the silicate seafloor could provide the ideal environment for the origin of life [19], [26]–[28]. Even though a number of mole probe missions to drill or melt through the European ice and explore the ocean underneath have been proposed [29]–[31], these concepts are highly

theoretical. Even the significantly thinner Antarctic ice sheets on Earth have proven challenging for exploratory probes. As a result of this, even Earth's own ocean underneath its ice sheets has remained relatively unknown and unexplored. Constraints associated with the application in space, let alone on such a distant planetary target with largely unknown composition, would deem such a mission impossible with the current technology.

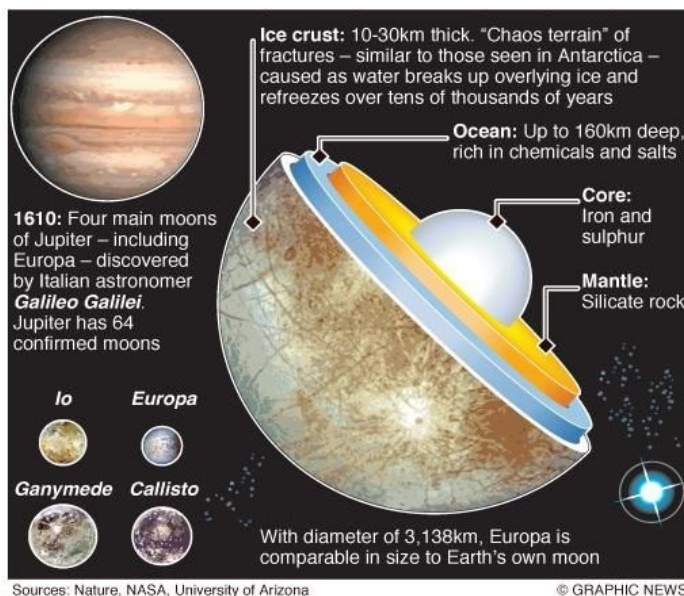


Figure 1-1 Jupiter's moon Europa [373]

To this date, there have been 5 missions that have caught a glimpse of Europa during their fly-by of Jupiter, however, a dedicated mission to Europa is yet to be flown. The first observation of Europa was conducted by Pioneer 10 in 1973 during its fly-by of Jupiter. The probe was too distant to obtain a high quality image, however, some albedo variations on the surface were observed [32]. Similarly, Pioneer 11 could only observe some surface variations during its fly-by of Jupiter in 1974 [32]. In 1979, Voyager 1 made a fly-by of Europa, studying the gravity interactions in the Jovian system, shortly followed by Voyager 2. The Voyager probes provided the first detailed images of Europa and discovered the discoloured cracks on the smooth surface of the moon, leading scientists to the conclusion that the surface is not rocky as previously believed, but rather predominantly made of ice [33]–[35]. This could potentially mean an ocean underneath the ice, which represented a major discovery as the only place in the Solar System known to contain liquid water at the time was Earth [33]–[35]. It was this discovery that also fuelled the following mission exploring the Jovian system, Galileo. The Galileo probe orbited Jupiter between 1995 and 2003 and provided details of Europa's thin atmosphere and high resolution images of the European surface [36], shown in Figure 1-2. Most importantly, however, it provided compelling evidence of the presence of liquid ocean underneath Europa's icy crust [36]. This fuelled further speculations about the presence of extraterrestrial life on Europa and the motivation for further exploration of the distant icy moon.

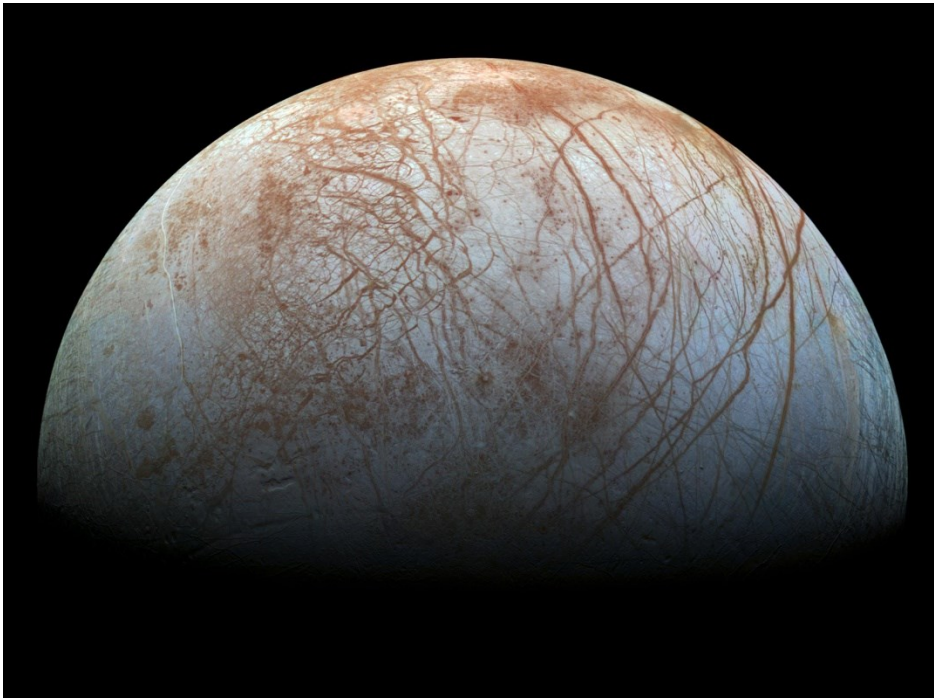


Figure 1-2 The surface of Europa as captured by Galileo [37]

There are two fly-by missions more closely focused on the exploration of Europa currently under development, Europa Clipper and Jupiter Icy Moons Explorer (JUICE), both expected to launch in the early 2020s. A lander mission to Europa has not been confirmed as of yet, however, a conceptual study proposing such a mission was released by NASA in 2016 [19], [26].

Despite not being able to reach the ocean, the proposed Europa lander mission aims to assess the presence of life by sampling the sub-surface material from at least 10 cm depth below the surface [19], [22]. At this depth, potential signs of extraterrestrial life delivered to the surface by geochemical processes would be protected from the outside destructive radiation environment [19], [38]. Consequently, a community announcement was issued in 2017 by NASA encouraging the scientific community to research in-situ instrumentation for the exploration of Europa, specifically focusing on searching for the evidence of life, assessing its habitability and characterising its surface properties [39]. Most recently, a preliminary call for instruments for the in-situ exploration of Europa was issued by NASA NSPIRES in order to assist with the definition of the Europa lander mission concept currently under development at JPL in terms of instrument accommodation in the payload bay and to expand the understanding of the instrument requirements and interfacing [22]. This mission is in its conceptual stage, however, it endorses the necessity for a detailed study of Europa in-situ instrumentation for a potential lander mission as there are many questions yet to be answered. Additionally, many of these questions can also be extrapolated to the exploration of other Icy Worlds, which are also likely to be the target of future planetary exploration [9], [10], [14]–[17], [19], [23], [40]. Most notably, the detection of organics

in space exploration has proven to be challenging in the past and the harsh environmental and mission constraints associated with a mission to Europa introduce additional limits to the design of a life-detecting instrument.

Besides the severely low temperatures and extremely high radiation environment on Europa, detection constraints specific to the exploration of the European surface and sub-surface, such as low concentrations of target molecules in an ice matrix, can have a major impact on the effectiveness of traditional chemical characterization techniques. Similarly, a high level of autonomy and simplicity are highly desirable, if not essential, to ensure the success of a mission to such a distant planetary body with very limited or no connection to Earth during its operation. Additionally, the allowable payload mass and volume requirements for a mission to Europa are significantly stricter than to other more immediate planetary targets such as Mars, thus making the miniaturization of the instrument a high priority goal, if not a necessity. These constraints have not been fully addressed before as most scientific instruments are currently tailored to Mars, the most imminent target for space exploration.

Among the life detecting instruments proposed to date, Raman spectroscopy stands out as an exceptionally versatile non-destructive compositional analysis technique that does not require any sample preparation. It has gained popularity in planetary exploration over the last decade due to its ability to unambiguously identify a vast spectrum of molecules including both minerals and biomolecules important for extraterrestrial exploration. Raman spectra can also reveal information on the molecular structure, material phases and atom arrangements, which is of high importance in contemporary in-situ planetary research [14], [19], [46], [47], [23], [30], [40]–[45].

While Raman spectroscopy was limited to Earth applications due to its size and mass until early 2000s, recent developments in optics and laser technology allowed Raman instruments to be adapted for space applications. Particularly, the most recent Mars lander mission, NASA's Mars 2020, as well as the imminent ESA Mars lander mission, ExoMars, carry Raman spectrometers on board [48]–[51].

However, despite its many advantages, Raman spectroscopy faces a few crucial challenges in terms of the detection of extraterrestrial life and its signatures. One of the main challenges in Raman spectroscopy is the fluorescence interference that may impede the detection of molecules by partially or completely overshadowing the molecule's spectroscopic signature. The severity of the fluorescence noise depends on the sampled material and the excitation wavelength, which makes the choice of the laser source a critical design parameter that needs to be specifically tailored to the targeted molecules. Fluorescence can severely restrict the pool of detectable molecules without the use of an effective fluorescence suppression mechanism and is particularly

Chapter 1

concerning for biological and organic samples, as they tend to be inherently fluorescent, especially at visible excitation wavelengths.

More importantly, most Raman reference spectra are traditionally collected at room temperatures (15-25 °C) and only a very limited number of molecules relevant to astrobiology have been analysed at cryogenic temperatures analogous to Europa [47], [52]. Raman spectroscopy relies on the vibrational properties of molecules and the molecular bonds, which are variable across different temperatures. As such, the extremely low temperatures on Europa can severely impact the resulting Raman spectra. Moreover, the thermal changes within the spectra can be very molecule specific, which makes research into the thermally induced changes in the Raman spectra of relevant molecules critical for the development of a Raman instrument for the exploration of Europa.

Furthermore, traditional Raman spectroscopy is not particularly sensitive to trace molecules within a sampled material. This is particularly concerning for the search for biosignatures on Europa and Icy Worlds as the concentration of the biomolecules is predicted to be extremely low [9], [19], [23]. Research conducted to date indicates that the concentration of organics in the European ice could be in the order of ppb (part per billion) and as low as 0.01 ppb [9], [19], [23]. The Europa Lander Mission currently under development at NASA requires the limit of detection (LOD) for vibrational spectroscopy as low as 1 nM (0.1ppb) [19]. Detection at such low concentrations is not achievable with traditional Raman spectroscopy.

This research aims to explore and assess the critical limitations in Raman spectroscopy for the exploration of Europa and identify key design parameters for the development of a Raman instrument optimized for the detection of biosignatures on Icy Worlds. By mapping the current development in the field of in-situ planetary instrumentation and Raman spectroscopy, this work provides an assessment of a suitable Raman instrument design as well as the key limitations of contemporary Raman technology and techniques. The outcome is then used to propose future directions in Raman spectroscopy research in order to allow the development of instruments compatible with a landed mission to Europa and its scientific goals.

Chapter 2 Background

The search for extraterrestrial life has always been one of the most important motivating factors for planetary exploration. With its saline ocean and silicate seafloor providing the ideal environment for the emergence of life [19], [26]–[28], Europa represents one of the most likely extraterrestrial sites to harbour life in our solar system. As such, it generates a lot of interest in the field of astrobiology and it has been named by both NASA and ESA as a high priority target for future planetary exploration [14], [18]. A Europa Lander mission has also been proposed and the concept is currently under development at NASA [19], [26].

Located in the outer Solar System and orbiting in a high radiation field of Jupiter, any mission to Europa will be exposed to an extremely harsh environment and subject to mission constraints baring severe functional implications on the instrumentation on board. Similarly, as an Icy World predominantly composed of water, Europa is a very different planetary target to the rocky surfaces of Mars or the Moon, which have been the primary focus of planetary exploration to date. This introduces a unique challenge in the field of space instrumentation, which has historically always relied on flight heritage and prioritized proven technology over innovation, as instruments with flight heritage from Martian missions may not be compatible with a mission to Europa at all or may need significant modifications to meet the mission's criteria. Since most contemporary instruments for planetary exploration have been designed to operate on Mars, instrumentation for the exploration of the vastly different environments on Icy Worlds, such as Europa, remains a relatively unexplored territory. The development of robust life-detecting instruments compatible with a lander mission to Europa is thus a critical step towards the exploration of this distant planetary target. Indeed, ESA's Voyage 2050 plan for future directions in planetary exploration, which states a mission to either Saturnian or Jovian Icy Moons as a high priority target, explicitly highlights the lack of technology readiness of in-situ instrumentation for these missions to be a major challenge and encourages further development in this area [18]:

“Surface elements, although of the utmost scientific interest, present critical technological challenges. Instrument development for such missions is strongly encouraged to achieve and boost the scientific return, for example in the characterisation of complex chemicals.”
[18]

The maturation of in-situ instrumentation technologies for the exploration of Icy Worlds is also critical to progress the Europa Lander mission currently under development at NASA, or any other Europa lander mission, past the conceptual stage. This necessity is also supported by the release of the community announcements and preliminary call for instruments encouraging scientists to focus on in-situ instrumentation compatible with the NASA's Europa lander mission concept and

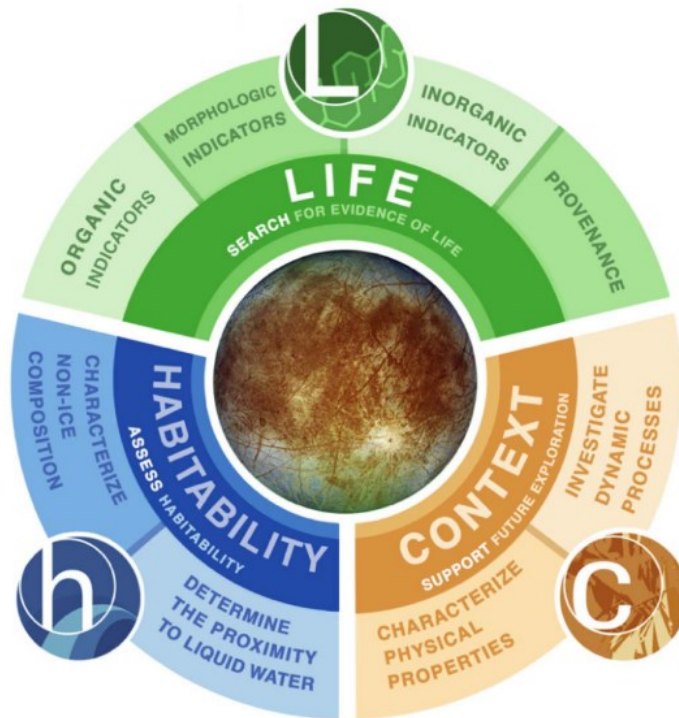


Figure 2-1 Europa lander mission concept science goals and objectives, searching for the evidence of life being the highest priority goal, followed by assessing the habitability and then supporting future exploration [19]

its scientific goals (shown in Figure 2-1), especially focusing on detecting life, assessing the moon's habitability and characterizing its surface and subsurface [22], [39].

However, setting aside the harsh environmental and mission constraints of a mission to Europa, the task to detect extraterrestrial life itself has proven challenging at best in the past. As of yet, no instrumentation has been able to provide a uniformly accepted unambiguous proof of the presence of life on any of the explored extraterrestrial sites to date. This is not necessarily due to the lack of life or signs of life in the sampled material. Rather, it may be due to insufficient detection capabilities, the nature of the employed detection methods and their limitations and, to a broader extent, the definition of life and an unambiguous biosignature itself [5].

2.1 Life Detection on Europa

Ever since the Viking missions, there has been no in-situ attempt at directly detecting life on another planet and even this attempt failed to provide conclusive results. Even though the results of individual experiments performed by various instruments could be interpreted as a proof of metabolic activity, the results of the entire Viking instrument suite together could not confirm or exclude the presence of life [5], [6].

All subsequent astrobiology missions focused on indirect detection of life by targeting so called biosignatures, molecules or features characteristic of life as we know it. Biosignatures include simple molecular targets that are only known to be produced or used by life or complex organic matter that is unlikely to be formed without the presence of life. However, biosignatures can also be features such as concentrations, distribution and ratios of molecules, and processes connected to biological activity [5], [44]. Naturally, these biosignatures provide various levels of confidence in the presence of life [5], [43], [44], [53], [54]. The idea of biosignatures is also based on the assumption that extraterrestrial life is similar to life on Earth or originated through similar processes [23]. This alone leads to some elemental issues with the definition of a biosignature due to the scientific controversies associated with the origin of life on Earth [54]. Additionally, the biochemistry of alien life could be entirely, or at least significantly, different to terrestrial biochemistry. A theory of chance and necessity states that even though extraterrestrial life would most likely use the same building blocks, it could also only use the simplest and earliest evolutionary forms of these building blocks and any subsequent evolution would be dependent on the environment, just as it was on Earth [55]. This means that complex structures such as phospholipids, proteins or even entire cells that were not present on the prebiotic Earth and could be targeted as a direct sign of life, could not actually be present in any life form on Europa, Mars or Titan. On the other hand, a simple amino acid such as alanine or glycine, that are the most abundant, could represent the necessary prebiotic building blocks and any more complex amino acids would simply be a result of evolutionary adaptation to the specific environment [55]. However, these simple amino acids can also be formed abiotically and have also been found in meteorites and their detection would thus only signal the hypothetical possibility of future emergence of life at best [56].

Therefore, a single biosignature is not a sufficient evidence of life and multiple lines of distinct biosignatures will have to be detected in order to confirm the presence of life [19], [43], [44]. Despite the main focus being on molecular organic biosignatures, morphological as well as biomineral signs of life are also targeted by the Europa Lander mission [19], [22]. This also introduces additional difficulty in the search for life in space as it calls for instrumentation capable of detecting a wide range of compounds, the chemistry of which might not be known on Earth [57].

Furthermore, while the signs of terrestrial-like life are universal across the Solar System and even further, the likelihood of detection varies significantly depending on the environment. I. e. the overall set of chemicals that signal the presence of terrestrial life is the same regardless of the location in the universe. However, certain chemicals might be very likely to signal Martian life on Mars while very unlikely to occur on Europa. The likelihood of occurrence, and consequently the

probability of detection, is especially crucial for a mission to Europa that can only carry a couple of simplified instruments on board. The biosignatures that have been proposed to date are numerous and vary greatly in terms of ambiguity, abundance, ease of detection, durability and, most importantly, likelihood of occurrence on Europa. A detailed review of biosignatures surveying these aspects in reference to Europa, its environment and possible indigenous life forms is therefore needed.

2.2 Mission Constraints and Environmental Limitations

Besides selecting appropriate molecular targets, other important factors affecting the development of scientific instruments for in-situ exploration of Europa are the constraints associated with the mission architecture and limitations imposed by the European harsh environment. These limitations are discussed in detail in the following sections.

2.2.1 Mass and Size

Due to the nature of exploring the unknown, the general consensus is that multiple instruments working in conjunction with one another are necessary to provide an unambiguous proof of extraterrestrial life [19], [58]. However, for a mission to Europa, the payload bay will be very limited in mass and size due to the direct impact of these parameters on the mission cost. As such, only a few simplified instruments could be accommodated, stressing the necessity to select only the most versatile and capable set of instruments that could achieve this goal while also complying with the mission's constraints.

While the Europa Lander mission has not been given the green light yet and the final mass allocations can change significantly and also differ for any other mission to Europa, the Science Payload Draft Proposal Information Package allocates 32.7 kg and 34.5 l volume for the payload [22]. This includes a baseline payload of 5 instruments [22]. In the most recent mission update, the payload mass has been increased to 42.5 kg including margin [26], however, this is still significantly less than the payload mass allocated by most of the Martian lander missions flown to date. Table 2-1 shows the mass allocation comparison of the planned Europa Lander mission and a few notable Mars missions. The payload mass on the Curiosity rover is approximately twice the Europa Lander payload mass and includes more than twice as many scientific instruments. The payload mass on Perseverance, the most recently launched Martian rover, is much less than the Curiosity payload mass, however, it is still much higher than the payload mass on the planned Europa Lander mission. It is also important to note that the Perseverance rover is much heavier overall, 1025 kg as opposed to the Europa Lander's 575 kg. While the overall mass is not allocated

to the scientific instruments directly, the instruments can still benefit from it as it allows the accommodation of additional supporting systems and mechanisms, which may not be available on the European lander. This in turn calls for higher autonomy, robust instrument design and simplicity in both the design and the instrument's operation.

Mission	Launch Year	Payload Mass (kg)
Europa Lander	TBC	32.7/42.5
Viking 1	1975	91
Curiosity	2007	80
Phoenix	2011	55
InSight	2018	50
Perseverance	2020	52

Table 2-1 Comparison of payload mass between a mission to Europa and a few notable missions to Mars flown to date (based on publicly available data from NASA and [19], [22], [26])

2.2.2 Target Molecule Concentration

Apart from the most obvious limitations of mass and size, there are other limits inherent to detecting life on Europa. Perhaps the most restricting when it comes to instrumentation is the low concentration of molecules in an ice matrix. Based on calculations of the Europa biomass, the concentrations of potential microbial cells are minimal [9], [23]. Likewise, observations of cell concentrations in Europa analogue sites, such as Lake Vostok, show that the cell concentrations in the near sub-surface ice of the European crust are very likely to be extremely low [19].

The low concentration of biological molecules in the sub-surface ice is also a very reasonable assumption given the possible pathways of the origin of life on Europa. The necessary energy for the emergence of life could have originated either through photosynthesis in the surface layers of the ice crust or through redox reactions at the water interface with the mineral sea floor. While photosynthesis is widely regarded as one of the most crucial processes in the evolution of life as we know it on Earth, the available energy from radiation on the surface of Europa is significantly lower than on Earth. This makes photosynthesis potentially less pivotal in the evolution of life on Europa. Additionally, severe ionizing radiation would destroy any organic material on the surface of the European ice crust [23]. Even though just a relatively thin layer of ice would protect any potential life forms from the destructive radiation on the surface, it is questionable whether there would be enough energy from radiation for photosynthesis at these depths. This makes the

Chapter 2

theory of life originating at the sea floor of Europa and potentially migrating upwards towards the surface more favourable [19], [59].

This also gives rise to the question of biomass flux on Europa and whether organics near the surface could be detectable at all. The geochemical processes on Europa are not yet well understood due to many question marks associated with its composition that would drive these processes [59]. Figure 2-2 shows a geochemical model of the surface layers of Europa and possible habitable zones and sites for the detection of biosignatures. Due to the hydrothermal energy generated by tidal forces and the movement of ice sheets, the water at the water-ice interface and the ice crust itself is very likely to be in a slow but constant flux [9], [59], [60]. Molecules as well as microbial cells and colonies could thus travel up through the ice to the surface [9], [59], [60]. However, if this was the case, the concentrations near the surface could be extremely low.

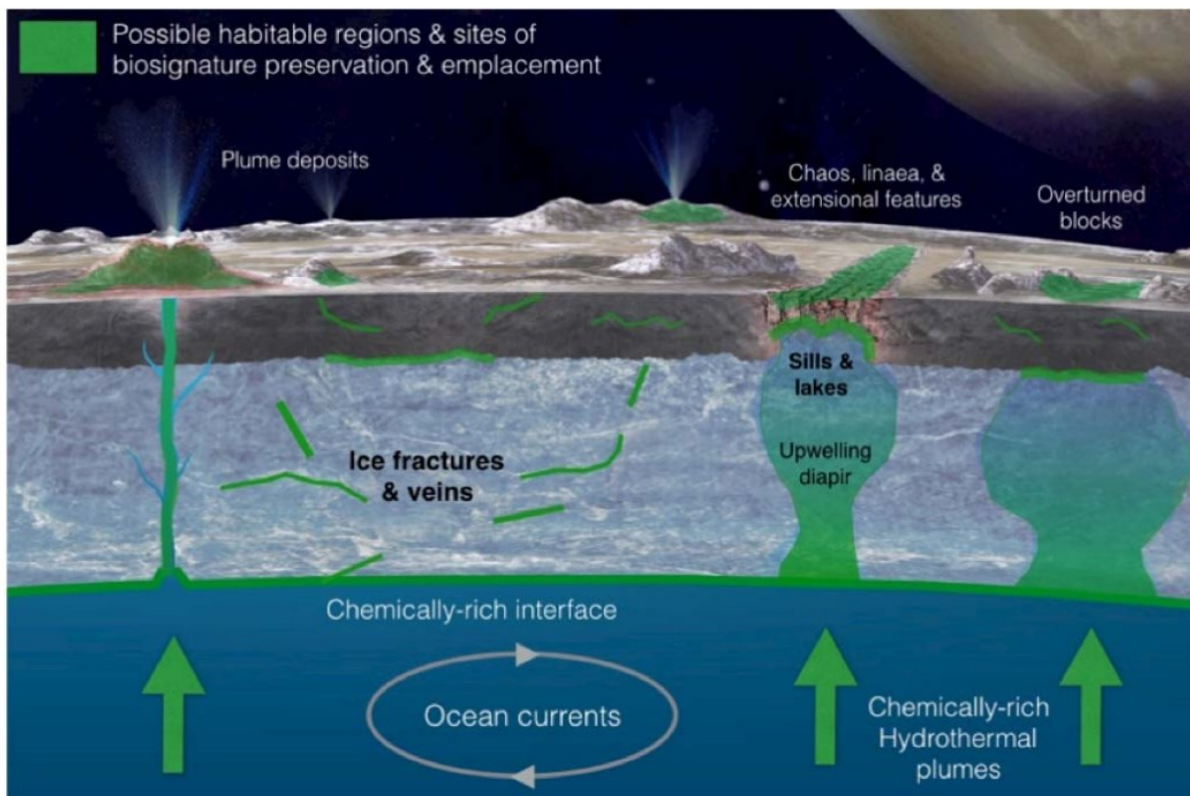


Figure 2-2 Geochemical processes on Europa delivering material from the ocean to the surface are likely to have a major impact on the distribution of any possible biosignatures on Europa. Potential habitable zones include extensional features, plumes, diapirs, sills and perched lakes [19]

Specifically, research conducted to date indicates that the concentration of organics in the European ice could be in the order of ppb and as low as 0.01 ppb [9], [19], [23]. The Europa Lander mission study currently under development at NASA proposes the required detection limit for

organics in the European soil of 1 picomole per gram of the sampled material and limit of detection (LOD) for vibrational spectroscopy as low as 1 nM (i.e. 0.1ppb) [19]. For comparison, the concentration of biomolecules in the Martian regolith is estimated to be between 0.35 wt% to 0.0001 wt% (i.e. 1 ppm), which is in the order of 10^3 to 10^8 magnitude higher than the concentration predicted on Europa [61]–[64]. This immediately imposes a strict constraint for many instruments and even those that are capable of detecting matter in such a low concentration could be restricted by the presence of ice and salts in the European soil [5], [43], [65]–[68]. It is also important to note that the concentration of biomolecules in the Martian ice, which remains unexplored to date and which has also been indicated as a high priority target for future planetary exploration [14], [42], [62], [69], [70], is estimated to be 1 ppb or lower, which is comparable to concentrations on Europa [61]–[63]. As such, the development of instruments capable of these extremely low limits of detection is not only relevant for the exploration of Europa and Icy Worlds but also for the future exploration of Mars.

2.2.3 Cryogenic Temperatures

Another key consideration for life detection on Europa is the extremely low temperature, which varies between -233 to -168 °C on the surface depending on the location and time of day [24], [71]. This is significantly lower than any temperature ever recorded on Earth or Mars. For comparison, the lowest temperature recorded on the surface of Earth is -89.9 °C, or -98 °C considering satellite observation data [72]. The average surface temperature on Mars is -63 °C with the lowest recorded temperature being -143 °C in the Martian polar regions as estimated from the Viking Orbiter Infrared Thermal Mapper data. Based on current estimates, the depth at which potential biosignatures would be shielded from the outside radiation varies from approximately 1 cm at the lower radiation sites around the poles to 10-20 cm at the high radiation region around the equator [38]. While drilling through kilometres of ice in the search for life would be challenging for a spacecraft mission, these depths should be relatively easy to achieve. The depth of 10 cm is also the minimum depth at which the proposed Europa Lander mission aims to collect samples [19], [26].

The temperature profile within the icy shell of Europa is shown in Figure 2-3. While the temperature on the surface could be as low as -233 °C, the temperature at the depth of 10 cm in the ice shell is expected to be roughly -175 °C [24], [71]. This would vary depending on the location and the time of day and it could be as low as -200 °C at the polar regions or if the 10 cm sampling depth is not achieved.

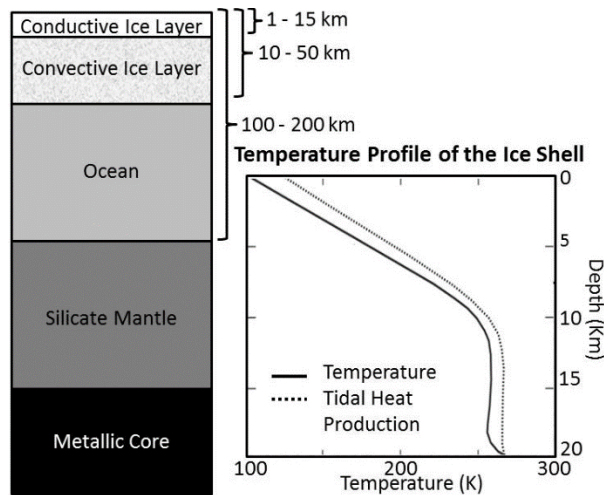


Figure 2-3 The temperature profile of the European ice crust (based on data from [71] and [73])

A mole probe mission to Europa could hypothetically reach lower layers of the European ice shell than a lander probe. As such, a mole probe would be exposed to higher temperatures as the temperature in the ice is thought to rise dramatically and could reach -98 to -75 °C at around 5 km below the surface and -33 °C at the depth of 10 km [71], [73]. However, even at 5 km depth the temperature could still be below any temperature ever recorded on Earth to date [72]. It is also important to note that even the relatively modest 5 km depth on Europa is approximately as deep as the thickest ice sheet on Earth [74] and could be very challenging to drill through for a space probe. Between 10 and 20 km below the surface, the temperature then stays uniform around -13 °C until it reaches 0 °C at the water-ice surface [71], [73], as displayed in Figure 2-3 [71], [73].

While there are no analogous sites on Earth for temperatures as low as -175 °C and terrestrial organisms can only survive temperatures around -20 °C to -26 °C before undergoing vitrification (a form of cryopreservation allowing hydrated cells to survive in cryogenic temperatures) [75], they can survive temperatures down to or below 10 K while vitrified and thus adapt to survive even the most extreme environment on Earth [75]. This signals that extremophilic life on Europa could have evolved to adapt to these critical temperatures. Additionally, cryopreserved life or its remnants from warmer lower layers of the ice shell or the ocean could be transferred to the colder surface layers by the convection within the ice.

However, these extremely low temperatures that are beyond any extreme environment encountered on Earth could be detrimental for scientific instruments. Many critical components for space instruments have a restricted operational temperature range. For electronics, the typical minimum temperature is around -55 °C as the performance of many electrical components, such as resistors and capacitors, changes dramatically with temperature. Likewise, many instruments rely on the molecular properties of the sample, which are dependent on the

temperature of the sample, and measurements at these extremely low temperatures can thus significantly affect the science output of the instrument.

Alternative to in-situ measurements within the icy shell and below, recent observations confirmed the presence of a water plume ejecting water from the European subsurface into the atmosphere [76], which could potentially contain biosignatures from the European ocean. This creates the possibility of performing some interesting in-situ experiments and analysis through a fly by mission to Europa without having to land on the surface or drill through the ice shell. However, once ejected from within the protective layer of the ice, the high radiation field at Europa would destroy any organics in the water plume that could be potentially detected by an orbiter spacecraft. The event was also found to be rare and highly localized and could be difficult to predict [76]. A lander scale mission and exposure to Europa's extremely cold surface and near sub-surface is therefore necessary to fully confirm or disprove the presence of life on Europa.

2.2.4 Interference

While the presence of large amounts of liquid water makes Europa a prime target in the search for extraterrestrial life, it can also be a challenging factor for life detecting instruments. While Infrared Spectroscopy is widely used on Earth and has been a popular choice for space applications as well, it is not suitable for aqueous solutions due to the intense water absorption that causes interference. There are solutions for extracting the water absorption from the data, however, these often introduce additional sample preparation and complexity and can prove ineffective for low concentrations [66], [77]. Thus, while IR spectroscopy can be effective for the exploration of Mars or the Lunar surface as reported from previous applications as well as the foreseen use for future missions [78]–[80], the predominance of ice in the European soil somewhat disqualifies the technique for a mission to Europa.

Similarly, the presence of salts and other non-volatile molecules causes potentially crucial ionization suppression issues for separation based mass spectrometry [5], [65]–[67]. The presence of salts could also impede the bonding of antibodies and thus severely limit the operation of instrumentation based on antibody microarray immunoassays [5], [81]. This is also an important consideration since the surface of Europa as well as its ocean are inherently saline [19], [82], [83].

2.2.5 High Radiation Environment

The high radiation environment in the Jovian system is also a uniquely challenging aspect of a mission to Europa. According to the Europa Lander concept study, the lander would experience 1.7 Mrad on the surface of Europa over its lifetime [22]. Even though shielding of the instrument

is provided to decrease the total ionizing dose to 150 krad, this is still a very harsh environment for most instruments and electronics and a total ionizing dose of 300 krad is proposed for the qualification of the instruments in order to account for uncertainties [22]. Table 2-2 shows a comparison of the total radiation dose experienced during various space missions [21]. The qualification level of the radiation dose for the proposed lander mission to Europa is more than thousandfold the radiation dose of a 3-year mission to Mars.

Mission	Radiation Dose (rad)
Space Shuttle Mission 41-C (8-day mission orbiting the Earth at 460 km)	0.559
Apollo 14 (9-day mission to the Moon)	1.14
Skylab 4 (87-day mission orbiting the Earth at 473 km)	17.8
ISS Mission (up to 6 months orbiting Earth at 353 km)	16
Estimated Mars Mission (3 years)	120
Europa Lander proposed instrument qualification load (1-month mission)	300 000

Table 2-2 Comparison of radiation dose experienced during various missions [21]

2.2.6 Transfer Time & Distance

Other key considerations include the long transfer time to Europa, which might take many years more to complete compared to other planetary targets such as Mars. Based on the current plans of the conceptual Europa Lander mission, it will take more than 7 years for the spacecraft to reach Europa [22]. Due to the distance between Europa and Earth there would also be a very limited contact between the lander module and Earth, calling for high autonomy and simplicity of the instruments to prevent critical failures [19].

2.3 Raman spectroscopy

Among life detecting instruments, the technique that stands out as one of the most powerful and versatile life detection tools for planetary in-situ exploration is Raman spectroscopy. It is a relatively young technique that was limited to Earth applications until very recently due to mass and size limitations. However, it has attracted a lot of attention in recent years due to its high potential for extraterrestrial exploration and Raman spectrometers are carried on board of both

the most recent Mars lander mission, NASA's Mars 2020, as well as the imminent ESA Mars lander mission, ExoMars [48]–[51].

As opposed to other spectroscopy techniques, Raman spectroscopy was extremely limited as an analysis method until the discovery of lasers in the 1960s [51], [84]. The technique was later overshadowed by the rapid developments in the Fourier transform Infrared Spectroscopy in the 1980s, however, since then it has become very popular in Earth based laboratories. Up until early 2000s, the size of the instruments was a somewhat limiting factor regarding applications in the field, let alone in space. However, due to advances in laser and optics technology, ever since then, there has been a continuous effort to adapt this technique for applications in planetary sciences and exploit its numerous merits in the search for extraterrestrial life [85].

Raman spectroscopy is based on inelastic scattering of incident monochromatic light, which provides a vibrational mode spectrum of the bonds within the illuminated molecules (as shown in Figure 2-4 and Figure 2-5). The incident laser causes excitation to a higher vibrational energy state by transmitting a photon of a certain energy to the illuminated molecule, the excited molecule then relaxes to a new lower energy state, emitting a photon of a different energy (i.e. inelastic scattering). The change in the energy also induces a change in the wavelength. This is measured by the Raman instrument and recorded as a "Raman shift". The Raman shift is dependent on the vibrational structure of a molecule. The resulting Raman spectrum shows the Raman shift (usually converted from wavelength to wavenumber) and each peak in the spectrum shows a vibrational mode of the illuminated molecule. The spectrum thus determines the vibrational structure of the excited molecule, which allows its identification. An example comparison of Raman spectra of water, ice and dry ice is provided in Figure 2-5. Molecules of water and ice share the same structure, however, the strength of the bonds within the molecule of ice is different due to the phase change and therefore the energy needed to excite the vibrational mode is also slightly different. The spectrum of dry ice is completely different as it is a completely different molecule.

Vibrational mode spectra are highly specific to each molecule, which provides a chemical fingerprint of the molecule and allows the unambiguous identification of various compounds or mixtures [23], [51], [86]. This is particularly useful for the characterization of molecules in a mixture of multiple compounds, especially if the composition of the mixture is not known prior to analysis. Furthermore, it can also provide information on the crystal structure, polymorph form or phase of the sample [86]. As shown in Figure 2-5, water and ice, which share their chemical composition, yield different Raman spectra due to the varying vibrational properties between the two phases.

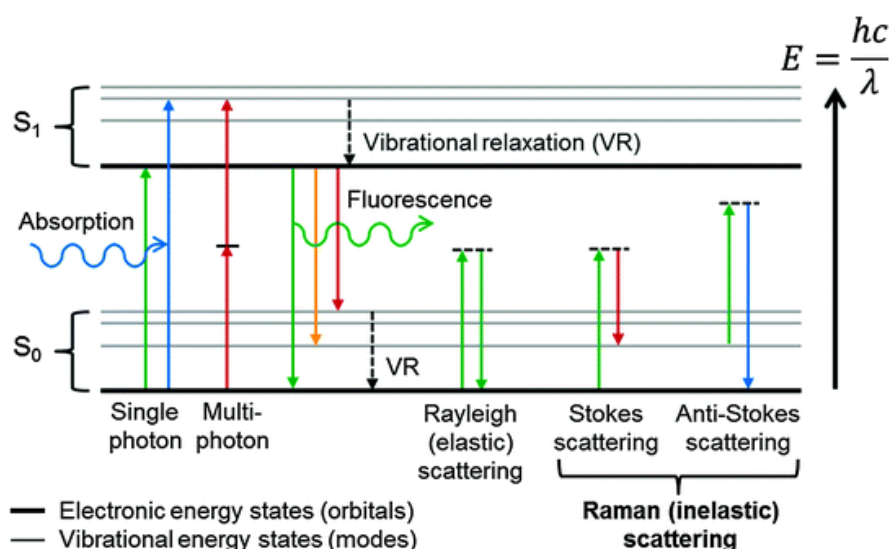


Figure 2-4 Jablonski energy level diagram showing the electronic and vibrational transitions in a molecule including absorption, fluorescence, elastic scattering and Raman scattering [87], E = energy; h = Planck's constant; c = speed of light; λ = wavelength)

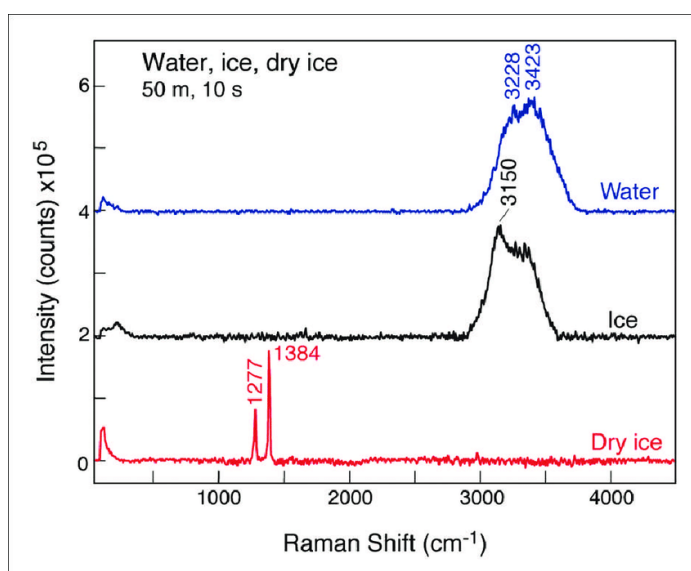


Figure 2-5 Raman spectra of water in liquid and ice form and dry ice [88]

Raman spectroscopy has been shown to be very sensitive and capable of analysing both mineral and organic chemical composition at high spatial and spectral resolution, which is particularly useful for planetary exploration as high versatility and sensitivity to unknown materials are key for such an application [23], [51], [89]–[94]. In particular, the ability to identify both organic and inorganic compounds makes Raman spectroscopy uniquely versatile among other analytical techniques and allows it to address all three science goals of the proposed Europa Lander mission shown in Figure 2-1.

Furthermore, water is a weak scatterer and thus the interference of the ice matrix with the spectra of potential organic matter would be minimal [95], [96]. There is also no need for contact with the sample, thus avoiding any possible contamination. This does not only eliminate any terrestrial contamination but also cross contamination between different samples. Such a feature is especially advantageous for assessing the distribution of compounds.

Raman spectroscopy is a rapid, non-invasive and non-destructive method capable of detecting solid, liquids and gases alike, without the need for any sample preparation. In fact, there have been reports of additional sample preparation degrading the obtained Raman signal [97]. These qualities are a major advantage for space applications as it reduces the complexity and possible failure modes. This is especially important for a mission to Europa where autonomy and simplicity of the instrumentation are highly desirable in order to ensure the success of the mission [19], [23].

Even though Raman spectroscopy is a relatively young technology compared to other molecular spectroscopy techniques, it is also one of the fastest growing areas within chemical composition instrumentation and it is used for a wide range of applications on Earth with excellent results. Due to continuous advancements in Raman spectroscopy and enabling technology, the field of its application is rapidly expanding [86].

Considering its capabilities, high versatility and numerous advantages, Raman spectroscopy is favoured by many for future in-situ space exploration [23], [51], [98]–[103], [53], [58], [70], [85], [89], [90], [93], [95]. Its potential is further highlighted by its inclusion in the payload of the most recent rover mission to Mars, Mars 2020 (developed by NASA), as well as the most imminent mission to Mars, ExoMars (developed by ESA & Roscosmos) [48]–[51]. Furthermore, it is also cited as one of the favoured instruments for the Europa Lander mission proposed by NASA [19], [26].

However, Raman spectroscopy for planetary exploration has very limited flight heritage to date and there are a few notable challenges associated with the technique and its application for the detection of organics in space.

2.3.1 Challenges: Mass and Size

Despite being widely used on Earth, Raman spectroscopy has only recently emerged as a possible strategy for material characterisation for space exploration due to the recent advances in optics and laser technologies. Until recently, Raman spectrometers were heavy and large instruments that were not suitable for application in space. Even though the recent developments have allowed sufficient miniaturization in order to be considered for missions to Mars, there are still

improvements to be made in order to fit the requirements for a mission to more distant targets such as Europa or Enceladus where the size and mass constraints are substantially stricter [23], [51], [89], [98].

Furthermore, while miniaturized and portable Raman spectrometers have become common for terrestrial exploration, their spectral resolution and capabilities are significantly lower than that of the available laboratory equipment. The detection of organic material using these miniaturized systems has proven particularly challenging due to fluorescence, which is also one of the main limitations of Raman spectroscopy [51], [90], [95].

2.3.2 Challenges: Fluorescence

Fluorescence occurs when a molecule is excited to a higher energy state upon receiving energy from the laser source and then emitting the received energy as it relaxes back to a lower energy state. This causes fluorescence interference in the spectra and it is one of the major concerns of Raman spectroscopy in the detection of organics and biological samples [51], [58], [91], [104]. Even though efforts have been made to eliminate or reduce this effect, these attempts usually result in size, mass or additional complexity trade-offs that are inconvenient for application in space exploration.

There are various methods of reducing the effect of fluorescence in Raman spectroscopy. The simplest method of mitigating the fluorescence interference is using computational methods to subtract the fluorescence background from the data. A range of fluorescence reducing computational methods have been developed to date including baseline estimation using wavelet transformation [105], principal component analysis [106], and polynomial curve-fitting [107]. The major advantage of these methods is their independence of the instrument set up and no need for physical implementation. However, this also significantly limits their performance. These methods estimate the fluorescence baseline and subtract the fluorescent background from the Raman spectra, however, this is ineffective if the fluorescence background completely overshadows the Raman signature as it cannot discriminate between the Raman signal and fluorescence.

In order to fully resolve the Raman signal from the fluorescence noise, computational methods need to be implemented in conjunction with a change of a physical parameter, such as the excitation wavelength in the Serially Shifted Excitation (SSE) method or the acquisition time in time gating. SSE is a computational method that processes a set of raw spectra of the sample collected repeatedly over a number of slightly shifted excitation frequencies, e.g. 1 cm^{-1} apart. The SSE algorithm then resolves the Raman and fluorescence components of the spectra by

numerically solving a matrix-vector system of equations constructed with the obtained data [108], [109]. SSE is based on Shifted Excitation Raman Difference Spectroscopy (SERDS) [110], which subtracts Raman spectra from a slightly shifted excitation wavelength but still fails to recover Raman bands if their intensity is less than the shot noise of the fluorescence. While SERDS uses only two excitation frequencies, SSE uses at least 3 shifted excitation frequencies to collect the raw spectra, which allows the SSE method to fully resolve the Raman and fluorescence spectral components and fully recover the Raman spectra even if completely buried in the fluorescence [108], [109]. This gives the method a significant advantage over traditional computational methods for fluorescence suppression. A comparison of the SSE output to other common fluorescence mitigation methods is displayed in Figure 2-6. However, it is also important to note that this method requires precise control of the laser source wavelength, which requires the use of tunable laser sources with a sufficiently narrow spectral linewidth, and which introduces additional complexity to the instrument design.

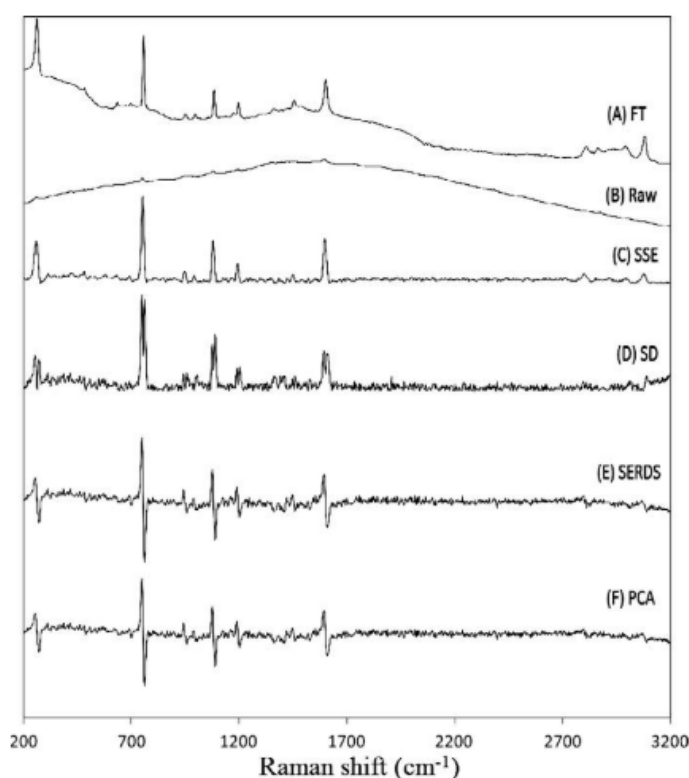


Figure 2-6 A comparison of the SSE method and other common fluorescence mitigation methods using 4-bromo-N, N-dimethyl-aniline. (A) Fourier-Transform (FT) Raman spectrum acquired using 1064 nm laser. (B) Unprocessed dispersive Raman spectrum at 785 nm laser. (C) Raman spectra processed using SSE. (D) Standard deviation (SD) Raman spectrum. (E) SERDS spectrum (using 2 spectra acquisitions). (F) Principal Component Analysis (PCA) Raman spectrum [111].

Chapter 2

Another highly efficient method of reducing the fluorescence background is time gating, such as implemented on SuperCam, one of the most recently launched Raman instruments for Mars SuperCam [50]. This method exploits the instantaneous character of Raman scattering as opposed to fluorescence which occurs in picoseconds to milliseconds after the Raman signal [90], [112], [113]. Collecting data only over short pulses of the operation of the excitation source can therefore exclude the fluorescence from the obtained spectra. This method can be very efficient, however, it also relies on fast pulsed lasers and excellent capabilities of the detector to resolve on the sub nanosecond timescale providing a sufficient time resolution. Time gating has until recently relied on complex streak cameras, which are traditionally heavy and not suited for spacecraft applications [90], [100], [101], [113]. Nowadays, single photon avalanche diode arrays (SPAD arrays) are capable of nanosecond time gating, which allows for miniaturization for their application in planetary sciences [90], [100], [101]. Despite being a very efficient method, it has not been able to avoid fluorescence all together, especially for organics where fluorescence takes place after sub-nanosecond intervals which has proven to be problematic to resolve with current SPAD arrays [90], [112].

By far the simplest method of avoiding fluorescence interference is tailoring the wavelength of the excitation source to the detection target. The excitation wavelength of the laser source is one of the most critical design parameters in Raman spectroscopy as it is directly tied with the fluorescence interference, signal strength as well as the type of molecules detectable with the particular instrument. Various excitation wavelengths are suited for different molecules and some molecules may not be detectable with wavelengths within a certain range at all. Likewise, the excitation wavelength causing fluorescence is also dependent on the sample and its composition. For instance, most organics will exhibit fluorescence in the visible spectrum [58], [85], [104], [114], [115].

Visible spectrum and near infrared (NIR) spectrum lasers have been most commonly used for Raman spectroscopy as they represent a well developed and readily available technology. This is also why they have been popular for miniaturized Raman systems as well [90]. UV and deep UV Raman systems are less common due to the lower technology readiness of UV lasers and other enabling technology associated with the difficulties of incorporating these high energy lasers into the Raman system.

The general rule is that higher wavelengths approaching the infrared spectrum, such as 785 nm and 1064 nm, generate less fluorescence due to the decrease in the excitation energy that is not sufficient to excite the molecules to higher energy state [90], [113], [115], [116]. However, this also has direct implications on the resulting Raman signal, which decreases at longer wavelengths

as well. The intensity of the Raman scattering signal is inversely proportional to the fourth power of the excitation wavelength and thus longer wavelengths yield significantly weaker signals [90], [98], [115]. As a result of this, IR excitation source would generate largely fluorescence-free spectra but at the cost of generating very low Raman signal, which would make some molecules, especially those in low concentrations, undetectable [103].

Using near infrared excitation wavelengths has been common practice for the analysis of biological or organic samples in order to reduce the effect of fluorescence while partially avoiding the weaker signals of IR excitation. Particularly, the wavelength of 785 nm has been routinely employed for biological samples. However, this wavelength still exhibits fluorescence that is critical for some organic samples [90], [117]. The less common wavelength of 1064 nm has also been used, showing significantly decreased levels of fluorescence [117]. Nevertheless, the weaker Raman signal would make the detection of molecules dispersed in a low concentration solution very challenging [51].

An effective solution of reducing the fluorescence background interference is using a deep UV excitation wavelength as the fluorescence and Raman scattering signals are well separated in this region. This method is used on one of the most recently launched Mars Raman instruments, SHERLOC [118]. Figure 2-7 shows the fluorescence emission region of a number of different materials compared to the emission range of a DUV Raman system at 224 nm, 248 nm and 266 nm.

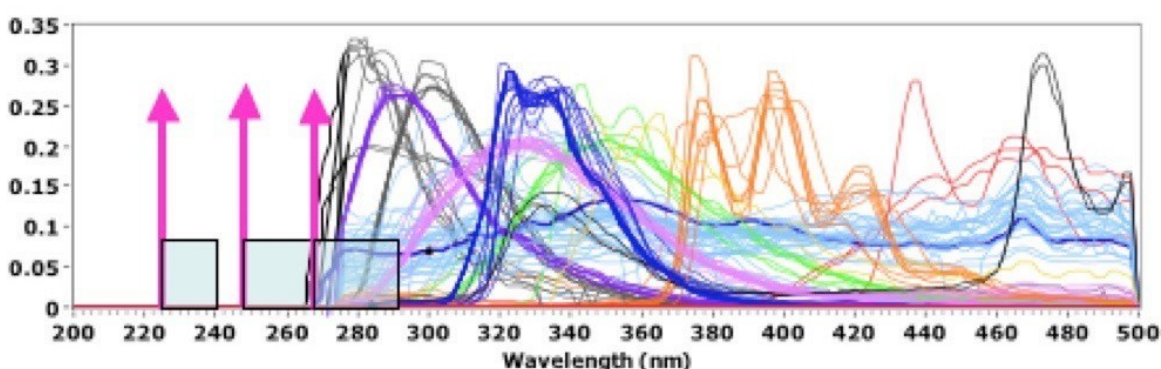


Figure 2-7 The fluorescence emission region of a number of different materials compared to the emission range of a DUV Raman system at 224 nm, 248 nm and 266 nm [119]

Due to the inverse dependence of the Raman signal on the excitation wavelength, UV excitation yields very strong Raman signals compared to NIR, which is particularly favourable for detecting molecules at low concentrations [58], [85], [98], [115], [120]. Furthermore, organics often experience a resonance effect in the UV region which enhances the signal up to 10^6 times [114],

[115], [120]–[123]. This signal enhancement detected in carbonaceous and aromatic organics makes this method especially favourable for applications where the detection of biological and organic molecules is the primary interest [98], [104], [114], [115], [121], [122], [124].

One of the concerns associated with deep UV Raman spectroscopy for the detection of organics is the thermal damage caused by the high energy laser source [86], [98]. The thermal degradation of the sample could greatly affect the quality of the resulting spectra. Up until recently, large Raman systems employing complex mechanisms keeping the sample in a continuous movement were necessary in order to avoid its degradation and to explore the fluorescence-free UV enhanced signals with resonance and pre-resonance effects. While advances in pulsed laser technology mitigate this issue to a certain degree, deep UV lasers are also traditionally sizeable and heavy instruments compared to visible and IR lasers, making their use somewhat limited for both terrestrial and extraterrestrial in-situ exploration.

While visible and IR Raman systems have been proposed and studied as a viable solution for planetary exploration for over a decade now, deep UV Raman spectroscopy has only recently emerged as a possible life detection technique for space applications [85], [94], [98], [104], [120]. Recent advances in optics and laser technologies have allowed sufficient miniaturization of deep UV laser sources at a reasonable power input in order to be considered for extraterrestrial exploration [85], [98]. Especially in combination with time gating, this method could be a powerful tool in the search for extraterrestrial life. In fact, the Raman instrument on board of the Mars 2020 mission uses deep UV excitation of 248.6 nm, further supporting the suitability of this technique for planetary exploration [49], [89], [98].

An alternative technique to avoid fluorescence could be using dual or multi excitation instead of a single excitation source. This method combines two or more excitation wavelengths in order to collect spectra without fluorescence noise. This could be a very effective method, however, it still requires careful wavelength selection and it also calls for a significantly more complex design. Multiple excitation wavelengths can be implemented either by using separate laser sources with mechanically interchangeable optics or by coupling the optical path to fit both (or multiple) excitations. However, the former requires a precise mechanism for the optics change and cannot take simultaneous measurements at multiple excitations, which is not ideal for application in planetary sciences. This method is common for many lab or commercial Raman instruments, however, there is also a severe mass and size penalty using this approach. Likewise, the additional complexity associated with the optics mechanism does not make this method a very good candidate for planetary exploration. The latter has been proposed for a dual 532/785 nm wavelength Raman spectrometer relatively recently and uses dual-band gratings for the two

excitation laser lines [125]. The dual-band grating combines holographic gratings at a slight angle to one another, which creates two horizontal dispersion stripes across the detector and allows simultaneous measurements at both excitations [125]. This can be realized in a much smaller and simpler design and does not require any mechanisms, however, it is a conceptual design with a low technology readiness level that requires practical validation. Additionally, it is still considerably more complex than a single line Raman and could be ineffective for molecules at low concentrations or molecules that are either not detectable or experiencing high fluorescence at both 532 and 785 nm, e.g. nucleic acids.

2.3.3 Challenges: Trace Detection

One of the most limiting factors in Raman spectroscopy for the exploration of Europa is the limit of detection (LOD) as Raman spectroscopy is not particularly sensitive to trace molecules within sampled material. This is particularly concerning for the search for biosignatures on Europa and Icy Worlds as the concentration of the biomolecules is predicted to be extremely low [9], [19], [23]. As already mentioned in Section 2.2.2, the concentration of organics in the European ice could be in the order of ppb and as low as 0.01 ppb [9], [19], [23] and the Europa Lander Mission currently under development at NASA requires LOD for vibrational spectroscopy as low as 1 nM (0.1ppb) [19]. Detection at such low concentrations is not achievable with traditional Raman spectroscopy, however, methods of enhancing the limit of detection are available. These methods include Resonance Raman Spectroscopy (RRS), Deep Ultraviolet (DUV) Raman spectroscopy and Surface Enhanced Raman spectroscopy (SERS).

The simplest method of enhancing the Raman signal strength is using a DUV excitation wavelength. The Raman signal is inversely proportional to the 4th power of the incident light wavelength and as such, deep UV Raman instruments can provide a much stronger Raman signal than the more traditional visible or NIR Raman instruments. While this provides significant signal enhancement, in practice the signal enhancement in the DUV region is also limited by the high laser energy, which may damage the samples [126]–[128]. Additionally, using DUV Raman spectroscopy alone cannot achieve signal enhancement of the order of magnitude necessary for trace detection in the European ice.

RRS relies on the similarity of the energy of the laser excitation wavelength to the electronic transition of the examined molecules. This can improve the signal to noise ratio and enhance the signal by a factor of 10^2 to 10^6 , however, it is also very molecule specific [129]. For instance, carotenoids tend to be resonant at visible excitation while aromatic amino acids, nucleic acids and polyaromatic hydrocarbons (PAHs) are resonant at deep UV excitation [130]. As such, this

enhancement cannot be successfully applied to all targeted molecules with a single excitation laser source and RRS does not represent a comprehensive solution. While the specific signal enhancement depends on the specific molecule and the excitation wavelength, even the maximum signal enhancement due to resonance is unlikely to be enough for trace molecule detection on Europa. For some molecules, RRS may be successfully combined with DUV Raman spectroscopy, however, this is still highly restrictive to specific molecules. While the LODs achievable with a combination of RRS and DUV Raman spectroscopy are potentially much lower than spontaneous Raman scattering and traditional Raman systems, it still falls short of the extremely low LOD required for a mission to Europa.

One of the most effective methods of enhancing the Raman scattering signal is Surface Enhanced Raman spectroscopy (SERS), which was discovered in 1974 at the University of Southampton [131]. SERS exploits the amplification of electromagnetic fields via the excitation of surface plasmons concentrated on metallic nanostructures using noble metals such as silver or gold, which significantly enhances the Raman signal of the molecules. A signal enhancement by the factor of 10^7 to 10^{11} has been demonstrated using SERS [132], [133] allowing detection of organic molecules at concentrations as low as 10^{-3} - 10^{-17} M (i.e. 1 ppth to 10^{-8} ppb) [134] with some studies also reporting single molecule detection [135]. This significant increase in sensitivity as well as SERS' ability to increase the Raman signal by many orders of magnitude above the fluorescence background makes SERS particularly useful for low concentrations as well as for eliminating fluorescence interference [95], [132], [136], [137].

However, SERS faces a few critical challenges in order to be considered for extraterrestrial exploration. SERS requires molecules to be dissolved into a solution with colloidal nanoparticles or dissolved and deposited onto a substrate material. Despite its considerable merits, SERS has not been able to gain grounds in real world applications due to the dependence of the SERS Raman spectra on the specific SERS substrate or colloid and its properties and associated reproducibility issues [138], [139].

Metal colloids are widely used for this application but they also exhibit crucial issues with stability and reproducibility [140]–[142]. While colloids stable for several months have been reported in studies exploring the application of SERS for an in-situ Mars mission, this is nowhere near sufficient to survive the transfer time to Europa [136].

SERS substrates are a slightly more controllable medium than SERS colloids and have been widely used in research, especially in biomedical and life sciences. However, SERS substrates face similar issues with stability and reproducibility, which has prevented the method from becoming a widely adopted analytical method. SERS substrate properties such as the material, its structure and the

suitability of the substrate material for a given excitation wavelength and molecule size can significantly affect the resulting Raman spectra [132]. Adapting SERS to UV Raman spectroscopy has been particularly challenging due to issues with finding material that is SERS active in the UV excitation region as the most efficient SERS active materials in the visible and NIR region, silver and gold, are not SERS active in UV [132]. Among materials tested to date, aluminium substrates show promising results [132], [143]–[145], however, more research is necessary to optimise the signal enhancement in the UV region.

Furthermore, SERS spectra can also vary significantly depending on the location of the measurement within the same substrate [133]. Most importantly, SERS substrates are susceptible to oxidation and carbon contamination which degrades them over time, eventually leading to inactivity [146]. The longest reported period for a SERS substrate to retain its function is just over a year after production [147]. This limitation of conventional SERS substrates makes SERS incompatible with long duration space flight and planetary exploration, especially for distant targets such as Europa [141].

Likewise, a very intimate contact between the substrate and the targeted molecules is needed to enhance the signal, potentially causing cross-contamination between samples or with terrestrial contaminants. Consequently, perhaps the most limiting factor for the use of SERS in a highly autonomous instrument suitable for a Europa lander mission is the deposition of the sample onto the substrate or the colloid material onto the sample. This process can be very well managed in a laboratory environment, however, it would require complex and precise mechanisms in order to ensure sufficient results in a fully automated instrument [95].

Likewise, the key factor greatly affecting the signal enhancement is the absorption capability of the target molecules. Since close proximity is key for signal enhancement, molecules that can absorb onto the substrate material exhibit high signal enhancement, however, molecules absorb to various levels and some molecules do not benefit from the SERS signal enhancement [148]. Studies have shown that the size of the target molecules has an effect on the factor of signal enhancement by SERS and some long organic molecules that are often associated with life in astrobiology may thus not benefit from SERS signal enhancement [149], [150]. However, this coupling of the molecule size with a substrate depends on the distribution of the metal nanoparticles within the substrate, which can be to a certain degree controlled. A more even and controlled distribution can be achieved either through modification of the chemical deposition process by introducing stabilising agents such as PVA or controlling the environment of the process [151]. This has been shown to control the size, shape and distribution of the nanoparticles

Chapter 2

[151], however, the efficiency of this process is limited and it is still an area of active development.

Another method of ensuring less variable SERS spectra and tailoring the substrate to the molecule size is using a nanostructured substrate surface, which can be designed with an extremely even and controlled surface geometry and thus produce more consistent Raman spectra [152], [153]. Additionally, it has been shown that surface roughness is one of the major factors in SERS signal enhancement, which gives rough nanostructured surfaces an advantage over simple nanoparticle deposition [143], [152]. However, this approach can be very molecule specific and similar to controlling the nanoparticle deposition process, it is still a subject of intensive research.

Consequently, another significant drawback of SERS is that it is still a relatively new technology and the interpretation of the spectra can be challenging. The spectra obtained from SERS can differ to conventional Raman spectra and can also be affected by the chemical interaction with the metal particles of the substrate [154]. This is particularly concerning as the substrates and their effect on the molecules have not been fully understood yet and it has been challenging to reproduce substrate materials [141].

SERS has been widely used in biomedical sciences and attempts have been made to introduce this method in the field of in-situ instrumentation for planetary exploration [95], [103], [136], [137], [155]–[157]. These efforts have been mostly unsuccessful to date, however, most recently a promising novel in-situ activated SERS substrate concept has been proposed to mitigate the lifetime limitations of conventional SERS substrates [146], [158]. This method relies on the relative stability of AgCl nanoparticles that act as a precursor for the SERS active Ag nanoparticles [146], [158]. A layer of AgCl nanoparticles is deposited onto a base substrate and can then be activated in-situ using either UV or visible excitation [146], [158], which can be provided by the Raman laser before the measurement. The implementation of this method is shown in Figure 2-8. This method could ensure SERS substrates can survive the transfer to Europa or other planetary targets without any degradation. However, the in-situ activated SERS substrates produced with this method have not been fully characterized and understood yet in terms of the reproducibility of the Raman spectra and their lifetime once activated as well as effectiveness for various molecules. Additionally, there are currently no reference spectra for these substrates for molecules relevant for planetary exploration and further development is necessary for this method to achieve the required technology readiness level for planetary exploration.

In conclusion, SERS is a potentially very effective method of signal enhancement and fluorescence suppression that could meet the extremely low LOD requirement of a mission to Europa and other Icy Worlds, however, substantial research into its implementation is necessary.

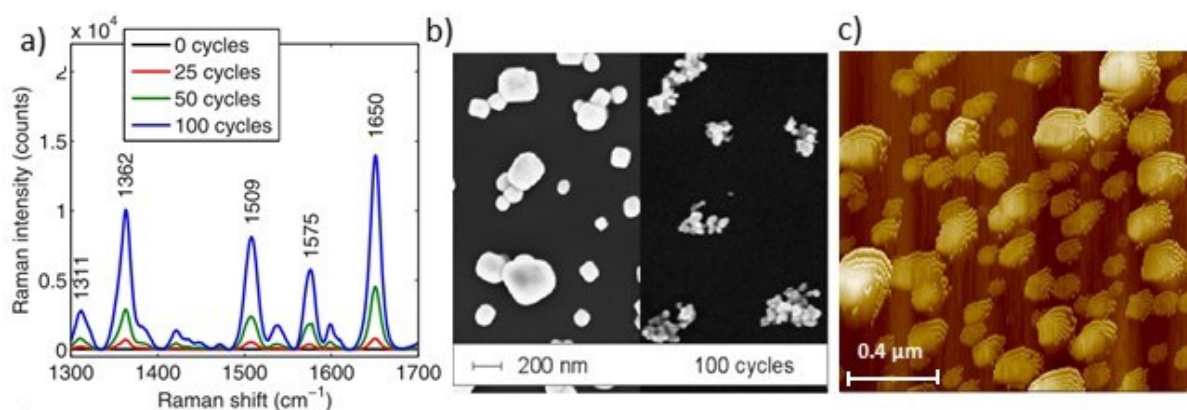


Figure 2-8 (a) SERS signal enhancement of otherwise undetectable Rh6G molecules using in-situ activated AgCl SERS at a varying number of submersion cycles during manufacture [158]. (b) A SEM scan of the AgCl non-activated (left) and activated nanoparticles (right) [158]. (c) An AFM scan of AgCl precursor non-activated nanoparticles deposited onto a quartz substrate as a part of this research at the University of Southampton to confirm the method.

2.3.4 State-of-the-Art Instruments

The current state-of-the-art Raman instruments for planetary exploration (SHERLOC and SuperCam on the Mars 2020 lander and ExoMars RLS respectively) have all been primarily designed for the detection of bulk minerals in the Martian regolith [48]–[51].

SHERLOC, shown in Figure 2-9, uses a deep UV excitation wavelength at 248.6nm which shifts the resulting Raman spectra to a “fluorescence-free” wavelength range below 280nm [89]. SHERLOC’s deep UV excitation wavelength provides a much stronger Raman signal than the more traditional visible or NIR Raman instruments. Additionally, aromatic amino acids and polyaromatic hydrocarbons (PAHs) are resonant at deep UV and the resonant-enhanced Raman scattering enables the instrument to provide 1ppm to 0.01 wt% limit of detection (LOD) for these compounds [89]. While this is just enough to detect trace biosignatures in the Martian regolith, it may not be enough in all cases and it is still below the 1ppb to 0.01ppb LOD required for the detection of biosignatures on Europa [9], [19], [23].

Furthermore, limitations in the laser/optics technology associated with the deep UV excitation do not allow SHERLOC to take measurements across the full spectral range of 150-4000 cm^{-1} desirable for planetary exploration. It also limits SHERLOC’s spectral resolution to 49 cm^{-1} [118]. This is insufficient to identify many molecular species important to astrobiology as the spectral resolution required for unambiguous identification of most minerals is 8 cm^{-1} and 16 cm^{-1} for organic compounds at room temperatures [46]. Furthermore, SHERLOC’s limited spectral range

Chapter 2

(810 – 4000 cm^{-1}) cannot identify astrobiologically significant minerals such as hematite, sulfides, pyroxene, magnetite, plagioclase feldspars, ilmenite, and olivine. While studies have shown no sample degradation in many astrobiologically relevant samples, the 4.98 eV energy provided by the DUV laser also surpasses the 3.6 eV carbon-carbon bond dissociation energy [159], which makes sample degradation of organics a possibility without careful laser power selection [126]–[128], [160].

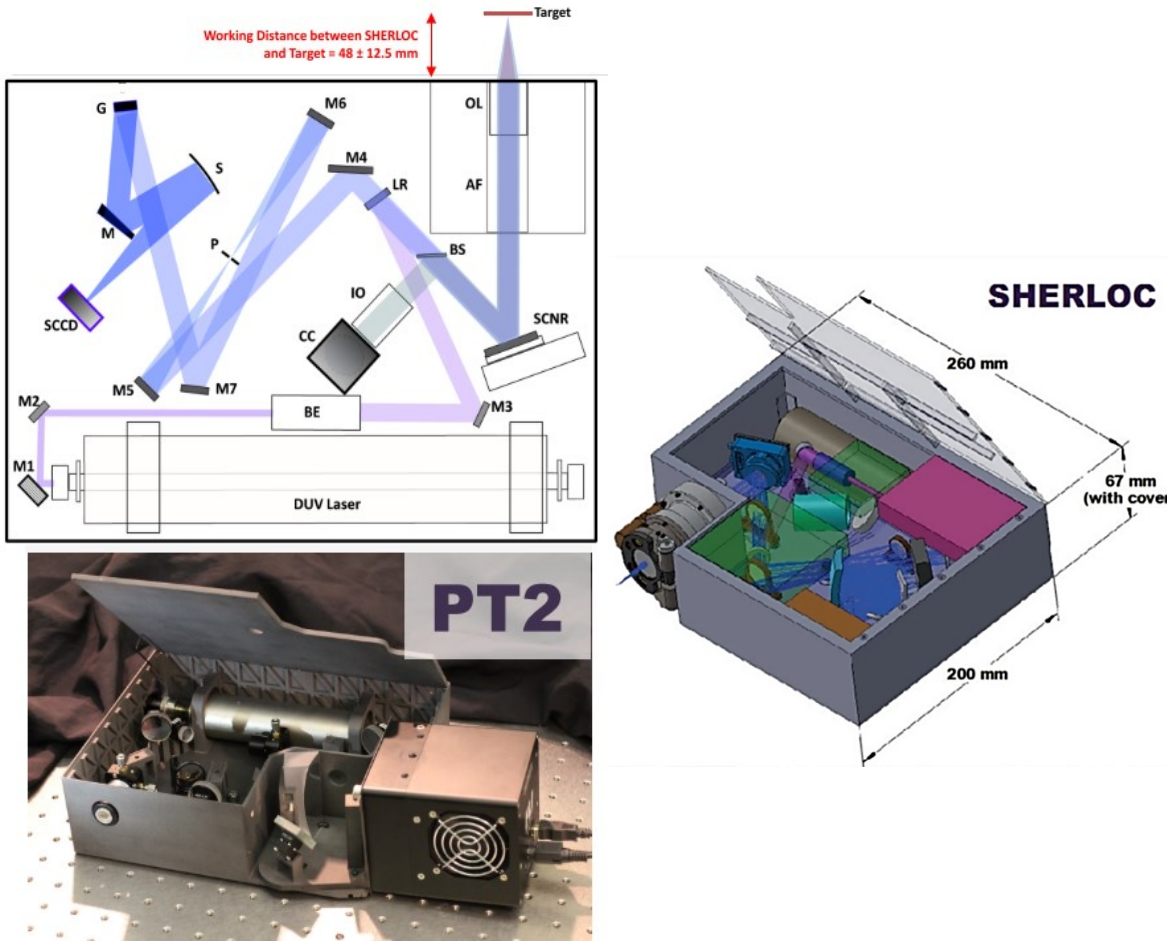


Figure 2-9 The optical path (top) and prototype 2 (PT2, bottom) of SHERLOC and a 3D model (right), A DUV Raman instrument for the Mars 2020 mission [89] [161]. Mx: mirrors, OL: objective lens, AF: autofocus, SCNR: scanning mirror, BS: beam splitter, BE: beam expander, IO: imaging optics, CC: context camera, LR: laser rejection filter, P: pinhole, M: convex mirror, S: spherical reflector, G: grating. DUV laser radiation is represented by purple and the fluorescence/Raman emission from the target are represented by blue [89]

The SuperCam instrument, shown in Figure 2-10, contains a Raman system with a pulsed 532 nm laser that allows stand-off spectral acquisition at 2-7 meters even in daylight [50]. SuperCam uses time-gating to reduce the impact of fluorescence by exploiting the instantaneous nature of Raman

scattering and separating it from fluorescence which typically occurs over a larger timescale after excitation [50]. However, as a stand-off instrument, SuperCam collects significantly less light than conventional instruments due to its high f-number. SuperCam also uses a lens-coupled iCCD design, which is key to survive the launch loads but reduces its sensitivity by $\geq 90\%$ compared to traditional fiber-optic faceplate-based iCCDs [162].

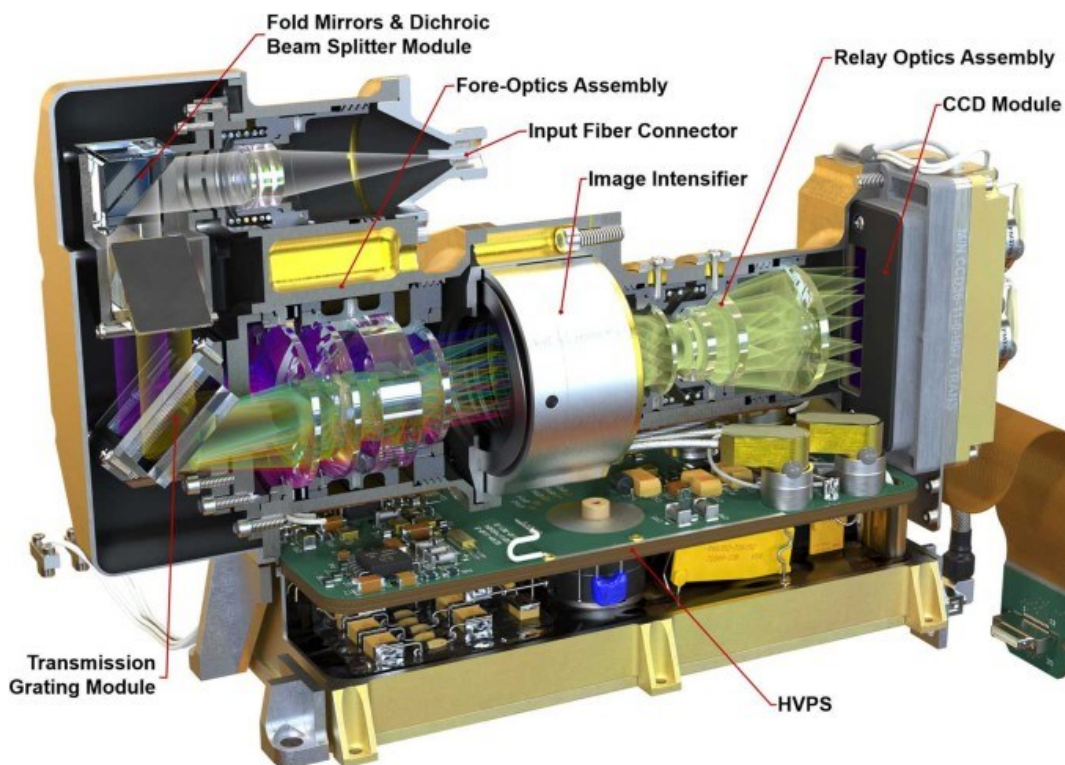


Figure 2-10 SuperCam's transmission spectrometer cutaway rendering, the transmission spectrometer includes Raman and TRL spectroscopy, while providing enhanced capabilities for LIBS and passive VIS reflectance spectra [163]

The ExoMars RLS Raman instrument uses a continuous-wave (CW) 532 nm laser source with a fluorescence quenching algorithm to optimize the SNR (Signal to Noise Ratio) of the collected Raman spectra and avoid fluorescence noise [51]. Notably, the same laser source is also used for the RAX Raman spectrometer designed for the Martian Moons eXploration (MMX) mission to Phobos set to launch in mid 2020s [164]. The RLS system pulses the laser while periodically collecting Raman spectra in order to identify changes in the fluorescent background and optimize the output [51]. Both RLS and SuperCam offer adequate spectral range ($150\text{-}4000\text{ cm}^{-1}$) and spectral resolution ($6\text{--}8\text{ cm}^{-1}$) for planetary exploration [50], [51], however, while their LODs are unpublished, the LOD required to detect biomolecules in the European ice is impossible to achieve with such systems [19].

2.3.5 Raman spectroscopy for Europa

In summary, none of the existing flight Raman instruments for planetary exploration are currently adapted to detect life and its signatures at the required detection limits for lander missions to Europa and other Icy Worlds. This significantly limits the scientific output of the instruments as well as the science return of the mission as it restricts the search for life only to minerals and bioindicators in relatively high concentrations. This is a critical issue for the exploration of Europa and further research is necessary to adapt Raman spectroscopy for trace molecule detection.

Likewise, the extreme thermal conditions on Europa could have a severe impact on the performance of Raman instruments as well as the instrument design requirements, which has not been addressed in research to date. Most Raman spectra are traditionally collected at room temperatures (15-25 °C), however, Raman spectroscopy relies on the vibrational properties of molecules and the molecular bonds, which are variable across different temperatures. As such, the extreme low temperatures on Europa can severely impact the measurements and spectra collected at much higher terrestrial temperatures are thus not representative of the spectra collected on Europa. Furthermore, these thermal changes within the spectra can be very molecule specific. To date, low temperatures have been shown to induce shifting of Raman bands towards lower or higher frequencies as well as changes in Raman band width and intensity [52], [165]–[170]. The emergence of new Raman bands in the spectra or the diminishing of specific or all bands have also been reported [52], [166], [168]–[170]. As highlighted in Figure 2-11 showing the Raman spectra of water and saturated brine (NaCl in water) across a range of negative temperatures, low temperatures can have a considerable impact on the Raman spectra and further research involving relevant molecules is necessary [171].

While the Raman spectra of some simple molecules, such as water (shown in Figure 2-5), and some other inorganic materials not significant for astrobiology have been analysed at low temperatures, the data available is very limited [52], [165], [167]–[169], [171]–[173]. Only very few molecules relevant to astrobiology have been analysed at low temperatures. Raman spectra of some minerals relevant to planetary exploration have been obtained at temperatures between 21 and -95 °C [170]. Some organic compounds including organic minerals, carboxylic acids and nitrogen-containing aliphatic and aromatic compounds, which are relevant for the search for extraterrestrial life, have also been studied, however, only in the temperature range from 5 to -25 °C [174]. There is only very limited data available on the Raman spectra of compounds relevant to astrobiology at temperatures analogous to Europa including studies of methane, ammonia and some olivines [47], [52].

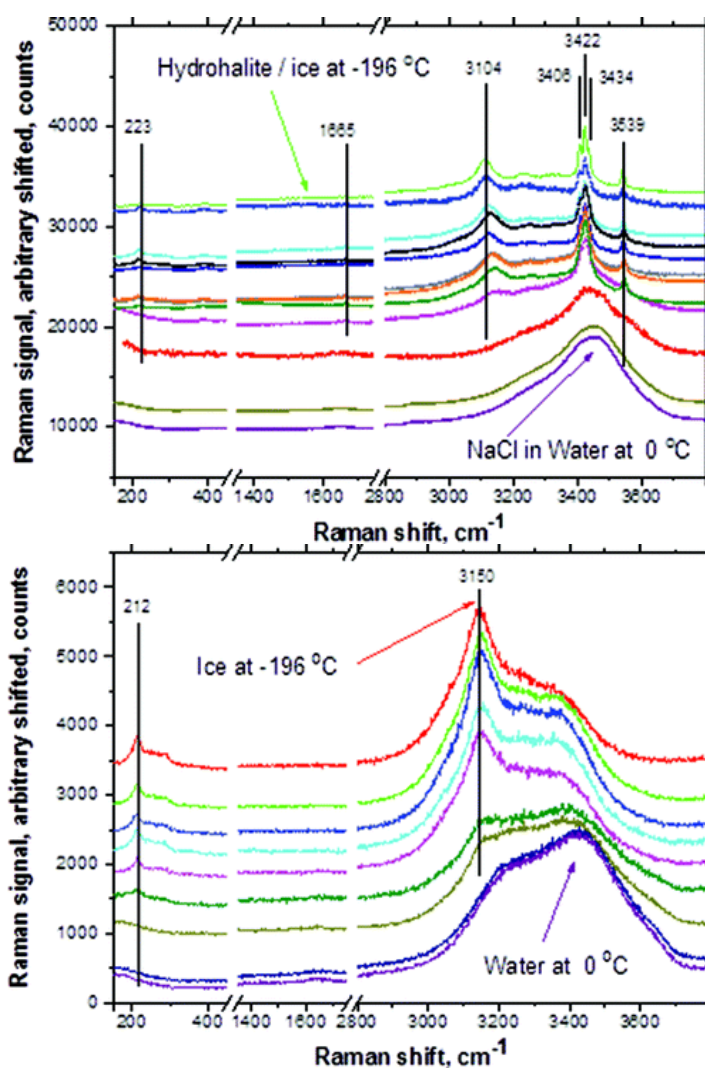


Figure 2-11 Raman spectra of water/ice (top) and saturated brine, NaCl in water, (bottom) excited with 488 nm [171]

A complete understanding of the thermally induced changes within the Raman spectra of relevant molecules at appropriate temperatures is crucial for an effective and accurate data analysis for any future in-situ mission to Europa and other Icy Worlds and requires further research. More importantly, the thermally induced changes in the spectra will affect the instrument design requirements, such as the required spectral resolution. This makes investigations into the effects of cryogenic temperatures on Raman spectra critical for the development of Raman instruments aiming to explore Europa.

Other important detection limits that may severely impact the instrument design requirements, such as the effect of fluorescence or laser induced damage, have also not been fully assessed for molecules relevant for the exploration of Europa to date. Additionally, the adaptation of Raman spectroscopy for the exploration of Europa requires a further reduction in size and mass and

Chapter 2

further miniaturization avenues need to be explored in order to meet the mission's strict requirements.

In conclusion, detection at extreme low concentrations and temperatures, as well as further miniaturization and identification of relevant molecular targets together with the impact of fluorescence and laser damage, represent critical issues for adapting Raman spectroscopy for any future missions to Europa and other Icy Worlds. These critical issues need to be addressed in order to allow the development of Raman instruments compatible with a mission to Europa and its scientific goals.

Chapter 3 Scope and Overall Methodology

3.1 Aims and Objectives

The aim of this research is to assess and identify the optimal design of a miniaturized Raman instrument for in-situ detection of biosignatures on Europa through the identification of the instrument critical design requirements, as well as to identify the limitations and future directions in Raman spectroscopy for the development of instruments compatible with a landed mission to Europa and its scientific goals.

In order to build a reference frame for the suitability of the instrument for the exploration of Europa, high confidence and high priority biosignatures relevant to the search for life on Europa are identified. The selected target molecules are then used to identify the most suitable Raman instrument configuration. This is achieved by assessing the detection limits and the effectiveness of various excitation wavelengths at detecting the target molecules in conditions analogous to Europa, i.e. at extremely low temperatures and in extremely low concentrations in an ice matrix. The detection limits explored in this study are the thermally induced changes and fluorescence interference in the Raman spectra of relevant molecules, sample degradation upon exposure to the laser excitation, and the sensitivity of various excitation wavelengths to relevant molecules at low concentrations. Please note that other potential detection limits relative to the search for life on Europa, such as high radiation or cosmic rays, are not within the scope of this project. However, they could be a suitable topic of any future work expanding this project further.

The experimentally derived detection limits are then used to identify critical instrument design requirements and assess suitable instrument designs compatible with a mission to Europa, its constraints and scientific goals. Proposing an optimal design of a miniaturized Raman instrument for the detection of biosignatures on Europa and identifying limitations of contemporary Raman spectroscopy techniques then provides information on the future directions in Raman spectroscopy research for the exploration of Europa and other Icy Worlds. These aims and objectives are summarized in Figure 3-1.

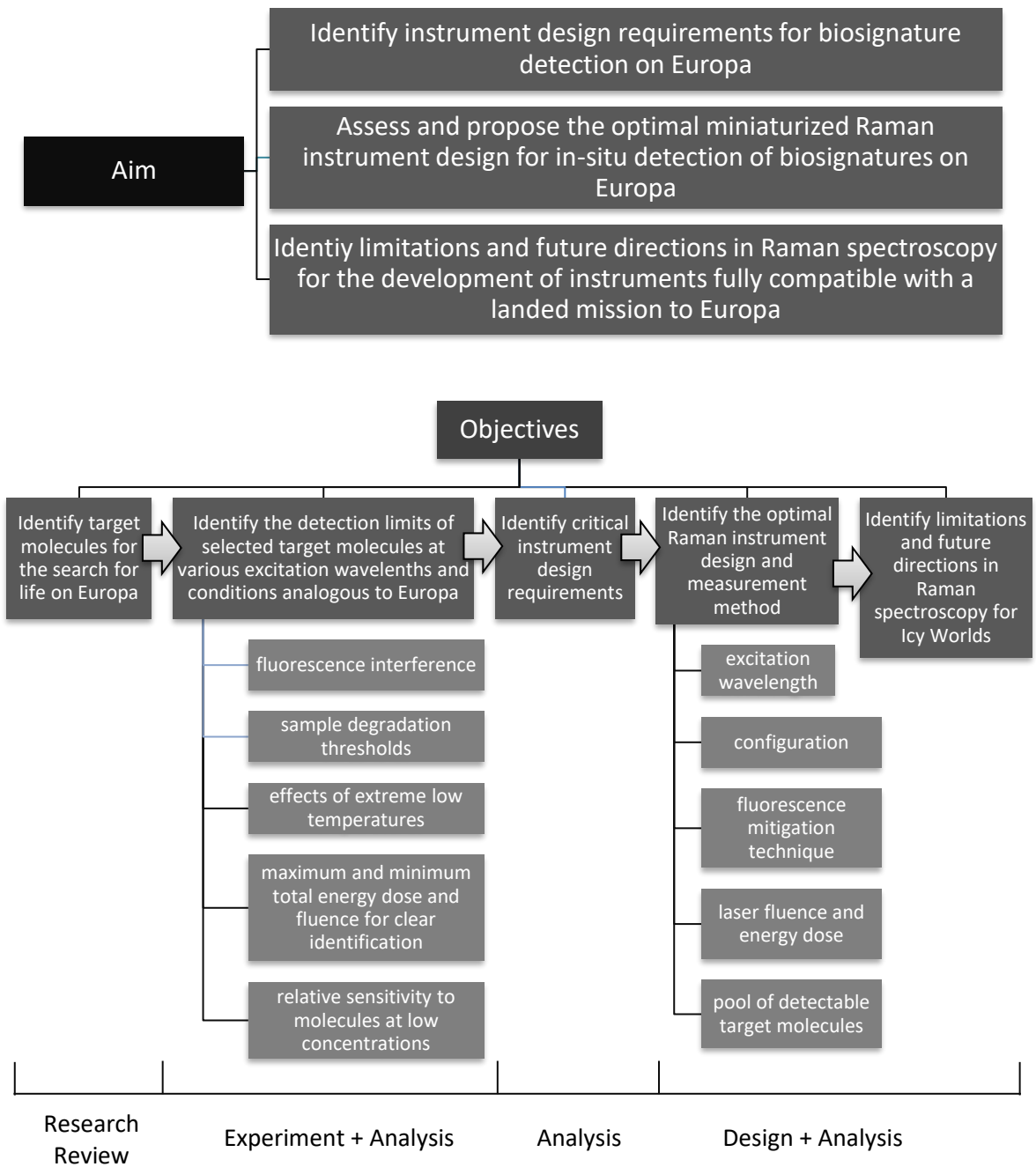


Figure 3-1 Aims and objectives with the applied method of research outlined below

3.2 Methodology

In order to identify the optimal miniaturized Raman instrument design for the detection of biosignatures in the European soil, three separate milestones need to be achieved. These milestones are outlined in Figure 3-2. Each milestone represents a key objective to be achieved in order to successfully design an optimised Raman instrument for the detection of life on Europa. The achievement of each milestone also represents a novel contribution to science in terms of understanding the limitations of in-situ exploration of Europa and providing critical information



Figure 3-2 Key milestones to achieve for the development of an optimal miniaturized Raman instrument for the detection of biosignatures on Europa

enabling the development of Raman instruments capable of detecting life on Europa and other Icy Worlds.

The high-level methodology employed to achieve the aims and milestones of this research is described below. Since each milestone requires highly specific methods and relies on the completion and results of previous milestones, a more detailed methodology description is included in the corresponding chapter covering each milestone, i.e. Chapter 4: Detection Target Molecules (Milestone 1), Chapter 5: Detection Limits (Milestone 2) and Chapter 10: Instrument Design and Requirements (Milestone 3).

Milestone 1: First, a list of targeted molecules relevant to in-situ exploration of Europa needs to be generated. This is essential for identifying relevant detection limits and assessing the optimal instrument design as it is directly linked to the instrument design requirements, such as the spectral resolution and range. Since biosignatures specific to the search for life on Europa have not been discussed in detail in literature to date, a detailed review of the potential signs of life, their relevance, as well as priority for the exploration of Europa, needs to be completed. The assessment of the relative priority of potential biosignatures for the search of life on Europa is based on the likelihood of occurrence in terms of environmental conditions, biogenicity, abundance, uniqueness to life on Earth as well as representation in the 3 terrestrial domains of life and extremophile organisms living in sites analogous to Europa.

Milestone 2: Samples of the selected target molecules are then examined in thermal conditions analogous to the European soil in order to identify critical detection limits and assess the suitability of various Raman instrument configurations for the detection of biosignatures on Europa. Raman instrument configurations including representative excitation wavelengths in the visible, NIR and UV range are used for the assessment.

The effectiveness of the employed Raman configurations is measured by the quality of spectra obtained for each molecule, including the clarity and signal to noise ratio of the major Raman peaks necessary for identification, the severity of the fluorescence background and thermal

Chapter 3

degradation at various levels of fluence and total energy doses. The effect of extremely low temperatures is identified at each excitation wavelength and for each target molecule together with the minimum and maximum fluence and total energy dose necessary for successful and unambiguous detection. This provides information on the sensitivity of the excitation wavelength to relevant molecules, which is used to derive implications on the instrument's limit of detection at extreme low concentrations analogous to Europa. The quantity and priority of representative target molecules detectable by each Raman excitation wavelength and the limits of their identification are then used as the measure of suitability for in-situ life detection on Europa.

Milestone 3: The experimental results obtained in Milestone 2 are then used to derive critical instrument design requirements, such as the spectral resolution and range, for the development of an optimal miniaturized Raman instrument for the search for life on Europa. These experimentally derived design requirements are used together with the identified limitations associated with a lander mission to Europa, such as the payload mass and size, in order to assess and propose an optimal miniaturized Raman instrument design compatible with a landed mission to Europa. Finally, the results of this study are used to identify critical limitations of contemporary Raman instrumentation techniques for life detection on Europa and characterize future directions in Raman spectroscopy for the development of instruments fully compatible with a landed mission to Europa and its scientific goals.

Chapter 4 Detection Target Molecules

In order to provide a reference frame and ensure an accurate assessment of the capabilities of an instrument for in-situ life detection on Europa, a representative list of targeted molecules corresponding to the mission objectives needs to be generated. Since biosignatures specific for the search for life on Europa have not been fully characterized in literature to date, this forms the first milestone of the research.

The selection process, key considerations and the final list of identified high priority biosignatures for the search for life on Europa are described in the following sections. The results of this research form the basis for the selection of representative samples used in further stages of the research to identify the detection limits and test the capabilities of Raman instrumentation for the detection of life on Europa.

4.1 Selection of the Detection Target Molecules

There have been various attempts at identifying the most suitable biomarkers for the search of extraterrestrial life [5], [43], [53], [54], [57]. As indicated previously, the identification of biomarkers has generated some discussions in the scientific community due to the inherently ambiguous definition of life, as well as persisting question marks regarding the origin of life and its signatures [54], [55]. In some cases, attempts of identifying biosignatures for the search for extraterrestrial life published to date have also been proven to be erroneous. For instance, branched aliphatic alkanes with a quaternary substituted carbon atom were proposed as a potential biomarker of extraterrestrial life due to their widespread occurrence in ancient sediments [43]. Their source was unknown, however, they were believed to be of microbial origin [43], [175]. Their supposedly biological origin has since been disproven and their occurrence assigned to synthetic contamination related to the manufacture of plastics [176].

Additionally, most literature has been focusing on biomarkers relevant to the search of life on Mars. Despite the definition of a biosignature being largely universal, their relevance might vary depending on the environment and mission objectives. For instance, most extant biosignatures such as proteins or DNA would not survive the harsh radiation environment on the Martian surface and therefore fossil biomarkers have been mostly targeted to search for life on Mars [43], [54], [57], [177]. However, ice has very good preservation capabilities and macromolecules, such as DNA, that are otherwise unstable might survive for longer periods preserved in the European icy crust [23], [54], [177].

While some general guidelines exist, biosignatures specific for the search for life on Europa have not been fully addressed in detail as of yet. For instance, the Europa lander concept study performed by NASA broadly outlines the targeted classes of biosignatures, namely amino acids, carboxylic acids, lipids and other molecules of potential biological origin (biomolecules and metabolic products) [19]. In order to assess the moon's habitability and composition, the study also suggests targeting some biominerals, salts, radiation products and metals [19]. However, more specific targets need to be identified as these classes encompass a very broad spectrum of different molecules with different functions, properties and levels of relevance to the search of life on Europa.

4.2 Methodology

There are many factors to be considered when selecting and prioritizing the most relevant and representative target molecules for the detection of life on Europa.

Some biomarkers, such as amino acids, nucleobases and lipids, are present in all known forms of life and therefore represent a highly uniform biosignature across all 3 domains of life [44], [57]. However, they could also be formed abiotically, without the presence of life, thus providing a highly ambiguous result in terms of detecting life. However, for their essential role in the formation of life, amino acids and carboxylic acids have also been more frequently targeted by studies of instruments for space application, while other molecules, such as adenosine triphosphate (ATP), nicotinamide adenine dinucleotide (NAD) and porphyrins, even though equally as essential and universal, have not been analysed by Raman instruments for space application yet [85], [98], [178].

Molecules such as pigments or hopanes are only present in some organisms and can be quite specific to a class of microorganisms depending on their function. However, hopanes and pigments such as carotenoids, scytonemin, chlorophyll or phycocyanin do not have any known abiotic source and therefore, their detection would be a clear sign of life [43], [53], [54], [179], [180].

Moreover, some pigments are used by terrestrial extremophilic organisms as an adaptation technique or a protective mechanism from harsh environment. This is especially important for life on Europa due to its high radiation and UV light exposure, oxidative surface and extreme temperatures. For instance, scytonemin is the most common and widespread bacterial protection against damaging UV light [179], [181], [182]. Likewise, carotenoids are commonly found in radiation resistant organisms as they protect cells against oxidation and radiation damage [179], [183].

Furthermore, some biomarkers, such as ectoine or hopanes, are predominantly present in bacteria. However, since bacterial life is the most likely form of extraterrestrial life to be found on Europa, these compounds have higher priority than others that might be more uniformly distributed across eukarya, which is a more complex and developed domain and possibly highly specific to the environment on Earth [43], [54], [184].

Likewise, despite being highly conserved across all living forms, specific chaperone proteins and their levels can vary among different organisms [185], [186]. However, they are present in large quantities in cells and therefore their detection is likely, especially in the case of heat shock proteins and if the molecule is subjected to a temperature change [43]. A temperature change would be hard to avoid during the excavation from the soil by a sampling system and the subsequent analysis in the vault of the lander. Additionally, different heat shock protein families can be structurally similar and yield representative spectra for the heat shock protein class [187], [188].

Some complex compounds such as proteins or complex lipids are highly unlikely to be produced abiotically. However, they could also prove to be too specific to terrestrial life as the European environment could have supported an evolution of protein or lipid like molecules dissimilar to their terrestrial counterparts.

In this work the key considerations identified for the selection of the most appropriate molecular targets therefore include biogenicity, complexity and uniqueness to terrestrial life, stability and likelihood of occurrence in terms of abundance, representation among the 3 domains of life as well as in terrestrial organisms living in analogous environments. These considerations are described in Table 4-1 relative to how they are used in this study.

For each examined group of molecules as well as individual molecule, each consideration is assessed based on existing literature sources and weighted against all other considerations. This assessment is then used to identify biosignatures significant for the search for life on Europa and classify each biosignature based on its priority. The identified biosignatures are presented in the following section together with a tabulated overview of the assessment and their priority classification. The classification criteria is described in more detail in the following section. The section also includes further discussion on the assessment of the key considerations and classification specifically for each molecular category.

Consideration	Description
Biogenicity	Likelihood of biogenic origin or no known abiotic sources
Uniqueness to Terrestrial Life	Measure of how specific certain biosignatures are to terrestrial life, often related to their complexity or role and time of occurrence in the evolution of life on Earth
Stability	Ability to withstand harsh environments analogous to Europa and for geologically significant periods of time
Abundance	Expression in cells as well as overall abundance, especially in terrestrial sites and organisms analogous to Europa
Environmental Likelihood of Occurrence	Likelihood of occurrence on Europa based on occurrence in organisms in terrestrial environments analogous to Europa, often through adaptation or protection techniques in extremophile organisms
Representation in Domains of Life	A measure of abundance among the 3 terrestrial domains of life, especially focusing on expression in bacteria and archaea as the earlier and simpler forms of life on Earth

Table 4-1 Key considerations for the selection of high priority biosignatures for the search for life on Europa

4.3 Results and Discussion

Based on the above stated criteria, the most relevant biosignatures for the search for life on Europa have been selected and assigned priority from A to F, A being the highest priority and F the lowest. A detailed review of the selected molecular targets is shown in Table 4-2, Table 4-3, Table 4-4 and Table 4-5. Table 4-2 summarises some conventional biomarkers for astrobiology such as amino acids and organic metabolic products, Table 4-3 reviews lipids, which is one of the largest biomarker categories due to its inherent stability and Table 4-4 shows the review of other important biomolecules such as proteins, nucleic acids and porphyrins. Inorganic biosignatures and some alternative targets for the search of life on Europa are reviewed in Table 4-5.

Biosignatures in the A and B classes represent crucial target molecules for the detection of extraterrestrial life on Europa and signs of life that are the most likely to occur.

Class C and D were assigned to important biosignatures that might be either harder to detect or their occurrence might not be as likely due to low abundance or high complexity and specificity to terrestrial life. These classes also include biosignatures that are less likely to confirm the presence of life unambiguously.

Biosignatures assigned priority E and F are useful for the assessment of habitability or potential of life existing on Europa but unable or unlikely to prove its presence. These classes also contain biosignatures that are very rare or unlikely to occur.

Although not discussed in this study, other molecules that do not fall in the category of biosignatures, such as habitability markers and plausible inorganic molecules constituent to the European chemical composition, could also provide useful information regarding present, extinct or future life on Europa. They could also carry a significant impact on the detectability of some biosignatures and a detailed review of these compounds could be a subject for future research.

The selection of molecular targets is discussed in more detail in the following sections. Each biosignature class is discussed and a review of key aspects contributing to its relevance for the search for life on Europa is provided.

Class	Sub Class	Specific Compound	Priority	Type			Uniquely Biogenic	Occurrence in Life Forms		
				Extant	Fossil	Meteorite		Archaea	Bacteria	Eukarya
Organic	Amino Acids	L-Alanine	B	x	x	x	NO	x	x	x
		L-Aspartic Acid	B	x	x	x	NO	x	x	x
		L-Glutamic Acid	B	x	x	x	NO	x	x	x
		Glycine	A	x	x	x	NO	x	x	x
		L-Histidine	A	x	x		YES	x	x	x
		L-Leucine	C	x	x	x	NO	x	x	x
		L-Serine	C	x	x	x	NO	x	x	x
		L-Tryptophan	C	x	x	T	NO	x	x	x
		L-Tyrosine	C	x	x	T	NO	x	x	x
		L-Valine	C	x	x	x	NO	x	x	x
		α -Aminoisobutyric Acid	E	VR	VR	x	NO			NPvl
		D-Isovaline	E	VR	VR	x	NO			NPvl
		β -Alanine	D	R	R	x	NO	NP	NP	NP
	γ -Aminobutyric Acid	D	R	R	x	NO	NP	NP	NP	
	Organic Metabolic Products	Methane	B	x			NO h	x	xmg	
		Dimethyl Sulfide	A	x			YES	x	x	x
Dimethyl Disulfide		A	x			YES	x	x	x	
Methanethiol		C	x			YES	x	x	x	

Table 4-2 Selected molecular targets: amino acids and organic metabolic products, note that the list of amino acids is not exhaustive, only a sample of some important amino acids has been selected (T – trace, R – rare, VR – very rare, NP – non-proteinogenic, h – not uniquely biogenic but unlikely to be abiotic at high levels, l – limited occurrence, vl – very limited occurrence, mg – methanogenic)

	Sub Class	Specific Compound	Priority	Type			Uniquely Biogenic	Occurrence in Life Forms		
				Extant	Fossil	Meteorite		Archaea	Bacteria	Eukarya
Organic Biomolecules Lipids	Carboxylic Acids	Palmitic Acid	A	x	x		NO u		x	x
		Stearic Acid	A	x	x		NO u		x	x
		Myristic Acid	B	x	x		NO u		x	x
		Palmitoleic Acid	C	x	x		NO		x	x
		Ectoine	A	x	x		NO	l	x	l
	Isoprenoids	Pristane	B	x	x		YES	xm	x	x
		Phytane	B		x		YES	xm	x	x
		Squalene	C	x			YES	x	x	x
		Squalane	C		r		YES	x	x	
		Gammacerane	C		x		YES	x	x	
	Hopanoids	Diploptene	B	x	r		YES		x	l
		Diplopterol	B	x	r		YES		x	l
		Bacteriohopanetetrol	B	x	r		YES		x	l
	Hopanes	C30 Hopanes	A		x		YES		x	l
	Carotenoids	β -Carotene	A	x	r		YES	x	x	x
		α -Carotene	B	x	r		YES	x	x	x
		Lycopene	B	x	r		YES	x	x	x
		Lutein	B	x	r		YES	x	x	x
		Fucoxanthin	C	x	r		YES			xm
		Astaxanthin	B	x	r		YES	x	x	x
	Fossil Carotenoids	β -Carotane	A		x		YES		x	x
		Lycopane	A		x		YES		x	x
	Steranes	5 α -Cholestane	B		x		YES		l	x
		Ergostane	B		x		YES			x
	Sterols	Ergosterol	C	x	r		YES		vl	x
		Cholesterol	D	x	r		YES			x

Table 4-3 Selected molecular targets: lipids (r – recent, u – not uniquely biogenic but abiotic formation unlikely or abiotic sources very rare, l – limited occurrence, vl – very limited occurrence, m – main source, mg – methanogenic)

	Sub Class	Specific Compound	Priority	Type			Uniquely Biogenic	Occurrence in Life Forms			
				Extant	Fossil	Meteorite		Archaea	Bacteria	Eukarya	
Organic Biomolecules	Pigments	Scytonemin	A	x			YES		x		
		C-Phycocyanin	C	x			YES		x		
		Chlorophyll a	B	x			YES		x	x	
	Nucleic Acids	DNA	A	x	r		YES	x	x	x	
		RNA	C	x	r		YES	x	x	x	
	Nucleobases	Purines	Adenine	B	x	x	x	NO	x	x	x
			Guanine	B	x	x	x	NO	x	x	x
		Pyrimidines	Cytosine	B	x	x		NO	x	x	x
			Thymine	B	x	x		NO	x	x	x
			Uracil	B	x	x	x	NO	x	x	x
		Proteins	Chaperones	HSP70	B	x			YES	x	x
	HSP90			C	x			YES		x	x
	CSP			B	x			YES	x	x	x
			ATP Synthase	B	x			YES	x	x	x
	Carbohydrates	Trehalose	A	x			YES	x	x	x	
		Teichoic Acids	B	x			YES		x		
		Lipopolysaccharide	B	x	r		YES		x		
	Coenzymes	Nicotinamide	A	x			YES	x	x	x	
		NAD	B	x			YES	x	x	x	
		NADP	B	x			YES	x	x	x	
		Riboflavin	C	x			NO	x	x	x	
		FAD	C	x			YES	x	x	x	
	Oxalates	Calcium Oxalate	C	x			NO u			x	
	Porphyrins	Protoporphyrin IX	A	x			YES	x	x	x	
		Hemin	A	x			YES	x	x	x	
		Octaethylporphine	B	x			YES	x	x	x	
	Fossil Porphyrins	Nickel Porphyrin	A		x		YES	x	x	x	
		Vanadyl Porphyrin	A		x		YES	x	x	x	
Phosphate Biomolecules	ATP	A	x			YES	x	x	x		
	Phosphoenolpyruvate	C	x			YES	x	x	x		

Table 4-4 Selected molecular targets: biomolecules (r – recent, u – not uniquely biogenic but abiotic formation unlikely or abiotic sources very rare)

	Sub Class	Specific Compound	Priority	Type			Uniquely Biogenic	Occurrence in Life Forms		
				Extant	Fossil	Meteorite		Archaea	Bacteria	Eukarya
Inorganic	Inorganic Metabolic Products	Oxygen	B	x			NO h		x	x
		Nitrous Oxide	B	x			NO u	x	x	x
		Water	B	x			NO	x	x	x
		Carbon Dioxide	E	x			NO	x	x	x
		Sulfur Dioxide	E	x			NO			x
		Ammonia	C	x			NO		x	x
	Biominerals	Weddellite	B		x		NO u		x	x
		Whewellite	B		x		NO u		x	x
		Mellite	E		x		YES			x
		Magnetite	D		x		NO		x	x
		Silica	D		x		NO			x
	Iron Sulfides	Pyrite	C		x		NO		x	
		Carbonates	Aragonite	B		x		NO		x
	Vaterite		B		x		NO		x	x
Calcite	C			x		NO		x	x	
Dolomite	C			x		NO		x	x	
Magnesite	D			x		NO		x	x	
Other	Cells/Bacteria Colonies	Bacteroidetes	E	x			YES			
		Proteobacteria	F	x			YES			

Table 4-5 Selected molecular targets: inorganic biosignatures and other targets (u – not uniquely biogenic but abiotic formation unlikely or abiotic sources very rare, h – not uniquely biogenic but unlikely to be abiotic at high levels)

4.3.1 Amino Acids

Amino acids are the fundamental building blocks of all life on Earth. They are also widely accepted biosignatures and have been commonly targeted by astrobiology missions. However, with the exception of examples such as histidine, most of the 20 fundamental amino acids most commonly used by terrestrial life can be formed abiotically [189]. While amino acids can be formed without the presence of life, life itself cannot exist without amino acids. Therefore they represent a suitable, if not unambiguous, target.

The biogenicity of some important amino acids most commonly used by terrestrial life is shown in Figure 4-1 [19], [189]. Other non-terrestrial amino acids have been found on meteorites and do not represent a sign of life [56]. It is unclear whether life can be based on these amino acids,

however, it indicates that different non-terrestrial amino acid structures can evolve in different parts of the universe and therefore could be the building blocks of extraterrestrial life.

Glycine, the simplest amino acid and one of the likely first steps in the origin of life on Earth, could represent an early evolutionary stage necessary to build more complex amino acids. Furthermore, the accumulation of glycine can lower the freezing point of cytoplasm and shows an increased expression in psychrophilic organisms [190], [191]. This makes it an exceptionally suitable molecular target for the search of life on Europa.

Some non-proteinogenic amino acids are not usually associated with life as they occur in nature only very rarely, for instance D-isovaline and α -aminoisobutyric acids only occur in some microfungi and are often considered to be abiotic [192]. The detection of these amino acids could, however, provide useful information regarding possible meteorite contamination and their ratios to biotic amino acids is a useful tool to assess the potential of life arising on Europa.

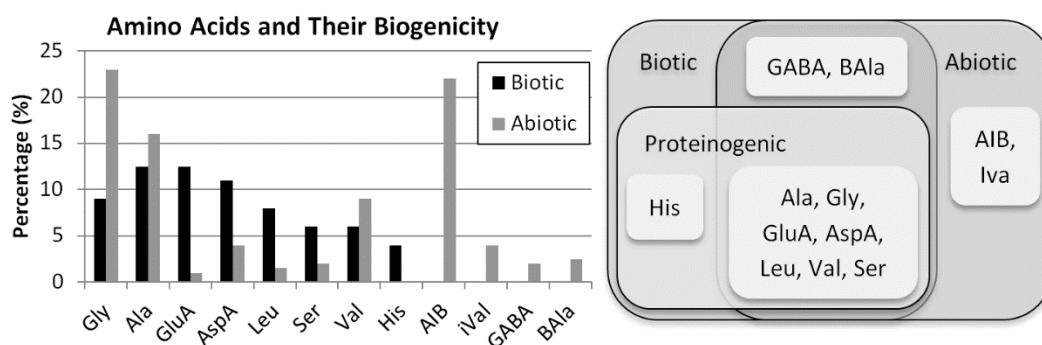


Figure 4-1 Biogenicity of some important amino acids (redrawn based on data from [19], [189]), Gly – Glycine, Ala – Alanine, GluA – Glutamic Acid, AspA – Aspartic Acid, Leu – Leucine, Ser – Serine, Val – Valine, His - Histidine, AIB - α -Aminoisobutyric, iVal – Isovaline, GABA - γ -Aminobutyric Acid, BAAla – β -Alanine

4.3.2 Carboxylic Acids

Carboxylic acids are widespread in nature due to their crucial role in cellular membrane formation essential for the early evolution of cellular life [193].

Long-chain fatty acids with more than 5 carbons in their alkyl chain form the phospholipids in the membranes of most living organisms (bacteria and eukarya) with the exception of archaea, which uses isoprenoids to form membrane lipids [193], [194]. However, evidence shows that long chain fatty acids, especially palmitic acid, are also used by some archaea [195]. Even though fatty acids can also be synthesized abiotically, the process is not likely to produce very long straight chain acids [43]. Abiotic carboxylic acids found on meteorites only contain up to 12 carbons in their

chain [196]. Additionally, they are quite stable and for this and their uniformity among many organisms, they are also considered to be high priority biosignatures of extinct and extant life for space exploration [43], [197].

Acids with even numbers of carbons (C14, C16, C18, C20 etc.) are predominantly used by terrestrial life as 2 carbon atoms are attached at a time during their synthesis (5 in archaea) [198]. Palmitic acid (C16), stearic acid (C18) and myristic acid (C14) are the most common and abundant fatty acids across organisms [199], [200]. Membrane fatty acids in psychrophiles tend to have shorter carbon chains [191], palmitic acid being the most universal and the most abundant, followed by stearic or myristic acid depending on the organism strain [201]–[204].

While saturated fatty acids tend to be more common across terrestrial organisms, the levels of unsaturated fatty acids are increased in psychrophiles [190], [191], [205]. Especially common is palmitoleic acid, C16:1 [200], [204]. Nevertheless, unsaturated fatty acids are not as stable as saturated fatty acids and are prone to oxidation, which makes them less favourable as target biosignatures [206].

Ectoine is a carboxylic acid that acts as an osmoprotectant in extremophiles and represents one of the most widespread osmolytes among organisms [207]. It is synthesized predominantly by most bacteria but also by some archaea and eukarya [207]. Apart from its function as an osmoregulatory compatible solute, ectoine plays an important role in protecting biomolecules or entire cells from harsh environments such as freezing, high temperatures or salinity [207]–[209]. Studies have shown that it also protects eukaryotic cells from ionizing radiation and UV damage [207], [208]. In fact, among other common compatible solutes (hydroxyectoine, trehalose, sucrose, maltose, betaine) ectoine and trehalose (discussed in Section 4.3.7) were found to be the most prominent osmoprotectants [209].

4.3.3 Isoprenoids

Isoprenoids are a class of uniquely biogenic and extremely geologically stable molecules, many of which have been commonly used as organic biomarkers of biomass in terrestrial sediments [210]–[212]. All organisms synthesize or require isoprenoids and due to their inherent stability and resilience to biodegradation, they are an excellent target for astrobiology [43], [54], [213].

Pristane and phytane are products of chlorophyll biodegradation and are found in marine sediments as a biomarker of fossil photosynthesizing microorganisms [211], [212]. They have no known abiotic source and their stability and persistence make them a reliable biosignature of fossil life [212]. Pristane can also signal extant life since it commonly occurs in living organisms

Chapter 4

and very recent sediments [210], [211]. It is especially widespread in marine life and can be found in most, if not all, marine organisms [214]. Nevertheless, as biomarkers of phototrophic life, pristane and phytane might not be as prominent on Europa, if present at all, given the low solar radiation influx.

Squalene is an isoprenoid similar in structure to β -carotene and can be found widely in nature both in prokaryotes and eukaryotes [215]. It is a crucial biosynthesis intermediate of sterols and hopanes and both squalene and its fossil form squalane commonly occur in terrestrial sediments, especially in hypersaline environments [43], [215]–[217]. However, squalene is known to be unstable compared to other isoprenoids and subject to degradation on Earth due to its photosensitivity and while it is abundant in living organisms and recent sediments in its fossil form, its role in the fossil record is not as prominent [43], [217], [218]. While this leads to squalene being assigned a lower priority for the search for life on Mars [43], Europa's significantly lower solar influx and layers of ice could, to a certain degree, limit the photodegradation effect.

The most prominent isoprenoids in the terrestrial fossil record are hopanes, the fossil counterparts of hopanoids from cellular membranes of bacteria and some eukaryotes [5], [216]. Hopanes are highly chemically stable and can survive in sediments for billions of years, which makes them highly attractive targets for searching for microbial life in sediments [54], [179], [219]. They have been used as bacterial biomarkers in terrestrial fossil records and have also been suggested as biosignatures for the search of extraterrestrial life [5], [43], [53], [54], [179], [216].

The most common source of hopanes in sediments are bacteriohopanetetrol, which is the most common hopanoid in prokaryotes, and diploptene and diplopterol, which are the most widespread hopanoids [43], [54], [216]. The most abundant hopanes in terrestrial fossil records are isomers of C27-C35 hopanes, especially isomers of C30 hopanes [216], [220].

Another class of isoprenoids particularly important for astrobiology is carotenoid pigments. They are one of the most common pigments in nature and are widespread among both prokaryote and eukaryote organisms [180]. In marine environments, carotenoids are the most widespread pigments biosynthesized by organisms ranging from bacteria and archaea to fungi (especially marine yeast) and algae [221]. Carotenoid pigments are vital for energy harvesting but they also play an important role in UV protection of cells and damage repair [180], [183], [221]–[224], which makes them an excellent target for the search for life on Europa.

Just like other isoprenoids, carotenoids have no abiotic source and have been named as potential biomarkers for astrobiology [43], [53], [180]. Some of the most common carotenoids on Earth include β -carotene, α -carotene, lycopene, lutein, fucoxanthin and astaxanthin [221]. Some

carotenoid pigments, such as β -carotene, are very common among a wide range of organisms, while others can be specific to a particular branch of species [43], [180], [225]. For instance, fucoxanthin is mainly biosynthesized by brown marine seaweed [221], [223].

β -carotene could be especially crucial for the search for life on Europa due its photoprotective properties. β -carotene has been shown to protect extremophile cells from radiation, UV oxidative stresses and aid cell damage repair [179], [180], [183], [221]–[226], and like other carotenoids, represents a common cold adaptation feature in psychrophile organisms [190], [224], [226]–[228]. Its protective properties and widespread occurrence signalling an origin at an early evolutionary stage make β -carotene a high priority target for life detection on Europa.

The diagenetic fossil counterparts of general carotenoids, such as β -carotane or lycopane, are exceptionally stable over geologically significant periods of time and can be preserved for up to 1.6 billion years [229], [230]. The preservation of intact general carotenoids depends on the depth and oxygen levels in the environment, however, they have been reported to survive up to 20 million years in sediments with low oxygen concentration [230], [231].

Gammacerane is more stable than hopanes and represents one of the major biomarkers in the analysis of depositional environments on Earth [232]. High concentrations of gammacerane are commonly present in stratified water columns and signal highly reducing hypersaline conditions [216]. However, in general it is not as abundant as hopanes [43], [216].

Steranes, fossil derivatives of sterols, are also very stable chemical compounds often found in fossil organic matter [5], [43], [44], [57], [233]. There are reports of sterane extraction from shales 2.7 billion years old [57], [219]. Tetracyclic triterpanes such as cholestane and ergostane represent some of the major sterane hydrocarbons found in fossil material on Earth [233]. Their extant forms, cholesterol and ergosterol, represent the most common sterols produced by eukaryotes. Compared to hopanoids, both steranes and sterols receive a lower priority ranking for the search for life on Mars as sterols require oxygen for synthesis, the presence of which on early Mars is uncertain [43], [179]. However, Europa's thin atmosphere almost entirely composed of oxygen could easily provide enough oxygen for aerobic life [234]. Nevertheless, besides a few representatives of bacteria, sterols are almost exclusively produced by eukaryotes [235]. Representing a later and more complex evolutionary stage of organisms on Earth, eukaryotes might not be present on Europa or might not use similar patterns, making sterols a somewhat less reliable biosignature. Sterols can also be quite kingdom-specific [43], [235], making their detection more complex. Furthermore, sterols are less stable than hopanes [43], [236].

4.3.4 Pigments

Scytonemin is a highly stable sunscreen pigment present in the extracellular sheath of bacteria to protect cells from harmful UV radiation [182], [226]. This is especially important in the high radiation zone at Europa. It is predominantly synthesized by cyanobacteria and represents an important UV protective mechanism for extremophilic life [182], [226]. Besides carotenoids it is the most common photoprotection pigment used by cyanobacteria [225]. Furthermore, it has been identified as a unique and unambiguous sign of life [53].

Likewise, the light-harvesting pigments phycocyanin and chlorophyll have been suggested as unique to life and unambiguous biosignatures for astrobiology [53]. Chlorophyll is the most common photosynthetic pigment on Earth and is abundant in plants, algae and bacteria [237], although absent in archaea [238]. Similar to carotenoids, it also protects cells from excessive UV radiation and oxidative stress [223]. Phycocyanin is an analogous bacterial photo-harvesting pigment with antioxidant properties produced by cyanobacteria [239]. However, while photosynthesis is a process uniquely associated with life and perhaps the most important process for the evolution of life on Earth, light-harvesting might not be a dominant source of energy for organisms on Europa due to its low levels of Sun radiation. In fact, phototrophic life might not be a part of Europa's biomass at all. Thus, despite being an attractive molecular target for the search of life on Mars, the significance of photo-harvesting pigment biomarkers for the exploration of Europa is somewhat reduced. Furthermore, the production of phycocyanin in bacteria is dependent on optimal light conditions and is mostly common in tropical environments [239].

4.3.5 Nucleic Acids & Nucleobases

Nucleic acids, macromolecules responsible for storing terrestrial genetic information, are essential for all life on Earth and due to their high complexity they are a definitive evidence of the presence of life [43], [240]. They are biopolymers composed of sugars, phosphates and nucleobases, most commonly known as DNA and RNA. Nucleobases, the building blocks of nucleic acids, have also been found on meteorites delivered to Earth from space [240]–[242]. This suggests that extraterrestrial life could easily adopt similar macromolecules to DNA and RNA to store genetic information [240].

The drawback of nucleic acids as biosignatures for the search of extraterrestrial life is their relative instability [43], [54], [240]. DNA and RNA are easily susceptible to biodegradation and hydrolysis outside of living cells [54]. This is also why they are often assigned a lower level of importance for the search for life on Mars as they would not survive the strong UV radiation and oxidizing conditions of the Martian surface [54], [240]. This is also why nucleobases (adenine,

thymine, uracil, cytosine and guanine), which are significantly more stable, are often favoured as biosignatures for the search of Martian life [54]. However, nucleobases can also be formed abiotically and, while they are crucial building blocks of life, compared to nucleic acids they do not represent compelling evidence of the presence of extraterrestrial life.

While it is unlikely nucleic acids would survive the harsh radiation environment on the surface of Europa, the extreme low temperatures and presence of salt in the sub-surface layers of the European ice could easily preserve nucleic acids or their remnants for significant periods of time. While the theoretical life span of nucleic acids is between 50,000 and 100,000 years [240], [243], there are reports of DNA recovered from ice in Greenland that are estimated to be between 450,000 and 800,000 years old [244]. Others report ancient DNA and even living organisms from millions of years old brine samples [240], [245], [246]. On Europa, living organisms could also be preserved in ice in a state of inanimation, similar to terrestrial psychrophiles living in extreme cold environments. Frozen bacteria on Earth have been reported to survive up to half a million years in the state of cryopreservation [247]. This would leave their genetic code intact and protected within their cells as DNA continues to be slowly repaired and maintained in the state of inanimation [247], [248]. This also makes nucleic acids a significant biosignature for the search of life on Europa, even despite their relative instability on Earth or Mars compared to other biosignatures such as lipids and amino acids.

4.3.6 Proteins

Proteins are uniquely biotic complex molecules formed of long chains of amino acids and are an essential element for all life. They are not as stable as lipids and are subject to biodegradation outside of living cells [54], which is why they have been classified as biomarkers of extant life only and have not been assigned significant importance for the search for life on Mars [54]. However, while fossil biosignatures are mostly targeted for the search for life on Mars due to the unlikely presence of extant life forms [54], the European environment could easily harbour living organisms and the search for extant biosignatures is not unjustified. Additionally, similar to DNA, proteins could also benefit from the preservation capabilities of the European icy crust, being conserved or partially conserved in organisms undergoing cryopreservation while sustaining some degree of metabolic activity [247].

Proteins have also been found preserved within bones and other fossilized tissues and minerals for millions of years [54], [249], [250]. Cold environments have been identified as particularly beneficial for preservation [250].

Chapter 4

While proteins are complex molecules and possibly specific to life on Earth, the conservation of some across all life forms, such as ATP synthase, suggests its formation early in the evolutionary stages of life [251]. This could make its formation in other extraterrestrial environments more likely. ATP synthase is an enzyme complex that produces ATP, a phosphate that serves to store energy. Due to its crucial role in sustaining life and early evolution in organisms, it is highly universal across all life on Earth and as such, it is an attractive biosignature for astrobiology [43], [251].

Similarly interesting targets for astrobiology are heat shock proteins that act as molecular chaperones in cells and assist the folding and synthesis of proteins [43]. They are highly conserved across all organisms and are present in high concentrations in cells, especially when subjected to environmental stress which can increase their concentration up to 30% of the proteins within a cell [185], [186], [252]. For their function as an adaptation mechanism to changes in environmental conditions and stresses such as temperature, salinity, pH, dehydration, oxidative damage, heavy metals or high intensity irradiation, they are especially important for the survival of extremophile organisms [186], [253]. This is particularly relevant for the search for life on Europa due to its harsh environment.

Among the heat shock protein families, HSP70 is present virtually in all living organisms and in psychrophilic organisms, HSP70 and HSP90 have been found the most uniform and abundant [186], [253].

Similarly, cold-shock proteins have been studied as the key mechanism allowing the survival of organisms in the cold environments of icy moons. [254] CspA, the most dominant among the cold shock proteins [255], [256], can reach up to 10% of the total protein production in a cell during the cold shock adaptation process [257], [258]. This signals about a 4 – 5 fold increase in production from the unstressed state [259]. There has even been evidence of 50 fold increase in the levels of CspA at low temperatures [256]. This increase might also aid the detection by a lander instrument as a sample excavated from the European subsurface would most likely experience a change of environmental conditions before being presented to the instrument. CspA production in a cell is not only limited to a cold shock state; CspAs are also present and fairly abundant at optimal temperature growth [256], [260].

4.3.7 Carbohydrates

Teichoic acids and lipopolysaccharides have been proposed as biosignatures of extraterrestrial life due to their crucial role in the formation of bacterial cellular walls [43]. Teichoic acids are polysaccharides that are the major component of cellular walls in Gram positive bacteria [261],

[262]. They can constitute up to 60% of the cell membrane and are present in most Gram positive bacteria [262], [263]. Similarly, the outer structure membranes of Gram negative bacteria are formed by lipopolysaccharides [262]. Neither teichoic acids or lipopolysaccharides can survive for geologically significant periods of time, as teichoic acids are susceptible to degradation and lipopolysaccharides have only been detected in very recent sediments [54]. However, for their high abundance in cells and crucial role in forming bacterial cellular structure, both teichoic acids and lipopolysaccharides are a very promising bacterial biosignature of extant life.

Similarly to ectoine (see Section 4.3.2), trehalose is an osmoprotectant that protects cells against harsh environmental factors, particularly freezing, dehydration and oxidative stress [190], [264], [265]. It has been identified as one of the most effective osmoprotectants among other common compatible solutes [209]. Trehalose is used by all domains of life and it is particularly common in psychrophiles and organisms that undergo inanimation in extreme cold conditions [186], [190], [264], [265]. Similar to heat shock proteins, its expression was also found to increase after a sudden change of environmental conditions [186]. As such, it represents an incredibly attractive biosignature of life for the exploration of Europa.

4.3.8 Coenzymes

Nicotinamide adenine dinucleotide (NAD) and nicotinamide adenine dinucleotide phosphate (NADP) are metabolites of ATP responsible for electron transfer within cells [266], [267]. They are essential to maintain the function of living cells and are present in all known forms of cellular life [266], [267]. Their uniformity across all terrestrial life could signal an early evolution and their key role in the function of living cells indicates that a similar mechanism, if not the same, could be adopted by extraterrestrial life. They have been previously proposed as biomarkers for the exploration of Mars [43], [268] and their importance in the function of cells also makes them a very interesting general biomarker of life regardless of the planetary target.

The common base and an essential component of NAD and NADP is nicotinamide, an active form of vitamin B3, which could serve as a general indicator of their presence [269], [270]. While vitamin B3 has been found on meteorites and nicotinamide can be prepared in laboratories [56], there are no natural abiotic sources of nicotinamide and it is believed that prehistoric cells synthesized it into NAD *de novo* [271], [272].

The role of electron transfer, similar to NAD and NADP, is also fulfilled by flavin adenine dinucleotide (FAD), which is equally as crucial to all life on Earth and also has been suggested as a biosignature for the exploration of Mars [43], [268]. Similar to NAD, its importance also applies to other extraterrestrial sites, including Europa. Its precursor is riboflavin, vitamin B2, which is also

essential to terrestrial life [273]. Despite not being uniquely biogenic [269], riboflavin could also be a good indicator of the presence of FAD and a good general biosignature.

4.3.9 Metabolic Products

Signs of metabolic activity can represent very strong biomarkers since metabolic products tend to be present in higher concentrations than the biosignatures producing them [19]. However, most end products and by-products of metabolism can be also formed abiotically and therefore do not represent an unambiguous sign of life on their own [19], [274]. Nevertheless, their abundance or their presence alongside other potentially biogenic compounds as well as patterns associated with biogenicity could provide compelling evidence of their biogenic origin [19], [274].

Metabolic products vary among different lifeforms, however, the most widely discussed gaseous metabolic products associated with life on other planets are oxygen (O_2) and its product ozone (O_3), nitrous oxide (N_2O) and methane (CH_4) [274]–[276].

All of these chemicals can be also formed abiotically, however, they still remain an important biosignature as their relative abundance is a very strong indicator of metabolic processes [274]. Both O_2 and CH_4 are highly reactive and therefore can only remain present in high quantities if there is a mechanism continuously producing them [274]. There are no abiotic processes that could continuously form O_2 and therefore large quantities of this gas can only mean that metabolic activity is present [274]. Similarly, CH_4 is highly unstable and can only exist in high quantities if produced continually, typically through processes associated with life [274]. In this case, however, smaller amounts of CH_4 can also be produced by volcanic activity [274], [276].

While there are a few minor inorganic sources of N_2O on Earth, it is produced almost exclusively by microbial oxidation-reduction reactions and thus represents a relatively solid biosignature [275], [277] [276].

Similarly, dimethyl sulfide (DMS) and dimethyl disulfide (DMDS), metabolic by-products of both prokaryotic and eukaryotic life forms, also do not have any known abiotic sources [274], [278], [279].

Methanethiol, a metabolic intermediate of DMS and DMDS and an end product of biomass degradation, can be found in sediments and represent a biomarker of metabolic activity [280], [281]. However, its concentration in sediments was found to be significantly lower than the concentration of DMS [281].

Ammonia (NH_3) is a significant metabolic waste product of terrestrial organisms and represents a promising biosignature for extraterrestrial exploration [276]. However, primordial ammonia could be present on Europa without the contribution of any living organisms [276]. Despite not being an unambiguous sign of life, ammonia is still an important indicator of life due to its key role in metabolic processes.

Other biosignature gases such as carbon dioxide (CO_2) or sulphur dioxide (SO_2) are not particularly useful as signs of life due to their significant abiotic sources [274]. However, as radiation products, their detection could be a useful habitability marker on Europa.

Water (H_2O), while amongst the most important products of metabolic processes, does not represent a significant sign of life due to the relative abundance of its abiotic form that greatly out-weighs any biogenic sources. Nevertheless, its crucial role in the formation and sustainability of life makes liquid water an important habitability marker of great significance to astrobiology [9], [274], [275]. While the presence of liquid water on Europa has already been widely accepted based on existing evidence [33], this is yet to be confirmed in-situ.

4.3.10 Porphyrins

In terrestrial life, porphyrins are globally occurring molecules that are used virtually by all forms of life as we know it [124]. They are exclusively biogenic and stable for long periods of time, which is why they have been suggested as an ideal and unambiguous sign of life for astrobiology [43], [282]. The precursor of porphyrins, chlorophylls, heme and bacteriochlorophylls, are crucial molecules for metabolic processes performed by terrestrial cells and are believed to have occurred early in the evolution of life [124]. This would also suggest similar molecules could have evolved elsewhere in the universe [124]. Porphyrins previously studied for the purposes of astrobiology include protoporphyrin IX, hemin and octaethylporphine [124].

Porphyrins complexed with metals are significantly more stable and can be found in terrestrial sediments as molecular fossils of chlorophylls and related biomolecules, most commonly as nickel or vanadyl porphyrins [283], [284].

Recent studies have also suggested that porphyrins could have formed abiotically on prebiotic Earth, however, the porphyrins produced differ to the biosynthesized porphyrins of extant terrestrial life [285], [286].

4.3.11 Phosphate Biomolecules

One of the most fundamental molecules for all life on Earth is adenosine triphosphate (ATP) [287], [288]. It serves as a universal intercellular energy transfer mechanism for all forms of life [287], [288]. Additionally, it is also uniquely biogenic [5]. This has already placed it on a list of suitable biomarkers for Mars exploration [43], however, its crucial function makes it a highly ubiquitous biosignature of life regardless of the location within the universe or environmental conditions. A similar function is also carried out by phosphoenolpyruvate, which is an important intermediate in living organisms and also has been identified as a possible molecular target for Mars exploration [43], [289]. Neither of these molecules can survive outside a cell for geologically significant periods of time and have been used only to signal the presence of extant biomass [43], [290], [291]. While extant forms of life might be unlikely on Mars, the European ocean or even subsurface layers of its icy crust might be rich in living microorganisms, making extant biomarkers an important tool for life detection.

4.3.12 Biominerals

Life leaves an imprint in its surrounding inorganic environment, which can be used as a biosignature in the search of extraterrestrial life [193]. Most notably, life creates inorganic compounds (minerals) through a process known as biomineralization, which is widely adopted by organisms from all domains of life, from bacteria to mammals [193], [292]. Biomineralization forms mineralized tissues, such as bones, cell walls, teeth and shells that can be preserved for long periods of time. This is also why they are excellent biomarkers in the search for fossil extraterrestrial life.

Calcium oxalate minerals are by far the most widespread in nature and they represent the most abundant group of organic minerals found in sediments [293]–[295]. Calcium oxalate minerals occur in two hydration states, whewellite (monohydrate) and weddellite (dihydrate), whewellite being the more stable hydrate [293]. Moreover, calcium oxalates can account for up to 80% of the dry weight of some plants [295], [296]. Calcium oxalate minerals stem from the organic compound calcium oxalate and both calcium oxalate and its hydrated mineral forms have been proposed as unambiguous signs of life for extraterrestrial exploration [53], [297]. However, calcium oxalate can also be produced by very rare geological processes abiotically [297].

Another exclusively biogenic mineral is mellite, which is formed from mellitic carboxylic acid [53], [298]. However, mellite is an incredibly rare mineral on Earth [298], [299], and while it could be present elsewhere in the universe in a greater abundance, based on its rarity on Earth, the likelihood of occurrence on Europa is relatively low compared to other biominerals.

Although not exclusively biogenic, silica is one of the most widespread biogenic minerals on Earth [300], [301]. It is predominantly produced by diatoms, single cell algae, and represents one of the dominant minerals in terrestrial marine sediments [300]–[302]. It has been proposed as a suitable biomineral target for astrobiology and could also serve as a measure of habitability due to its connections to geochemical processes on Europa [19]. Additionally, it could provide encapsulation for cellular structures [19], [301], thus protecting the cells from the outside extreme environment. Despite abiotic silica being a very common mineral, the detection of silica could prove to be an important bioindicator for the search of life on Europa.

Similarly, magnetite and iron sulfides such as pyrite do not have an exclusively biogenic origin but have been suggested as biomineral targets for detection on Europa [8].

Biogenic pyrite is present in most marine sediments and forms as a result of bacterial activity [303], [304], while magnetite is produced by bacteria, as well as some members of eukarya, but only constitutes a very small percentage of marine sediments [193], [305], [306].

These ferrous compounds may also play an important role in the European geochemical cycle and their detection could provide information about the geochemical and biochemical processes on Europa [59]. The characterization of such processes can provide an evaluation of the chemical equilibrium in the ocean, or the lack of, which could indicate the presence of metabolic processes [59].

Carbonates, formed by shells and skeletons of marine plankton, molluscs and corals, are major components of terrestrial marine sediments [307]. While sediments with low terrigenous deposit influx are dominated by carbonates in warm water, cold environments with low terrigenous influx more analogous to Europa can be predominantly siliceous. This could make carbonates less abundant on Europa, however, they are still an important terrestrial biomineral of major significance for astrobiology [5], [19], [53], [308]. Common terrestrial carbonates that have been suggested as targets for extraterrestrial exploration include calcite, aragonite, dolomite, magnesite and vaterite [53]. Additionally, aragonite and vaterite have been suggested as exclusively biogenic and could represent unambiguous signs of life [53]. While this claim is somewhat misleading as both minerals have abiotic sources, there is evidence that the biotic and abiotic forms can be distinguished [309]. All carbonates are also a useful habitability indicator [5], [19], [308].

4.3.13 Cell Colonies

An alternative approach to targeting molecular biosignatures could also be detecting entire cells, such as bacterial colonies from Europa analogous sites. Flavobacterium has been identified as the most common bacterial class living in cold environments, Gammaproteobacteria also being very common. However, while cell colonies in general are a clear sign of the presence of life and potentially useful for analysis and testing of instruments, focusing on specific terrestrial cell colonies is too specific and very unreliable for the search of extraterrestrial life.

Chapter 5 Experimental Methodology

This chapter covers the methodology used to assess the detection limits of Raman spectroscopy for the detection of biosignatures on Europa. The results of these experiments are provided in Chapter 6, Chapter 7, Chapter 8 and Chapter 9. The detection limits explored in these chapters are some of the most important limitations in Raman spectroscopy relevant to the search for life on Europa that have an impact on the instrument design requirements. These critical detection limits include fluorescence interference and laser damage (covered in Chapter 6), the effect of extreme low temperatures on the Raman spectra (Chapter 7) as well as the laser fluence and total energy dose limits and sensitivity to the relevant target molecules (Chapter 8). These limitations are investigated experimentally using lab grade Raman systems at various excitation wavelengths in order to quantify the impact and identify key design criteria for the development of a Raman Spectrometer for biosignature detection on Europa. A broader discussion on the overall detectability and instrument design considerations derived from the results presented in Chapter 6 to Chapter 8 is then provided in Chapter 9. Please note that some of these results have been presented and discussed in peer reviewed journal articles arising from this PhD research, which are referenced here [310], [311].

5.1 Methodology

The detection limits are assessed using a representative selection of the target molecules identified in Chapter 4. These samples represent a reference frame for the identification of biosignatures on Europa, which allows quantification of the impact of the limitations on the instrument design requirements. The selected samples, as well as the specific experimental set up and methodology for the assessment of each detection limit, are described in the following sections.

5.1.1 Samples

Samples used as a reference frame for the assessment of the detection limits were chosen based on the high priority target molecules for life detection on Europa identified in Chapter 4. The selection was driven primarily by the priority of the identified target molecules and representative samples from most of the targeted molecular classes were chosen in order to encompass a broad spectrum of relevant molecules. However, availability within the timescale and budget of this research was also a factor in the selection. The complete list of molecules selected for the detection limits testing can be viewed in Table 5-1.

Class	Compound	Priority	Purity & Form	Supplier
Amino Acids	Alanine	B	≥99% powder	Alfa Aesar
	Glutamic Acid	B	≥99% powder	Sigma Aldrich
	Glycine	A	≥99% powder	Sigma Aldrich
	Histidine	A	≥99% powder	Sigma Aldrich
	Tryptophan	C	≥99% powder	Alfa Aesar
	Tyrosine	C	≥99% powder	Sigma Aldrich
	β-Alanine	D	≥99% powder	Sigma Aldrich
Carboxylic Acids	Palmitic Acid	A	≥99% powder	Sigma Aldrich
	Ectoine	A	≥95% powder	Sigma Aldrich
Isoprenoids	Pristane	B	95% liquid	Fisher Scientific
	Squalane	C	98% liquid	Alfa Aesar
Carotenoids	β -Carotene	A	99% powder	Alfa Aesar
	Astaxanthin	B	≥98% powder	Fisher Scientific
Steranes	5α-Cholestane	B	>98% liquid	Fisher Scientific
Pigments	C-Phycocyanin	C	50-70% powder	Sigma Aldrich
	Chlorophyll A	B	≥85% powder	Sigma Aldrich
Nucleic Acids	DNA	A	≥95% powder	Sigma Aldrich
	RNA	C	≥92% powder	Sigma Aldrich
Nucleobases	Adenine	B	≥99% powder	Sigma Aldrich
	Guanine	B	98% powder	Sigma Aldrich
	Cytosine	B	≥99% powder	Sigma Aldrich
	Thymine	B	≥99% powder	Sigma Aldrich
	Uracil	B	≥99% powder	Sigma Aldrich
Carbohydrates	Trehalose	A	≥99% powder	Sigma Aldrich
Coenzymes	Nicotinamide	A	≥99.5% powder	Sigma Aldrich
Porphyrins	Protoporphyrin IX	A	>98% powder	PorphyChem
	Hemin	A	>97% powder	Alfa Aesar
Inorganics	Palagonite (HWMK101)*	NA	NA	Dick Norris (NASA – JSC)
Natural Mixtures	Carrot Root (natural carotene)*	NA	NA	NA
	Spinach Leaf (natural chlorophyll)*	NA	NA	NA

Table 5-1 Selected samples for testing, their priority, purity, form and the supplier

(*complementary samples)

An additional complementary sample of palagonite was included in order to test inorganic soil-like materials that would provide more information about naturally occurring compounds that could interfere with the biosignature spectra on Europa. There is currently no simulant material of the European soil available on the market and the exact composition of European soil has not yet been determined. Therefore, terrestrial volcanic soil in the form of a Hawaiian palagonite has been chosen to test the inorganic interference. Likewise, carrot root and spinach leaf were included in order to test naturally occurring mixtures of some important pigments, i.e. carotene and chlorophyll. The measurements of these additional compounds are not a pivotal part of this

research and only serve to complement the results in order to provide a more complete understanding of the interference and detection limits.

5.1.2 Measurements and Experimental Set Up

Each detection limit explored in this study represents a unique metric and requires different and highly specific methods. However, while the experimental set up and methodology vary across the experiments and are described in separate sections dedicated for each examined detection limit, some general methods are applicable to all experiments.

With the exception of a few experiments exploring the sensitivity detection limit, all samples were examined in their pure form as stated in Table 5-1. Two Raman Renishaw Spectrometers at 4 different excitation wavelengths, with representative excitation in the UV (325 nm), visible (532 nm, 633 nm) and NIR (785 nm) range, were used across the experiments. The specification of each configuration - including the nominal laser power, optical set up, spectral resolution and spot size - are summarised in Table 5-2. All Raman systems used in this study are standard laboratory grade instruments with a high spectral resolution ranging between from approximately 0.5 to 2 cm^{-1} and 0.3 cm^{-1} when using the FWHM (Full Width Half Maximum) integrated function. Standard built-in calibration using Silicon standard was used for system at visible and NIR excitation and a diamond standard at UV excitation. Calibration was performed before and after measurements to monitor any drift in the nominal Raman shift. Measurements were taken within the spectral range of 100 to 4000 cm^{-1} at various laser power settings. However, in all cases the maximum setting used was the 100% laser power setting at the nominal laser power as specified in Table 5-2. Each measurement comprises a single acquisition of 120 seconds total exposure time (10 seconds nominal exposure). Peak fitting and FWHM methods were used for the identification of the Raman bands, the Raman band width and the signal intensity. The in-built Renishaw WIRE software was used for data generation and initial analysis. Further data analysis and visualisation were performed in Python and Microsoft Excel.

A quartz microscope slide or fused silica crucible compatible with the cooling stage for low temperature testing were used as substrates for the measurements. The sample layer thickness was approximately 0.5 mm during all measurements and all substrates and deposition tools were cleaned with Acetone and IPA between measurements to prevent cross-contamination. With the exception of low temperature testing, which requires liquid nitrogen cooling and nitrogen purged environment, all experiments were carried out in ambient environment and at room temperature (nominally $22\text{ }^{\circ}\text{C}$).

Instrument & Facilities	Excitation Wavelength [nm]	Nominal Laser Power at Sample [mW]	Objective Lens & NA	Spectral Resolution [cm^{-1}]	Laser Spot Diameter [μm]
Raman Renishaw InVia Microscope (Cambridge Graphene Centre, University of Cambridge)	325	0.9	40x 0.5 NA	1.49 @4000 cm^{-1} 1.937 @1000 cm^{-1} 2.02 @500 cm^{-1} 0.3 cm^{-1} (FWHM)	0.793
Raman Renishaw InVia Microscope (University of Southampton)	532	44.9	5x 0.12 NA	0.7 @4000 cm^{-1} 1.199 @1000 cm^{-1} 1.283 @500 cm^{-1} 0.3 cm^{-1} (FWHM)	5.41
	633	10.4		1.15 @4000 cm^{-1} 1.859 @1000 cm^{-1} 1.99 @500 cm^{-1} 0.3 cm^{-1} (FWHM)	6.44
	785	115		0.56 @4000 cm^{-1} 1.131 @1000 cm^{-1} 1.243 @500 cm^{-1} 0.3 cm^{-1} (FWHM)	7.98

Table 5-2 Raman instrumentation set up and specification

The experimental set up and methodology specific to the assessment of each detection limit, as well as the overall detectability and instrument design considerations, are described in the following sections.

5.1.2.1 Detection Limit 1: Fluorescence

In order to assess the impact and severity of the fluorescence interference, samples listed in Table 5-1 are examined using representative Raman excitation wavelengths across the UV, visible and NIR wavelength regions. Using the two Raman systems listed in Table 5-2, Raman spectra were collected at 325 nm, 532 nm, 633 nm and 785 nm. Raman spectra of all samples were collected at 532 nm, 633 nm and 785 nm, however, only selected samples were examined using the 325 nm excitation wavelength due to constraints associated with the facility use and timeline of the research project. In order to ensure an effective assessment of the fluorescence interference at this excitation, high priority representative samples from each category were selected and tested at 325 nm. The selected samples are shown in Table 5-3.

All samples were examined at room temperature (nominally 22 °C) and in an ambient environment, however, fluorescence trends were also monitored during low temperature measurements and the results are described in Chapter 7.

	Compound	Priority
Amino Acids	Glutamic Acid	B
	Glycine	A
	Histidine	A
	Tyrosine	C
Carboxylic Acids	Palmitic Acid	A
Carotenoids	β-Carotene	A
	Astaxanthin	B
Steranes	5α-Cholestane	B
Pigments	C-Phycocyanin	C
Nucleic Acids	DNA	A
	RNA	C
Nucleobases	Adenine	B
	Guanine	B
	Cytosine	B
	Uracil	B
Carbohydrates	Trehalose	A
Coenzymes	Nicotinamide	A
Porphyrins	Protoporphyrin IX	A
	Hemin	A

Table 5-3 A representative selection of samples tested at the 325 nm excitation

In order to evaluate the severity of the fluorescence interference in the spectra, a Signal to Noise Ratio (SNR) was calculated using the following formula:

$$\frac{S}{N} = \frac{I_S - I_N}{\sqrt{I_N}} \quad (1)$$

The absolute intensity of the most dominant Raman band in the spectra (I_S) was used to calculate the SNR. The absolute intensity of a point in the spectra not containing any Raman bands was used to represent the noise (I_N). The same Raman bands and noise readings were used for the SNR calculation in the spectra of the same molecule across different excitation wavelengths. In the presence of a fluorescent background, the highest intensity of the noise was used. The SNR was calculated at each power setting and was used to compare the detectability of the molecule across different excitations.

However, while the SNR comparison method is a very useful tool for assessing the noise levels in Raman spectra of the same molecule at different laser power or with a different set up, it is very limited when comparing different molecules or different excitations. This is due to the variability of the signal as well as the noise reference points. The location of the highest point of the fluorescence background may not be constant at different excitations, which limits the comparison of the fluorescence in the spectra of the same molecule as some regions in the

spectra may be particularly critical for the identification of the molecules. On the other hand, higher fluorescence in some other regions in the spectra may not restrict the detectability of peaks at all and may thus not be critical. Likewise, the most dominant Raman band may not be the same at all excitation wavelengths. The SNR also fails to fully describe the detectability of the molecules as minor peaks in the spectra may also be critical for the identification but are not included in the calculation. Averaging the SNR of multiple peaks can also be very misleading. Due to the limits of the SNR calculation, it was only used as a reference for the fluorescence assessment. Rather, the impact of the fluorescence and its severity is assessed and quantified using the overall detectability of both major and minor Raman bands critical for the identification of the molecule.

Based on the identified fluorescence severity, the target molecules are classified into 5 classes. Class 1 includes fully detectable target molecules experiencing no fluorescence. Class 2 includes molecules with mild fluorescence where all major and at least most minor Raman peaks important for identification are clearly detectable. Class 3 comprises molecules with significant fluorescence where minor peaks are not visible but major peaks can still be detectable in some cases. Some peaks might only be detectable at higher laser power and molecules in this category might thus not be detectable at all at certain laser fluence. The fluorescence background in this group is critical for the identification of the molecule. Molecules in class 4 experience severe fluorescence where most major Raman peaks are not visible and the sample is not detectable. Class 5 includes completely undetectable molecules with very severe fluorescence that overtakes the entire spectrum and no major or minor peaks are visible.

The resulting classification of the tested molecules and their priority is used to assess and compare the performance of each excitation wavelength. The suitability of each excitation for the detection of biosignatures on Europa is discussed in line with available fluorescence mitigation techniques.

5.1.2.2 Detection Limit 2: Laser Damage

The same Raman spectra collected for the assessment of the impact of the fluorescence noise were used to analyse the laser damage thresholds and the impact of sample degradation on the overall identifiability of the target molecules. The spectra acquisition method including the instrumentation and measurements methodology is described in Section 5.1.2.1. While these spectra were obtained at room temperature, the following methodology was also applied to monitor the impact of laser damage at cryogenic temperatures, the results of which are discussed in Chapter 7.

The impact of laser damage on the Raman spectra was monitored through a visual examination of the sample under a microscope as well as through spectral evidence of laser damage in the resulting Raman spectra. The samples were examined under a microscope before and after the measurement and any visible changes in the spectra and sample properties were reported. Microscope images of the sample were obtained both before and after the measurement. Most visible evidence of laser damage constitutes discolouration, i.e. darkening, lightening or general change of colour of the sample at the location of the laser incidence. Depending on the severity of the damage, the discolouration may extend beyond the location of laser incidence, which was also monitored.

Spectral laser damage is usually signalled by variance in the obtained spectra, shifting of peaks to higher frequencies or broadening of Raman bands. Strong background noise or the presence or strengthening of radiation product peaks could also occur as a result of laser damage. These effects were monitored and recorded during the analysis of the spectra.

The lowest laser fluence and total energy dose at which signs of degradation occurred were identified as the **laser damage threshold** and the type of degradation first observed, i.e. visual or spectral, was recorded for each molecule. Since laser damage might have various effects on the detectability of the molecule from only minor background noise to complete change of the spectra, measurements at higher laser fluence were taken if the molecule was still detectable at its laser damage threshold. The laser fluence and total energy dose at which the molecule becomes undetectable is then identified as the **laser damage detectability threshold**.

Apart from the laser damage threshold and laser damage detectability threshold, the most laser damage sensitive molecules are also identified. The results are discussed in terms of the impact of laser damage on the spectra of biosignatures relevant for the exploration of Europa as well as potential methods of laser damage reduction.

5.1.2.3 Detection Limit 3: Effects of Extreme Low Temperatures

In order to observe the effects of the European extreme low temperatures on Raman spectra, Raman spectra of samples listed in Table 5-1 were obtained at temperatures analogous to the European surface and sub-surface (-196 °C and -100°C) and compared to room temperature measurements (22 °C). Depending on the location and time of day, the temperature of -196 °C represents the European surface or near sub-surface temperature [24], [71] and a similar temperature could be expected at 10 cm below the surface, which is the minimum sampling depth of the Europa Lander Mission proposed by NASA [19], [24], [71]. The temperature of -100 °C represents the conditions at the depth of 5 km within Europa's icy shell [71], [73] and

Chapter 5

serves as a gauge measurement that provides further information about the profile of the spectral changes at decreasing temperatures and corresponding depth within the ice.

A Raman Renishaw system with 532 nm and 785 nm excitation, as described in Table 5-2, was used to collect the Raman spectra. Excitations at 532 and 785 nm were used in order to observe the cryogenically induced changes within the spectra at two different excitations as well as to ensure Raman spectra of all target molecules can be obtained at the selected excitations.

The samples were cooled to the required temperature using a Linkam THMS600 temperature controlled stage with a liquid nitrogen cooling system. The Linkam THMS600 stage system is a standard temperature-controlled stage widely used for Raman measurements and the stage platform for the sample is shown in Figure 5-1. When connected to the liquid nitrogen system, the stage allows measurements at temperatures ranging to $-196\text{ }^{\circ}\text{C}$ at temperature accuracy and stability of $0.01\text{ }^{\circ}\text{C}$.



Figure 5-1 An open Linkam THMS600 cooling stage showing the cooling block used for the experiments. The stage is closed and purged with liquid nitrogen via the liquid nitrogen tubes on the left-hand side. A temperature controller is connected to the stage and a PC interface software, which is used to set the temperature profile.

All measurements were performed in a nitrogen purged environment and the temperature rate of change was $55\text{ }^{\circ}\text{C}/\text{minute}$. In order to ensure the samples were cooled to the required temperature, a dwell time of 6 minutes was applied. Three measurements as described in Section 5.1.2 were taken at each temperature setting. The optimal laser power, as determined by previous tests at room temperature, was used for the measurements in order to ensure good quality Raman spectra. Due to the variability of the spectra across various laser powers and temperatures, the three measurements at each temperature were taken at various laser powers for some samples and at the same laser power for others as appropriate. This was to ensure sufficient Raman signal strength without saturating the detector. For molecules requiring measurements at a different laser power, the same three laser power settings were used at each

temperature. The laser power range used for each sample and at each excitation wavelength, expressed also in terms of laser fluence and total energy dose for clarity, is shown in Table 5-4.

		Measurement Laser Power, Fluence and Total Energy Dose	
	Compound	532 nm	785 nm
Amino Acids	Alanine	2.25, 4.49, 22.5 mW 1.17, 2.35, 11.7 MJ/cm ² 0.27, 0.54, 2.69 J	5.75, 11.5, 57.5 mW 1.38, 2.76, 13.8 MJ/cm ² 690 mJ, 1.38 J, 6.9 J
	Glutamic Acid	0.45, 2.25, 4.49 mW 0.23, 1.17, 2.35 MJ/cm ² 53.9 mJ, 0.27 J, 0.54 J	1.15, 5.75, 11.5 mW 0.28, 1.38, 2.76 MJ/cm ² 138 mJ, 690 mJ, 1.38 J
	Glycine	0.45, 2.25, 4.49 mW 0.23, 1.17, 2.35 MJ/cm ² 53.9 mJ, 0.27 J, 0.54 J	1.15, 5.75, 11.5 mW 0.28, 1.38, 2.76 MJ/cm ² 138 mJ, 690 mJ, 1.38 J
	Histidine	0.45, 2.25, 4.49 mW 0.23, 1.17, 2.35 MJ/cm ² 53.9 mJ, 0.27 J, 0.54 J	11.5, 57.5, 115 mW 2.76, 13.8, 27.6 MJ/cm ² 1.38, 6.9, 13.8 J
	Tryptophan	44.9 μ W, 0.22 mW, 0.45 mW 23.5 kJ/cm ² , 117 kJ/cm ² , 0.23 MJ/cm ² 5.39, 26.9, 53.9 mJ	5.75, 11.5, 57.5 mW 1.38, 2.76, 13.8 MJ/cm ² 690 mJ, 1.38 J, 6.9 J
	Tyrosine	0.45, 2.25, 4.49 mW 0.23, 1.17, 2.35 MJ/cm ² 53.9 mJ, 0.27 J, 0.54 J	5.75, 11.5, 57.5 mW 1.38, 2.76, 13.8 MJ/cm ² 690 mJ, 1.38 J, 6.9 J
	β -Alanine	2.25, 4.49, 22.5 mW 1.17, 2.35, 11.7 MJ/cm ² 0.27, 0.54, 2.69 J	11.5, 57.5, 115 mW 2.76, 13.8, 27.6 MJ/cm ² 1.38, 6.9, 13.8 J
Carboxylic Acids	Palmitic Acid	0.45, 2.25, 4.49 mW 0.23, 1.17, 2.35 MJ/cm ² 53.9 mJ, 0.27 J, 0.54 J	5.75, 11.5, 57.5 mW 1.38, 2.76, 13.8 MJ/cm ² 690 mJ, 1.38 J, 6.9 J
	Ectoine	0.22, 0.45, 2.25 mW 117 kJ/cm ² , 0.23 MJ/cm ² , 1.17 MJ/cm ² 26.9 mJ, 53.9 mJ, 0.27 J	5.75, 11.5, 57.5 mW 1.38, 2.76, 13.8 MJ/cm ² 690 mJ, 1.38 J, 6.9 J
Isoprenoids	Pristane	22.5 mW 11.7 MJ/cm ² 2.69 J	115 mW 27.6 MJ/cm ² 13.8 J
	Squalane	2.25 mW 1.17 MJ/cm ² 0.27 J	115 mW 27.6 MJ/cm ² 13.8 J
Carotenoids	β -Carotene	44.9 μ W 23.5 kJ/cm ² 5.39 mJ	0.115 μ W 27.6 J/cm ² 13.8 μ J
	Astaxanthin	2.25 mW 1.17 MJ/cm ² 0.27 J	0.115 μ W 27.6 J/cm ² 13.8 μ J
Steranes	5 α -Cholestane	4.49 mW 2.35 MJ/cm ² 0.54 J	115 mW 27.6 MJ/cm ² 13.8 J
Pigments	C-Phycocyanin	U	0.58 mW 0.14 MJ/cm ² 69 mJ

	Chlorophyll A	U	U
Nucleic Acids	DNA	U	U
	RNA	U	11.5 mW 2.76 MJ/cm ² 1.38 J
Nucleobases	Adenine	44.9 μ W, 0.22 mW, 0.45 mW 23.5 kJ/cm ² , 117 kJ/cm ² , 0.23 MJ/cm ² 5.39, 26.9, 53.9 mJ	0.58, 1.15, 5.75 mW 0.14, 0.28, 1.38 MJ/cm ² 69, 138, 690 mJ
	Guanine	44.9 μ W, 0.22- mW, 0.45 mW 23.5, 117 kJ/cm ² ; 0.23 MJ/cm ² 5.39, 26.9, 53.9 mJ	1.15, 5.75, 11.5 mW 0.28, 1.38, 2.76 MJ/cm ² 138, 690 mJ; 1.38 J
	Cytosine	44.9 μ W; 0.22, 0.45 mW 23.5 kJ/cm ² , 117 kJ/cm ² , 0.23 MJ/cm ² 5.39, 26.9, 53.9 mJ	0.58, 1.15, 5.75 mW 0.14, 0.28, 1.38 MJ/cm ² 69, 138, 690 mJ
	Thymine	0.22, 0.45, 2.25 mW 117 kJ/cm ² , 0.23 1.17 MJ/cm ² , 1.17 MJ/cm ² 26.9 mJ, 53.9 mJ, 0.27 J	11.5 mW 2.76 MJ/cm ² 1.38 J
	Uracil	0.45 mW 0.23 MJ/cm ² 53.9 mJ	57.5 mW 13.8 MJ/cm ² 6.9 J
Carbohydrates	Trehalose	4.49 mW 2.35 MJ/cm ² 0.54 J	115 mW 27.6 MJ/cm ² 13.8 J
Coenzymes	Nicotinamide	2.25 mW 1.17 MJ/cm ² 0.27 J	5.75 mW 1.38 MJ/cm ² 690 mJ
Porphyrins	Protoporphyrin IX	44.9 μ W 23.5 kJ/cm ² 5.39 mJ	0.115 μ W 27.6 J/cm ² 13.8 μ J
	Hemin	2.25 mW 1.17 MJ/cm ² 0.27 J	5.75 mW 1.38 MJ/cm ² 690 mJ
Inorganics	Palagonite (HWMK101)	4.49 mW 2.35 MJ/cm ² 0.54 J	11.5 mW 2.76 MJ/cm ² 1.38 J
Natural Mixtures	Carrot Root (natural carotene)	2.25 mW 1.17 MJ/cm ² 0.27 J	115 mW 27.6 MJ/cm ² 13.8 J
	Spinach Leaf (natural chlorophyll)	44.9 μ W 23.5 kJ/cm ² 5.39 mJ	11.5 mW 2.76 MJ/cm ² 1.38 J

Table 5-4 Measurement laser power, laser fluence and total energy dose for experiments exploring the effects of cryogenic temperatures on the Raman spectra (U denotes samples and/or excitations that did not allow investigations of the cryogenically induced changes due to laser damage or excessive fluorescence impeding any further characterisation and that were excluded from these experiments)

Raman spectra of some molecules, as highlighted in Table 5-4, did not allow investigations of the cryogenically induced changes due to laser damage or excessive fluorescence impeding any further characterisation.

The collected spectra of each sample at each temperature are compared in order to identify and quantify the effects of the extreme low temperatures analogous to Europa. Monitored effects include variability between individual measurements at each temperature, shifts in the Raman band position, width and shape. The emergence of new Raman bands, changes in the overall signal intensity (i.e. SNR) or diminishing individual Raman bands, as well as any changes in the fluorescence noise were also recorded. Changes in the minimum peak-to-peak distance in the spectra at various temperatures were also investigated in order to assess the impact of cryogenic temperatures on the spectral resolution requirements. Where possible, the profile of change was also investigated and any common trends identified and described. Peak fitting is used for the identification of the Raman spectral shift and the width and intensity of Raman bands are assessed using the Full Width Half Maximum (FWHM) method. Furthermore, the significance of the observed spectral shifts and band width changes at low temperatures was assessed using sigma error bars. 1σ (32% error probability), 2σ (4.6% error probability) and 3σ (0.3% error probability) error bars were calculated for each Raman band over the three measurements at each power and temperature setting in order to investigate the variation in the changes relative to the instrumental and experimental error.

Due to the variance in the characteristics of the target molecules and their Raman spectra, additional experimental or analytical methods were applied in some cases to ensure a complete understanding of the observed effects:

Amino Acids - The number of different amino acid samples with a wide range of molecular structures within the same molecular category provides an ideal opportunity to examine these molecules in more detail. As such, an analysis of the thermally induced changes in the context of the molecular vibrational modes was performed. An optimized Density Functional Theory (DFT) vibrational frequency calculation was used for the Raman band assignments in conjunction with Split Valence Polarization (SVP) and polarizability calculations for Raman vibrational frequencies and Raman activity as well as a review of previously published assignments [312], [313], [322]–[326], [314]–[321]. In order to build sufficient confidence in the vibrational mode assignments, sigma error bar analysis was studied particularly in detail for amino acids. Additionally, the experiments were expanded by four additional temperature reference points (-20 °C, -60 °C, -132 °C, -164 °C) during the investigation of glycine in order to gain a more complete understanding of the trends and profiles observed.

Porphyryns – Porphyrin spectra at low temperatures showed significant changes in signal intensity that varied across all Raman bands, which requires a more in-depth analysis of the changes specific to each band. In order to evaluate the signal strength change in the context of individual bands rather than the entire spectra, a signal to noise ratio (SNR) was calculated for all major Raman peaks in the spectra. The absolute intensity of the peaks was used as the I_S term and a noise intensity at an adjacent valley in the spectra was used as the I_N term in the SNR calculation. This prevents any fluorescence or background noise irrelevant to the signal change from affecting the SNR data in order to assess the signal enhancement while also allowing evaluating the overall impact of the fluorescence noise in light of the signal change at each peak.

While the signal enhancement was the main focus of the porphyrin analysis, optimized DFT and SVP calculations similar to the one used for the analysis of amino acids were also performed in order to assign Raman bands to vibrational modes. This allows further analysis of the relationship between various vibrational modes and the cryogenically induced changes. It also serves to confirm results from the analysis of amino acids. However, it is important to note that unlike the previously presented amino acid data, the low quality of the spectra of both porphyrins at room temperature may have lacked the necessary definition to accurately determine the Raman band frequency. As such, the vibrational mode assignment analysis may not be as accurate. A sigma error bar analysis was performed to quantify the confidence in both the Raman shift changes observed in the data as well as the changes in the SNR.

Carotenoids – Carotenoid molecules tend to have relatively similar Raman spectra with strong Raman band signals at both 532 nm and 785 nm excitation, which can be used to accurately track and compare the thermally induced changes between these two excitations. As such, the sigma error bar analysis described previously was used to assess the significance of the observed changes in order to establish whether the excitation wavelength has any impact on the thermally induced changes. Additionally, similar to porphyrins, carotenoid spectra showed much higher intensity spectra at low temperatures even despite the fluorescence noise, which was contradictory to trends observed in the study of all other molecules except for porphyrins. As such, a similar SNR analysis of individual bands as described for porphyrins was used to analyse this effect further.

Isoprenoids – Pristane and squalene have very similar Raman signatures, which provides an ideal opportunity to study any differences between the cryogenic changes that could potentially help to distinguish between the two compounds. Hence, pristane and squalene are compared in terms of the cryogenically induced changes in their spectra, such as the width and shift change observed

for individual Raman bands. A detailed sigma error bar analysis was used to confirm the validity of the differences.

Steranes – 5 α -cholestane has a very complex Raman spectrum with numerous Raman bands, which calls for a detailed analysis of the minimum peak-to-peak distance between individual Raman bands. This then provides information for the assessment of the spectral resolution requirements. In order to accurately determine the minimum necessary spectral resolution, the Raman band width and the signal strength of adjacent bands were evaluated together with the peak-to-peak distance.

Nucleobases – Similar to amino acids, nucleobases offer an opportunity to compare between molecules with similar structures. As such, cryogenically induced changes in the spectra of nucleobases were also discussed in terms of the vibrational modes in order to confirm results observed in amino acids. Assignments of the vibrational modes in the spectra of nucleobases are available in previously published literature and therefore DFT calculation of the vibrational modes was not necessary. Similar to amino acids, sigma error bars were utilized to support any conclusions regarding cryogenically induced changes relative to mode assignments.

Coenzymes – Although fluorescent at 532 nm, Raman measurements of nicotinamide yield good spectra at both 532 nm and 785 nm excitation. Since the full nicotinamide signature can be obtained at both excitations and across the entire examined temperature range, the data can be used to compare the effect of fluorescence on the variability of the measurements. In order to do this, the three collected spectra at each temperature were used to calculate the average variance across all Raman bands within the spectra. This was recorded for each temperature and each excitation and compared. The results were also compared to the variance trends observed in other fluorescent molecules as well as other fluorescence-free spectra.

Inorganics - Inorganic materials in the sampled material could potentially obscure the Raman signature of any organics or biogenic matter. While it is not the primary focus of this research, studying the effect of cryogenic temperatures on the spectra of inorganic materials is an important aspect of ensuring a successful detection of biosignatures on Europa. As such, a simple Raman study of Hawaiian palagonite was performed at various temperatures in order to assess any potential interference of inorganic soil material with biosignature Raman spectra as a result of cryogenically induced spectral changes. Palagonite is a type of volcanic glass similar to basalt, which is of volcanic origin. While the composition of Europa's crust is not fully understood yet, studies have shown that material similar to terrestrial basalt may be present on Europa [327]. The cryogenically induced changes in the spectra of palagonite were recorded and discussed in terms of potential interference.

5.1.2.4 Detection Limit 4: Minimum and Maximum Laser Fluence and Total Energy Dose

The laser power necessary for full and unambiguous identification is a key parameter for successful life detection on Europa. As explored in detail in Section 6.2, measurements at high laser power can lead to disastrous laser sample damage and each molecule may have different laser damage thresholds. Likewise, molecules yield spectra of various signal strength levels and Raman spectra of some molecules can be obtained at much lower laser power than others. As such, the presence of molecules of higher intensity Raman signature may completely overshadow lower intensity signatures in the sample. Very high signals can also saturate the detector and render the measurement void. The maximum and minimum laser power for detection are thus critical parameters to choose the optimal measurement method for in-situ spectra collection on Europa.

Since laser power is not a very reliable measure across different instruments with various excitation wavelengths and optical set up, the laser power was converted into laser fluence and total energy dose as shown below. Laser power density has also been used for these purposes in literature available to date [104], [160].

$$\text{Fluence} \left[\frac{J}{cm^2} \right] = \frac{P \times t}{A} \quad (2)$$

$$\text{Power Density} \left[\frac{W}{cm^2} \right] = \frac{P}{A} \quad (3)$$

$$\text{Total Energy Dose [J]} = P \times t \quad (4)$$

$$\text{Laser Spot Diameter} [\mu m] = \frac{1.22 \times \lambda}{NA} \quad (5)$$

Where: P = laser power at sample

A = laser spot area at sample

t = exposure time

λ = laser excitation wavelength

NA = numerical aperture of the microscope objective

Converting laser power into laser fluence and total energy dose allows comparison between different instruments with different optical set up and excitation wavelength. More importantly, the minimum laser fluence and total energy dose necessary for unambiguous identification can provide information on the optical configuration of the Raman instrument necessary for successful detection at each excitation wavelength. This allows the identification of an appropriate objective, its magnification and numerical aperture (NA), laser spot size, as well as duration of sample exposure and laser power. These are key parameters defining the instrument design requirements for biosignature detection on Europa. The minimum laser fluence and total

energy also indicate the Raman signal strength of each selected target molecule, which is an important measure of the overall detectability of the target molecules and the sensitivity (LOD) of the instrument necessary for detection.

The dataset collected for the analysis of the fluorescence interference and laser damage as described in Section 5.1.2.1 and 5.1.2.2 was also used to record the minimum and maximum laser fluence and total energy dose that allows full identification of the examined molecules. Raman spectra of samples were taken at 532 nm, 633 nm and 785 nm excitation at various laser powers and the full experimental set up has already been described in Section 5.1.2 to 5.1.2.1. Please note that the 325 nm dataset was excluded as it was not possible to perform a full set of measurements across the full laser power range with sufficiently small laser power increments between individual measurements. While sufficient for a limited analysis of the fluorescence interference, any results discussing the laser fluence and total energy dose for successful detection could be misleading as a result of this.

The obtained spectra at each laser power setting were classified into 4 categories: undetectable (U), limited detectability (L), detectable (D) and ideal spectral signature (I). A 5th category, oversaturated (O), was also introduced to denote measurements of very high signal strength that oversaturated the detector, which rendered the resulting spectra unusable. The classification was based on the SNR calculation introduced in Section 5.1.2.1 for the assessment of the fluorescence interference. However, as already described in Section 5.1.2.1, SNR comparison is very limited when comparing different molecules or measurements at different excitations. This is due to the difference in the Raman signature and the reference points as well as different number and characteristics of the identifying bands in the spectra. As such, the SNR method was complemented by an assessment of the visibility and signal strength of Raman bands important for the identification of the molecule. The categories thus include measurements that do not yield any identifiable signature (U) and measurements that are missing most minor bands and may lack the definition or some spectral features for full identification but may still allow the identification of the molecular species (L). Measurements resulting in a sufficient SNR spectrum with all major bands and at least most minor bands are classified as (D) and measurements leading to high SNR spectra with the full set of both major and minor bands are classified as (I).

The classification is then used to compare the signal strength of each molecule at different excitations as well as to other molecules. For the purposes of the analysis, limited detectability (L) is considered in case molecules are not fully detectable, i.e. (D) or (I), within the given laser power range at a given excitation wavelength. The baseline for comparison between molecules was class (D) as it represents the lowest fluence allowing the identification of the molecule. The results are

then discussed in terms of the optimal laser power setting for in-situ spectral acquisition on Europa and the impact on the detectability of the examined molecules.

Furthermore, the maximum and minimum laser fluence and total energy dose analysis is also used for the assessment of the limit of detection of the examined molecules in low concentrations at different excitations. This is described in detail in the following section.

5.1.2.5 Detection Limit 5: Sensitivity

Data obtained in the minimum and maximum laser fluence and total energy dose study at 532 nm and 785 nm, as described in the previous section, were used for the calculation of the theoretical lowest detectable concentration (i.e. limit of detection) of each target molecule at either excitation wavelength. The 633 nm excitation was excluded as the results of the study, detailed in Section 6.1 to 8.1.1, indicate there is little to no benefit of using the 633 nm excitation for the detection of biosignature over the 532 nm excitation, which generates higher Raman signal, or 785 nm excitation, which is less affected by fluorescence.

The theoretical limit of detection (LOD) for each molecule and each excitation is an important parameter for the selection of the excitation wavelength for an instrument aiming to detect biosignatures on Europa. However, very limited LOD data is available in literature sources. This is predominantly because the LOD depends on the configuration of the instrument, optical set up, laser power and other variable parameters, which make the data highly specific. The lowest detectable concentration is also affected by the solubility of the molecule as insoluble or partially-soluble molecules create localized higher concentration clusters. This would make experimental study of the LOD rather inaccurate and specific to the experimental set up. For this reason, a theoretical calculation of the theoretical lowest detectable concentration of each sample at each wavelength was performed instead. This calculation is described in detail below. It is important to note that any such calculation is bound to be a rough estimate, which is, nevertheless, sufficient for the purposes of this study as the concentration of biomolecules on Icy Worlds is measured in parts per billion, which allows for a relatively high margin of error. While experimental measurements were not within the scope of this research work, any future experimental study of the lowest detectable concentrations of biomolecules using Raman spectroscopy would be a very helpful and informative contribution.

The calculation is based on the minimum fluence required for full detection, which allows comparison between different instruments, excitations and optical set up. The minimum fluence required for full detection for each molecule and at each excitation is compared to the minimum fluence of a control molecule and its lowest detectable concentration at a particular excitation,

which was obtained experimentally. High signal water-soluble molecules were chosen for each excitation, adenine for 532 nm and nicotinamide at 785 nm, in order to allow a wider range of measurements at various concentrations without any data variation due to insolubility. A spectrum of each control molecule and at each excitation was obtained at 100 wt%, 5 wt%, 0.1 wt% and 0.01 wt% concentration.

The lowest detectable concentration of the control molecule was then used to extrapolate the lowest concentration of other target molecules using direct proportionality. The method was verified experimentally using a secondary control molecule, glycine, which is also fully water-soluble and which was tested at both excitations at 100 wt%, 50 wt%, 5 wt%, 0.1 wt% and 0.01 wt% concentration. The experimentally obtained lowest detectable concentration of glycine was then compared to the predicted value in order to verify that the theoretical calculation yields sufficiently accurate results.

The calculated LOD was expressed in wt% as well as parts per million (ppm) and parts per thousand (ppth) and discussed in terms of the detection limit requirements for a lander mission to Europa.

5.1.2.6 Overall Detectability and Instrument Design Considerations

This section summarises the results of the detection limits studies described in previous sections and highlights the observed trends. The results of each study are discussed alongside all other analysed detection limits and any overarching trends and tendencies are described and considered in terms of biosignature detection on Europa and other Icy Worlds. The impact of the results of the detection limits study on the development of a Raman instrument for life detection on Europa is presented and discussed together with implications on the instrument design requirements. The key design parameters considered in the discussion are:

1. Excitation Wavelength
2. Fluorescence Mitigation Technique
3. LOD
4. Spectral Resolution and Range
5. Miniaturization Techniques

Chapter 6 Detection Limits: Fluorescence and Laser Damage

Damage

The following sections present and discuss the results of investigations assessing the impact of the fluorescence noise and laser damage on the target molecules. Each effect is discussed separately in this chapter and discussed in context of all detection limits as well as the overall instrument design considerations in Chapter 9.

6.1 Fluorescence

Fluorescence trends of the selected target molecules have been observed across UV to NIR excitation wavelengths and the severity of the observed fluorescence interference at each excitation wavelength is summarized in Table 6-1. The molecules were classified into 5 groups based on the impact on the molecule's detectability as described in Section 5.1.2.1. This classification is based on room temperature Raman spectra. Further research revealed that cryogenic temperatures have a significant impact on the fluorescence noise in Raman spectra. This is discussed in detail in Chapter 7, which describes the effects of extreme low temperatures on Raman spectra in the context of each molecule category.

	Compound	Priority	325 nm	532 nm	633 nm	785 nm
Amino Acids	Alanine	B		1	1	1
	Glutamic Acid	B	1	3	3	1
	Glycine	A	1	3	2	1
	Histidine	A	1	3	2	1
	Tryptophan	C		3	3	2
	Tyrosine	C	2 [^]	3	3	1
	β-Alanine	D		1	1	1
Carboxylic Acids	Palmitic Acid	A	2	1	1	1
	Ectoine	A		4	3	2
Isoprenoids	Pristane	B		1	1	1
	Squalane	C		1	1	1
Carotenoids	β-Carotene	A	5 ^{^^}	2	2	1
	Astaxanthin	B	2 [^]	2	1	1
Steranes	5α-Cholestane	B	2	1	2	1
Pigments	C-Phycocyanin	C	1	5 ^{^^}	5 ^{^^}	4 ^{^^}
	Chlorophyll A	B		5 ^{^^}	4 ^{^^}	4 ^{^^}
Nucleic Acids	DNA	A	4 ^{^^}	5	5	5
	RNA	C	4 ^{^^}	5	5	3
Nucleobases	Adenine	B	2	3	3	2
	Guanine	B	5 ^{^^}	3	3	1
	Cytosine	B	2	3	3	1

	Thymine	B		3	3	2
	Uracil	B	1	3	3	1
Carbohydrates	Trehalose	A	2	2	1	2
Coenzymes	Nicotinamide	A	2	2	2	1
Porphyrins	Protoporphyrin IX	A	1 [^]	2 [^]	3 [^]	5 ^{^^}
	Hemin	A	1 [^]	1 [^]	3 [^]	3 [^]
Inorganics	Palagonite (HWMK101)*	NA		4	5	3
Natural Mixtures	Carrot Root (natural carotene)*	NA		2	3	2
	Spinach Leaf (natural chlorophyll)*	NA		2 [^]	5 ^{^^}	3

Table 6-1 Fluorescence interference across various excitation wavelengths and different target molecules for the exploration of Europa, 1 = no fluorescence and fully detectable, 2 = mild fluorescence but fully detectable at all laser power settings, 3 = moderate to severe fluorescence depending on the laser power, detectable at high laser power, 4 = severe fluorescence with some Raman bands still visible but not enough for full identification, 5 = very severe fluorescence, no Raman signal visible (*complementary sample, [^]undetectable due to laser damage despite relatively low fluorescence noise, ^{^^}critical level of fluorescence noise most likely associated with laser damage)

Molecules experiencing no fluorescence are classified as class 1. These molecules are fully detectable and also do not represent any challenges in mixtures solely due to fluorescence. Even at higher relative concentrations, class 1 molecules do not generate any fluorescence that could potentially overshadow other molecules with weaker signals. It is important to note that a high concentration of a class 1 molecule could still bury the signal of a weaker molecular signature in the spectra, however, the presence of fluorescence significantly lowers the relative concentration threshold at which other molecules are undetectable. An example of a class 1 Raman spectrum is shown in Figure 6-1, which compares the spectrum of glycine at 785 nm excitation (class 1) and at 532 nm excitation (class 3). The figure also shows glycine at 325 nm and 633 nm, highlighting the changes, such as the fluorescence noise level or different peak intensity, that can occur in the spectra at various excitations.

Class 2 molecules show mild levels of fluorescence noise, which does not impact the molecule's detectability at any laser power setting, i.e. all major and minor Raman peaks are still visible regardless of the laser power. This excludes measurements at low laser power at which some Raman peaks are not visible, however, this is due to the low laser power being insufficient to excite the signal rather than fluorescence interference. Figure 6-2 shows the spectra of ectoine, which is classified as a class 2 molecule at 785 nm excitation, at different laser power settings. While a mild fluorescence background is present in the spectra at all laser power settings, all ectoine Raman bands are clearly visible. While fluorescence does not affect the detectability of class 2 molecules, it may be problematic in mixtures as it could bury the signal of weaker

Chapter 6

molecules in the sample. This is important for in-situ measurements where mixtures of various molecules are expected.

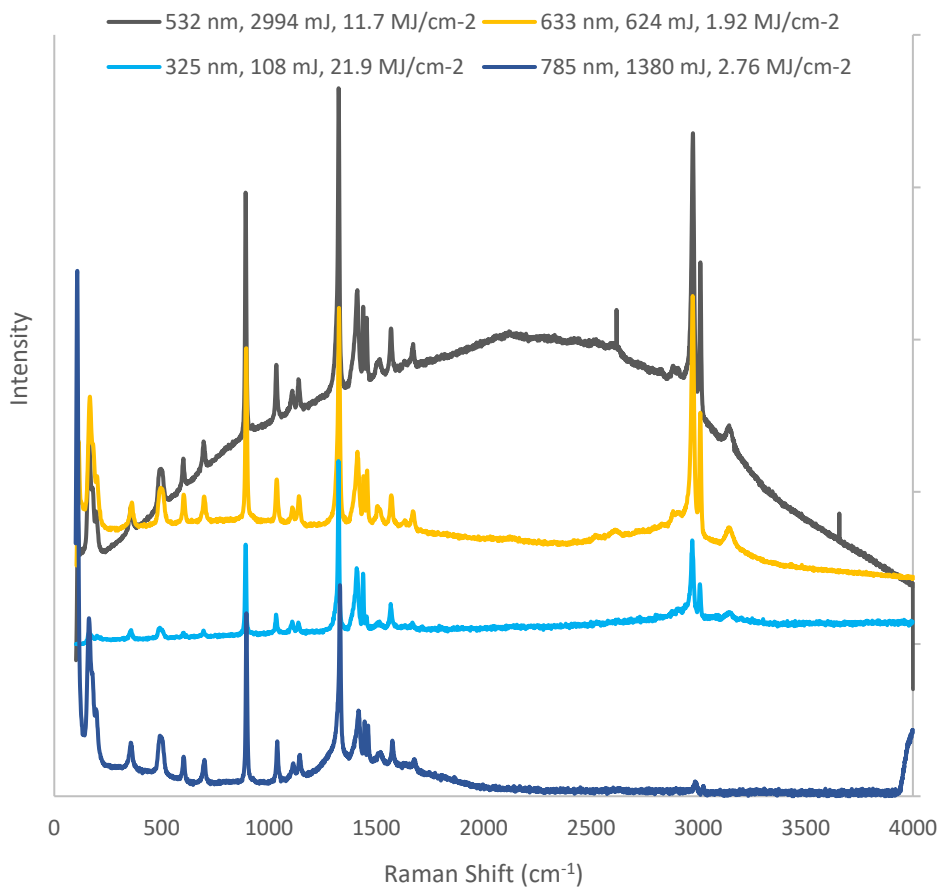


Figure 6-1 Comparison of glycine Raman spectra at 532 nm (class 3), 785 nm (class 1), 633 nm (class 2) and 325 nm (class 1)

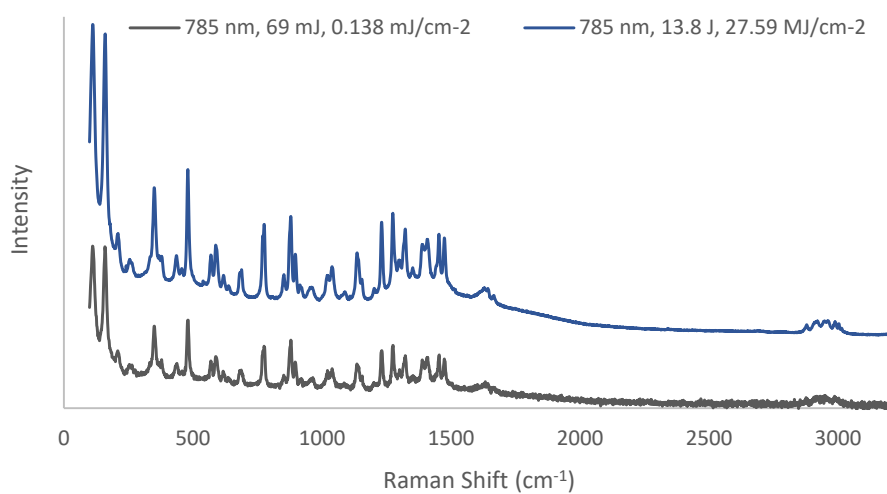


Figure 6-2 Raman spectra of ectoine collected at 785 nm excitation (class 2) and at various laser power

As shown in Figure 6-1 and Figure 6-3, class 3 molecules experience a relatively high level of fluorescence that may be critical at least at certain laser power settings. The fluorescence noise in the spectra of class 3 molecules may fully overshadow all minor Raman bands but major bands can still be visible at least at higher laser power. This is visualized in Figure 6-3, which shows the comparison of glycine at different laser power at 532 nm. While fully detectable at high laser fluence (11.7 MJ/cm^2), only a couple of faint major Raman bands of glycine are visible at lower laser fluence (0.117 MJ/cm^2), which does not allow full identification. While molecules in class 3 are detectable, the fluorescence noise in the spectra is critical and full identification may only be possible at higher laser power. In terms of in-situ exploration of Europa, class 3 molecules can also be a significant risk factor for the detectability of other molecules in mixtures. Since mixtures of various molecular species are likely to occur in the sampled European soil, it is very likely that the presence of a class 3 molecule and its high fluorescence background noise will prevent the detection of other molecules with weaker signals or at a lower concentration.

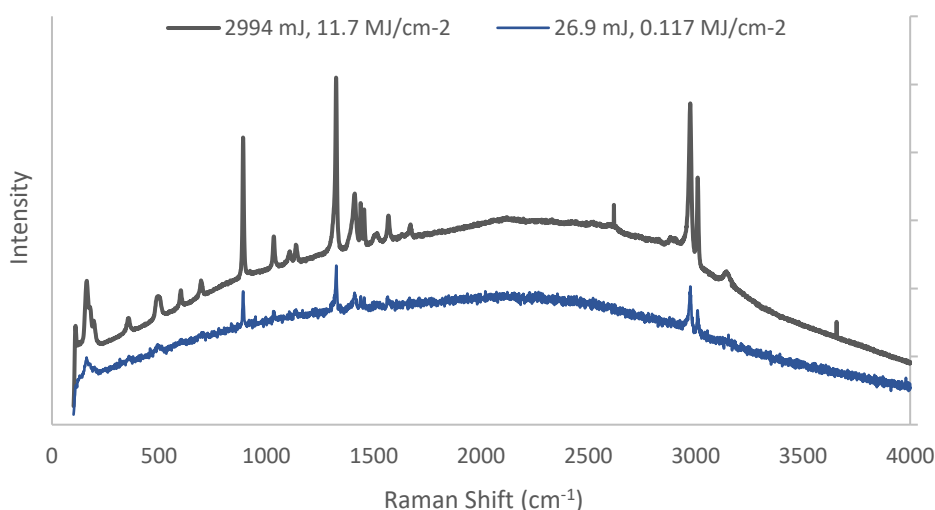


Figure 6-3 Comparison of glycine Raman spectra at 532 nm at two different laser power settings (class 3), most Raman bands are lost in the spectra at a lower laser fluence

As opposed to class 3 molecules, class 4 molecules are not identifiable. Although some major Raman bands are visible at higher laser power, this is not sufficient for unambiguous identification. Figure 6-4 shows ectoine, which is classified as class 4 at 532 nm excitation. The figure displays the comparison of the ectoine spectra at 532 nm (class 4) and 633 nm (class 3). The figure shows the barely visible major bands of ectoine at 532 nm in comparison with the 633 nm spectra where fluorescence is also prominent but the higher SNR of the Raman bands still allows identification.

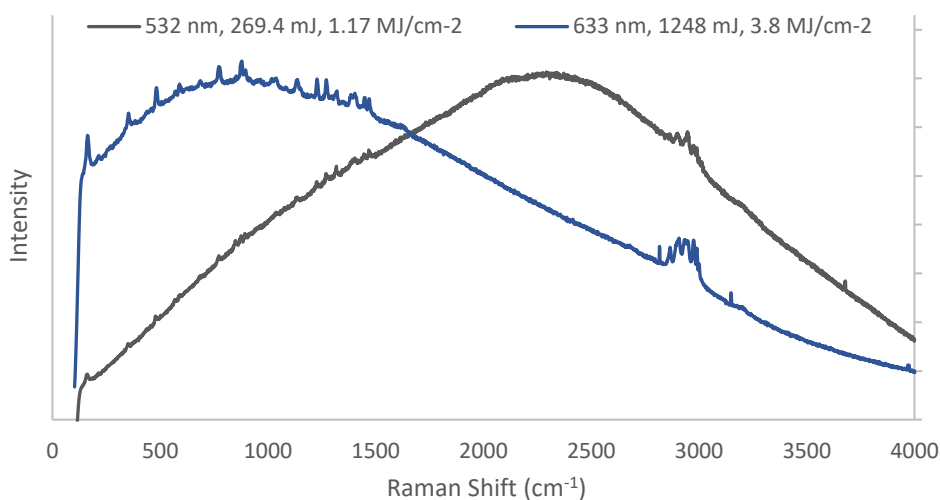


Figure 6-4 Raman spectra of ectoine at 532 nm excitation (class 4) compared to 633 nm excitation (class 3)

Molecules with a very high fluorescence background that overshadows all Raman bands at all laser power settings and that are not detectable at all are classified as class 5. Both class 4 and 5 can be a major limiting factor in the detectability of molecules in mixtures.

It is important to highlight that some molecules may experience high fluorescence at a certain excitation wavelength but not within the spectral range important for the molecule's identification. As such, this fluorescence does not have any impact on the detectability of the molecule. The most prominent example of this are porphyrins. Protoporphyrin IX experiences a severe fluorescence noise at 532 nm, however, only in the region above 2200 cm^{-1} , as shown in Figure 6-5. Since the spectroscopic signature of protoporphyrin lies between 200 – 1800 cm^{-1} , where the fluorescence noise ranges from none to mild, the interference has no impact on the identifiability of the molecule and protoporphyrin is thus classified as category 2 at 532 nm.

Further to this, while porphyrin derivatives such as hemin, protoporphyrin IX and chlorophyll and some other molecules, do not nominally show high fluorescence in their spectra - such that would impede their identification - they were undetectable nevertheless due to the severe laser damage which decreases their signal strength. As shown in Figure 6-5, only a mild fluorescence noise is present in the signature region of protoporphyrin at 532 nm, however, the Raman signal of the signature is very low and the molecule is not fully identifiable. This is the result of protoporphyrin's photosensitivity leading to signal reduction due to laser damage. This is denoted by a caret mark in Table 6-1 and the phenomenon is described further in Section 6.2. Likewise, some molecules experienced very high levels of fluorescence, which made them completely undetectable, however, the critical level of fluorescence was most likely associated with laser damage. This mostly includes laser damage susceptible molecules at the high energy 325 nm

excitation and pigment molecules at visible and NIR excitation. This is highlighted in Table 6-1 by a double caret sign and further discussion on the laser damage is provided in Section 6.2.

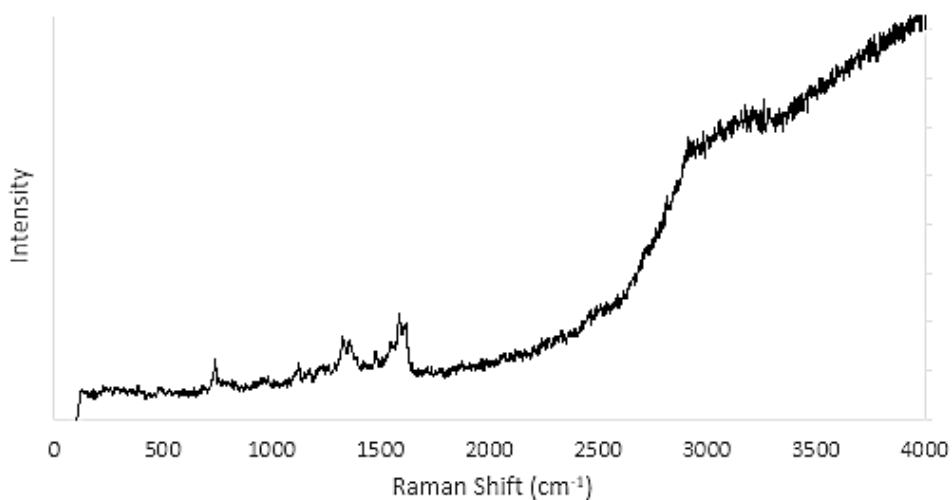


Figure 6-5 Full range Raman spectra of Protoporphyrin IX at 532 nm

The data shows that some classes of target molecules, such as pigments, nucleic acids and inorganics, exhibit a very strong fluorescence background at all tested excitation wavelengths. Similarly, some target molecules are fully detectable or experience only low fluorescence background at all measured excitation wavelengths. These molecules include trehalose, palmitic acid, 5 α cholestane and nicotinamide. Most amino acids and nucleobases could also be detectable to some degree at all measured excitation wavelengths given an appropriate laser power setting.

Overall, the data shown in Table 6-1 clearly demonstrate that 785 nm excitation outperforms both visible and UV excitation in terms of the impact of fluorescence on the spectra of target molecules. With the exception of nucleic acids, which are not detectable at any of the tested wavelengths, and porphyrins and their derivatives, which show lower fluorescence interference in the visible, 785 nm excitation offers spectra with much lower fluorescence interference for most molecules. It is important to state that this does not consider any minerals and inorganic compounds, for which 532 nm excitation is typically preferred and which could still excite fluorescence at 785 nm.

While a significant risk of interference would still exist, a 785 nm Raman system could be potentially used without employing a fluorescence mitigation mechanism as long as a high spatial resolution is available. This would be an extremely simple and inexpensive solution that could still achieve reasonable scientific results in case such an approach is necessary.

Depending on the relative concentrations and signal strength of the target molecules, a simple computational fluorescence mitigation method based on fluorescence baseline subtraction may

also still be effective in some cases. While this could also be an attractively simple solution, it would only be effective if only class 1 and 2 molecules are expected to be present in the sample and at relatively even concentrations or if high spatial resolution is possible to prevent general spectral interference. As this is unlikely on Europa, a more sophisticated fluorescence mitigation technique such as time gating or SSE would be advisable. Additionally, a signal enhancement mechanism to offset the low Raman signal at 785 nm would be necessary, which would counteract the simplicity of the 785 nm design even if no fluorescence reduction mechanism was used.

While measurements at 325 nm only comprise an incomplete set of target molecules and thus cannot be used to draw definitive conclusions, the data also show that many high importance molecules such as amino acids, nucleobases, trehalose and nicotinamide show the same or lower fluorescence noise at 325 nm compared to visible excitation. Most notably, Raman spectra of phycocyanin, which fluoresces very strongly at visible to NIR excitation, were successfully obtained at 325 nm without any fluorescence interference. This indicates that UV excitation may be more suitable than visible excitation for the detection of the targeted molecules and in some cases, it may be the only option. While this trend could not be confirmed in the DUV excitation wavelength region as this was not within the scope of the research project, even better results could be potentially obtained using DUV excitation. The fluorescence signal would be well separated from the Raman signal at excitation wavelengths below 250 nm [114], which could reduce the impact of fluorescence significantly. Notably, this effect is used to mitigate fluorescence by SHERLOC, one of the Raman instruments on launched the most recent Mars mission [118]. However, many molecules that experience high fluorescence levels at visible, NIR or UV excitation are also susceptible to laser damage, which makes measurements at the high energy DUV excitation challenging. As described in Section 6.2, laser damage was much more prominent at the UV excitation compared to visible and NIR, which could be even more critical at DUV excitation. Particularly, porphyrins and porphyrin derivatives fluoresce the most in NIR and higher visible and the severity of the fluorescence interference decreases significantly towards lower excitation wavelengths in the visible and UV region. However, porphyrins are extremely photo sensitive and not detectable at either of the tested excitations even despite the low fluorescence. This can be assigned to the signal decrease due to laser damage, which is described in more detail in Section 6.2. Note that this only refers to room temperature measurements as Raman spectra of porphyrins at low temperatures show much higher signals allowing full identification. This is described in more detail in Chapter 7.

As it stands, a UV system would be unlikely to mitigate the fluorescence enough on its own and DUV excitation would be necessary to effectively reduce the fluorescence interference. Such a

system could be a relatively simple solution without the need for a fluorescence mitigation mechanism and would also provide higher sensitivity than longer excitation wavelengths. However, as discussed in Section 8.1.2 and Chapter 9, this may still not be enough for the detection of biosignatures on Europa. Additionally, even with no fluorescence mitigation and signal enhancement mechanisms, DUV Raman systems are still much more complex than Raman spectrometers using the more traditional visible or NIR excitation. This is associated with the additional complexity of incorporating the high energy DUV lasers and technology readiness and availability issues of these laser systems and DUV compatible optics.

Based on the fluorescence data, neither 532 nm or 633 nm excitation is particularly suitable for the detection of biosignatures on Europa without an efficient fluorescence mitigation technique. This result was expected as most biosignatures are organic molecules, which are known to generate a high fluorescence background, especially at visible excitation wavelengths. Nevertheless, the detectability of some important biosignatures such as amino acids, nucleobases or trehalose across all measured excitation wavelengths also indicates that a Raman instrument with a visible excitation wavelength, although not ideally suited for the purposes, could potentially detect a limited number of biosignatures. This means that a visible excitation Raman instrument that is tailored to a different purpose than the detection of life, such as the detection of minerals, could also be used for the detection of some biosignatures even despite its limited effectiveness compared to instruments with a more suitable excitation wavelength. Notably, a green excitation laser was selected for the RLS instrument, which is a Raman spectrometer for the upcoming ExoMars mission [51].

Solely based on the fluorescence interference, the 633 nm excitation slightly outperforms the green 532 nm excitation, however, there are benefits in using 532 nm instead of the less widely used 633 nm. Firstly, 532 nm excitation provides a higher Raman signal without exceeding the carbon to carbon bond dissociation energy [159] and inducing excessive laser damage similar to UV excitation. It is also one of the most commonly used excitation wavelengths with high TRL lasers and optics readily available. It has been particularly popular for mineralogy and inorganics and an effective fluorescence mitigation technique such as time gating or SSE could allow the detection of most of the targeted molecules. This could make 532 nm just as suitable as 785 nm excitation at a higher nominal Raman signal.

It is important to note that only a limited set of target molecules could be explored in this research and, while representative molecules were selected where possible, this may not necessarily reflect the content of the sample material collected on Europa. This review also does not include any potential minerals present in the soil, which may cause interference and which

are also an important detection target for a future mission to Europa. It is important to state that Raman spectra and the fluorescence interference of minerals at different excitations have been successfully mapped in the ruff database, which is publicly available and contains 3527 of the 4895 mineral species known on Earth [328], [329]. Since no such database exists for biomolecules and biosignatures for extraterrestrial exploration, this research focuses mainly on these molecules. While it was impossible to cover a higher number of biomolecules as a part of this research, a review of the fluorescence impact in the spectra of other molecules important for astrobiology across visible, NIR and DUV excitation would be a highly valuable resource. For reference, the ruff database has successfully recognized that 84% of the minerals contained in the database can be identified by both 532 nm and 785 nm excitation with only 8% of the minerals completely unidentifiable by either [329]. A similarly broad review of biosignatures and their Raman spectra would be a very useful asset for the future of Raman spectroscopy in planetary sciences.

6.2 Laser Damage

Laser induced sample degradation can severely impact the identifiability of molecules in Raman spectra. The observed laser damage thresholds at each excitation wavelength are shown in Table 6-2 together with the type of damage observed, i.e. change in the spectra or physical change of the sample. The occurrence of laser damage signs in the spectra or physical appearance of the sample did not automatically make the molecule undetectable and the laser damage threshold for detectability is thus shown in Table 6-3. In this case, the threshold refers to the detectability limit solely due to laser damage and as such, the limit was not possible to determine for molecules that were not detectable at all due to other reasons, i.e. fluorescence or weak signal. This is highlighted in Table 6-3 where appropriate.

	Compound	Priority	Laser Damage Threshold: Damage Type (S = spectral, V = visible) Laser Fluence [kJ/cm ² or MJ/cm ²] Total Energy Dose [mJ]			
			325 nm	532 nm	633 nm	785 nm
Amino Acids	Alanine	B		none	none	none
	Glutamic Acid	B	S 10.9 MJ/cm ² 54 mJ	none	none	none
	Glycine	A	none	none	none	none
	Histidine	A	S 1.1 MJ/cm ² 5.4 mJ	none	none	none
	Tryptophan	C		none	none	none

	Tyrosine	C	S 1.1 MJ/cm ² 5.4 mJ	none	none	none
	β-Alanine	D		none	none	none
Carboxylic Acids	Palmitic Acid	A	none	none	none	none
	Ectoine	A		none	none	none
Isoprenoids	Pristane	B		none	none	none
	Squalane	C		none	none	none
Carotenoids	β-Carotene	A	S 2.2 MJ/cm ² 10.8 mJ	none	none	none
	Astaxanthin	B	S 1.1 MJ/cm ² 5.4 mJ	none	none	none
Steranes	5α-Cholestane	B	S 2.2 MJ/cm ² 10.8 mJ	none	none	none
Pigments	C-Phycocyanin	C	S 0.22 MJ/cm ² 1.1 mJ	none	none	none
	Chlorophyll A	B		S 1.2 MJ/cm ² 269.4 mJ	none	none
Nucleic Acids	DNA	A	V 0.22 MJ/cm ² 1.1 mJ	none	none	none
	RNA	C	SV 0.22 MJ/cm ² 1.1 mJ	none	none	none
Nucleobases	Adenine	B	S 10.9 MJ/cm ² 54 mJ	none	none	none
	Guanine	B	SV 2.2 MJ/cm ² 10.8 mJ	none	none	none
	Cytosine	B	V 1.1 MJ/cm ² 5.4 mJ	none	none	none
	Thymine	B		none	none	none
	Uracil	B	SV 10.9 MJ/cm ² 54 mJ	none	none	none
Carbohydrates	Trehalose	A	none	none	none	none
Coenzymes	Nicotinamide	A	SV 1.1 MJ/cm ² 5.4 mJ	none	none	none
Porphyryns	Protoporphyrin IX	A	SV 1.1 MJ/cm ² 5.4 mJ	S 0.12 MJ/cm ² 26.94 mJ	S 1.92 kJ/cm ² 0.62 mJ	none
	Hemin	A	SV 1.1 MJ/cm ² 5.4 mJ	S 2.35 MJ/cm ² 538.8 mJ	S 0.19 MJ/cm ² 124.8 mJ	S 27.6 kJ/cm ² 13.8 mJ
Inorganics	Palagonite (HWMK101)	NA		none	none	none

Natural Mixtures	Carrot Root (natural carotene)	NA		none	none	none
	Spinach Leaf (natural chlorophyll)	NA		none	none	none

Table 6-2 Laser damage thresholds of selected target molecules at UV, visible and NIR excitation, the lowest laser damage thresholds at each wavelength are highlighted in red

	Compound	Priority	Laser Damage Detectability Threshold: Damage Type (S = spectral, V = visible) Laser Fluence [MJ/cm ²] Total Energy Dose [mJ]			
			325 nm	532 nm	633 nm	785 nm
Amino Acids	Alanine	B		none	none	none
	Glutamic Acid	B	S 10.9 MJ/cm ² 54 mJ	none	none	none
	Glycine	A	none	none	none	none
	Histidine	A	SV 21.9 MJ/cm ² 108 mJ	none	none	none
	Tryptophan	C		none	none	none
	Tyrosine	C	U	none	none	none
	β-Alanine	D		none	none	none
Carboxylic Acids	Palmitic Acid	A	none	none	none	none
	Ectoine	A		none	none	none
Isoprenoids	Pristane	B		none	none	none
	Squalane	C		none	none	none
Carotenoids	β-Carotene	A	U	none	none	none
	Astaxanthin	B	U	none	none	none
Steranes	5α-Cholestane	B	S 10.9 MJ/cm ² 54 mJ	none	none	none
	Pigments	C-Phycocyanin	C	none	U	U
Chlorophyll A		B		U	none	none
Nucleic Acids	DNA	A	U	U	U	U
	RNA	C	U	U	U	none
Nucleobases	Adenine	B	none	none	none	none
	Guanine	B	U	none	none	none
	Cytosine	B	SV 10.9 MJ/cm ² 54 mJ	none	none	none
	Thymine	B		none	none	none
	Uracil	B	none	none	none	none
Carbohydrates	Trehalose	A	none	none	none	none
Coenzymes	Nicotinamide	A	SV 10.9 MJ/cm ² 54 mJ	none	none	none
	Porphyrins	Protoporphyrin IX	A	U	S 1.2 MJ/cm ²	U

				269.4 mJ		
	Hemin	A	U	S 2.35 MJ/cm ² 538.8 mJ	U	U
Inorganics	Palagonite (HWMK101)	NA		none	U	U
Natural Mixtures	Carrot Root (natural carotene)	NA		none	none	none
	Spinach Leaf (natural chlorophyll)	NA		none	U	none

Table 6-3 Laser damage detectability thresholds of selected target molecules at UV, visible and NIR excitation, U = molecules for which laser damage detectability thresholds could not be identified as they were undetectable regardless of the laser damage

Spectral damage observed in the tested molecules included a decrease in signal strength, inconsistent spectra, the presence of carbon signature bands, photoproduct bands and higher background noise. Typically, a signal decrease was followed by an appearance of carbon bands in the spectra at higher laser fluence. As the content of carbon in the sample increases due to continued laser damage, the SNR of the molecule's Raman signature decreases until the carbon signature replaces the molecule's original spectrum completely. This trend is shown in Figure 6-6 and Figure 6-7 showing histidine at different laser fluence levels at 325 nm excitation. Figure 6-6 shows histidine before laser damage (at 1.08 mJ total energy dose) and at 10.8 mJ total energy dose, where carbon signature appears around 1550-1600 cm⁻¹ in the spectra together with higher background noise as the sample becomes damaged. Figure 6-7 then shows that at even higher laser fluence, the Raman peaks of histidine are suppressed and eventually carbon becomes prominent and replaces the spectra completely. Interestingly, histidine remains fully detectable across a relatively wide range of laser fluence even after laser damage appears in the spectra at 1093 kJ/cm⁻² (5.4 mJ).

Visible damage observed during testing included exclusively discolouration of the sample at the location of laser incidence. While the damage was apparent in most samples, in dark samples such as carotenoids or porphyrins the discolouration proved difficult to detect underneath the microscope and an earlier occurrence of laser damage than recorded in Table 6-2 and Table 6-3 is possible. The physical damage of cytosine across the range of 1093 kJ/cm⁻² (5.4 mJ) to 21.9 MJ/cm⁻² (108 mJ) is shown in Figure 6-8. The corresponding spectra are shown in Figure 6-9. The laser damage ranges from a barely visible darker spot and no visible spectral damage at 1093 kJ/cm⁻² (5.4 mJ) to a distinct burn and overwhelming carbon spectral signature at 10.9 MJ/cm⁻² (54 mJ).

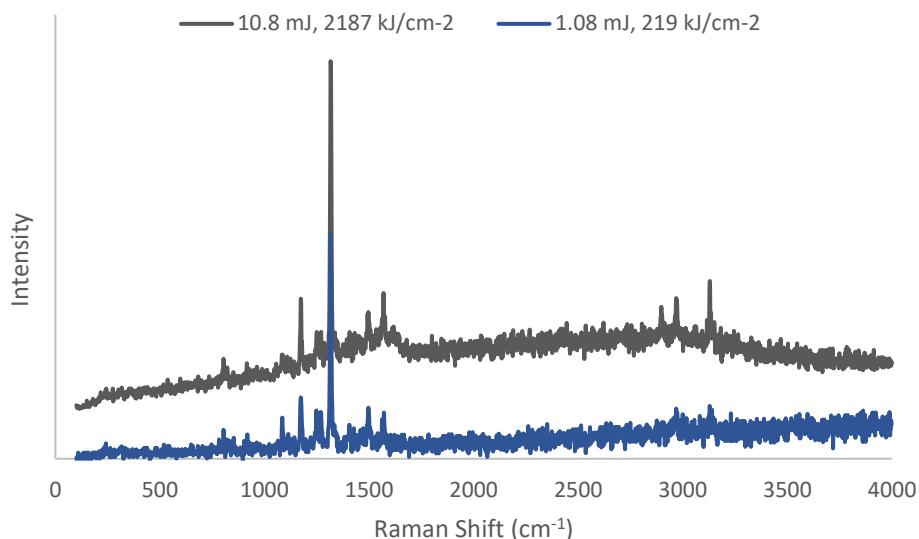


Figure 6-6 Histidine laser damage at UV excitation (325 nm) compared to 325 nm spectra below the laser damage threshold

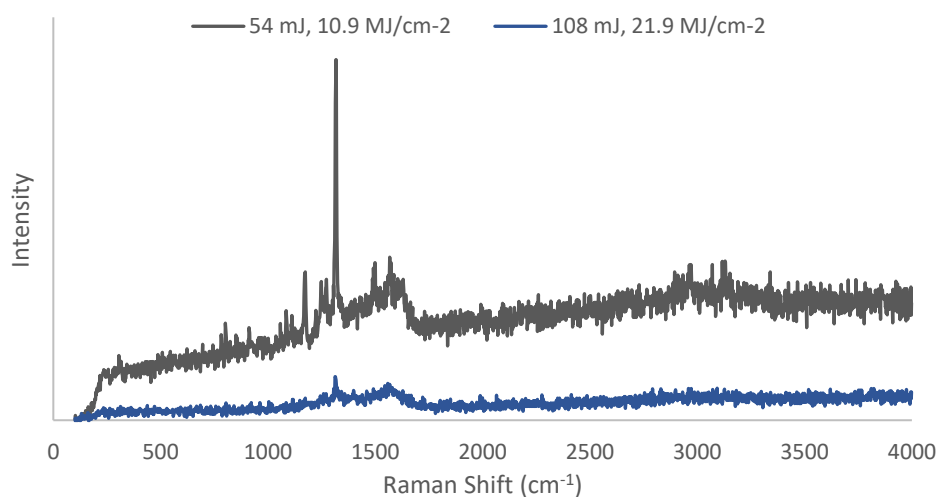


Figure 6-7 Histidine laser damage progression at UV excitation (325 nm) at a high laser fluence

In most cases, the first signs of laser damage occurred in the spectra and visible damage followed at a higher laser fluence. However, in some cases, such as protoporphyrin, uracil, guanine, and RNA at 325 nm, both types of laser damage signs occurred at the same time. In a few cases, namely DNA and cytosine at 325 nm, visible damage occurred before any signs of damage appeared in the spectra.

The data clearly shows that the high energy UV laser at 325 nm is much more destructive than excitation at visible or NIR wavelength. Most molecules examined at 325 nm excitation experienced some degree of laser damage, however, the testing revealed that successful detection is possible and that the damage thresholds are relatively high for many of the tested

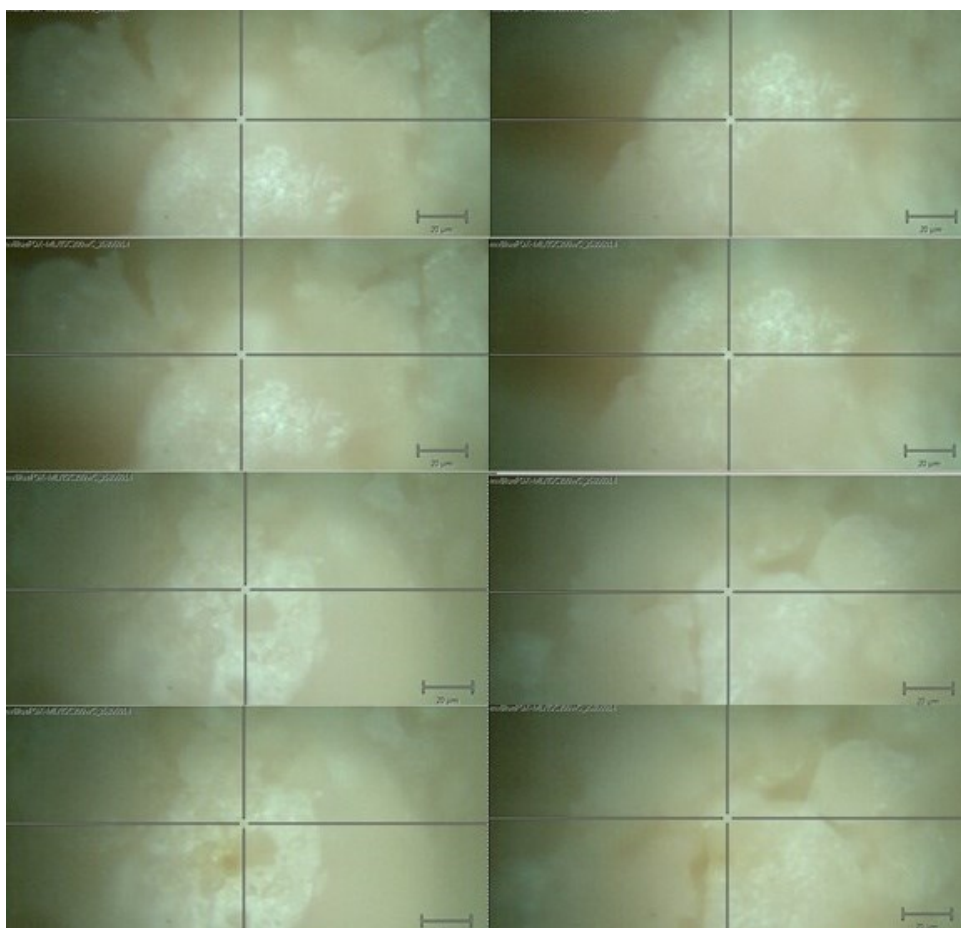


Figure 6-8 Physical signs of laser damage of cytosine at 325 nm, top left - 1093 kJ/cm^2 (5.4 mJ), top right - 2187 kJ/cm^2 (10.8 mJ), bottom left - 10.9 MJ/cm^2 (54 mJ), bottom right - 21.9 MJ/cm^2 (108 mJ)

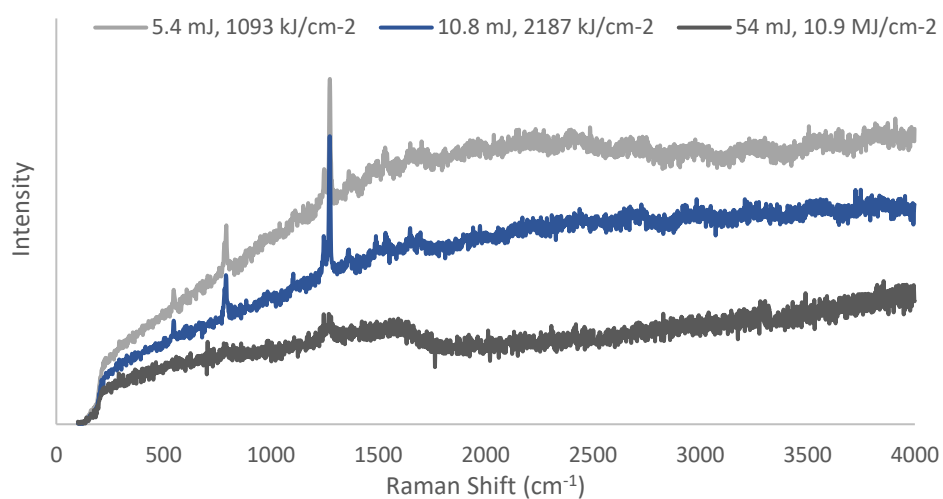


Figure 6-9 Cytosine laser damage at UV excitation (325 nm)

molecules. Notably, amino acids, palmitic acid (representing carboxylic acids) and nucleobases, which are traditionally important biosignatures for the search of extraterrestrial life, can be detected at UV excitation with no or mild fluorescence background even despite the laser damage at higher laser fluence levels. These molecules are traditionally perceived as photosensitive organic compounds and short excitation wavelengths are deemed unsuitable for their detection due to laser damage concerns. However, the identified laser damage thresholds are relatively high and full detection is possible across a relatively wide range of laser fluence in most cases. In many cases, full identification is possible even despite the laser damage. This is shown in Figure 6-6 and Figure 6-7, which show the spectra of histidine at 325 nm at different laser power settings. As seen in Figure 6-6, histidine displays no spectral laser damage at 219 kJ/cm^{-2} (1.08 mJ) and remains fully identifiable even with the carbon signature appearing in the spectra and signalling laser damage at 2187 kJ/cm^{-2} (10.8 mJ). Figure 6-7 then shows that histidine remains fully detectable at even higher laser fluence of 10.9 MJ/cm^{-2} (54 mJ) with more prominent spectral signs of laser damage and only becomes unidentifiable at 21.9 MJ/cm^{-2} (108 mJ). A similar trend is observed in the spectra of cytosine shown in Figure 6-9. Moreover, within the tested laser power range, no laser damage was detected in the spectra of palmitic acid, glycine, cholestane and trehalose.

The lowest detected laser damage threshold at 325 nm was at 219 kJ/cm^{-2} (1.08 mJ) in the spectra of phycocyanin, DNA and RNA. However, most of the tested molecules exhibited laser damage at 1093 kJ/cm^{-2} (5.4 mJ) or above. The lowest detectability threshold was 10.9 MJ/cm^{-2} (54 mJ). It is important to note that these are relatively high thresholds and optimization of the laser fluence below these limits can yield high quality Raman spectra. The most photosensitive molecules at 325 nm were nucleic acids and phycocyanin.

Some samples, such as carotenoids or nucleic acids, were not successfully detected at 325 nm before laser damage occurred, however, this was mainly due to the fluorescence background impeding the identification of Raman peaks. As such, the laser damage thresholds could not be accurately determined. It is possible that excitation at a shorter wavelength would decrease the fluorescence effect and allow a more complete assessment of the laser damage thresholds. Nevertheless, it is also important to note that a lower excitation wavelength could also cause more severe laser damage at much lower laser fluence levels.

Porphyryns, which were also not identifiable at 325 nm, reached laser damage before any Raman signal was obtained. Porphyryns are known to be extremely photosensitive and this result was expected. However, this might have been also caused by the large laser fluence increments during

testing. As such, porphyrins could be detectable at laser fluence levels between the laser fluence levels of the measurements during the experiment.

As shown in Table 6-2 and Table 6-3, only porphyrin derivative molecules are susceptible to laser damage in the measured laser power range at visible and NIR excitation. Namely, signs of laser damage were observed in the spectra of chlorophyll at 532 nm, protoporphyrin IX at 532 nm and 633 nm and hemin at 532 nm, 633 nm as well as 785 nm. Only hemin showed signs of photodamage at NIR. This is not a surprising result as porphyrins and their derivatives are known to be extremely photosensitive. Out of these molecules, only hemin and protoporphyrin IX are identifiable and only at 532 nm excitation. The Raman spectra of hemin and protoporphyrin IX at 532 nm excitation across various laser power settings is shown in Figure 6-10. Please note that the following results have been published in an article for the Analytical Methods journal [311].

As shown in the figure, only a relatively small change in the laser power density can severely affect the Raman signature of porphyrins in terms of the signal strength, definition and occurrence of sample degradation signs. A spectral signature of hemin can be distinguished in the Raman spectra obtained at 9.77 kW/cm^2 , however, the signal gradually decreases until it is barely resolvable at 1.95 kW/cm^2 and no signal is detected at any lower power setting. Likewise, the hemin signature intensity also reduces at laser power density above the 9.77 kW/cm^2 level and becomes increasingly overshadowed by the Raman signature of photodegradation products. Even at a relatively small laser power increase of 2.24 mW (i.e. 9.73 kW/cm^2 power density), the hemin signal disappears completely within the carbon signature induced by sample thermal degradation.

As shown in Figure 6-10, protoporphyrin seems to be even more photosensitive as a significant signal decrease caused by laser damage is observable even at a slightly higher laser power density than the 195 W/cm^2 setting, at which spectra with optimal signal strength could be obtained. The signal then becomes unresolvable at 1.95 kW/cm^2 even despite the absence of a significant carbon photodamage signature in the spectra.

Even at the optimal power setting, the Raman spectra of both hemin and protoporphyrin only barely allow the identification of the molecules. Only a very weak and low-definition Raman signature of hemin can be obtained and the spectra of protoporphyrin only show its most dominant Raman bands.

While carbon signature signalling photodamage appeared in the spectra of chlorophyll at 532 nm, chlorophyll is not identifiable at this excitation and laser damage at a lower energy level could have occurred without any obvious signs in the spectra. This may be partly due to the severe fluorescence background, however, the absence of photodamage in the naturally occurring

chlorophyll in spinach indicates that a reduction in the pure chlorophyll signal strength may have occurred due to laser damage. This would decrease the SNR and make the molecule undetectable even despite relatively low nominal fluorescence background noise. This also explains the low signal strength observed in the spectra of porphyrins.

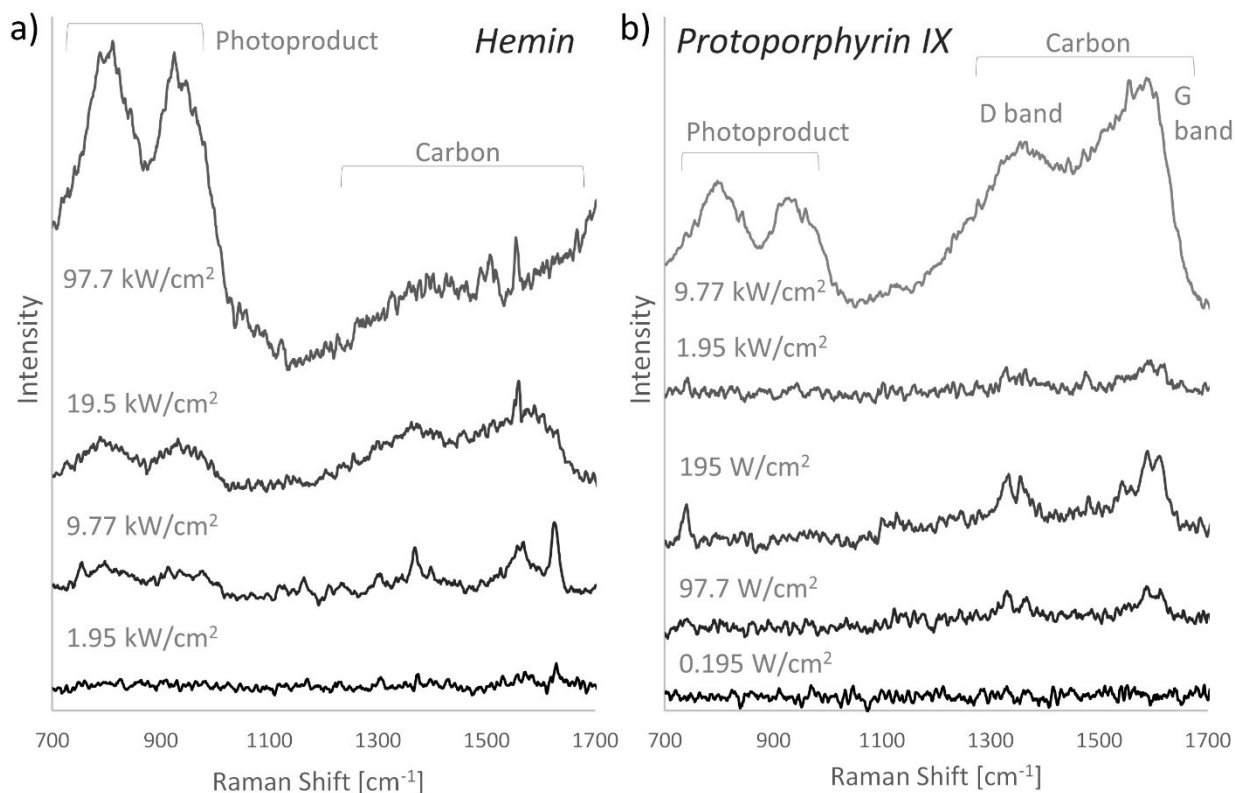


Figure 6-10 Raman spectra of hemin (a) and protoporphyrin IX (b) at 532 nm excitation across different laser power settings at room temperature (22 °C) showing low signal strength even at the optimal power density of 9.77 kW/cm² for hemin and 195 W/cm² for protoporphyrin [311]

There are two separate types of photodegradation that could contribute to the sample damage observed in the spectra, photochemical and photothermal degradation. Photochemical degradation in organic samples is often associated with photooxidation. This would be mitigated in a nitrogen purged environment such as applied during testing at cryogenic temperatures and further discussion on this is provided in Chapter 7. Photothermal degradation, which is most likely the degradation observed in the porphyrin spectra, is the result of localized heat build-up. This can be mitigated or potentially prevented entirely by applying a heat sink. Previous research shows reduced photothermal degradation as a result of mixing the pure porphyrin sample with a KBr at 1% concentration and pressing the sample into a pellet, which acts as a heat sink [330]. The main constituent of spinach is chlorophyll, which is a porphyrin derivative molecule. However, the naturally occurring chlorophyll in spinach is embedded in a tissue of organic matter at a much

lower concentration than the pure chlorophyll sample. Based on the results, this tissue matrix seems to act as a heat sink, which thus limits the photothermal degradation of a naturally occurring porphyrin derivative. As shown in Figure 6-11, as opposed to the pure sample, some major bands of chlorophyll are visible in the spectra of spinach.

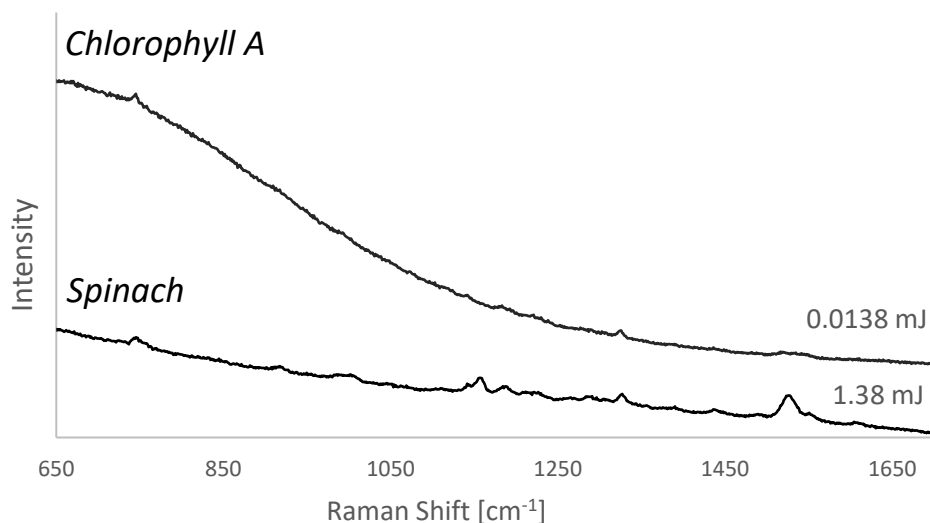


Figure 6-11 Comparison of the Raman spectra of pure chlorophyll and spinach obtained at 785 nm

This may be an important factor in the detection of biosignatures on Europa as all target molecules on Europa would be naturally mixed in a low concentration water/ice solution. While the low concentration may be an issue in terms of the instrument requirements, it may be a very beneficial factor in reducing the impact of laser damage. While this needs to be confirmed experimentally, the results indicate that the higher energy lasers and higher laser power may be much less damaging to in-situ European samples than to pure terrestrial samples. This would make the fluorescence-free high energy DUV lasers, which may also allow lower LOD than traditional lower energy lasers, a potentially attractive choice for the exploration of Europa. Furthermore, the extreme low temperature on Europa could provide further heat dissipation in the sample, which could further mitigate laser damage and allow the detection of photosensitive samples undetectable at terrestrial conditions. The effect of extreme low temperatures on sample laser damage is explored as a part of the low temperature detection limit testing and the results are described in detail in Chapter 7.

Besides porphyrin derivative molecules, no other molecular species displayed signs of laser damage at visible and NIR excitation. However, it is important to state that laser damage could have not been immediately obvious in the spectra of molecules that were undetectable at visible and NIR excitation due to high fluorescence noise. These molecules include nucleic acids and phycocyanin, which are typically considered to be very photosensitive, and while no damage was observed, it may have been present within the high fluorescent background noise impeding their

identification. Furthermore, laser damage can cause fluorescence to appear in the spectra or increase its relative intensity to the Raman signal, which could have also contributed to the critical levels of fluorescence impeding the identification of these molecules. However, it is also important to state that despite a high fluorescence noise and alleged photosensitivity, RNA was identifiable at 785 nm excitation. The Raman spectra of RNA obtained at 785 nm at various laser power is shown in Figure 6-12. The spectra do not show any indication of laser damage.

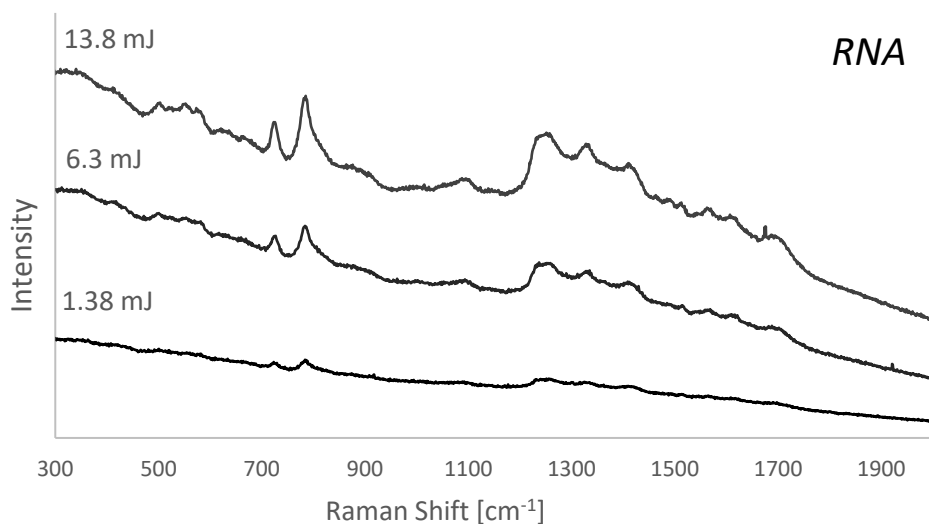


Figure 6-12 Raman spectra of RNA at 785 nm and various total energy dose

Overall, the most sensitive molecule at 532 nm excitation was protoporphyrin IX with the lowest laser damage threshold of 0.12 MJ/cm^2 (26.94 mJ). Protoporphyrin IX was also the most sensitive molecule at 633 nm with the lowest laser damage threshold of 1.92 kJ/cm^2 (0.62 mJ).

Interestingly, no laser damage was recorded in the spectra of protoporphyrin IX at 785 nm excitation and the only damaged molecule at this excitation was hemin with a laser damage threshold of 27.6 kJ/cm^2 (13.8 mJ). These are much lower thresholds than most laser damage thresholds observed even at the high energy excitation of 325 nm, which highlights how sensitive porphyrin molecules are compared to the other target molecules. Interestingly, the porphyrin laser damage thresholds at 325 nm were higher than at visible and NIR excitation even despite the higher energy of the laser. Laser damage detectability thresholds at visible and NIR excitation could only be determined for hemin and protoporphyrin IX at 532 nm as other molecules experiencing photodamage at these excitation wavelengths were not detectable at all due to high fluorescence noise. Among the two porphyrins, the laser damage threshold for detectability was lower for protoporphyrin at 1.2 MJ/cm^2 (269.4 mJ), which is one order of magnitude higher than its laser damage threshold.

The maximum fluence of the laser or maximum total energy dose delivered to the sample by the laser radiation in order to avoid sample degradation is dependent on the specific laser source, its

power, instrument set up and exposure time [160]. However, a 3 mJ total energy dose or fluence of 59 J/cm² have been suggested as a safe limit with good results as demonstrated by previously proposed UV Raman systems for the detection of organic material [98]. Studies have also shown no detectable sample degradation of organic material at DUV excitation up to 400 J/cm², only reaching detectable spectral degradation of nucleotides and amino acids at 4000 J/cm² [98], [160]. Some reports have shown no degradation of organic samples at 1000 J/cm² [85], [98], [104]. This is also closely connected with the choice of optics for the instrument as the spot size of the laser can reduce or increase the sample fluence.

Compared to the experimental results, the safe limit of 3 mJ total energy dose for UV Raman systems proposed in the literature seems fairly well aligned with the experimental results at 325 nm. In most cases, higher thresholds were identified, but the 3 mJ total energy dose would be a safe level for most examined molecules. Having said that, phycocyanin, and nucleic acids showed much lower thresholds than the suggested 3 mJ total energy dose.

As opposed to the total energy dose threshold, the laser fluence threshold does not account for the exposure time and it is more indicative of the optics set up. As such it can differ across different Raman systems. This is also evident from the wide range of laser degradation thresholds proposed to date. Compared to the suggested values, the experimentally obtained laser fluence thresholds are orders of magnitude higher. This shows that the total energy dose may be a much more reliable metric for the assessment of sample degradation thresholds.

Chapter 7 Detection Limits: Effects of Extreme Low Temperatures

The effects of the extreme low temperatures analogous to Europa on the Raman spectra of target molecules are very specific for each molecule. As such the thermally induced changes in the spectra are discussed in the context of the molecule class in the following sections. The overall impact of the observed effects on the detectability of target molecules and the instrument design considerations is discussed in Chapter 9 together with the impact of other detection limits examined in this study. The instrument design requirements are then discussed in more detail Chapter 10.

7.1 Amino Acids

The amino acids class of target molecules offers an opportunity to compare the thermally induced changes within the spectra at cryogenic temperatures between molecules with varying molecular structure and complexity that are nevertheless within the same molecular species and chemically similar. Unfortunately, strong fluorescence in the spectra collected at 532 nm excitation prevents any meaningful assessment of the thermally induced changes except for an analysis of the fluorescence noise tendencies at cryogenic temperatures. However, the spectra collected at 785 nm provide a much clearer picture. Particularly, a comparison between L-Alanine, Glycine, L-Histidine and L-Tryptophan at 785 nm is especially insightful due to the different properties of the Raman spectra and molecular structures of these molecules. Specifically, L-Tryptophan is mildly fluorescent at 785 nm excitation, which allows investigation of the impact of the extreme low temperature on the fluorescence noise without the noise overshadowing the spectra entirely as is typically the case at 532 nm. Glycine is the simplest amino acid compared to other amino acids and has no chirality. Alanine is the second simplest, after Glycine, but also includes an additional methyl side chain, which provides more information on the spectral changes at low temperatures in the context of the molecular structure. Both L-Tryptophan and L-Histidine include an aromatic ring, however, L-Histidine does not experience any fluorescence at 785 nm. This provides more information on the behaviour of aromatic structures at cryogenic temperatures without fluorescence noise affecting the data. The Raman spectra of L-Histidine is also relatively complex compared to other amino acids and the large number of Raman bands can provide more insight into the thermally induced spectral changes in the context of spectral interference. The study of the thermal changes observed in the spectra of these 4 amino acids is described in detail below. These results have also been published in the *Astrobiology* journal prior to the completion of this

thesis [310]. Please note that re-use of the text is permitted by the journal self-archiving policy. Aspects of this work were also presented at the Fall 2021 AGU Conference [331].

7.1.1 Glycine

The Raman spectra of the simplest amino acid, Glycine, obtained at various temperature points ranging from room temperature (22 °C) to -196 °C at 785 nm excitation are shown in Figure 7-1. As displayed in this figure, Raman bands of Glycine shift to higher frequencies with decreasing temperature. Table 7-1 shows the numerical comparison of the Raman bands at room temperature, -100 °C and -196 °C.

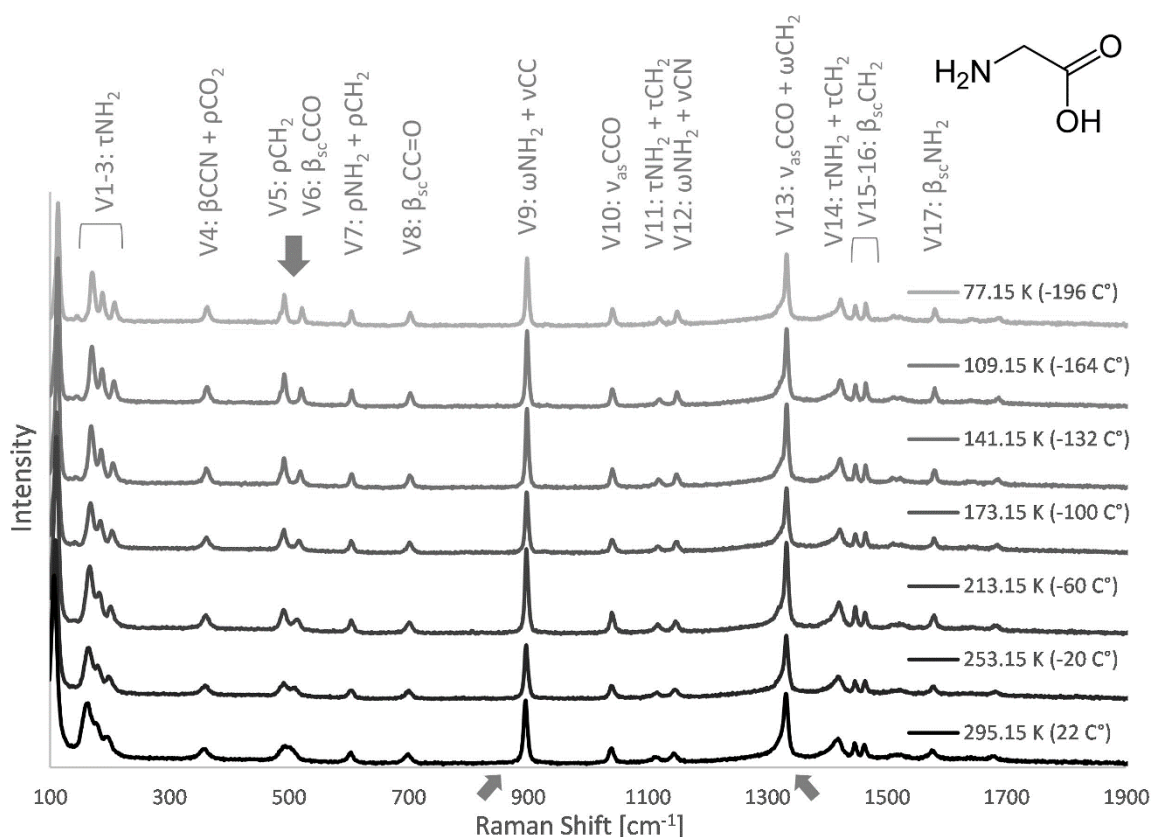


Figure 7-1 Raman spectra of Glycine at various temperatures in the range of 22 °C to -196 °C, where v = stretching, ω = wagging, ρ = rocking, β = bending, τ = torsion, sc = scissoring, as = asymmetric. Assignments are based on an optimized Density Functional Theory (DFT) vibrational frequency calculation using Split Valence Polarization (SVP) and polarizability calculations for Raman vibrational frequencies and Raman activity together with a review of previously published assignments [312]–[314]. A vertical arrow highlights the split of the 497 cm^{-1} band, diagonal arrows highlight bands detailed in Figure 7-2 [310]

As a result of these shifts, some Raman bands nominally not resolvable at room temperature are detectable at lower temperatures. Most notably, Raman band nominally at 497 cm^{-1} that appears as a single wide Raman band at $22\text{ }^{\circ}\text{C}$, visibly splits into two separate Raman bands, 491 cm^{-1} (CH_2 rocking) and 509 cm^{-1} (CCO scissoring), at $-20\text{ }^{\circ}\text{C}$ and becomes fully resolvable as two separate Raman bands at $-100\text{ }^{\circ}\text{C}$. This is highlighted with an arrow in Figure 7-1. Similarly, Raman bands at around 185 cm^{-1} and 196 cm^{-1} that blend with the Raman band at 163 cm^{-1} (all associated with NH_2 torsion) and are not individually resolvable at room temperature also show better definition at lower temperatures. The Raman band at 196 cm^{-1} can be first detected at $-20\text{ }^{\circ}\text{C}$ and is fully resolvable at $-196\text{ }^{\circ}\text{C}$. Likewise, first detectable at $-100\text{ }^{\circ}\text{C}$, the emerging Raman band at 185 cm^{-1} continues to separate and become more defined with decreasing temperature, however, it was not fully resolved within the measured temperature range.

Band (Figure 7-1)	v1	v2	v3	v4	v5	v6	v7	v8	v9	v10	v11	v12	v13	v14	v15	v16	v17
Raman shift at $22\text{ }^{\circ}\text{C}$	163			358	497		602	699	895	1039	1112	1144	1331	1417	1446	1462	1576
new bands*		185 (-100 $^{\circ}\text{C}$)	196 (-20 $^{\circ}\text{C}$)			509 (-20 $^{\circ}\text{C}$)											
Raman shift at $-100\text{ }^{\circ}\text{C}$	168	185	204	361	491	516	604	702	897	1041	1118	1147	1332	1421	1447	1464	1579
Raman shift at $-196\text{ }^{\circ}\text{C}$	171	188	208	363	492	522	605	703	898	1041	1120	1149	1332	1422	1447	1465	1580

Table 7-1 Glycine Raman bands at $22\text{ }^{\circ}\text{C}$, $-100\text{ }^{\circ}\text{C}$ and $-196\text{ }^{\circ}\text{C}$ (*temperature at which the new band is first detectable in the brackets) [310]

Figure 7-2 shows the profile of the Raman shift of the 1331 cm^{-1} (asymmetrical stretching of CCO) and 895 cm^{-1} (NH_2 wagging) bands, the two most dominant bands in the Glycine spectra, at decreasing temperature, as well as the profile of the Raman band width narrowing. Other Raman bands of Glycine show similar trends.

As displayed in Figure 7-2, the Raman bands shift towards higher frequencies with decreasing temperature and the rate of change decreases significantly towards the lowest measured temperature. All Glycine Raman bands shifted towards higher frequencies except for the Raman band nominally at 497 cm^{-1} (CH_2 rocking), which shifted towards lower frequencies with decreasing temperature. However, this is likely due to the split of the 497 cm^{-1} band into two separate bands at lower temperatures as the centre Raman shift of the two blended peaks at

room temperature would have been detected in between the Raman shift of the two individual peaks.

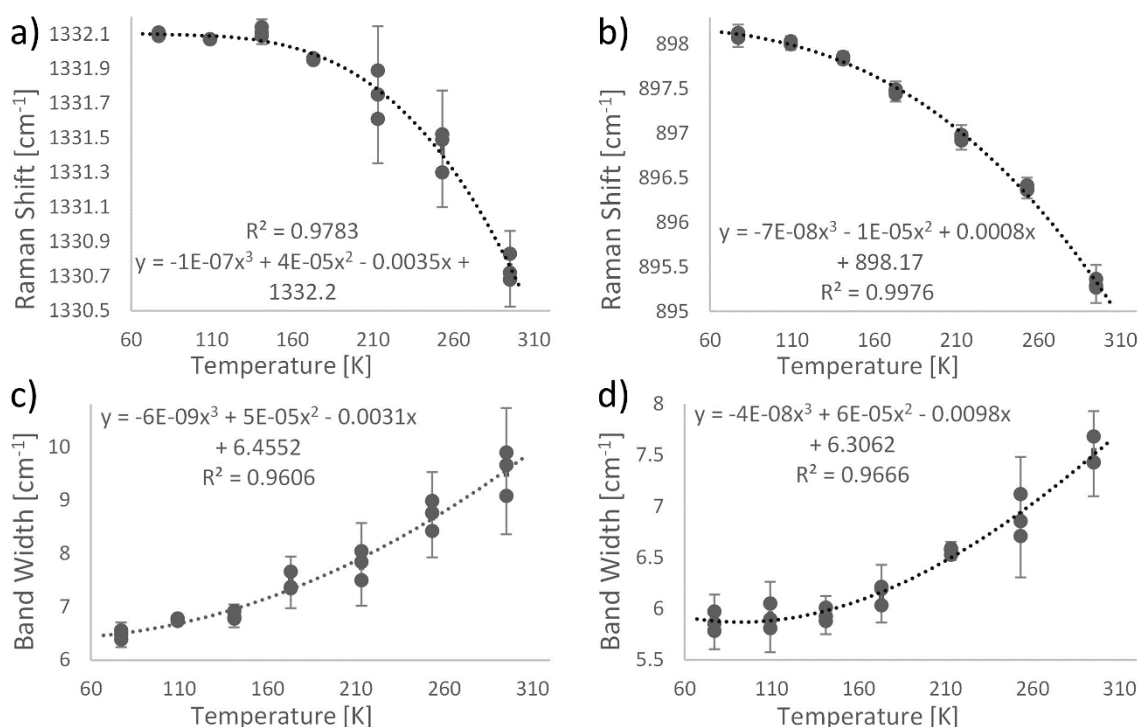


Figure 7-2 The profile of the changes in the Raman band shift and width of the Glycine asymmetrical stretching of CCO Raman band at 1331 cm⁻¹ (a and c respectively) and NH₂ wagging at 895 cm⁻¹ (b and d respectively). These bands are highlighted with arrows in the spectra in Figure 7-1. A general trend of the change is highlighted using a 3rd order polynomial curve. 2σ error bars calculated for these peaks at each temperature over 3 measurements at 3 different power settings are included in (a), (c) and (d) to indicate the relative significance of the changes. 3σ error bars are displayed in (b) as the change was too great for 2σ error bars to be visible [310]

The maximum measured shift difference between the room temperature and -196 °C Raman spectra was 24.97 cm⁻¹ (509 cm⁻¹ Raman band CCO scissoring) and the minimum 1.16 cm⁻¹ (1446 cm⁻¹ Raman band assigned to CH₂ scissoring). Both are well beyond the room temperature 3σ error threshold (1.21 cm⁻¹ and 0.21 cm⁻¹ respectively). This indicates that even the minimum shift difference measured in the Glycine spectra is a significant change that cannot be attributed to variability in the spectra or instrumental error. However, the maximum shift difference was likely measured higher than the true shift difference as a result of the nominal room temperature shift of 509 cm⁻¹ band being lower than its true room temperature shift whilst merged with the 497 cm⁻¹ band. All changes in the Raman shift observed at -196 °C were greater than the room temperature 3σ error thresholds of the corresponding Raman bands. This indicates that the

observed changes including minimal changes of less than 2 cm^{-1} are unlikely to be the result of variability between measurements and can be assigned to thermal effects.

Bands that on average shifted to higher frequencies at low temperatures by more than 2.6 cm^{-1} (and up to the overall measured maximum of 24.97 cm^{-1}) were all associated with vibrational modes involving the molecule extremities, that is, the NH_2 group or the COO group, or vibrations along the entire main chain of the molecule, that is, NCC bending, or a significant part of it, that is, CCO or $\text{CC}=\text{O}$ bending. All Raman bands that shifted to lower frequencies at low temperatures or higher frequencies but only by a relatively small amount ($<2.4\text{ cm}^{-1}$) compared to other bands (note that the absolute minimum positive shift was 1.16 cm^{-1} as stated previously) were predominantly associated with stretching vibrational modes or vibrational modes involving the inner atom of the molecule (CH_2). No band solely assigned to a stretching vibration increased in frequency at lower temperatures by more than 2.36 cm^{-1} .

The change of the Raman band width with temperature, as shown in Figure 7-2, demonstrates a significant narrowing of the Raman band width at lower temperatures. Similarly to the Raman shift, the rate of change decreases towards the lowest measured temperature. The maximum measured Raman band width difference between that at room temperature and at $-196\text{ }^\circ\text{C}$ measurements was 24.67 cm^{-1} at 497 cm^{-1} (CH_2 rocking), which corresponds to a 80.14% change in width and falls well beyond the room temperature 3σ error threshold of 1.48 cm^{-1} . The minimum Raman band width difference between the temperature extremes was 1.9 cm^{-1} (895 cm^{-1} band mostly attributed to NH_2 wagging) which is a 24.72% change from the nominal room temperature band width and also significantly higher than the 3σ error threshold of 0.62 cm^{-1} for this particular band. Similar to the Raman shift, the changes observed in the width of the Raman bands at $-196\text{ }^\circ\text{C}$ across all Glycine bands were greater than the corresponding 3σ error thresholds. This indicates that the observed narrowing of the Raman bands is too significant to be attributed to variability in the measurements or instrumental error.

Both the Raman shift and width data suggest that there is a relationship between the temperature and the level of variance between the individual spectra obtained at each temperature reference point, as the individual measurements seem to show less variance at lower temperatures. This is also clearly visible in the band shift and width profiles at 1331 cm^{-1} and 895 cm^{-1} , as displayed in Figure 7-2.

To visualize and characterize this occurrence, the average variance of individual spectra across all Glycine Raman bands was plotted against the temperature at which the spectra was obtained, as shown in Figure 7-3. The figure shows a clear linear decrease in the shift variance with decreasing temperature. The Raman band width data also indicates a decrease in the width variance at lower

temperatures, however, this relationship is not as clear and does not show a strong linear relationship. This is possibly due to experimental discrepancies or the width measurements being more susceptible to discrepancies due to handling, environmental or material differences within the sample.

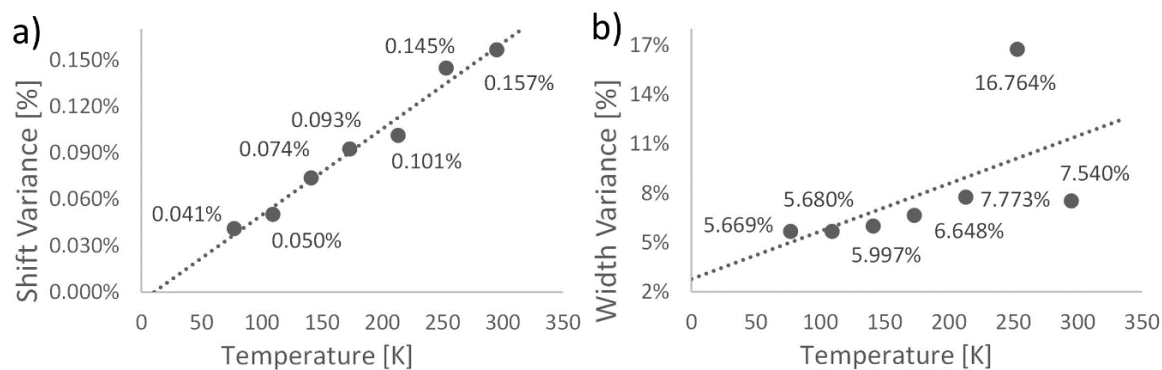


Figure 7-3 Variance of Raman band shift (a) and width (b) across individual Glycine spectra as a function of temperature [310]

While the average Raman shift variance between different measurements at room temperature can be as high as 0.157% compared to the average value, at $-196\text{ }^{\circ}\text{C}$ the average Raman shift variance drops to 0.041%. Likewise, at $22\text{ }^{\circ}\text{C}$ the average Raman band width variance across all Glycine Raman bands is 7.54%. At $-196\text{ }^{\circ}\text{C}$ the variance decreases to 5.669%. In this case, the average width variance at $-20\text{ }^{\circ}\text{C}$ (i.e., 16.764%) breaks away from the decreasing pattern as it is far greater than the variance at room temperature. The data shows that this significant fluctuation is the result of an abnormally low measurement of the 1417 cm^{-1} band (NH_2 and CH_2 torsion) width at $-20\text{ }^{\circ}\text{C}$ and inconsistent measurements of the same band at room temperature most probably caused by experimental discrepancy during the measurement.

The relationship between the Glycine spectra intensity and the temperature was found to be too inconsistent to derive a definitive profile, however, there is a visible increasing trend towards lower temperatures. All 15 fully detectable Glycine Raman bands show an increase in their intensity at $-196\text{ }^{\circ}\text{C}$ compared to the room temperature measurement. The Raman signal intensity change between room temperature and $-196\text{ }^{\circ}\text{C}$ across Glycine Raman bands is shown in Figure 7-4. The lowest increase in intensity was 5.5% at 509 cm^{-1} (CCO scissoring), however, the intensity increase data in this case could be inaccurate due to the split of 509 cm^{-1} from 497 cm^{-1} below room temperature. The second lowest increase in intensity, 6.1%, was detected at 1446 cm^{-1} (CH_2 scissoring) and might be a more accurate representation of the intensity increase minimum within Glycine spectra at $-196\text{ }^{\circ}\text{C}$. The maximum intensity increase between room temperature and $-196\text{ }^{\circ}\text{C}$ was 67.8% at 497 cm^{-1} (CH_2 rocking), which could have also been affected by the split of 509 cm^{-1} from 497 cm^{-1} . The second highest increase in intensity was 45% at 1144 cm^{-1} (mostly

assigned to NH₂ wagging), which might be more representative of the potential maximum increase in intensity. The average increase in intensity across all Glycine Raman bands was 26.5% and while the intensity increase is band specific and does not accurately describe the overall trend, it might still have some level of statistical value as a general guideline for the Raman signal intensity increase that could be expected at -196 °C.

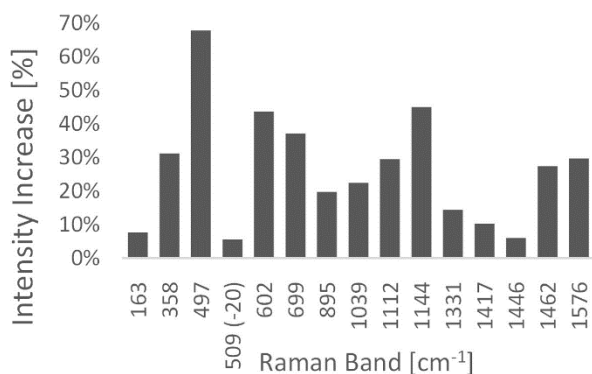


Figure 7-4 Intensity increase of Glycine Raman spectra at 196 °C compared to room temperature measurements [310]

7.1.2 Alanine

The comparison of Raman spectra of Alanine, the second simplest amino acid after Glycine, obtained at 22 °C, -100 °C and -196 °C is shown in Figure 7-5. As shown in the figure, a shift of Alanine Raman bands to higher frequencies was observed at lower temperatures, however, this shift was not as consistent as in the Glycine spectra discussed earlier. Additionally, some Alanine bands also shifted to lower frequencies. The Raman band assigned to NH₂ and CH₃ rocking nominally at 283 cm⁻¹ at room temperature moved to 274 cm⁻¹ at -100 °C and then to a higher frequency of 285 cm⁻¹ at -196 °C again. Similarly, 654 cm⁻¹ band (NCC=O bending) moved to 653 cm⁻¹ at -100 °C and then 655 cm⁻¹ at -196 °C. The average shift change from room temperature to -196 °C in this case was exactly 1 cm⁻¹, which is within the 3σ error region (0.88 - 1.33 cm⁻¹), which indicates that there is only a negligible probability of these measurements being the result of variability in the data or an error rather than the result of thermal changes within the spectra. Likewise, the Alanine band at 775 cm⁻¹ (C-COOH stretching) at room temperature moved to 774 cm⁻¹ at -100 °C where it remained also at -196 °C. The average shift decrease from room temperature to -196 °C in this case was 1.6 cm⁻¹, which is beyond the 3σ error threshold of 1.11 cm⁻¹ for this band and thus also very unlikely to be an outlier or an error in the data.

Similarly to the spectra of Glycine, the Alanine spectra also shows new Raman bands emerging at lower temperatures that were not visible or detectable at room temperature. While visible at room temperature and -100 °C, the Raman band at 146 cm⁻¹ (COOH torsion) is only fully

resolvable at $-196\text{ }^{\circ}\text{C}$. At $-100\text{ }^{\circ}\text{C}$, a small peak at 227 cm^{-1} appears in the spectra and seems to gain more intensity as it travels to 232 cm^{-1} at $-196\text{ }^{\circ}\text{C}$. While this peak is too weak to be resolvable, it is clearly visible in the spectra at lower temperatures. Similarly, the broad Raman band at 328 cm^{-1} (mixed vibration of CH_3 rocking and CCN bending) seems to diminish at $-100\text{ }^{\circ}\text{C}$ and two very weak bands at 322 cm^{-1} and 340 cm^{-1} take its place. While the 322 cm^{-1} band is too weak to be detectable, the 340 cm^{-1} band appears stronger and becomes very clearly distinguishable at $-196\text{ }^{\circ}\text{C}$ as it shifts to 346 cm^{-1} and gains more intensity.

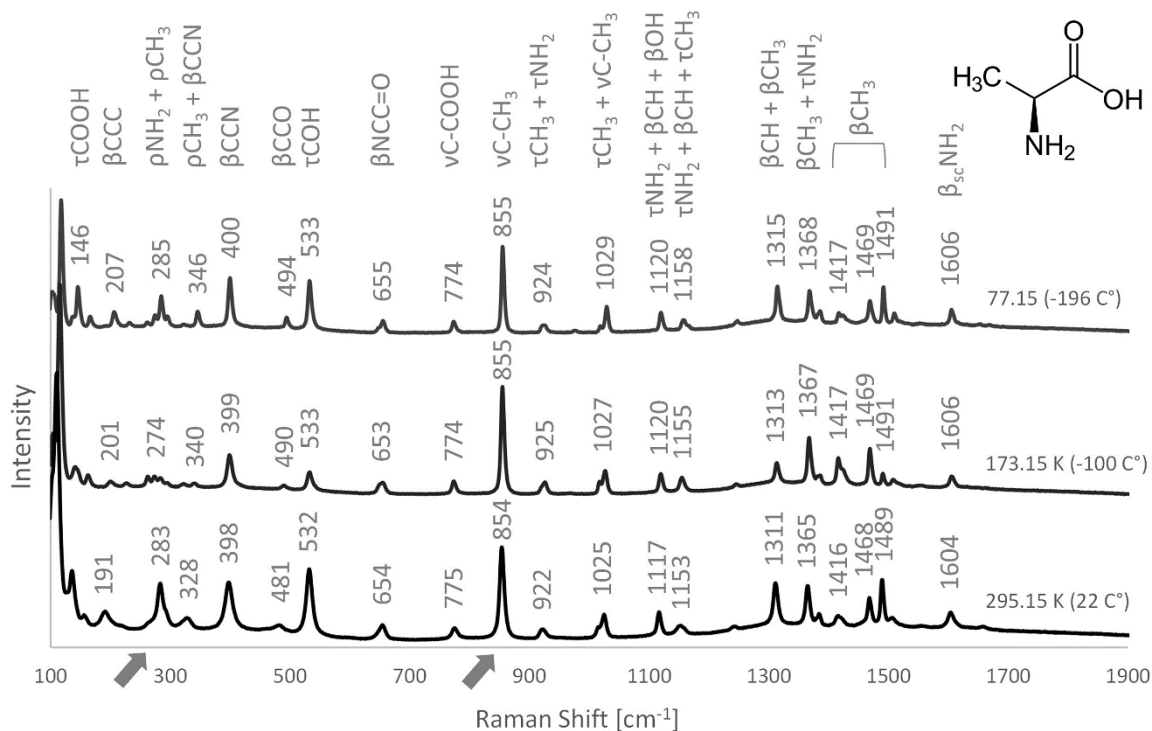


Figure 7-5 Raman spectra of Alanine at $22\text{ }^{\circ}\text{C}$, $-100\text{ }^{\circ}\text{C}$ and $-196\text{ }^{\circ}\text{C}$, where ν = stretching, β = bending, τ = torsion, sc = scissoring. Assignments are based on an optimized DFT vibrational frequency calculation using SVP and polarizability calculations for Raman vibrational frequencies and Raman activity together with a review of previously published assignments [314]–[320]. Arrows highlight bands detailed in Figure 7-6 [310]

Interestingly, the Alanine 283 cm^{-1} band (NH_2 and CH_3 rocking), which appears as a single wide band at room temperature, splits into 3 separate peaks at $-100\text{ }^{\circ}\text{C}$, which then become even more defined at $-196\text{ }^{\circ}\text{C}$ as the intensity of the middle peak rises. Only the middle peak is fully resolvable.

While the most dominant Raman band of Alanine, 854 cm^{-1} (C-CH_3 stretching), and most other Alanine bands follow the same general Raman shift and width pattern as Glycine bands (as shown in Figure 7-6), this is not necessarily the case for all Alanine Raman bands. As already mentioned, not all the Alanine bands shifted to higher frequencies and while most bands show a decreasing

rate of change in the Raman shift and width at decreasing temperature, the profile is not as consistent as with the spectra for Glycine. For comparison, Figure 7-6 shows the Raman shift and width profile of the 283 cm^{-1} band which shifts to a lower frequency at $-100\text{ }^{\circ}\text{C}$ and higher again at $-196\text{ }^{\circ}\text{C}$.

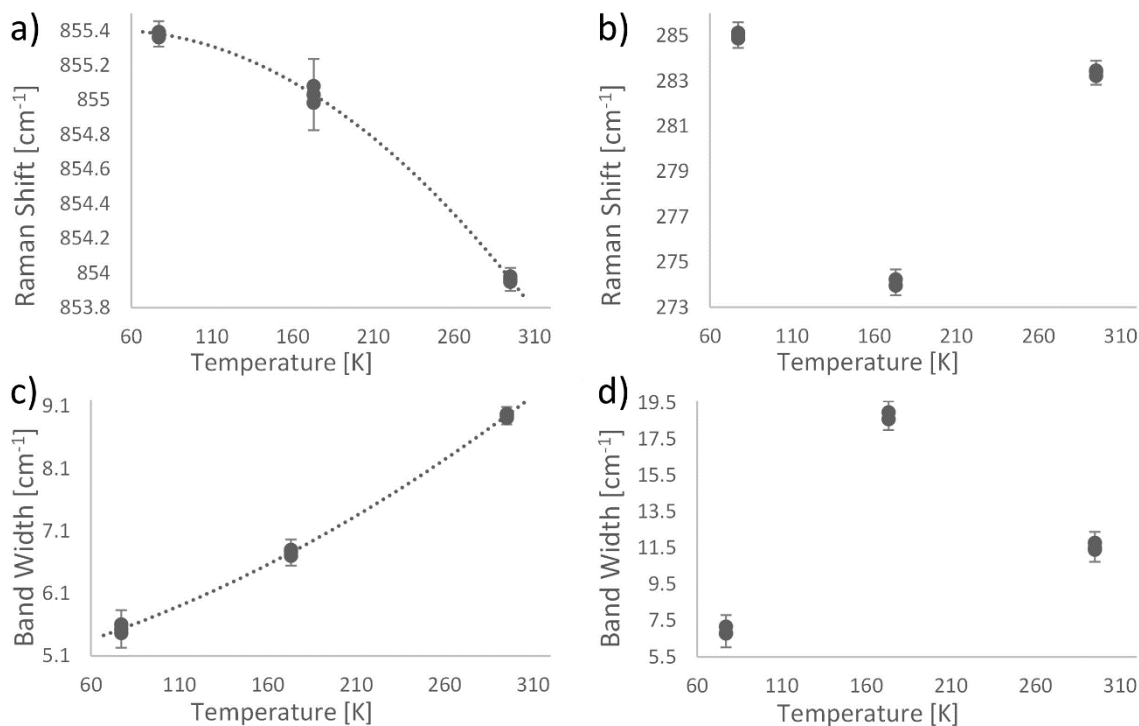


Figure 7-6 Alanine profile of Raman band shift and width change as a function of temperature for the C-CH_3 stretching band at 854 cm^{-1} (a and c) and NH_2 and CH_3 rocking band at 283 cm^{-1} (b and d). A general trend of the change, similar to Glycine Raman shift and width change profile, is highlighted in a and c. These bands are highlighted with arrows in the spectra in Figure 7-5. 3σ error bars calculated for these peaks at each temperature over 3 measurements at 3 different power settings are included to indicate the relative significance of the changes [310]

Across all Alanine Raman bands the minimum change between the room temperature and $-196\text{ }^{\circ}\text{C}$ Raman shift was 0.92 cm^{-1} at 532 cm^{-1} (COH torsion). The maximum change was 18.78 cm^{-1} and it occurred at 328 cm^{-1} (mixed vibration of CH_3 rocking and CCN bending). Both of these shifts lie beyond the 3σ error threshold for these peaks, 0.46 cm^{-1} and 3.74 cm^{-1} respectively. Overall, the recorded changes in the Raman shift from room temperature to $-196\text{ }^{\circ}\text{C}$ were beyond the 3σ region for all Alanine Raman bands except for the 654 cm^{-1} band (NCC=O bending), where the recorded shift lies within the 3σ region, and the 1416 cm^{-1} band (CH_3 bending), where the recorded shift falls within the 2σ region. While this signals greater variability in the data than in the spectra of Glycine, it also indicates at least 99.7% confidence (95.4% for the 1416 cm^{-1} band) that none of the recorded shift changes are the result of an error or variability in the data.

Similar to the bands of Glycine, all Alanine bands that on average shifted to higher frequencies at low temperatures by more than 1.6 cm^{-1} (and up to the overall measured maximum of 18.78 cm^{-1}) are associated with vibrations of the outside parts of the molecule, that is, its methyl side chain (CH_3) and its amine functional group (NH_3), or vibrations along the length of the main molecule chain, that is, CCO, CCC or CCN bending. The only shift that decreased in frequency at low temperatures is assigned to a stretching vibrational mode and none of the alanine bands solely assigned to a stretching vibration increased in frequency by more than 1.42 cm^{-1} at low temperatures.

Despite some inconsistencies in the data, a general trend of Raman band narrowing at decreasing temperature was observed. The minimum Raman band width across all Alanine bands was measured at the 1489 cm^{-1} band at all temperatures; 5.81 cm^{-1} at $22\text{ }^\circ\text{C}$, 4.36 cm^{-1} at $-100\text{ }^\circ\text{C}$ and 4.18 cm^{-1} at $-196\text{ }^\circ\text{C}$. The maximum Raman band width at room temperature was 15.82 cm^{-1} at 1153 cm^{-1} . At $-100\text{ }^\circ\text{C}$ it was 18.79 cm^{-1} measured at the 274 cm^{-1} Raman band and 11.64 cm^{-1} at $-196\text{ }^\circ\text{C}$ at the Raman band of 1417 cm^{-1} .

The minimum measured difference between the Raman band width between room temperature and $-196\text{ }^\circ\text{C}$ was exactly 1 cm^{-1} at 1468 cm^{-1} (CH_3 bending) which corresponds to a 14.3% change from the nominal room temperature value. While this is a minimal change within the spectra, it lies beyond the 3σ error threshold of 0.21 cm^{-1} for this peak. The maximum Raman band width change was 12.18 cm^{-1} at 283 cm^{-1} (62.4%) attributed to NH_2 and CH_3 rocking, however, in terms of the highest change in percentage to the nominal value, it was 64.7% at 481 cm^{-1} (CCO bending), which was 10.67 cm^{-1} . Overall, most changes recorded in the width of Alanine Raman bands were beyond their corresponding 3σ error thresholds, only the width change recorded at the 328 cm^{-1} and 481 cm^{-1} bands was within the 3σ error range, and 922 cm^{-1} and 1365 cm^{-1} bands within the 2σ error range. While this signals a higher variance in the width change data than the shift change data, it still indicates high confidence in the width change being the result of the thermal changes rather than any discrepancy in the data.

Just like in the case of Glycine, the average variance of the individual Raman shift measurements across all fully detectable bands decreases at lower temperatures showing a clear linear relationship, as displayed in Figure 7-7. The average variance across all peaks at room temperature is 0.072% from the nominal value while at $-196\text{ }^\circ\text{C}$ the variance drops to 0.050%. Similar to Glycine, the Raman band width variance across individual measurements is less consistent than the variance of Raman shift as shown in Figure 7-7. While it displays a decreasing trend towards lower temperatures, the decrease is almost level and there is no clear linear relationship indicated in the data. At room temperature, the band width variance is 10.3% which

then decreases to 8.15% at -100 °C and rises again to 10.15% at -196 °C. The Raman band width data can be more severely impacted by spectral changes, such as the emergence of new peaks and severe intensity changes between measurements at various temperatures, as shown in the spectra of Alanine in Figure 7-5. As such, this discrepancy could be assigned to the varied changes in the Alanine spectra between 22 °C and -196 °C.

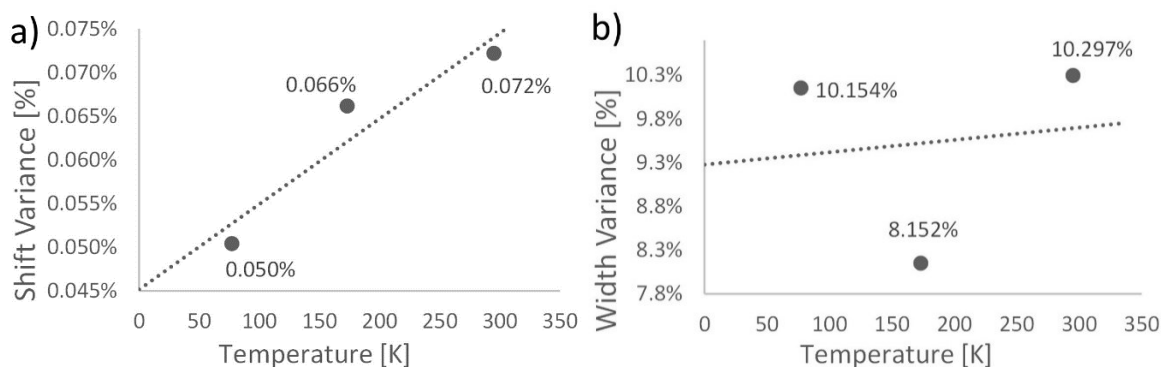


Figure 7-7 Variance of Raman band shift (a) and width (b) across individual Alanine spectra as a function of temperature [310]

Similarly, the intensity of the majority of Alanine bands decreased at lower temperatures. This is different to that observed for the Glycine Raman bands, where the intensity increased at lower temperatures. Figure 7-8 shows the intensity change of all fully detectable Alanine bands from room temperature to -196 °C. All 19 fully detectable Alanine bands showed a signal intensity decrease. The average decrease in intensity across all bands was 18.2% with the maximum decrease being 35.4% at 283 cm^{-1} (NH_2 and CH_3 rocking) and the minimum 1.5% at 1025 cm^{-1} (mainly attributed to CH_3 torsion).

It is also important to note that the intensity of Alanine peaks changes a lot more dramatically with temperature as shown in the spectra in Figure 7-5. Some bands, such as 398 cm^{-1} (CCN bending), 532 cm^{-1} (COH torsion) and 1489 cm^{-1} (CH_3 bending), decrease in intensity significantly at -100 °C (beyond their 3σ error threshold) and then visibly rise again compared the rest of the spectra at -196 °C. The rise in intensity at -196 °C lies beyond the 3σ error threshold for 1489 cm^{-1} and within the 3σ region for 398 cm^{-1} and 532 cm^{-1} , which indicates that these changes are induced by the varying temperature rather than being the result of variability in the data. Similarly, while the overall intensity of the 481 cm^{-1} band (CCO bending) decreases, the band is barely detectable at room temperature and becomes increasingly more distinguishable towards lower temperatures even despite the overall intensity decrease.

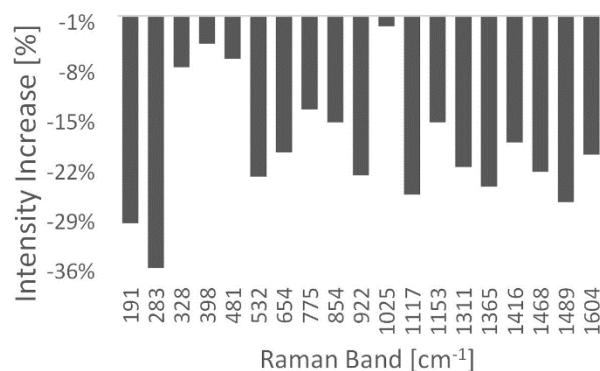


Figure 7-8 Intensity decrease of Alanine Raman spectra at 196 °C compared to room temperature measurements [310]

7.1.3 Histidine

The comparison of Raman spectra of Histidine, an aromatic fluorescence-free amino acid at 785 nm, obtained at room temperature, -100 °C and -196 °C is shown in Figure 7-9. Histidine has a more complex molecular structure than Glycine and Alanine, leading to a more varied Raman spectrum. However, the changes at lower temperatures display similar trends and no other additional effects were observed. A shift to higher frequencies was observed for most Histidine bands with a couple of exceptions; 404 cm⁻¹ (CH₂ rocking and out of plane bending of CH₂-CH-NH₂), 966 cm⁻¹ (breathing of the ring) and 1145 cm⁻¹ (asymmetrical stretching of CH₂-CH-NH₂), that shifted to lower frequencies. Some bands, including 627 cm⁻¹ (out of plane deformation of the ring) and 657 cm⁻¹ (CH₂-ring stretching), only exhibited very minor Raman shift changes not resulting in any substantial Raman band shifts in the spectra. While the minimal change in the shift of the 657 cm⁻¹ band was most likely a result of variance in the spectra (1σ error region), the change recorded in the shift of the 627 cm⁻¹ band was within the 3σ error region and thus a result of the thermal change. However, in both cases the data indicates that both of these bands are very thermally stable. Similar to some Alanine bands, the Histidine CH₂ torsion band nominally at 1255 cm⁻¹ shifted to 1257 cm⁻¹ at -100 °C and then to 1256 cm⁻¹ at -196 °C. However, in this case this could have also been a result of excessive variance in the spectra. Additionally, the emergence of new bands that were not visible in the spectra at room temperature was recorded. Previously undetectable peaks at 340 cm⁻¹ (CH₂ rocking) and 431 cm⁻¹ (CC=O bending) appear in the spectra at -100 °C and become more distinguishable at -196 °C as they shift to 431 cm⁻¹ and 435 cm⁻¹ respectively. Moreover, the band clearly visible at 213 cm⁻¹ at room temperature becomes unresolvable at -100 °C and -196 °C as it fades and blends with the 240 cm⁻¹ band, both assigned to CH₂-ring and C-NH₂ bending.

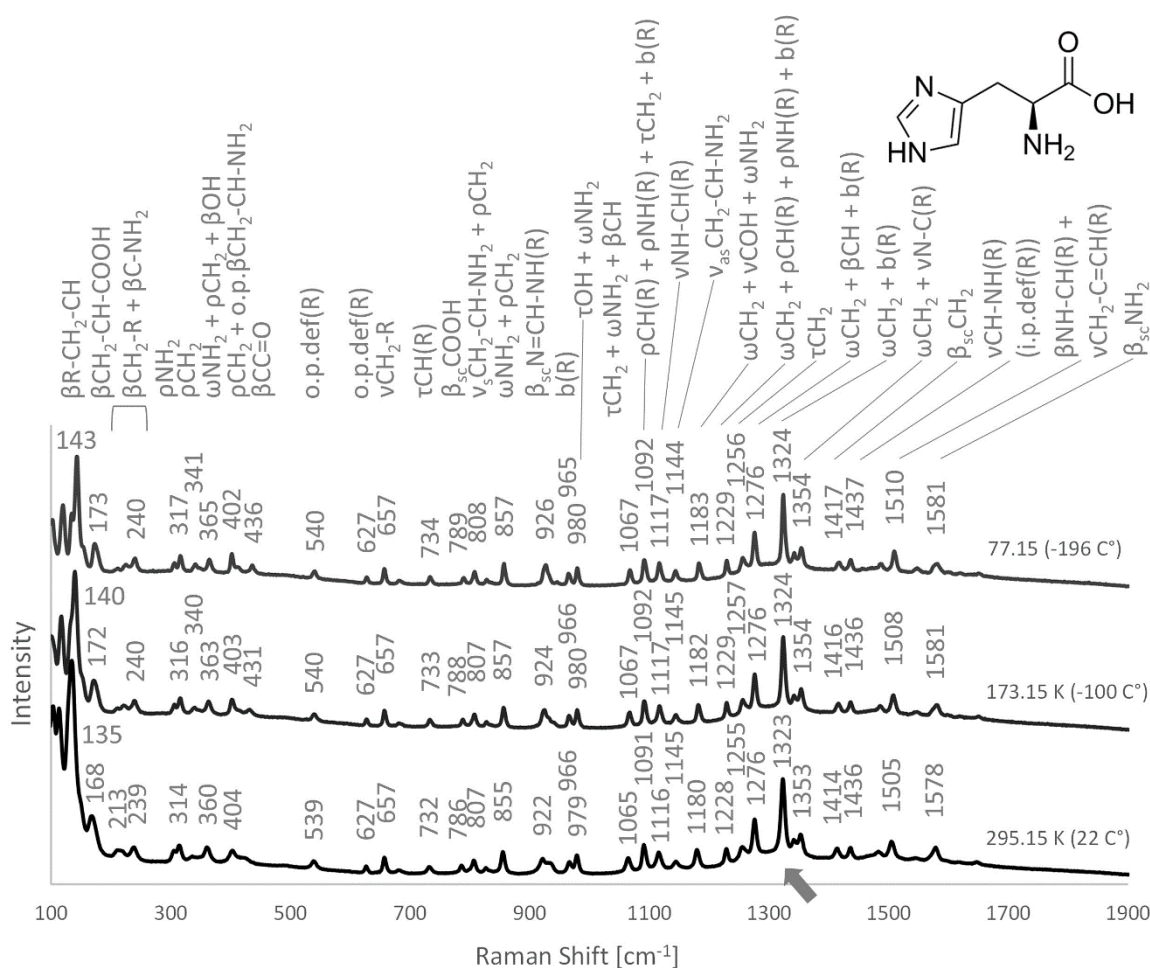


Figure 7-9 Raman spectra of Histidine at 22 °C, -100 °C and -196 °C, where R = ring (i.e. imidazole ring), v = stretching, ω = wagging, ρ = rocking, β = bending, τ = torsion, b = breathing (i.e. in phase stretching of the ring), def = deformation (i.e. out of phase stretching of the ring), sc = scissoring, as = asymmetric, s = symmetric, o.p. = out of plane, i.p. = in plane, brackets denote the location of the vibration. Assignments are based on an optimized DFT vibrational frequency calculation using SVP and polarizability calculations for Raman vibrational frequencies and Raman activity together with a review of previously published assignments [321]–[325]. A diagonal arrow highlights the band detailed in Figure 7-10 [310]

Most Histidine bands display similar change profiles in Raman shift and width with decreasing temperature, as already described in Figure 7-2 and Figure 7-6 (a and c) for Glycine and Alanine. The profile of the Raman shift and width change as a function of temperature for the most dominant Histidine Raman band at 1323 cm^{-1} (mixed vibration of CH_2 wagging and ring breathing) is shown in Figure 7-10. While most Histidine bands displayed a similar profile, there were some exceptions as some bands shifted to lower frequencies or diminished at lower temperatures all together as described above.

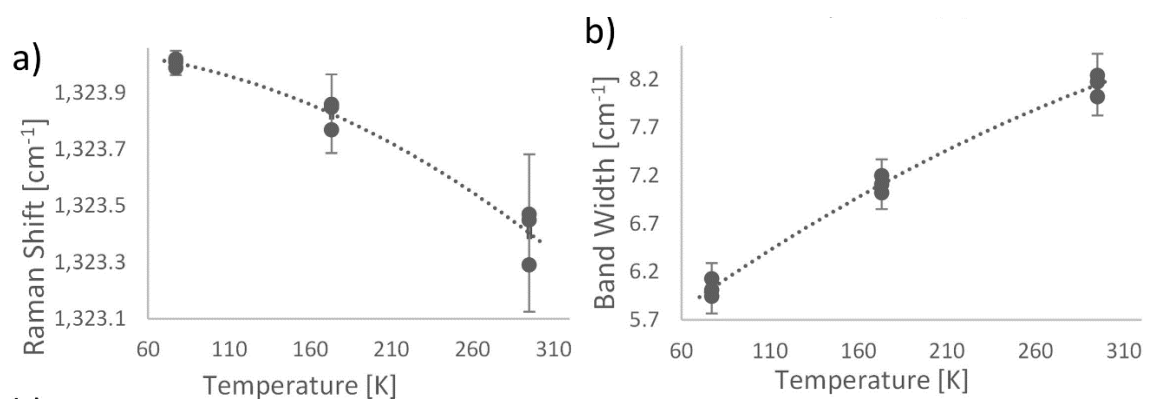


Figure 7-10 Histidine profile of Raman band shift and width change as a function of temperature for the 1323 cm⁻¹ band (a and b respectively) assigned to mixed vibrations of CH₂ wagging and ring breathing. A general trend of the change is highlighted. This band is highlighted with an arrow in the spectra in Figure 7-9. 2σ error bars calculated for this Raman band at each temperature over 3 measurements at 3 different power settings are included to indicate the relative significance of the changes [310]

The minimum change in the Raman shift between room temperature and -196 °C across all Histidine bands was 0.35 cm⁻¹ at 1276 cm⁻¹ (mixed vibration of CH₂ wagging, CH bending and ring breathing). This shift lies in the 3σ error region, which indicates that the change is highly unlikely to be attributed to variance in the spectra and represents a genuine thermally induced change. Nevertheless, this minimal change also signals that the 1276 cm⁻¹ band is very thermally stable. The maximum Raman shift change was 8.79 cm⁻¹ at 135 cm⁻¹ (ring-CH₂-CH bending). While some Histidine Raman bands were undetectable at room temperature and error bars could not be generated, the shift change of all fully detectable bands except for 5 was greater than their 3σ error thresholds, 4 were within the 3σ error region and, as discussed earlier, the 657 cm⁻¹ band was within 1σ error region but only very minor change was recorded.

Unlike Glycine and Alanine, the Histidine molecule has an imidazole ring in its structure, however, the observed trends in the thermally induced shifts of its vibrational modes were similar. All the Histidine bands that on average shifted to higher frequencies at low temperatures by more than 3.5 cm⁻¹ (and up to the overall measured maximum of 8.79 cm⁻¹) were assigned at least partially to vibrational modes involving the molecule's outer atoms, that is, the amine group (NH₂) or the carboxylic acid group (COOH), or bending along the length of the molecular chain, that is, bending of the ring and CH₂ or bending of the ring or the carboxylic acid group against CH₂-CH. Bands associated with in plane bending within the imidazole ring also displayed shifts to higher frequencies greater than 3.5 cm⁻¹. Histidine bands that displayed a shift to lower frequencies at low temperatures or that shifted to higher frequencies only by less than 0.55 cm⁻¹ were predominantly assigned to stretching vibrational modes, that is, stretching between individual

atoms as well as ring breathing or ring in plane deformation, or vibrational modes including inner atoms of Histidine (CH_2 or CH). None of the bands assigned to out of plane ring deformation generated shifts to higher frequencies at low temperatures greater than 0.82 cm^{-1} . None of the bands solely or predominantly assigned to stretching vibrations shifted to a higher frequency by more than 1.4 cm^{-1} .

As already observed with Glycine and Alanine, Raman band width narrowing was observed in the spectra of Histidine at low temperatures. The decrease in Raman band width from room temperature to $-196 \text{ }^\circ\text{C}$ was as high as 15.45 cm^{-1} at 922 cm^{-1} ($\text{N}=\text{CH}-\text{NH}$ scissoring in the ring) which roughly corresponds to 67.92% of the room temperature width. The minimum change in the Raman band width was 1.03 cm^{-1} (15.26%) as observed at 1436 cm^{-1} ($\text{CH}-\text{NH}$ stretching in the ring) or 4.36% (1.21 cm^{-1}) at 627 cm^{-1} (out of plane deformation of the ring), both within the 3σ error region. Overall, most fully detectable Raman bands displayed changes in the band width greater than their 3σ error thresholds, however, 5 bands were within the 3σ error region and 1 in the 2σ error region. This signals a high probability that all the recorded changes can be attributed to the temperature decrease rather than the variance in the data. Compared to Alanine and Glycine, Histidine bands in general are narrower and potentially more restrictive in terms of spectral resolution for successful detection. At room temperature the narrowest band is 1.81 cm^{-1} wide at 1065 cm^{-1} , at $-100 \text{ }^\circ\text{C}$ it is 2.65 cm^{-1} at 404 cm^{-1} and at $-196 \text{ }^\circ\text{C}$ it is 2.66 cm^{-1} at 1116 cm^{-1} .

The variance between individual Histidine Raman spectra at each measured temperature is summarized in Figure 7-11. Across all Histidine bands, the variance of the Raman shift decreases linearly with decreasing temperature, which corresponds to the Glycine and Alanine variance trend described previously. From a variance of 0.041% at room temperature, the Raman shift variance drops to 0.033% at $-100 \text{ }^\circ\text{C}$ and 0.022% at $-196 \text{ }^\circ\text{C}$.

While there is a clear decreasing trend in the Raman band width variance across all fully detectable Histidine bands towards lower temperatures, the relationship is not as clearly linear as

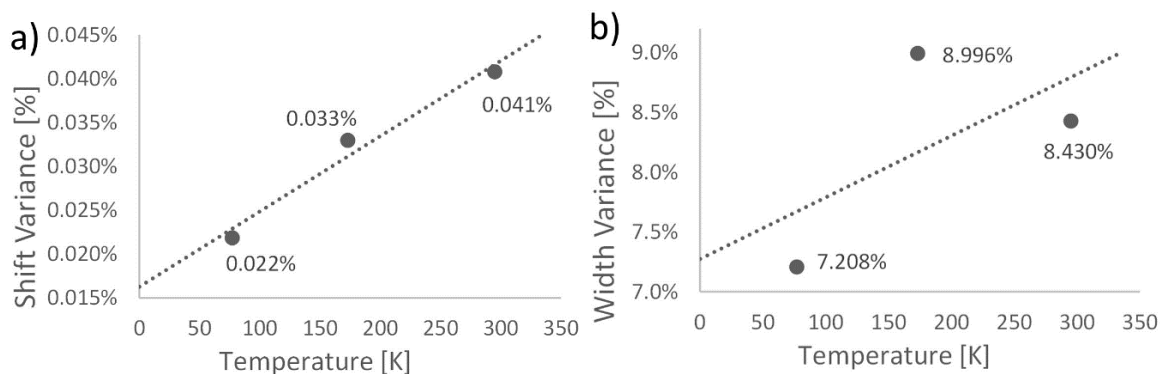


Figure 7-11 Variance of Raman band shift (a) and width (b) across individual Histidine spectra as a function of temperature [310]

the Raman shift variance profile. As shown in Figure 7-11, the band width variance at room temperature is 8.43%, rising slightly to 8.996% at -100 °C and then dropping to 7.208% at -196 °C.

Overall, most Histidine bands displayed higher intensity at -196 °C than at room temperature. As shown in Figure 7-12, out of 24 fully detectable bands, 15 increased and 9 decreased in intensity at -196 °C compared to 22 °C. The average intensity change across Histidine bands was a 2.05% increase, however, the maximum change was a 37% decrease at 135 cm⁻¹ (ring-CH₂-CH bending) and the minimum change was a 25.22% increase at 404 cm⁻¹ (CH₂ rocking and out of plane bending of CH₂-CH-NH₂). Additionally, as discussed above, the 213 cm⁻¹ Histidine band diminishes at lower temperatures all together and 340 cm⁻¹ and 431 cm⁻¹ bands emerge in the spectra at 100 °C and become more distinguishable as they further intensify at -196 °C.

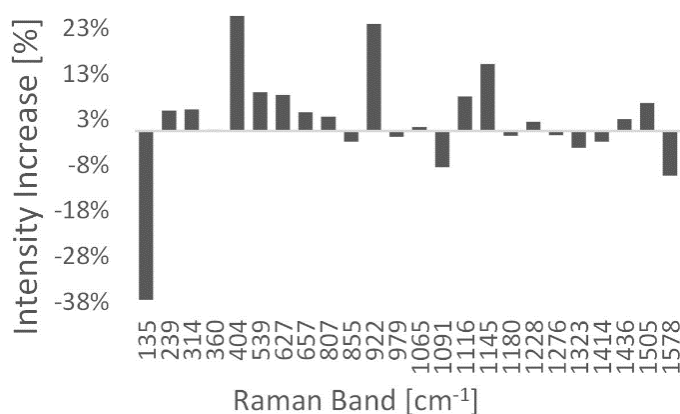


Figure 7-12 Intensity increase of Histidine Raman spectra at -196 °C compared to room temperature measurements [310]

7.1.4 Tryptophan

The Raman spectra of Tryptophan, a mildly fluorescent aromatic amino acid at 785 nm, obtained at room temperature, -100 °C and -196 °C are compared in Figure 7-13. While most bands shift to higher frequencies at lower temperatures as previously observed in the spectra of Glycine, Alanine and Histidine, the 164 cm⁻¹ (out of plane deformation of the indole rings) and 1256 cm⁻¹ (CH₂ wagging and indole breathing) bands shift to lower frequencies and the 1464 cm⁻¹ (in plane indole deformation) and 1565 cm⁻¹ (CH=C stretching in the pyrrole ring) bands shift to a higher frequency at -100 °C and then lower again at -196 °C. Additionally, some bands only shift by a very small amount. Namely, the 1012 cm⁻¹ band (CH=CH stretching in the benzene ring) shifts to a lower frequency and the 842 cm⁻¹ (benzene ring CH torsion) and 1494 cm⁻¹ (in plane indole deformation) bands shift to higher frequencies, but the changes do not exceed 0.7 cm⁻¹. Although minimal, these changes correspond to values higher than the 3σ error region, the 3σ error region and the 2σ error region respectively, and as such cannot be disregarded as variance in the data.

This also indicates that these bands are relatively thermally stable. In general, changes in the Raman shift across Tryptophan bands at lower temperatures are relatively minor compared to changes observed in the spectra of Glycine, Alanine and Histidine. The maximum measured shift from room temperature to $-196\text{ }^{\circ}\text{C}$ was 7.95 cm^{-1} at 123 cm^{-1} (in plane bending of the entire molecule) and the minimum measured shift of 0.45 cm^{-1} was at 757 cm^{-1} (benzene and pyrrole ring breathing). This change in the shift lies beyond the 3σ error threshold for this band and as such it indicates that the change is a result of the temperature decrease rather than variability in the data and that the band is thermally exceptionally stable. Among all Tryptophan Raman bands, the recorded changes in the shift are greater than the 3σ error threshold in most cases with 3 bands in the 3σ error region and 2 in the 2σ sigma error region. This provides high confidence that all recorded changes in the shift can be attributed to thermal effects rather than variability in the data.

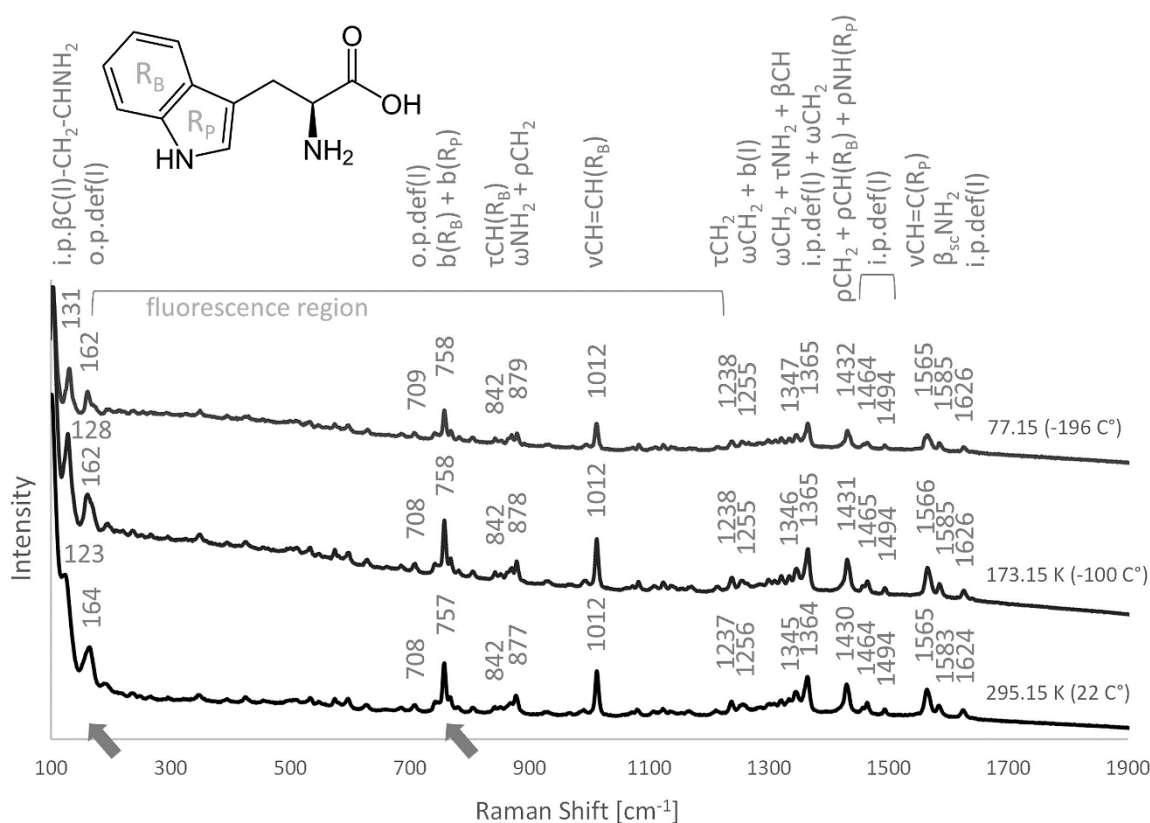


Figure 7-13 Raman spectra of Tryptophan at 22 °C, -100 °C and -196 °C, where R_B = benzene ring, R_P = pyrrole ring, l = indole group (i.e. benzene and pyrrole ring), ν = stretching, ω = wagging, ρ = rocking, β = bending, τ = torsion, b = breathing (i.e. in phase stretching of a ring), def = deformation (i.e. out of phase stretching of a ring), sc = scissoring, o,p = out of plane, i,p = in plane, brackets denote the location of the vibration. Assignments are based on an optimized DFT vibrational frequency calculation using SVP and polarizability calculations for Raman vibrational frequencies and Raman

activity together with a review of previously published assignments [318], [326].

Diagonal arrows highlight the bands detailed in Figure 7-15 [310]

No new Raman bands were detected emerging in the Tryptophan spectra at lower temperatures.

The molecule of Tryptophane includes an indole group composed of a benzene and pyrrole ring and the thermally induced shifts of its vibrational modes displayed similar trends observed in the spectra of Histidine. Similar to all the other examined amino acids, all Tryptophane Raman bands that shifted to higher frequencies the most at lower temperatures (by $>1.77\text{ cm}^{-1}$ and up to the absolute overall measured maximum of 7.95 cm^{-1}) were either assigned to the vibrations of the outer parts of the Tryptophan molecule, that is, its amine group, or vibrational modes including the entire molecule or most of its main chain, that is, bending of the indole group against the carboxylic acid group. Raman bands that either shifted to lower frequencies at lower temperatures or shifted to higher frequencies by less than 0.83 cm^{-1} were predominantly assigned to stretching vibrational modes, that is, stretching between individual atoms as well as in plane deformation of the ring or ring breathing, or vibrational modes associated with the inner atoms of the molecule, that is, CH_2 or CH , or out of plane deformation of the rings. The only band that shifted to a lower frequency by more than 2 cm^{-1} was assigned to out of plane deformation of the indole group. Additionally, similarly to Histidine, none of the bands associated with out of plane deformation of the rings shifted to higher frequencies at low temperatures by a significant amount compared to other Histidine bands ($<1.18\text{ cm}^{-1}$). This is also true for any bands associated with stretching vibrational modes which did not shift to higher frequencies by more than 1.44 cm^{-1} .

While no fluorescence was detected in the spectra of Glycine, Alanine and Histidine at 785 nm, a clear fluorescence background is visible in the Tryptophan spectra at all measured temperatures. As shown in Figure 7-13, the fluorescent background becomes more pronounced at lower temperatures and intensifies as the temperature decreases. As displayed in Figure 7-14, this is also reflected in the average Signal to Noise (S/N) ratio calculated for one of the most dominant Raman bands at 1012 cm^{-1} compared to the fluorescence background at 450 cm^{-1} . The S/N ratio drops linearly with decreasing temperature at the rate of 0.2786 K^{-1} .

The profile of the Raman shift and width change as a function of temperature for one of the most dominant Tryptophan bands at 757 cm^{-1} (benzene and pyrrole ring breathing) is shown in Figure 7-15. In general, all other Tryptophan bands that shift to higher frequencies at lower temperatures follow a similar pattern. A similar pattern was also observed for other analysed amino acids as discussed previously with a notable difference of the Tryptophan band width profile being more inconsistent and resulting in a more linear decrease. For comparison, image b

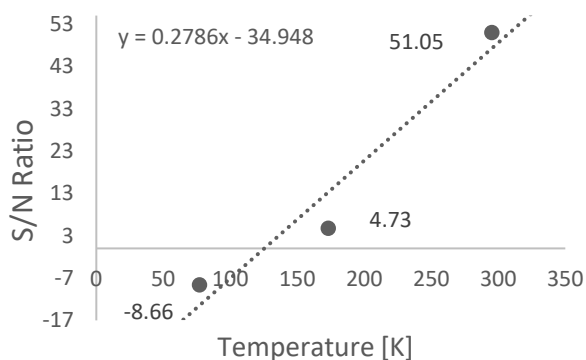


Figure 7-14 Average S/N ratio of Tryptophan fluorescence as a function of temperature [310]

and d in Figure 7-15 show the Raman shift and width change profile of band 164 cm^{-1} (indole out of plane deformation) which shifts to lower frequencies with decreasing temperature. As shown in the figure, the 164 cm^{-1} profile of Raman shift and width change is approximately an inverse of the profile of the bands that shift to higher frequencies, as displayed in Figure 7-2, Figure 7-6 (a and c), Figure 7-10 and Figure 7-15 (a and c).

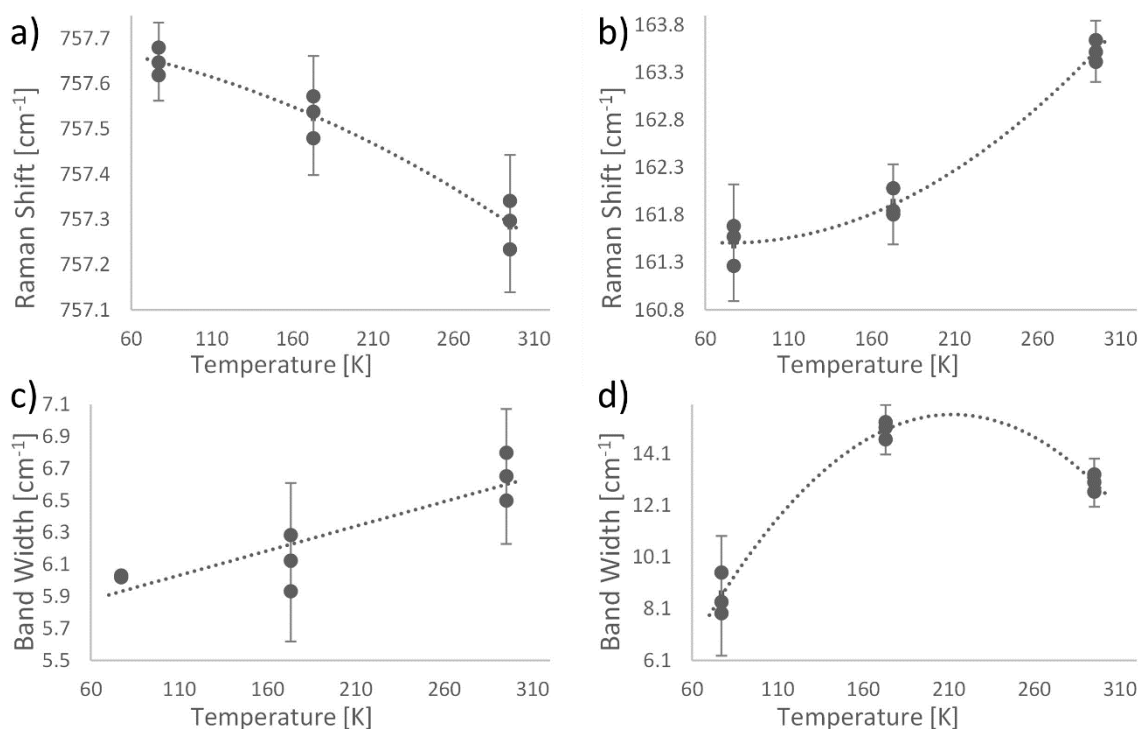


Figure 7-15 Tryptophan profile of Raman band shift and width change as a function of temperature for the benzene and pyrrole ring breathing band at 757 cm^{-1} (a and c) and the indole out of plane deformation band at 164 cm^{-1} (b and d). A general trend of the change is highlighted. These bands are highlighted with arrows in the spectra in Figure 7-13. 2σ error bars calculated for these Raman bands at each temperature over 3 measurements at 3 different power settings are included to indicate the relative significance of the changes [310]

Just like the spectra of other examined amino acids, Tryptophane bands show significant narrowing at lower temperatures, however, the data is not as consistent which might be partly a result of the fluorescence background. The overall maximum change in the band width from 22 °C to -196 °C was 10.95 cm⁻¹ at 877 cm⁻¹ (NH₂ wagging and CH₂ rocking) which is 67.76% of the nominal room temperature width. The minimum change in width across all Tryptophan bands was 0.87 cm⁻¹ at 757 cm⁻¹ (benzene and pyrrole ring breathing), which is 12.73% of the original width and lies beyond the 3 σ error threshold of 0.63 cm⁻¹. This indicates that even this minor change can be attributed to the temperature decrease rather than variability in the data. Similar to the changes recorded in the Tryptophan band shift, the changes in the band width were also greater than the 3 σ error threshold in most cases with 2 bands in the 3 σ error region and 3 bands in the 2 σ error region. While this indicates that the band width data may be more prone to variability in the data than the shift measurements, it still provides sufficient confidence that all observed changes are the result of the decrease in temperature. At room temperature the minimum band width across all Tryptophan bands was 4.20 cm⁻¹ at 1494 cm⁻¹, at -100 °C it was 3.64 cm⁻¹ at 842 cm⁻¹ and at -196 °C it was 3.16 cm⁻¹ at 1494 cm⁻¹.

The variance between individual Tryptophan Raman measurements as a function of temperature is shown in Figure 7-16. Both the Raman band shift and width variance show a decreasing trend at lower temperatures. However, the relationship is not linear as observed for other analysed amino acids. At room temperature, the Raman shift variance is 0.078%, which then drops to 0.031% at -100 °C and rises again to 0.066% at -196 °C. The same pattern is observed for the variance in the band width as the width variance drops from 17.78% at room temperature, to 9.90% at -100 °C, just to rise again to 16.03% at -196 °C. In this case it should be noted that the presence of fluorescence might have impacted the variance data.

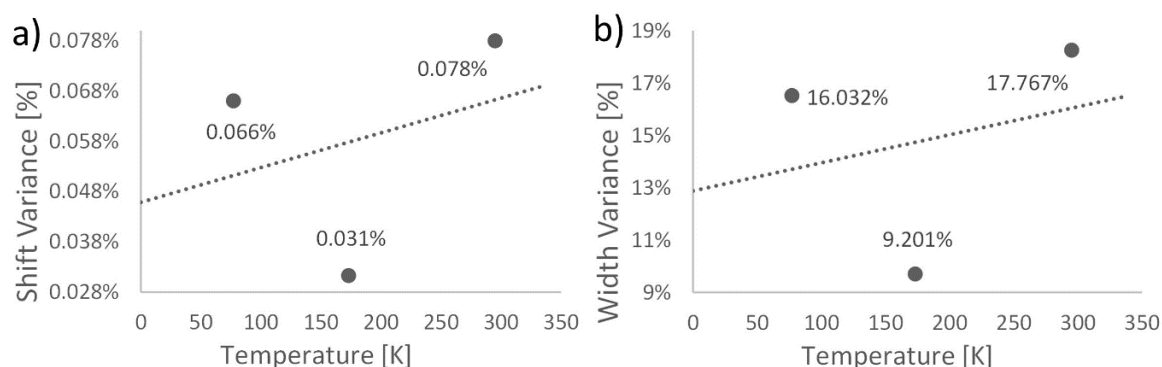


Figure 7-16 Variance of Raman band shift (a) and width (b) across individual Tryptophan spectra as a function of temperature [310]

The change in intensity across all fully detectable Tryptophan bands from 22 °C to -196 °C is shown in Figure 7-17. Of the 16 fully detectable bands, half decrease in intensity at lower

temperatures and the other half increase. The highest intensity increase was 25.1% at 842 cm^{-1} (benzene ring CH torsion) and the highest decrease was 30.5% at 708 cm^{-1} (indole out of plane deformation). However, as shown in Figure 7-17, the intensity of most bands did not change from room temperature to $-196\text{ }^{\circ}\text{C}$ by more than 10% and the average intensity change was a 3% decrease. While the increase in the fluorescence background affects the detectability of individual Tryptophan bands, no bands completely diminished at lower temperatures.

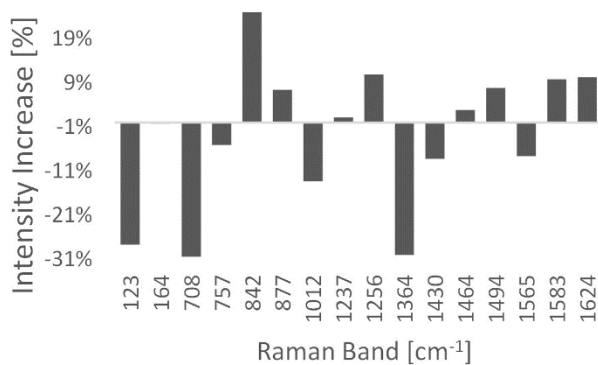


Figure 7-17 Intensity increase of Tryptophan Raman spectra at $-196\text{ }^{\circ}\text{C}$ compared to room temperature measurements [310]

7.1.5 Fluorescence at 532 nm

As already mentioned previously, fluorescence noise in the spectra of amino acids at 532 nm hindered any meaningful assessment of the Raman shift and width dependence on temperature, however, it also provided further insight into the fluorescence tendencies.

Figure 7-18 shows the comparison of room temperature spectra of fluorescent amino acids at 532 nm excitation and measurements at $-100\text{ }^{\circ}\text{C}$ and $-196\text{ }^{\circ}\text{C}$. A significant rise in the fluorescence noise is visible in the spectra of all 4 fluorescent amino acids at low temperatures and the corresponding SNR change is shown in Figure 7-19.

As opposed to the mildly fluorescent background noise in the spectra of Tryptophan at 785 nm, the Raman signature of Tryptophan is barely visible at 532 nm excitation due to the severe fluorescence noise. As shown in Figure 7-18, only a few major bands of Tryptophan are resolvable at room temperature and the fluorescence rise at lower temperatures almost entirely overshadows all signs of the Raman signature. Only very faint signs of the two major bands of Tryptophan nominally at 754 cm^{-1} and 1008 cm^{-1} remain at $-100\text{ }^{\circ}\text{C}$ and $-196\text{ }^{\circ}\text{C}$. Naturally, this is reflected in a significant drop in the SNR as shown in Figure 7-19. While Tryptophan could still be identifiable at 532 nm despite the strong fluorescence background at room temperature, identification would not be possible at extreme low temperatures. A similar trend was also observed in the spectra of Glutamic Acid, the spectra of which also only shows a few major bands

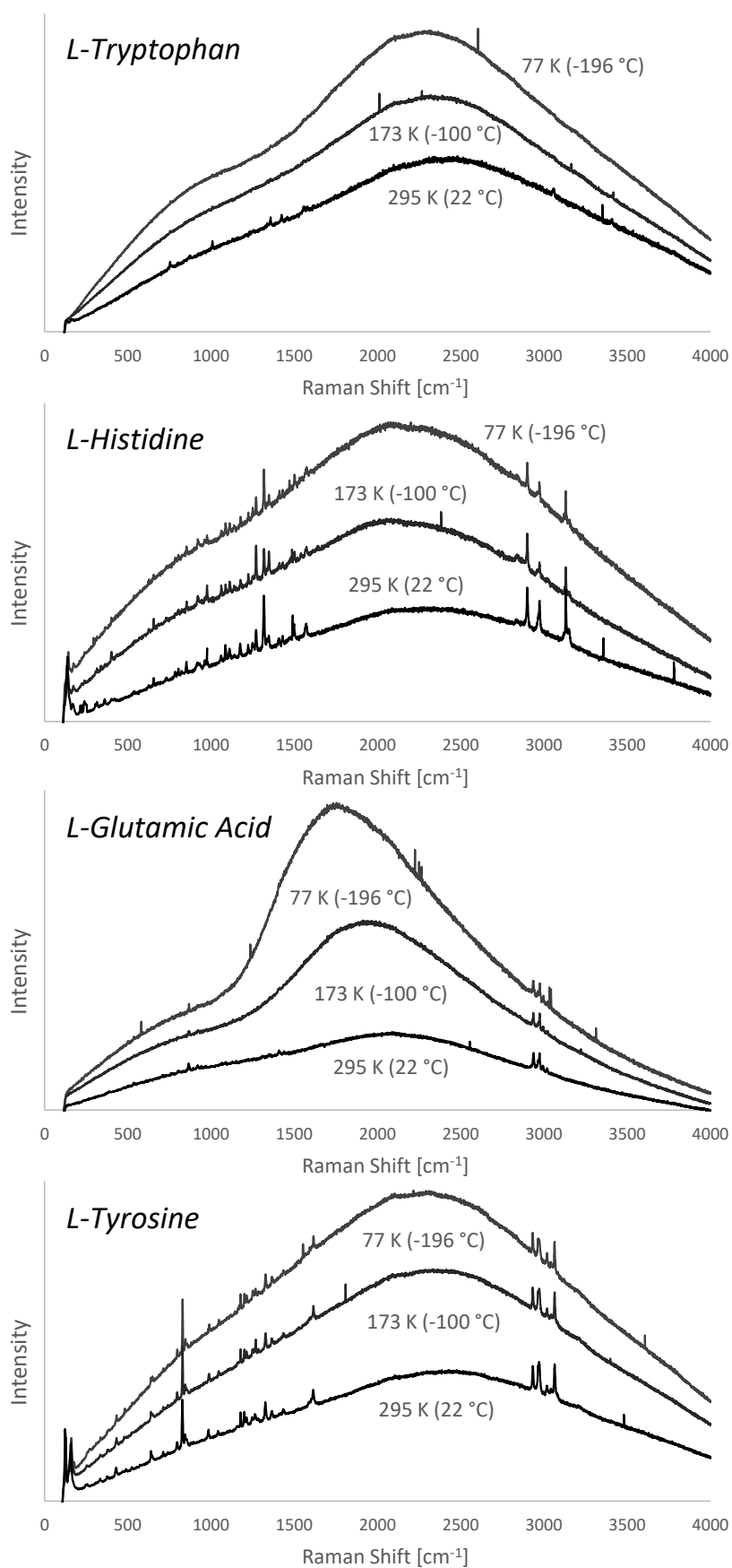


Figure 7-18 Raman spectra of amino acids fluorescent at 532 nm excitation collected at room temperature, -100 °C and -196 °C showing a visible increase in the fluorescence noise

even at room temperature at 532 nm. Interestingly, the significant rise in the fluorescence noise in the spectra of Glutamic Acid at lower temperatures was also accompanied by a notable shift to lower frequencies.

On the other hand, Histidine and Tyrosine are still fully detectable at 532 nm even despite the strong fluorescence background. However, as shown in Figure 7-18, the visible rise in the fluorescence noise at lower temperatures gradually decreases the SNR of the Raman peaks in the spectra and some bands disappear entirely in the fluorescence background.

The fluorescence increase at low temperatures is quantified in Figure 7-19, which shows the SNR change from room temperature to -100 °C and -196 °C for amino acids that are fluorescent at 532 nm and Alanine, which is not fluorescent at this excitation. As opposed to Alanine, there is a clear downwards trend in the SNR of fluorescent amino acids towards lower temperatures. The average

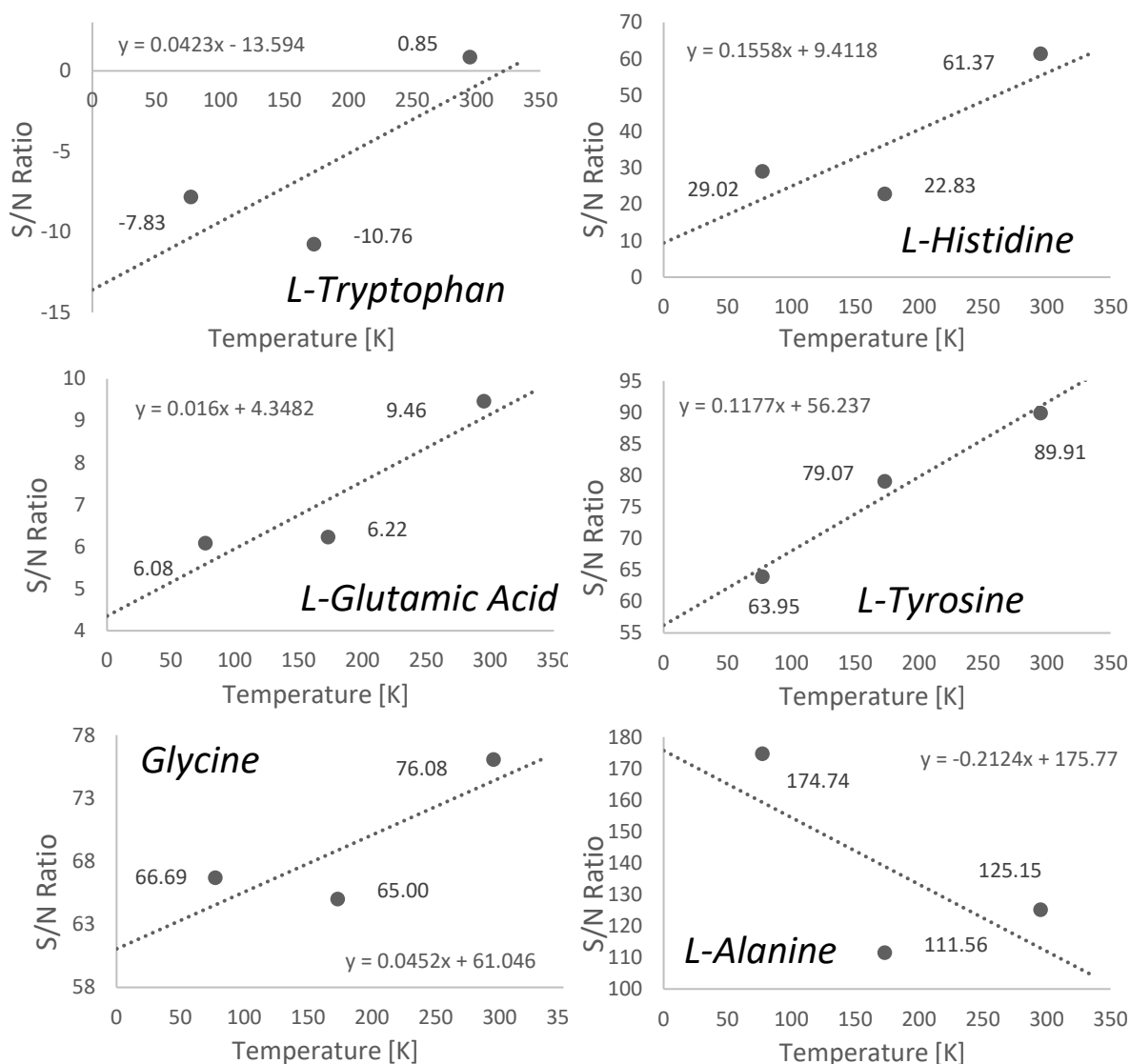


Figure 7-19 Comparison of the SNR change across varying temperatures for amino acids that are fluorescent at 532 nm and Alanine, which is not fluorescent at this excitation

SNR decrease among all examined amino acids that are fluorescent at 532 nm between room temperature and -196 °C was 34.25% with the lowest being 12.33% in the spectra of Glycine and the highest 52.71% in the spectra of Histidine.

While an overall SNR decrease at low temperatures is evident from the results in Figure 7-19, it is also important to note that the decrease does not appear to be linear. For all fluorescent amino acids except for Tyrosine and Glutamic Acid, the SNR at -100 °C was lower than at -196 °C and the SNR of the Glutamic Acid spectra at -100 °C is only marginally higher than the -196 °C value. This may be the result of an experimental error associated with the variation in the data or the selection of the noise reference point for the SNR calculation. However, the presence of this trend in the spectra of four different amino acids collected on different days indicates that this is most probably not an error or variance in the data but an actual phenomenon in the fluorescence behaviour at varying temperatures. A possible explanation of this trend would be a Raman signal increase at low temperatures that contradicts the fluorescence rise. As discussed previously, the change in Raman signal intensity at low temperatures is specific to each molecule and each Raman band, which also explains why this trend was not observed in the spectra of Tyrosine and Glutamic Acid. Additionally, Figure 7-19, also shows that the SNR of Alanine, which is not fluorescent at 532 nm, increases at cryogenic temperatures. It is thus possible that this signal increase counter balances the fluorescence noise increase in the spectra of some molecules.

7.1.6 Overview & Discussion

The results of this study show common trends in the spectral changes of the analysed amino acids induced by exposure to extreme low temperatures. These include the shifting of Raman bands to higher frequencies, Raman band narrowing and decreasing variance between individual measurements. Other changes observed, such as the emergence or diminishing of Raman bands, shifting of Raman bands towards lower frequencies, increased levels of fluorescence or changes in the signal intensity, were found to be specific to a particular molecule.

The most dominant Raman shift change among all amino acids was a shift to higher frequencies at lower temperatures. This shift is caused by the strengthening of the molecular bonds at these lower temperatures making the bond more rigid and thus causing it to vibrate at a higher frequency. The profile of this change was similar across most Raman bands in all amino acid spectra and it can be characterized approximately by a 3rd order polynomial curve. While no measurements were taken at temperatures below 77.15 K, it is reasonable to assume that the curve would converge to a flat line towards 0 K due to the restricted molecule vibrations at these

temperatures. This is visualized in Figure 7-20 (a), which displays the Raman shift and width at temperatures down to 0 K predicted based on the collected experimental data for Glycine.

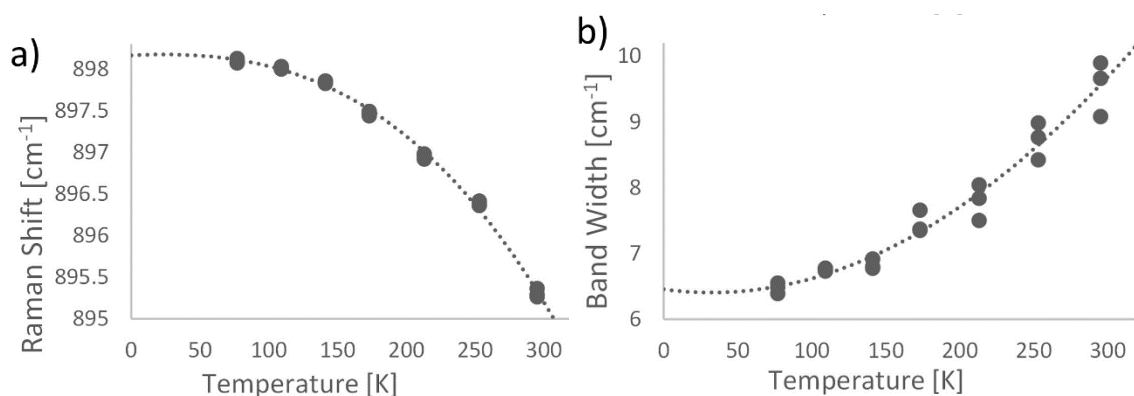


Figure 7-20 (a) The profile of the Raman shift change of Glycine band 895 cm^{-1} as a function of temperature and (b) the profile of the Raman band width change of Glycine 1331 cm^{-1} band as a function of temperature. A theoretical prediction corresponding to the general trend characterized by a 3rd order polynomial relationship for temperatures approaching 0 K is highlighted [310]

With the exception of Glycine, the spectra of all measured amino acids also contained bands that shifted to lower frequencies, indicating a relaxation of the molecular bond at lower temperatures. Additionally, some bands in the spectra of Alanine, Histidine and Tryptophan also initially shifted to lower frequencies at $-100 \text{ }^{\circ}\text{C}$ and then higher frequencies at $-196 \text{ }^{\circ}\text{C}$. This indicates a structural change occurring within the molecule and its bonds between these temperatures. It also suggests that Raman spectroscopy at extreme low temperatures can be a very useful tool for material characterisation as it could help diagnose the changes within the molecules as a function of temperature. This could be useful not only for life detection on Europa but also the exploration of Europa in general as well as for a wide spectrum of applications on Earth as it could provide more information about the sampled material and associated environmental or geological processes.

Among all analysed amino acids, Glycine displayed the most significant Raman shift changes from room temperature down to $-196 \text{ }^{\circ}\text{C}$, closely followed by Alanine. Histidine and Tryptophan showed relatively minor changes in the Raman band shift between the two temperatures and the Tryptophan spectra were the least impacted by the extreme low temperature at $-196 \text{ }^{\circ}\text{C}$ in terms of Raman band shift changes.

Across all the amino acids examined in this study, the largest Raman band shift change that was observed when comparing spectra at room temperature to those at $-196 \text{ }^{\circ}\text{C}$, was 24.97 cm^{-1} and the smallest was 0.35 cm^{-1} . While these changes are molecule specific and other amino acids could exhibit larger or smaller changes, the range of 0.35 cm^{-1} to 24.97 cm^{-1} could serve as a

general guideline of the foreseeable Raman band shift within the spectra of amino acids representing biosignatures for the search for life as collected on Europa at extreme low temperatures. Especially at the higher end of this range, this could be a major spectral change compared to the spectra obtained at Earth-like conditions and could severely impact the detectability and the analysis of the Raman spectra from samples collected on Europa or other Icy Worlds.

Nevertheless, across the examined amino acids, most Raman bands except for a few notable exceptions showed relative stability over the measured temperature range. While this may be molecule specific and other molecules relevant to astrobiology need to be examined at extreme low temperatures to make any definitive conclusions, this would indicate that databases of Raman spectra collected at higher terrestrial temperatures can still be useful for the identification of molecular species in the spectra collected at extreme low temperatures analogous to Europa or Enceladus.

A common trend was observed in the thermally induced shifts of the vibrational modes among all the examined amino acids. Raman bands that shifted to higher frequencies at lower temperatures the most were all assigned at least partially to the outer parts of the molecule such as its side chains or outer atoms or bending involving the main chain of the molecule or a significant part of the molecular main chain. For molecules with a ring in its structure, in plane bending within the ring also seems to generate a significant upwards frequency shift at low temperatures compared to the shift of bands associated with other types of vibrations. The actual shift is molecule dependant and dictated by the relative shift change at low temperatures across all Raman bands within the spectra and as such, it is impossible to determine a threshold for these vibrational modes. For Tryptophan, bands associated with these vibrations shifted to higher frequencies by more than 1.77 cm^{-1} , for Histidine 3.5 cm^{-1} , Alanine 1.6 cm^{-1} and Glycine 2.6 cm^{-1} .

Similarly, all bands among all examined amino acids that displayed relatively small upwards change in the Raman shift at low temperatures compared to other bands within the spectra or that shifted to lower frequencies were all assigned to stretching vibrational modes (including ring breathing and in plane deformation for molecules with a ring in their structure), vibrations involving inner atoms of the molecules or out of plane deformation of a ring. While a threshold is impossible to determine, these types of vibrations were associated with all bands that shifted to higher frequencies by less than 0.83 cm^{-1} in the spectra of Tryptophan, 0.55 cm^{-1} in Histidine, 1.42 cm^{-1} in Alanine and 2.4 cm^{-1} in Glycine. Across all examined amino acids, bands associated with stretching vibrational modes dominate among the shifts to lower frequencies and relatively small shifts to higher frequencies compared to other bands in the spectra. Across all the examined

amino acids, no band solely or predominantly assigned to a stretching vibration increased in frequency at lower temperatures by more than 2.36 cm^{-1} . For molecules with a ring in their structure, out of plane deformation of the ring also displayed relatively small or negative shifts to higher frequencies at low temperatures. None of the bands associated with out of plane deformation of the rings in the observed spectra of Tryptophan and Histidine shifted to higher frequencies by more than 1.18 cm^{-1} .

This leads to an assumption that bands associated with stretching vibrations, out of plane deformation of a ring or vibrations including inner atoms of a molecule are more likely to shift to lower frequencies at low temperatures or shift to higher frequencies by only a small amount compared to bands assigned to other vibrational modes. This may be the result of these vibrations being relatively well constrained within the structure of the molecule. On the contrary, bands that shift to a significantly higher frequency at lower temperatures are more likely to be associated with vibrations that are relatively less constrained within the molecule, that is, vibrational modes including the extremities of a molecule, such as its side chains, outer atoms and groups, or vibrations including most or all of the molecule main chain and in plane bending within a ring.

Additionally, the shifting Raman bands might also affect the spectral resolution necessary for successful detection, which has direct implications on the design of Raman instruments for life detection on Europa. The clearance between individual adjacent bands within Raman spectra of each amino acid was recorded and the minimum peak-to-peak distance for each amino acid at each measured temperature is shown in Table 7-2. The spectra of Histidine is the most complex among the measured amino acids and its spectra shows the lowest peak-to-peak distance between individual bands necessary to resolve two adjacent Raman bands. At room temperature the minimum peak-to-peak distance is 12.43 cm^{-1} , at $-100\text{ }^{\circ}\text{C}$ it is 13.91 cm^{-1} and at $-196\text{ }^{\circ}\text{C}$ it is 14.75 cm^{-1} , all within the spectra of Histidine. This suggests that the spectral resolution of a Raman instrument for the detection of biosignatures needs to be higher than these values to fully detect Histidine.

Furthermore, the spectral resolution required to successfully identify amino acids in a mixture of compounds will be higher due to interference of the bands within the spectra. On Earth amino acids occur predominantly in a mixture of various amino acids and without an instrument with an exceptional spatial resolution or employing SERS, this interference may prove to be critical for successful identification and may dictate the required spectral resolution. There are hundreds of known amino acids, however, just among the 4 amino acids presented in detail in this study at

Temperature [°C]		Glycine [cm ⁻¹]	L-Alanine [cm ⁻¹]	L-Histidine [cm ⁻¹]	L-Tryptophan [cm ⁻¹]
Minimum Peak-to-Peak Distance	22	15.99	21.09	12.43	18.75
	-100	17.06	21.53	13.91	17.41
	-196	16.76	22.35	14.75	16.60
Minimum Band Width	22	5.72	5.81	1.81	4.20
	-100	4.42	4.36	2.65	3.64
	-196	3.20	4.18	2.66	3.16

Table 7-2 Minimum peak-to-peak distance between adjacent Raman bands and Raman band width in the spectra of Glycine, Alanine, Histidine and Tryptophan at room temperature, -100 °C and -196 °C [310]

785 nm there are 8 Histidine bands that lie within 14.75 cm⁻¹ of at least 1 Glycine band, 7 of a Tryptophan band and 15 of an Alanine band at -196 °C. This includes dominant Raman bands that are important for identification and as such this spectral resolution would not be sufficient to resolve these amino acids in these mixtures. The number of potentially unresolvable bands of Glycine and Tryptophan in a mixture with Histidine with a 14.75 cm⁻¹ resolution is around half of the overall number of their fully detectable Raman bands, for Histidine and Alanine this is 68% of Alanine bands and almost 50% of Histidine bands. The number of potentially unresolvable bands in mixtures of the examined amino acids at 785 nm depending on the spectral resolution is summarised in Table 7-3 for both room temperature and -196 °C.

At -196 °C, there are 4 Histidine bands that lie within 5 cm⁻¹ of a Glycine band and that could be potentially unresolvable with spectral resolution less than 5 cm⁻¹. This is 24% of Raman bands within Glycine spectra and 12% within Histidine spectra. While most of these bands are not particularly important for the identification of Histidine, it includes the Histidine 1117 cm⁻¹ band which is a relatively dominant band and can be used for the identification of Histidine. This band lies merely 2.74 cm⁻¹ from an adjacent Glycine band and it is also the narrowest Raman band among all the examined amino acids at -196 °C. With a width of only 2.66 cm⁻¹, it could entirely disappear within the considerably wider 1120 cm⁻¹ Glycine band (7.74 cm⁻¹ width). It is also important to note that the detection of the extremely narrow 1117 cm⁻¹ band (1116 cm⁻¹ at room temperature) may be even more problematic at room temperature. While it is broader at -196 °C (3.99 cm⁻¹), it is also only 0.48 cm⁻¹ from the 1117 cm⁻¹ Alanine band which is also considerably wider and would most certainly prevent its detection. Furthermore, the most dominant Histidine band at 1324 cm⁻¹ is within 8.1 cm⁻¹ of one of the two most dominant Glycine bands (1332 cm⁻¹). Both these bands are relatively wide and while the peak-to-valley ratio cannot be determined as it depends on the relative concentration and intensity, it is likely that a resolution of at least 3-4 cm⁻¹ will be necessary to fully resolve these two bands at -196 °C. As both of these bands are

critical for the identification of Glycine and Histidine, the minimum spectral resolution for full identification is dictated by the proximity of these bands. Furthermore, a resolution of at least 2.74 cm^{-1} may be required to fully resolve the narrow Histidine 1117 cm^{-1} band.

Room Temperature								
Amino acid(s) in a mixture with Histidine	Peak-to-peak distance [cm^{-1}]						Suggested minimum spectral resolution necessary [cm^{-1}]	Suggested ideal spectral resolution [cm^{-1}]
	12.43	10	7	5	4	2		
	Number of peaks							
Glycine	8	7	6	5	4	3	<4.23	<2.8
Alanine	12	9	7	6	6	6	<2.64	<1.51
Tryptophan	8	6	4	2	1	1	<7	<4.5
Glycine Alanine Tryptophan	19	17	13	11	10	10	<2	<1.51
-196 °C								
Amino acid(s) in a mixture with Histidine	Peak-to-peak distance [cm^{-1}]						Suggested minimum spectral resolution necessary [cm^{-1}]	Suggested ideal spectral resolution [cm^{-1}]
	14.75	10	7	5	4	3		
	Number of peaks							
Glycine	8	7	6	4	4	4	<4	<2.74
Alanine	15	13	10	8	7	6	<2.02	<1.92
Tryptophan	7	6	5	3	1	1	<7	<5
Glycine Alanine Tryptophan	21	21	16	13	11	11	<2.02	<1.92

Table 7-3 The number of adjacent bands within potential mixtures of Glycine, Alanine, Histidine and Tryptophan with a suggested minimum spectral resolution necessary for full identification of these amino acids at room temperature and at -196 °C [310]

The detection of a mixture of Alanine and Histidine may be even more restricted in terms of spectral resolution. At -196 °C , one of the most dominant bands in the spectra of Alanine (1315 cm^{-1}) lies within 9.39 cm^{-1} of the Histidine band 1324 cm^{-1} . Both are dominant and wide bands that could merge and become unresolvable if a resolution greater than 9.39 cm^{-1} is not available, which would be critical for the identification of both Alanine and Histidine. Additionally, Alanine bands at 400 cm^{-1} and 533 cm^{-1} , which are also dominant Alanine bands and important for its identification, are within 2.67 cm^{-1} and 7.23 cm^{-1} of an adjacent Histidine band, respectively. Most importantly, one of the two most important Alanine bands at 855 cm^{-1} lies within only 2.02 cm^{-1} of a Histidine 857 cm^{-1} band. There are 6 Histidine bands within 3 cm^{-1} of an Alanine

band including at least 3 that are important for the identification of Histidine (657 cm^{-1} , 857 cm^{-1} and 926 cm^{-1}). These 6 potentially unresolvable bands represent 18% and 27% of all detectable Raman bands of Histidine and Alanine respectively. Out of these Histidine 6 bands, 3 lie within 2 cm^{-1} of one another and 1 band within 1 cm^{-1} , however, this band is not a particularly important marker in either spectra. A spectral resolution of $<2.02\text{ cm}^{-1}$ may be able to resolve all except for 3 Histidine bands with only 2 bands being potentially important for identification. In this case the majority of the bands could be resolvable and used for confirmation. Nevertheless, a resolution better than 1.92 cm^{-1} may be necessary for full and unambiguous identification.

On the contrary, the resolution of the mixture of Histidine and Tryptophan does not seem to require a very high spectral resolution in comparison to the mixtures of other amino acids. There are 6 potentially unresolvable Histidine bands within 10 cm^{-1} of a Tryptophan band at $-196\text{ }^{\circ}\text{C}$ and none of these Histidine bands are essential for its identification. However, the 6 potentially unresolvable bands represent 18% of all Histidine bands detectable at $-196\text{ }^{\circ}\text{C}$ and 35% of Tryptophan bands. As such it may be desirable to employ a higher spectral resolution than 10 cm^{-1} . The only Tryptophan band that may be important for its identification and that lies within close proximity to a Histidine band is the 1365 cm^{-1} band located 11.24 cm^{-1} from the 1354 cm^{-1} Histidine band. While the Histidine 1354 cm^{-1} band is a relatively minor peak, both bands are also relatively wide and depending on the relative concentration of these two amino acids, a higher resolution may be necessary to resolve them. While the required resolution is impossible to determine exactly as it depends on the relative concentration and peak intensity, a resolution of 5 cm^{-1} should be capable of resolving these two bands in most cases and could also resolve all except for 3 other non-essential bands of Histidine and Tryptophan. A spectral resolution of 7 cm^{-1} may also be sufficient with only 5 non-essential bands potentially unresolvable (which constitutes 29% of Tryptophan bands and 15% of Histidine bands).

For a mixture of all 4 amino acids, even a relatively high spectral resolution of 3 cm^{-1} would not be enough to resolve 11 Histidine bands including a number of bands important for the identification of the 4 amino acids. A spectral resolution of $<2\text{ cm}^{-1}$ would not be able to resolve only 6 Histidine bands (18%), however, this includes 2 bands potentially important for its identification. Similar to the resolution required for the identification of the mixture of Alanine and Histidine, a resolution better than 1.92 cm^{-1} could be sufficient to resolve all but 4 bands with only 1 being potentially important.

In comparison, SHERLOC, a miniaturized Raman Instrument developed for in-situ exploration of Mars that was launched on the Mars 2020 mission on the Perseverance rover, has a spectral resolution of 49 cm^{-1} [118], [332]. As shown in the data in Table 7-2, it is important to note that

the spectral resolution required based on the clearance between individual bands does not necessarily increase with decreasing temperature as some bands can shift further away from adjacent bands. This is also reflected in Table 7-3 which shows that while some peaks in a mixture of amino acids may shift closer and the number of potentially unresolvable bands at a certain resolution may thus increase at -196 °C compared to room temperature, a higher spectral resolution may not be required. On the contrary, a lower spectral resolution may be sufficient in some cases as some bands may not be essential for the identification of the amino acids and some dominant bands important for identification may shift further apart from possible interferants at extreme low temperatures.

Another effect observed in the spectra that could severely impact the effectiveness of Raman spectroscopy for life detection on Europa is Raman band narrowing at extreme low temperatures. Except for some discrepancies in the spectra of Tryptophan, likely caused by the presence of fluorescence in the spectra, all Raman bands within all amino acid spectra obtained in this study showed a decreasing Raman band width with decreasing temperature. This is caused by the damping of the scattered light in the extreme cold environment. As shown in Figure 7-20 (b), similarly to the Raman shift change, this relationship could also be described by a 3rd order polynomial curve that would eventually converge to a flat line towards 0 K.

Table 7-2 shows the narrowest band width that was measured for spectra of the amino acids presented in detail in this study at the temperatures 22 °C, -100 °C and -196 °C. Between 22 °C and -196 °C the most significant change in the Raman band width was a decrease of 24.67 cm⁻¹ which is 80.1% of the nominal room temperature width and was recorded in the spectra of Glycine. The minimum band width change was 0.87 cm⁻¹ (12.7%) or 4.4% in percentage (1.03 cm⁻¹) detected in the spectra of Tryptophan and Histidine respectively. Similar to the Raman shift change, this is specific to a particular molecule and a molecular bond. However, the data suggests that at temperatures analogous to Europa, amino acid Raman bands could narrow by as much as 80.1%. This represents a significant spectral change and could greatly affect the detectability of some molecules at extreme low temperatures analogous to Europa and the analysis of spectra obtained at these conditions. The narrower Raman bands might prove problematic for detection as a higher spectral resolution is needed. This is a particular concern for Raman spectroscopy for Europa and other extraterrestrial applications. Miniaturized Raman instruments tend to have a lower spectral resolution as a result of the mass and size trade off that is necessary in order to comply with the strict design constraints for extraterrestrial exploration.

The spectral resolution for an instrument aiming to fully detect Glycine, Alanine, Histidine or Tryptophan will need to be better than the values recorded in Table 7-2 and Table 7-3. For a

Raman instrument operating on Europa at $-196\text{ }^{\circ}\text{C}$ and aiming to detect Histidine, which is an important biosignature for the detection of extraterrestrial life, the minimum spectral resolution could be as high as 2.02 cm^{-1} , which could be a challenge for miniaturized Raman instruments. There are currently two Raman instruments for planetary exploration that have been launched to date, SHERLOC and SuperCam (both launched on the Mars 2020 Mission)[48]. As already discussed above, SHERLOC's deep UV excitation design is limited to the spectral resolution of 49 cm^{-1} and SuperCam has a spectral resolution of 12 cm^{-1} [48], [118]. Based on data collected in this study and as summarized in Table 7-2 and Table 7-3, this will not be sufficient to fully resolve the spectra of Glycine, Alanine, Histidine and Tryptophan and might be particularly problematic for the detection of Histidine. While concepts and prototypes of miniaturized instruments for planetary exploration with a better spectral resolution exist, none have space heritage to date and most do not meet the spectral resolution outlined in this study, particularly for the detection of amino acids in mixtures [90], [125], [333]–[335].

At the same time, as evident in the spectra obtained and shown in Figure 7-1, Figure 7-5, Figure 7-9 and Figure 7-13, the narrower bands might allow easier resolution of individual Raman bands at lower temperatures. Adversely, this could lead to a lower spectral resolution requirement for Raman instruments operating at extreme low temperatures. The narrower Raman bands at extreme low temperatures also offer higher precision measurements, which might be particularly useful in a mixture of compounds and for studies of material properties. Such an advantage might be beneficial for a much wider range of applications than extraterrestrial exploration and the detection of biosignatures on Europa.

The higher precision of Raman measurements at extreme low temperatures is also supported by the Raman shift and width variance data. All amino acids analysed as a part of this research show a decrease in the average variance of the spectra between individual measurements at extreme low temperatures. This could be assigned to the molecular bonding and vibrations being more constrained at lower temperatures. The variance dependence on temperature appears linear for the Raman shift data and drops from the highest room temperature average variance of 0.157% (Glycine) to the highest average variance of 0.066% (Tryptophan) at $-196\text{ }^{\circ}\text{C}$. While the Raman band width variance decrease towards lower temperatures proved to be less consistent than the Raman shift variance, a decreasing trend was observed in the spectra of all amino acids. The highest band width variance at room temperature across all amino acids was 17.7% (Tryptophan) and the highest variance at $-196\text{ }^{\circ}\text{C}$ was 16% (Tryptophan). The discrepancies in the band width variance data are attributed to the dependence of Raman band width readings on changes within molecular bonds and other material or environmental disturbances such as the presence of a fluorescent background.

Chapter 7

The decreasing variance at extreme low temperatures leads to higher precision Raman measurements, which could be beneficial for a mission to Europa where the sampled material is of unknown composition and might contain a variety of compounds with interfering Raman spectra. As mentioned above, other applications could also benefit from the higher definition offered by low temperature Raman spectroscopy.

The emergence of new Raman bands at low temperatures was recorded in the spectra of Glycine, Alanine and Histidine either due to enhanced definition as a result of narrower and higher intensity Raman bands or due to the shifting of Raman bands to higher or lower frequencies and splitting from an adjacent band. These additional data points only resolvable at extreme low temperatures could allow a more complete analysis of the studied material and provide more information about its composition and material properties. However, in some cases it could also increase the spectral resolution requirement. Particularly, two new bands previously undetectable at room temperature appear at $-100\text{ }^{\circ}\text{C}$ in the region between 300 cm^{-1} to 440 cm^{-1} in the spectra of Histidine. This results in 5 Raman bands closely packed in this region at extreme low temperatures rather than 3 at room temperature possibly causing discrepancies in Raman shift readings as the bands blend together in the spectra if the spectral resolution is insufficient. As mentioned above, this higher spectral resolution requirement might be challenging for miniaturized Raman instruments for in-situ space exploration and it may result in limited data output.

The diminishing of Raman bands at lower temperatures was also recorded in the spectra of Histidine and Alanine. This was mostly due to loss of intensity at lower temperatures as well as the Raman bands shifting towards adjacent bands and blending together. While the emerging peaks resulted in relatively minor changes in the spectra of the examined amino acids, in general the emergence and diminishing of Raman bands at extreme low temperatures could deem Raman spectra obtained on Earth and at room temperatures unrepresentative of the spectra potentially obtained on Europa or other Icy Worlds.

Significant changes in the signal intensity occurred in the spectra of all examined amino acids. However, the changes are specific to individual Raman bands rather than a uniform change across the entire spectrum. Overall, all fully detectable Glycine bands increased in intensity at $-196\text{ }^{\circ}\text{C}$ compared to that at $22\text{ }^{\circ}\text{C}$ and the overall trend in intensity change across Histidine bands also suggests an intensity increase at extreme low temperatures. On the contrary, the signal intensity of all the fully detectable Alanine Raman bands at 785 nm decreased at extreme low temperatures and there was an equal distribution of bands with increasing and decreasing intensity in the spectra of Tryptophan.

Across the examined amino acids the maximum signal increase observed between room temperature and $-196\text{ }^{\circ}\text{C}$ was 37% and the maximum decrease was 67.8%. While this could be specific to the Raman bands and spectra of the amino acids examined in this study, it could provide a general indication that the intensity of individual Raman bands at $-196\text{ }^{\circ}\text{C}$ on Europa could be as high as a 37% decrease or 67.8% increase. While the signal intensity data can be easily affected by experimental disturbances and may not be conclusive, the data collected also suggests that there is no clear common pattern in intensity changes induced by extreme low temperatures in the spectra of the examined amino acids.

A potentially detrimental effect for the detection of biosignatures on Europa observed at extreme low temperatures is the increase in the fluorescence background. This effect was only observed in the spectra of Tryptophan at 785 nm excitation and Glycine, Tryptophan, Histidine, Glutamic Acid and Tyrosine at 532 nm. While this only applies to molecules which fluoresce at room temperature at a certain excitation, most biosignatures fluoresce at excitations commonly used in Raman spectroscopy such as 532 nm and 633 nm. While most traditional biosignatures such as amino acids and nucleobases can be detected using 785 nm excitation without any fluorescent background in the spectra, there are exceptions such as Tryptophan and Adenine that do fluoresce mildly at this excitation. Other important biomarkers for astrobiology could also fluoresce at 785 nm excitation and the increase in fluorescence could greatly affect their detectability.

As shown in the S/N ratio analysis in Figure 7-14, the recorded rise in fluorescent background at decreasing temperature in the Tryptophan spectra at 785 nm appears linear with a 0.2786 K^{-1} rate of change. A similar linear decrease is also observed in the spectra of Tyrosine obtained at 532 nm shown in Figure 7-19. However, other amino acids fluorescent at 532 nm show a SNR decrease at this excitation that does not appear linear and suggests that a signal increase at extreme low temperatures may, to a certain extent, counter balance the fluorescence noise increase. While the SNR decrease from room temperature to $-196\text{ }^{\circ}\text{C}$ varied between approximately 12-52% among the examined amino acids, the average SNR decrease of 34.25% is a relatively good representation of the general trend. This rise in fluorescence can be assigned to the reduction of radiationless decay and extra energy heat loss due to collisions, as the lower temperatures impede the movement of molecules decreasing the transitional energy and thus reducing the number of collisions.

The rise in the fluorescent background could be particularly problematic for a mixture of compounds including fluorescing molecules which could then overshadow the spectra of other molecules in the mixture. Without prior sample manipulation, a sample collected on Europa

would inherently contain a mixture of compounds, some of which may be fluorescent. A successful detection of target molecules might thus require additional procedures or instrument design modifications, such as time-gating or the application of multiple excitation wavelengths, SERS and fluorescence reduction computational methods, in order to reduce the effects of the fluorescent background.

7.2 Porphyrins

As discussed in Section 6.2, both hemin and protoporphyrin IX are extremely photosensitive molecules. No meaningful investigation of cryogenically induced changes in the Raman spectra of hemin and protoporphyrin IX was possible at 785 nm excitation due to the high fluorescence noise and low signal strength most probably caused by photodamage. Investigations of porphyrins at 532 nm excitation benefit from lower fluorescence noise and the results are described below. Please note that these results have been published in the Analytical Methods journal prior to the completion of this thesis and the reference is provided here [311].

As shown in Figure 6-10, both hemin and protoporphyrin are barely detectable in the Raman spectra collected at room temperature, even at the optimal laser power setting. However, Raman spectra obtained at the same laser power at cryogenic temperatures shown in Figure 7-21 demonstrate a substantial improvement in the spectral definition and signal strength at these extremely low temperatures.

As shown in Figure 7-21, a remarkable signal enhancement can be observed in the Raman spectra of hemin obtained at -196 °C compared to the spectra obtained at room temperature. Some bands that are not observable at all at room temperature, namely 983 cm⁻¹, 1220 cm⁻¹, 1339 cm⁻¹, 1431 cm⁻¹ and 1555 cm⁻¹, become more visible at -100 °C and then clearly resolvable at -196 °C.

Additionally, strong Raman bands at 1303 cm⁻¹ and 1528 cm⁻¹ that appear remarkably well defined at -196 °C are not visible at all at 22 °C nor -100 °C.

While the enhancement of the spectra is not as dramatic as in the spectra of hemin, as shown in Figure 7-21, the spectra of protoporphyrin also shows a significant signal increase and much higher spectral definition at cryogenic temperatures. Previously unresolvable bands at 1163 cm⁻¹ and 1382 cm⁻¹ become distinguishable at -100 °C and occurrence of a minor band at 1418 cm⁻¹ in the spectra at -196 °C was also recorded.

It is important to note that all Raman bands displayed in the spectra of both porphyrins in Figure 7-21 at all temperature settings are associated with normal modes as external vibrational modes associated with low-energy phonons do not appear in the spectral region evaluated in this study.

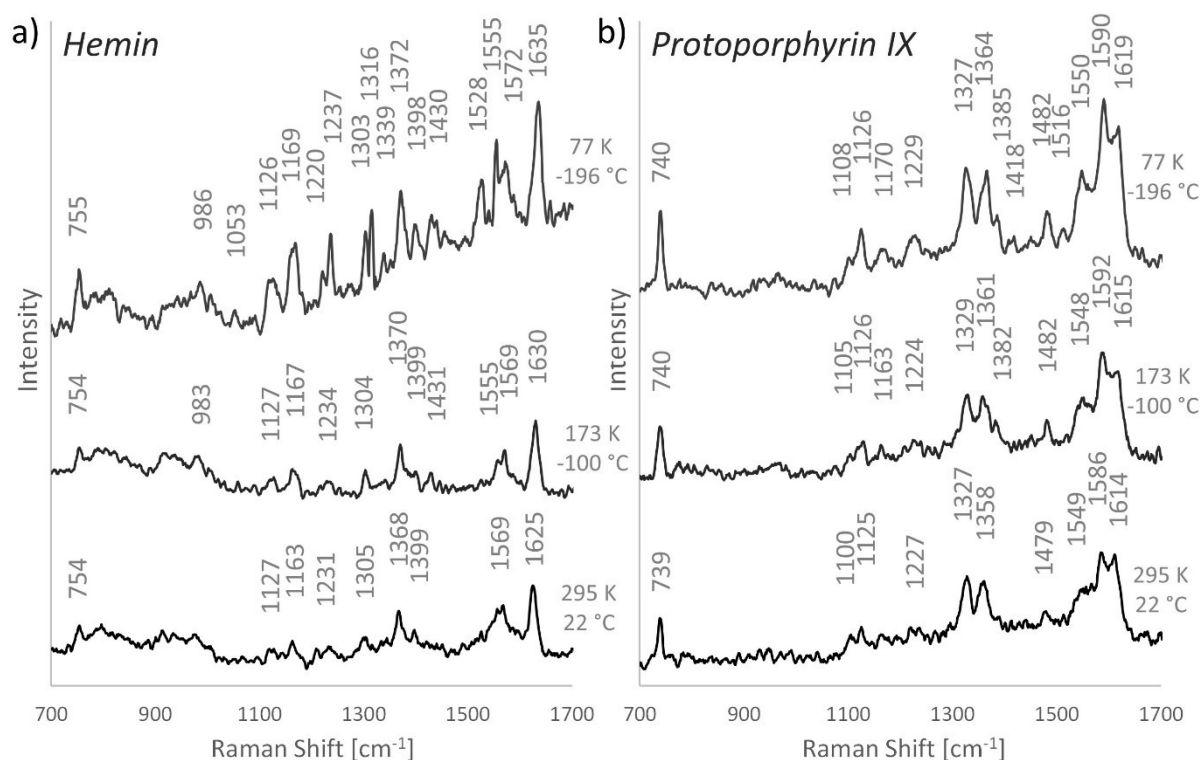


Figure 7-21 The comparison of hemin (a) and protoporphyrin IX (b) Raman spectra at cryogenic temperatures (-100 °C and -196 °C) and room temperature using 532 nm excitation and the same laser power density of 9.77 kW/cm² for hemin and 195 W/cm² for protoporphyrin [311]

As shown in Figure 7-21, the signal strength enhancement at low temperatures was accompanied by changes in the Raman band frequency. At -100 °C, frequency changes from 0.32 cm⁻¹ up to 4.71 cm⁻¹ compared to room temperature measurements were recorded in the spectra of hemin and between 0.54 cm⁻¹ and 6.28 cm⁻¹ in the spectra of protoporphyrin. At -196 °C, changes from 0.61 cm⁻¹ up to 11.26 cm⁻¹ compared to room temperature measurements were observed in the spectra of hemin and between 0.23 cm⁻¹ and 7.32 cm⁻¹ in the spectra of protoporphyrin.

Similar to the changes observed in the spectra of previously discussed target molecules, the frequency of porphyrin Raman bands shifted to both higher and lower frequencies at cryogenic temperatures. While frequency shifts to higher frequencies at low temperatures are expected due to higher frequency of molecular vibrations caused by the increased rigidity of molecular bonds at these temperatures, shifts to lower frequencies could be associated with specific molecular bonds as discussed in Section 7.1. The analysis of amino acid vibrational modes and the changes at cryogenic temperatures revealed that some vibrational modes, such as stretching modes, are more likely to shift to lower frequencies.

The assignments of each Raman band observed in the spectra of both porphyrins are provided in Table 7-4 with the molecular structure displayed in Figure 7-22. It is important to note that unlike the previously presented amino acid data, the low quality of the spectra of both porphyrins at room temperature may have lacked the necessary definition to accurately determine the Raman band frequency. As such, the vibrational mode assignment analysis may not be as accurate.

The majority of new bands that only became distinguishable in the spectra at cryogenic temperatures were associated with vibrational modes including the vibrations of CH₃ and CH₂ groups, particularly bending modes (rocking, wagging, scissoring or twisting). Additionally, Raman bands that shifted to higher frequencies by the largest amount were predominantly associated with vibrations in the outside chains and groups of the molecule. On the other hand, bands that shifted to lower frequencies or stayed relatively stable over the temperature range were at least

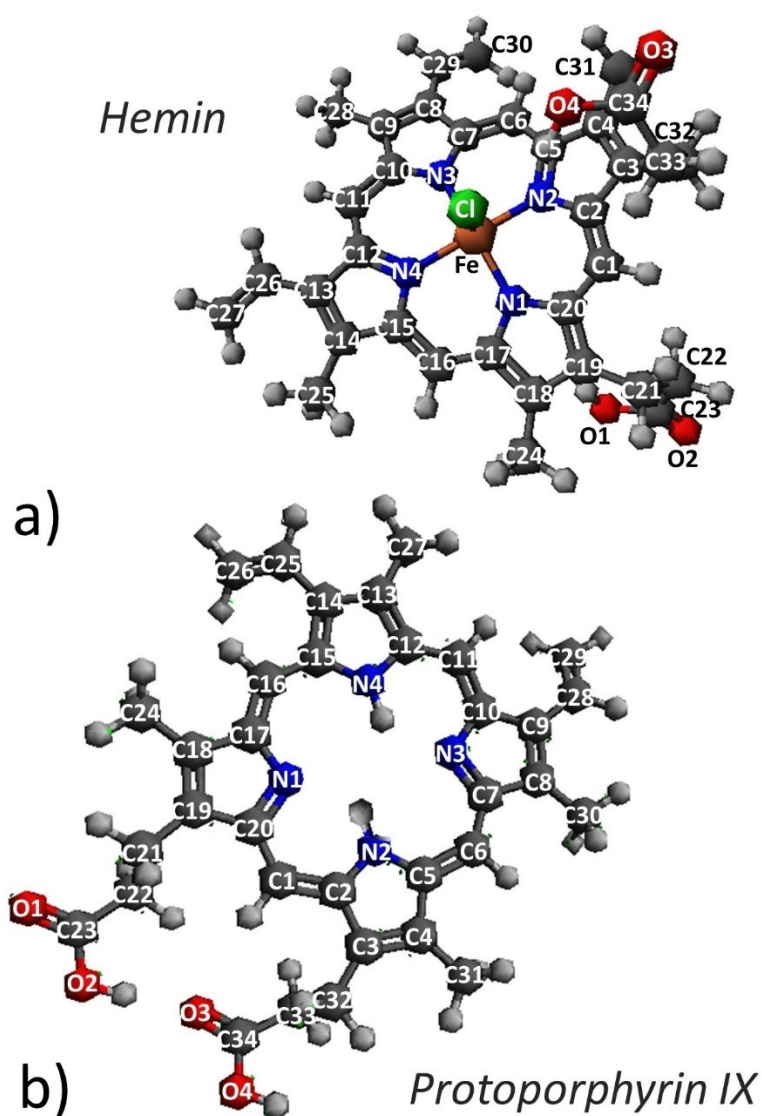


Figure 7-22 Molecular structure of hemin (a) and protoporphyrin IX (b) [311]

Protoporphyrin IX				Hemin			
Raman Band Frequency (cm ⁻¹)			Assignment	Raman Band Frequency (cm ⁻¹)			Assignment
RT	173 K	77 K		RT	173 K	77 K	
739	740	740	C1-C20=N1-C17=C16 symmetrical stretch, C32-C33-C34 scissoring/rock	754	754	755	CH (1) rock, CH ₂ (21) rock, OH (1) rock
1100	1105	1108	CH + CH ₂ + CH ₃ rock		983	986	CH ₂ (27) rock, CH ₂ (30) twist, CH ₃ (25, 28) rock, CH (29, 26) rock
1125	1126	1126	ring asymmetric stretching, CH + CH ₂ + CH ₃ rock			1053	CH ₃ + CH ₂ + CH rock
	1163	1170	CH + CH ₂ + CH ₃ rock, ring asymmetric stretching	1127	1127	1126	N1 ring asymmetric stretch, CH ₃ wag (24, 25), CH (1, 16) rock
1227	1224	1229	CH ₂ (32) rock, CH ₂ (33) wag, CH rock	1163	1167	1169	CH ₂ (21) twist H-O1-C23 scissoring, CH ₂ (22) wag
1327	1329	1327	CH ₃ (30, 31) wag			1220	CH rock, ring asymmetric stretching (N1, N3, N4)
1358	1361	1364	CH + CH ₂ + CH ₃ rock	1231	1234	1237	CH ₂ (30) rock, CH rock
	1382	1385	CH ₂ (21, 22) rock, CH ₃ scissoring	1305	1304	1303	ring asymmetric stretching, CH + CH ₂ + CH ₃ rock
		1418	ring asymmetric stretching			1316	CH rock, CH ₃ wag, CH ₂ wag
1479	1482	1482	N4 ring asymmetric stretching, CH ₂ (26) scissoring, CH ₃ (27) twist			1339	CH ₃ (24) wag
		1516	C9=C8 stretching, C28=C29 stretching, CH ₂ (29) scissoring, CH ₃ (30) scissoring	1368	1370	1372	CH ₃ wag, CH ₂ wag/scissoring, ring asymmetric stretching (N1, N2)
1549	1548	1550	C18=C19 stretching, C5=C6 stretching, C12-C11 stretching	1399	1399	1398	CH ₃ wag, CH ₂ scissoring, ring asymmetric stretching (N3, N4)
1586	1592	1590	C28=C29 stretching, CH ₂ (29) scissoring, C9=C8 stretching		1431	1430	ring asymmetric stretching (N3, N4), CH ₃ twist, CH ₂ (27) scissoring
1614	1615	1619	C26=C25 stretching, CH ₂ (26) scissoring, C14-C13=C12 symmetrical stretching			1528	C13=C14 + C8=C9 stretching, CH ₃ twist, CH ₂ scissoring

	1555	1555	ring asymmetric stretching (N1, N3, N4), CH ₃ (24, 25, 28) twist, CH ₂ (30) scissoring
1569	1569	1572	C27=C26 stretch, CH (27) scissoring, CH (26) rock, C15=C16 scissoring
1625	1630	1635	C29=C30 stretch, CH ₂ (30) scissoring, CH (29) rock, CH rock, ring asymmetric stretching

Table 7-4 Raman band assignments for hemin and protoporphyrin IX based on DFT calculation using SVP and polarizability functions for the calculation of Raman vibrational frequencies and Raman activity [311]

partially assigned to ring stretching modes and other stretching modes within the molecule's main structure.

Notably, the previously described increase in the fluorescence noise that appears to occur consistently in the spectra of all fluorescent target molecules at low temperatures, was not observed in the spectra of porphyrins. This is most probably the result of the signal increase observed at these temperatures, which may have counter balanced the fluorescence noise increase. A similar effect was also observed in the spectra of carotenoids as discussed in Section 7.3.

Based on experimental evidence, this enhanced definition and signal strength can be assigned to the reduction in the photothermal damage. As already discussed in Section 6.2, two separate types of photodegradation contribute to the laser damage observed in the Raman spectra of photosensitive samples, photochemical and photothermal. Photochemical degradation in organic samples is linked to photooxidation, which would be mitigated in a nitrogen purged environment such as applied during the test. However, the Raman spectra of porphyrins at all three temperature points shown in Figure 7-21 were collected in a nitrogen purged environment and a significant reduction in the photochemical degradation would result in a similar signal increase across all three measurements. As evident from Figure 7-21, this is not the case. Likewise, the Raman spectra of porphyrins collected in an ambient environment shown in Figure 6-10 do not display any significant difference compared to the spectra collected at the same laser power in a nitrogen purged environment in Figure 7-21. As such, the signal increase observed in the spectra of porphyrins at cryogenic temperatures is unlikely to be the result of a reduction in the photochemical degradation of the sample.

On the contrary, photothermal degradation is the result of localized heat build-up. This can be mitigated by providing a heat sink such as the Linkam cooling stage. In previous research, a reduction in the photothermal degradation was observed as a result of mixing the pure porphyrin sample with a KBr at 1% concentration and pressing the sample into a pellet, which acts as a heat sink [330]. Previous results discussed in Section 6.2 also show a reduction in the photothermal degradation in chlorophyll naturally occurring in spinach compared to a concentrated pure sample of chlorophyll. Similar to KBr, the tissue matrix of spinach acts as a heat sink and mitigates the photothermal degradation induced by the laser. In this experiment, the heat sink is effectively provided by the Linkam cooling stage, which reduces the temperature of the sample to cryogenic conditions and thus mitigates the photothermal degradation. As discussed previously, the results show no significant contribution of photochemical degradation to the signal increase at cryogenic temperatures, which indicates it is predominantly the result of the reduction in photothermal degradation.

As shown in Figure 7-23 and Figure 7-24, the signal enhancement is specific to each band in the spectra for both hemin and protoporphyrin. Specifically, the SNR comparison shows that the most dominant Raman bands clearly visible in the spectra even at room temperature (i.e. 1625 cm^{-1} , 1569 cm^{-1} and 1368 cm^{-1} hemin bands and 1614 cm^{-1} , 1358 cm^{-1} and 1327 cm^{-1} protoporphyrin bands) display much lower SNR increase at extreme low temperatures than bands that were unresolvable or appeared barely distinguishable in the room temperature spectra. This is evident in the spectra of both hemin and protoporphyrin. In the spectra of hemin, the highest SNR increase from room temperature to $-196\text{ }^{\circ}\text{C}$ occurred at nominally very weak bands at 1127 cm^{-1} , 1163 cm^{-1} and 1231 cm^{-1} . Similarly, the highest SNR increase in the spectra of protoporphyrin was observed at 1227 cm^{-1} , 1125 cm^{-1} and 1479 cm^{-1} , which are very weak bands only barely distinguishable at room temperature.

Figure 7-23 shows the signal enhancement of each band at cryogenic temperatures quantified in percentage of the nominal room temperature signal strength. The figure shows that at $-100\text{ }^{\circ}\text{C}$, a comparatively modest signal increase is possible for most porphyrin bands. At $-196\text{ }^{\circ}\text{C}$, Raman measurements of hemin can benefit from a signal enhancement of up to 310% and protoporphyrin 116%. A signal enhancement of 23% to 310% was observed at $-196\text{ }^{\circ}\text{C}$ across all resolvable bands of hemin. Most hemin bands increased in intensity by at least 80% with a significant number of bands increasing by more than 120%. Across Raman bands of protoporphyrin, a signal enhancement of 60% to 116% was observed.

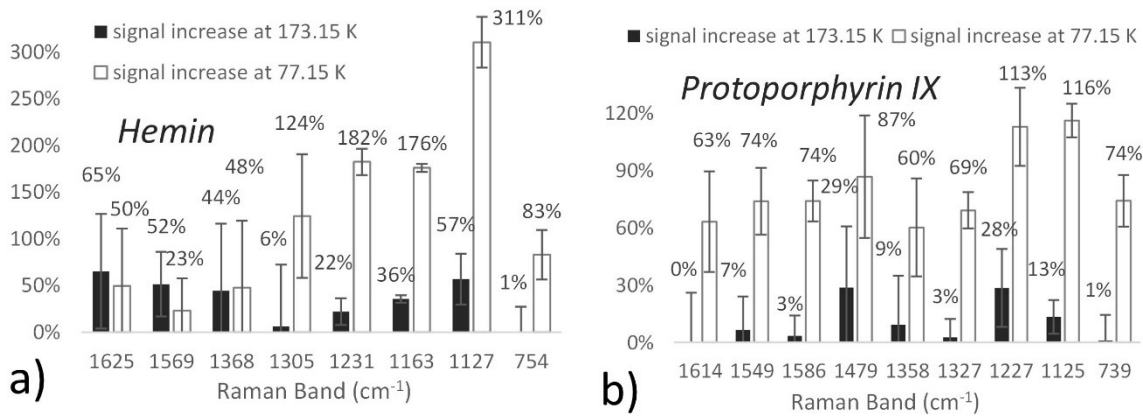


Figure 7-23 Relative SNR increase across all fully resolvable bands in the Raman spectra of hemin (a) and protoporphyrin IX (b) at cryogenic temperatures (-100 °C and -196 °C) compared to room temperature measurements. The SNR enhancement is quantified in percentage of the nominal room temperature signal strength including 2σ error bars (532 nm excitation at 9.77 kW/cm² laser power density for hemin and 195 W/cm² for protoporphyrin) [311]

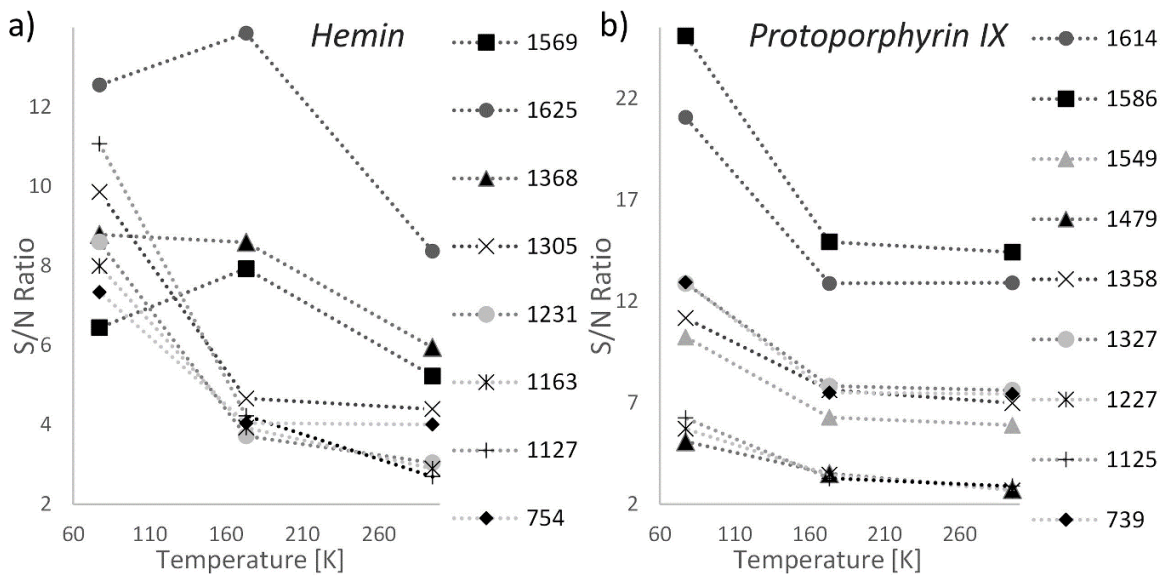


Figure 7-24 SNR enhancement across all fully resolvable bands in the Raman spectra of hemin (a) and protoporphyrin IX (b) at cryogenic temperatures (-100 °C and -196 °C) compared to room temperature measurements using 532 nm excitation and the same laser power density of 9.77 kW/cm² for hemin and 195 W/cm² for protoporphyrin [311]

Both the signal enhancement caused by the reduction in thermal degradation and the associated decrease of the relative fluorescence noise level and its impact could be very welcome effects in the context of the exploration of Europa. The cryogenic temperatures on Europa may allow the use of higher laser power and higher energy lasers without causing excessive laser damage. Likewise, the identification of extremely photosensitive biosignatures, such as porphyrin

derivatives, may also be possible at such conditions. This may greatly enhance the science output of Raman spectrometers on Icy Worlds and many other terrestrial applications may also benefit from this effect. Specifically, porphyrins and porphyrin derivatives are critical in many biological processes and as such, their structure and function are intensively studied in contemporary medicine and analytical biochemistry. Raman spectra of porphyrins and their derivatives have been studied to investigate ligand binding mechanisms [336]–[338], the oxygenation process of human erythrocyte [138], [339], [340] as well as for the analysis of hemoglobin and for whole blood analysis to monitor pathological changes in diagnostics and biomedical analysis [138], [341]–[343]. Raman spectroscopic investigations of porphyrin derivatives have also been used to study healthy and diseased blood cells, most notably to investigate drug interactions with cells infected by malaria [138], [344]–[346] or for the analysis of sickle cells [138], [339], [344]. Raman spectra have also shown a potential for early detection of Malaria infection [138], [347], [348].

However, the inherent photosensitivity of porphyrin based molecules affects the effectiveness of Raman spectroscopy in biomedical research [339], [340], [349], [350]. Various methods leading to signal enhancement of porphyrins have been studied including the effects of the excitation wavelength, resonance and different Raman configurations and methods [341]–[343]. Fourier Transform Raman spectroscopy (FT-R) at the NIR excitation of 1064 nm was suggested to reduce the sample damage effects in a study of whole blood and hemoproteins [342]. However, Raman scattering in the NIR range is much weaker than Raman scattering in the visible range and other studies report that the 1064 nm excitation provides only very weak Raman spectra of porphyrins compared to other more traditional excitation wavelengths [341], [346], [351]. A shorter excitation of 720 nm was suggested to be more practical for *in-vivo* measurements of whole blood and hemoglobin than visible or 1064 nm excitation as it can avoid fluorescence and carotenoid interference which occurs at visible excitations while still benefiting from resonance effects [341], [351]. Another study of the impact of the excitation wavelength selection on the Raman signal enhancement of β -hematin and hemin shows promising signal enhancement at 780–830 nm as well as at 564 nm excitation [346]. However, the study also demonstrates that the signal enhancement using resonance at these excitation wavelengths is very specific to individual vibrational modes and Raman bands [346]. More importantly, selecting a different excitation for signal enhancement may not be a viable option for many applications. This is due to interference from other molecules and fluorescence and in some cases, certain spectral features of interest may be only observable at very specific excitations [138], [341], [342], [346], [348]–[350].

A study of porphyrin derivatives at decreased temperatures has shown that lower temperatures and shorter exposure to the laser light can limit the photodegradation of the sample, however, only a very limited temperature range of 4 °C to 52 °C was used in this study [339]. This restricted

the investigation of thermally induced changes in the spectra of porphyrin molecules to relatively high temperatures and could not reveal the full potential of cryogenic Raman measurements nor inform the development of an instrument for the exploration of Icy Worlds. The study of porphyrin molecules at cryogenic temperatures presented in this research work demonstrates that cryogenic Raman measurements of porphyrins and porphyrin derivatives can be a very effective method of enhancing the signal strength and spectra quality. Moreover, decreasing the temperature of the sample is a relatively simple procedure that can be applied regardless of the excitation wavelength. Likewise, it does not require mixing the sample with KBr and pressing it into a pellet, which was shown to reduce the thermal degradation, as discussed previously, but may not be feasible for all applications. Nevertheless, it is also important to note that mixing the sample with KBr and reducing the temperature to cryogenic levels are not mutually exclusive and the two methods could be used in conjunction to achieve higher signal enhancement levels.

In conclusion, acquisitions of Raman spectra of porphyrins and their derivatives at cryogenic temperatures can be a very effective and simple method of improving the Raman signal strength and spectra quality regardless of the Raman instrument configuration and excitation wavelength. This can greatly enhance the scientific output of Raman spectroscopy both in extraterrestrial exploration as well as in biomedical research including drug design and development, diagnostics as well as disease monitoring and analysis.

7.3 Carotenoids

The distinct Raman bands in the spectra of carotenoids that are observed at similar frequencies at both visible and NIR excitation provide an ideal opportunity to compare the cryogenically induced changes between 532 nm and 785 nm excitation. Likewise, the similar spectra of β -carotene and astaxanthin allow an evaluation of the impact of the cryogenic changes on distinguishing two different molecules with similar Raman spectra.

The comparison of Raman spectra of β -carotene and astaxanthin at 22 °C, -100 °C and -196 °C at 785 nm excitation is shown in Figure 7-25 and at 532 nm in Figure 7-26. The Raman shift change from room temperature to -196 °C for both carotenoids at both excitation wavelengths is then compared in detail in Table 7-5. Both figures as well as Table 7-5 clearly demonstrate that the Raman shift change observed across all Raman bands in the spectra of β -carotene is very similar at both excitation wavelengths. At both excitation wavelengths, the highest Raman shift change in the spectra occurred at the same Raman band and all bands shifted in the same direction by approximately the same amount. Additionally, as shown in Figure 7-25 and Figure 7-26, the spectra of β -carotene at -196 °C becomes almost identical at 532 nm and 785 nm. The only

exception are minor bands nominally at 1991 cm^{-1} and 1449 cm^{-1} . The Raman shift of these bands is displayed with a 1 cm^{-1} difference in Figure 7-25 and Figure 7-26, however, this is the result of rounding the value up or down and the actual shift difference between the 785 nm and 532 nm spectra is only 0.15 cm^{-1} and 0.22 cm^{-1} respectively. While less consistent than β -carotene, the Raman shift changes observed in the spectra of astaxanthin are also similar at 532 nm and 785 nm. It is important to state, that Raman shift changes observed in the spectra of astaxanthin are smaller than changes in β -carotene, which could have also contributed to larger discrepancies. In general, as shown in Table 7-5, most bands display similar trends in the Raman shift change at cryogenic temperature regardless of the excitation and the specific carotenoid molecule.

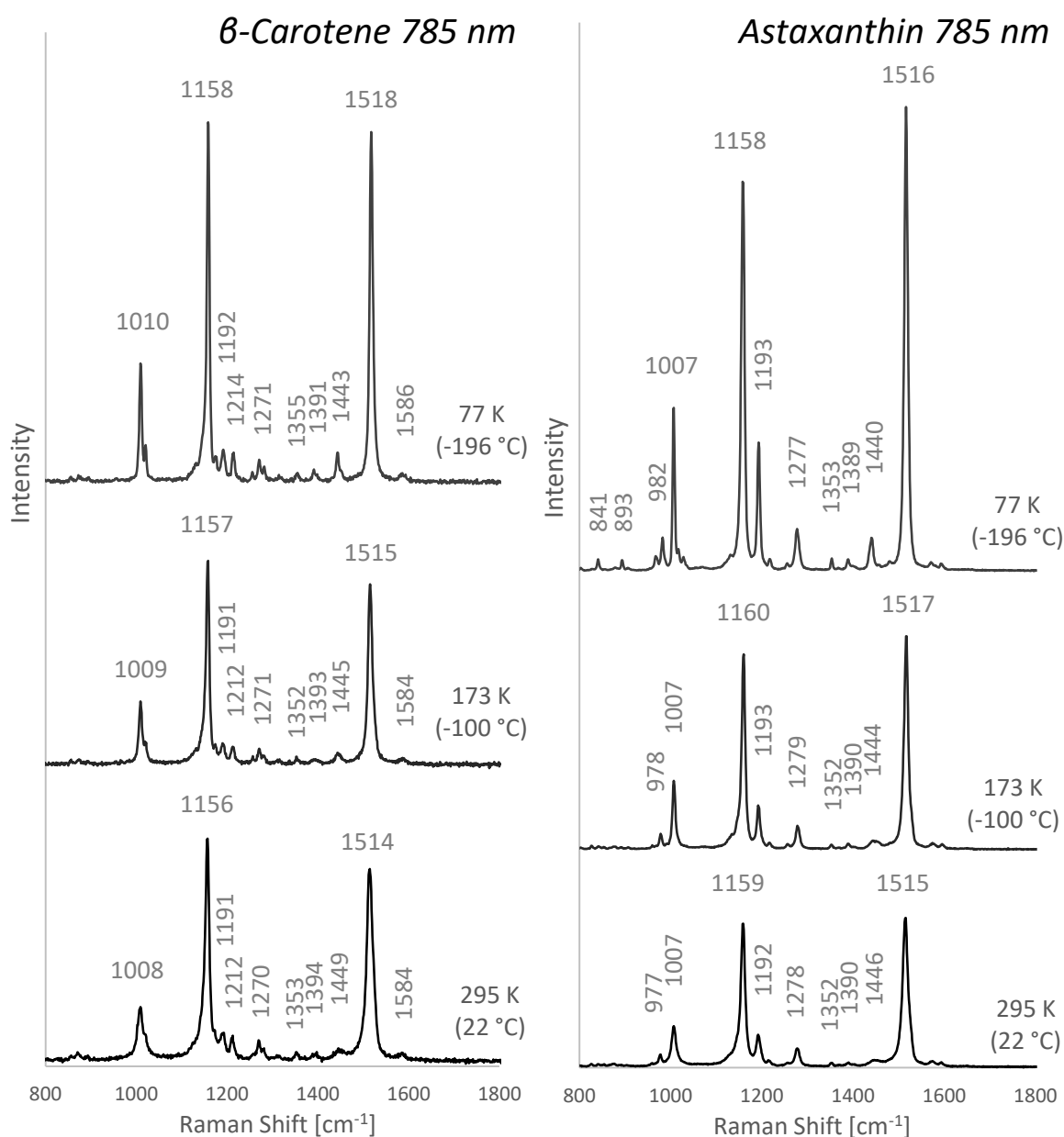


Figure 7-25 Raman spectra of β -carotene and astaxanthin at 22 °C, -100 °C and -196 °C at 785 nm excitation

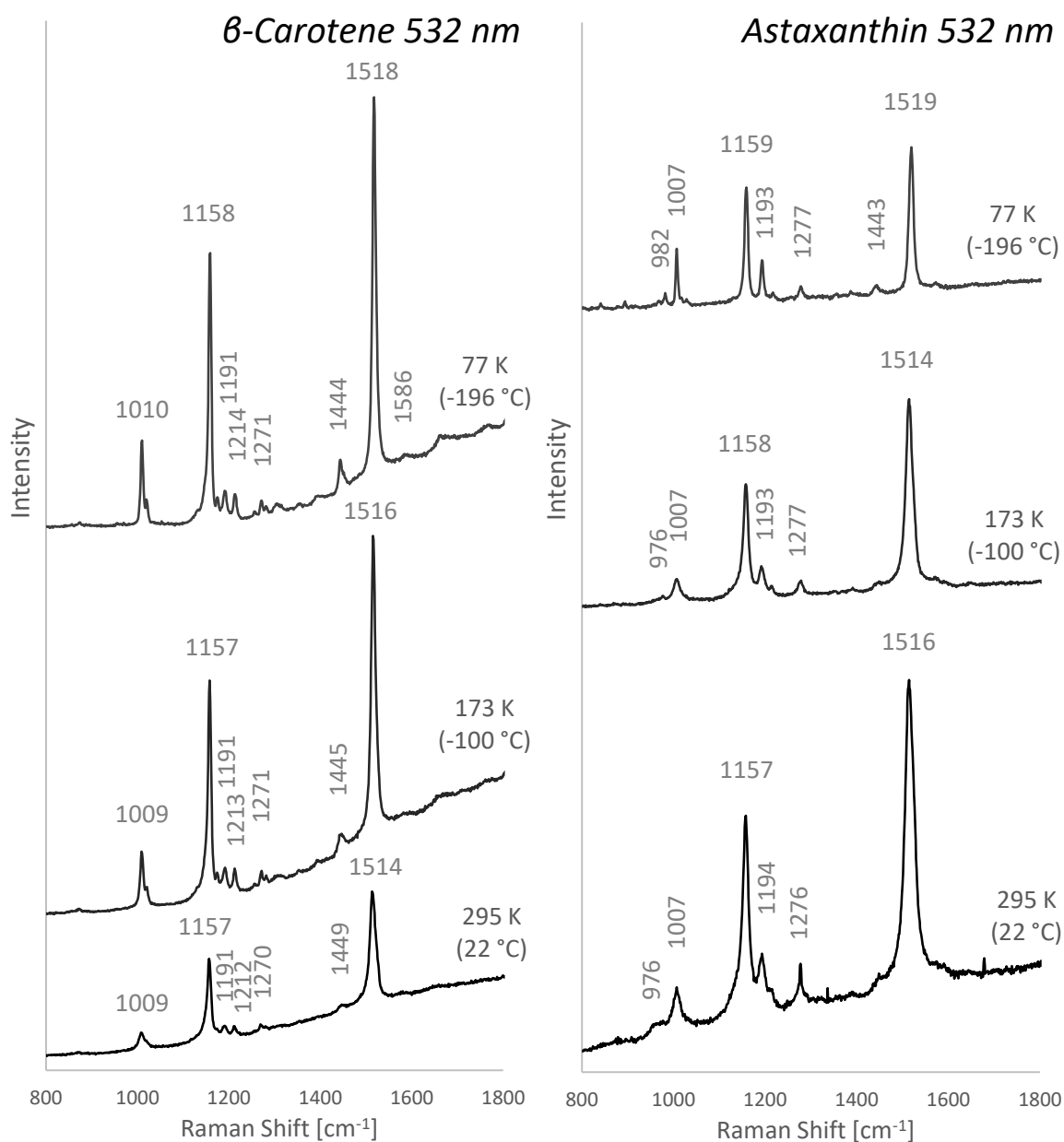


Figure 7-26 Raman spectra of β -carotene and astaxanthin at 22 °C, -100 °C and -196 °C at 532 nm excitation

The comparison of β -carotene and astaxanthin at both 785 nm and 532 nm shows that these two molecules could easily be confused if only the 3 major bands were considered, as it is often the case in contemporary research. As shown in Figure 7-25 and Figure 7-26, the β -carotene spectrum at -196 °C becomes very similar to the astaxanthin spectrum at room temperature and in fact, it becomes more similar to the astaxanthin room temperature spectrum than β -carotene room temperature spectrum. This may be an issue for the exploration of Icy Worlds as the lack of carotenoid reference spectra at cryogenic temperatures could lead to misidentification. It is important to note that the minor peaks in the spectra may help distinguish these two molecules, however, these bands may not be visible or fully resolvable, especially in low concentrations or if

fluorescence noise is present. Additionally, at 532 nm both β -carotene and astaxanthin share the 1158 cm^{-1} Raman band at low temperatures, which is not the case at room temperature. While other bands can still help distinguish the two molecules, this may still cause confusion if appropriate reference spectra are not available.

β-carotene Raman band (at 785 nm)											
	1008	1156	1191	1212	1270	1353	1394	1449	1514	1584	
Raman shift change from 22 °C to -196 °C											
785 nm	1.14	2.08	0.77	1.73	0.89	1.98	-2.82	-5.67	3.37	2.79	
532 nm	0.87	1.80	0.91	1.66	1.26			-5.14	3.21		
Astaxanthin Raman band (at 785 nm)											
	977	1007	1159	1192		1278	1352		1390	1446	
Raman shift change from 22 °C to -196 °C											
785 nm	5.15	-0.28	-0.31	0.58		-0.45	0.88	-0.66	-5.63	1.66	
532 nm	5.94	0.06	1.93	-0.51		1.15				3.43	

Table 7-5 Comparison of the Raman shift change from room temperature to -196 °C in the spectra of β -carotene and astaxanthin at 532 nm and 785 nm

As evident from Figure 7-25 and Figure 7-26, the spectral resolution and signal quality rises dramatically at lower temperatures and bands barely visible at room temperature become more prominent. Similarly, new bands undetectable at room temperatures appear in the spectra at low temperatures. Namely 2 minor bands appear in the region below 900 cm^{-1} in the spectra of astaxanthin at 785 nm. At 532 nm, a band at 1586 cm^{-1} and 1443 cm^{-1} appear in the spectra of β -carotene and astaxanthin respectively.

An example of the general profile of the Raman shift and band width change in β -carotene is shown in Figure 7-27 and appears similar as in previously discussed spectra of amino acids. The Raman shift increases with decreasing rate of change until it starts converging to a fixed value at around 70 K. The band width shows the same trend in reverse. While the band width trend seems to be the same for both carotenoids, the profile of the Raman shift change in the spectra of astaxanthin does not match the profile of β -carotene. This is also shown in Figure 7-27, which compares the Raman shift and width profile of the 1007 cm^{-1} Raman band (methyl rocking) in the spectra of β -carotene and astaxanthin. As opposed to the β -carotene Raman shift profile, astaxanthin Raman shift seems to rise at -100 °C and then drops again at -196 °C. This trend was observed at multiple, but not all, astaxanthin bands at both excitations. As such, it is unlikely to be a result of variance in the data, which suggests that this profile may be specific to the astaxanthin molecule. Additionally, while there is increased variability at the 1007 cm^{-1} band in the spectra of astaxanthin (shown in Figure 7-27), which places the observed change in the 1σ region at 532 nm, the change is beyond the 3σ threshold at 785 nm. Likewise, changes observed at other bands with the same shift profile lie between 2σ and 3σ regions and beyond, which makes the dissimilar

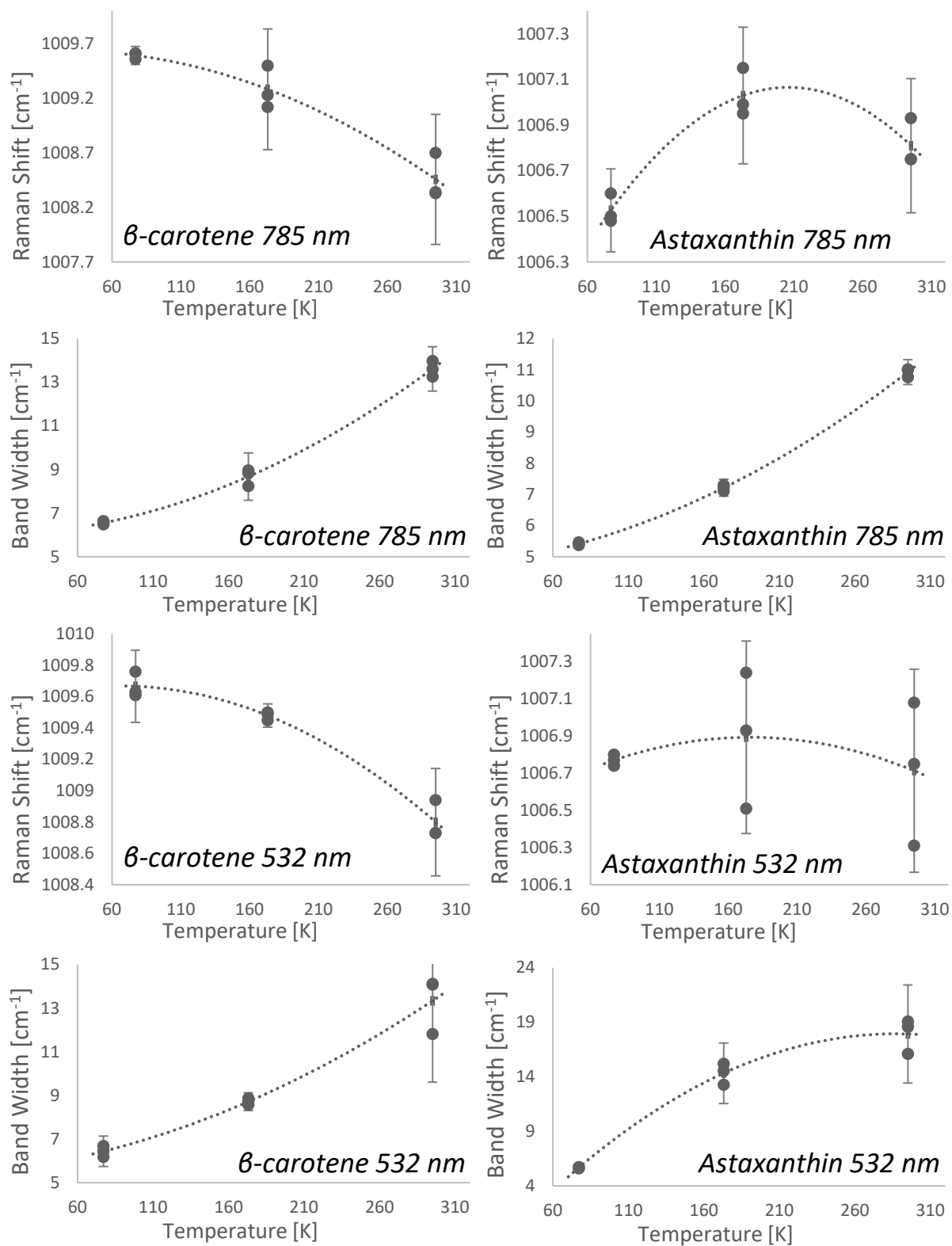


Figure 7-27 Raman shift and band width change of the 1007 cm⁻¹ Raman band (methyl rocking) in the spectra of β -carotene and astaxanthin across 22 °C, -100 °C and -196 °C at 785 nm and 532 nm excitation including 2 σ error bars (except for Raman shift change in astaxanthin at 532 nm, which is shown with 1 σ error bars)

profile unlikely to be the result of an instrumental error. This dissimilar behaviour at extreme low temperatures between β -carotene and astaxanthin molecules could potentially serve as a tool to distinguish these two molecules. As already discussed, this may be important, if not necessary, for a successful identification on Icy Worlds as these molecules mimic each other at low temperatures and could be easily confused.

It is also important to highlight that sigma error bar analysis classifies the changes observed in the spectra of both carotenoids at both excitations well beyond the 3σ threshold for most bands with a few within the 2σ region and only a couple in the 1σ region. This provides relatively high confidence that the observed changes are the result of the temperature change rather than an experimental error or variability in the data.

In general, the highest observed change in the Raman shift was 5.67 cm^{-1} and 5.14 cm^{-1} in the spectra of β -carotene at 785 nm and 532 nm respectively, and 5.63 cm^{-1} and 5.94 cm^{-1} in the spectra of astaxanthin at the same excitation. This consistent upper limit suggests that the spectra of carotenoids in general may not shift by more than approximately 6 cm^{-1} at cryogenic conditions. It is also important to state that these are a relatively minor change compared to the maximum change in the Raman shift observed in the spectra of amino acids, which reached up to 25 cm^{-1} . As discussed in Section 7.1, the highest changes were observed in the spectra of the simplest amino acids with Tryptophan, a relatively more complex aromatic amino acid, showing the smallest maximum change of 8 cm^{-1} . Carotenoids are much longer and structurally complex molecules than amino acids, which explains the relatively smaller changes in the Raman shift compared to amino acids. This supports the assumption discussed in Section 7.1 that more complex molecules display smaller changes across different temperatures and demonstrates that this is true regardless of the molecular species.

All bands except for 1394 cm^{-1} and 1449 cm^{-1} shifted to higher frequencies in the spectra of β -carotene. The two bands that shifted to lower frequencies also shifted to lower frequencies in the spectra of astaxanthin. Some other astaxanthin bands also shifted to lower frequencies, however, only by a relatively small amount ($<0.45\text{ cm}^{-1}$). In general, Raman shift changes observed in the spectra of astaxanthin at low temperatures are much smaller than in the spectra of β -carotene. This indicates the spectra of astaxanthin is more stable across different temperatures than β -carotene. As shown in Figure 7-28, as opposed to β -carotene, astaxanthin includes additional hydroxyl and ketone functional groups. This additional complexity may have been the result of the relatively smaller changes and relatively higher stability in its spectra at low temperatures. This would also be in line with the results in Section 7.1, which identified simpler molecules to be more likely to exhibit larger spectral changes at cryogenic conditions.

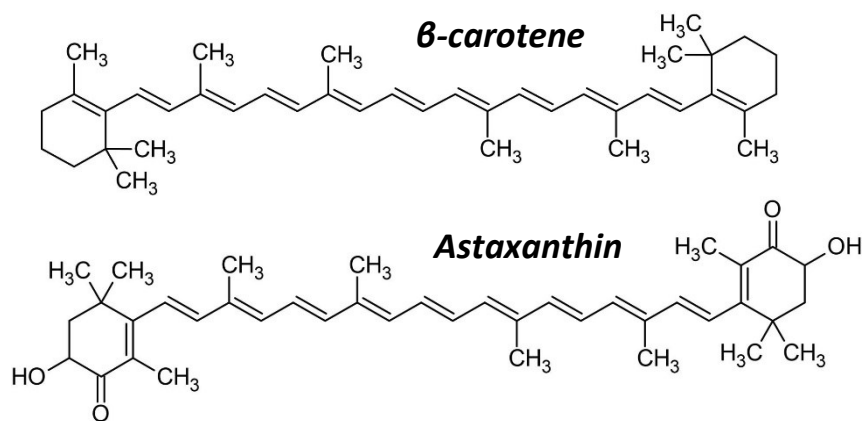


Figure 7-28 Molecular structure of β -carotene and astaxanthin

Similar to the changes in the band width observed in the spectra of amino acids, all bands in the spectra of both carotenoids at both excitation wavelengths decreased significantly at cryogenic temperatures. The band width decreased by 23-52% and 13-52% in the spectra of β -carotene at 785 nm and 532 nm respectively. A decrease by 10-50% was observed in the spectra of astaxanthin at 785 nm and 22-68% at 532 nm. This significant decrease in the Raman band width results in much higher accuracy of the Raman measurements at extreme low temperatures and could be potentially very beneficial for both the exploration of Europa as well as many other applications.

As shown in Figure 7-29, the Raman shift and band width variance in the spectra of β -carotene and astaxanthin decreases significantly at low temperatures. Apart from a few minor discrepancies, this effect was observed consistently at both 785 nm and 532 nm excitation for both carotenoids. This same trend was also observed in the spectra of amino acids, as discussed previously in Section 7.1. This suggests that the lower variance at low temperatures is independent of the molecular species or the excitation wavelength. As already discussed previously, this significant decrease in the variability of the spectra between individual measurements increases the precision of Raman spectroscopy at cryogenic temperatures, which can be beneficial for many applications beyond the exploration of Icy Worlds.

As shown in Figure 7-26, both β -carotene and astaxanthin display fluorescence noise at 532 nm excitation. However, as opposed to the fluorescence trend observed in amino acids at cryogenic temperatures, the fluorescence noise does not impede the identification of carotenoids and does not lower their SNR. On the contrary, the SNR of carotenoid Raman bands rises dramatically from room temperature to $-196\text{ }^{\circ}\text{C}$. This is shown in Figure 7-30, which compares the SNR trend of both carotenoids at both excitations. This increase in SNR may be the result of signal increase at low temperatures which may counterbalance the increase in the fluorescence noise. As pigment molecules, carotenoids are inherently more photosensitive than amino acids. As such, it is

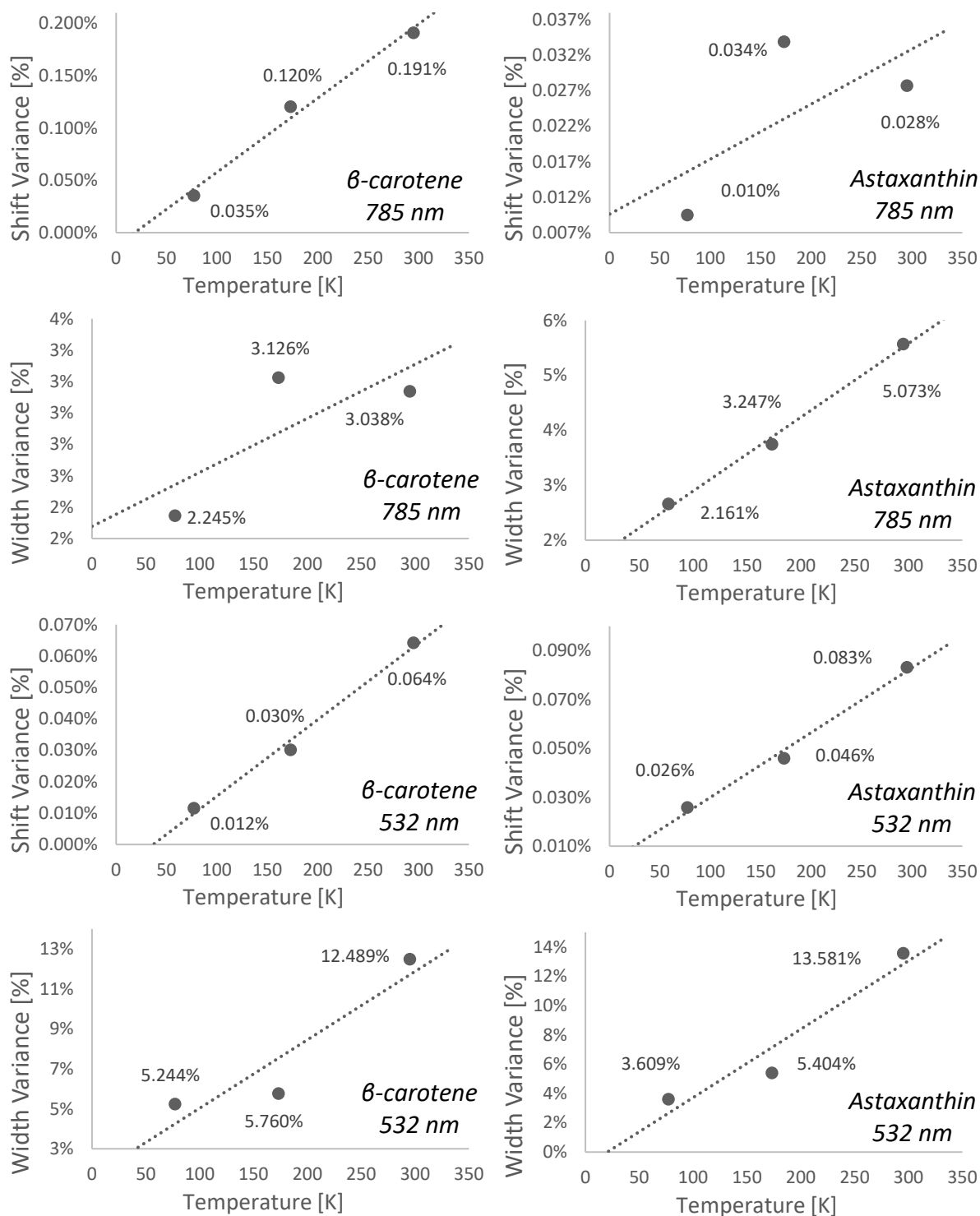


Figure 7-29 Average Raman shift and band width variance across all bands in the spectra of β -carotene and astaxanthin across 22 °C, -100 °C and -196 °C at 785 nm and 532 nm excitation

possible that the extreme low temperatures reduced the effect of photothermal damage that may have decreased the SNR at room temperature but may have not been obvious in the spectra. This dramatic increase in the SNR of carotenoid molecules at cryogenic temperatures is a very welcome effect for the search for life on Europa and other Icy Worlds. It may also be a useful tool

in other applications as carotenoids are often used as biomarkers in biomedical research and higher sensitivity to these molecules could make cryogenic Raman spectroscopy much more effective than traditional room temperature measurements.

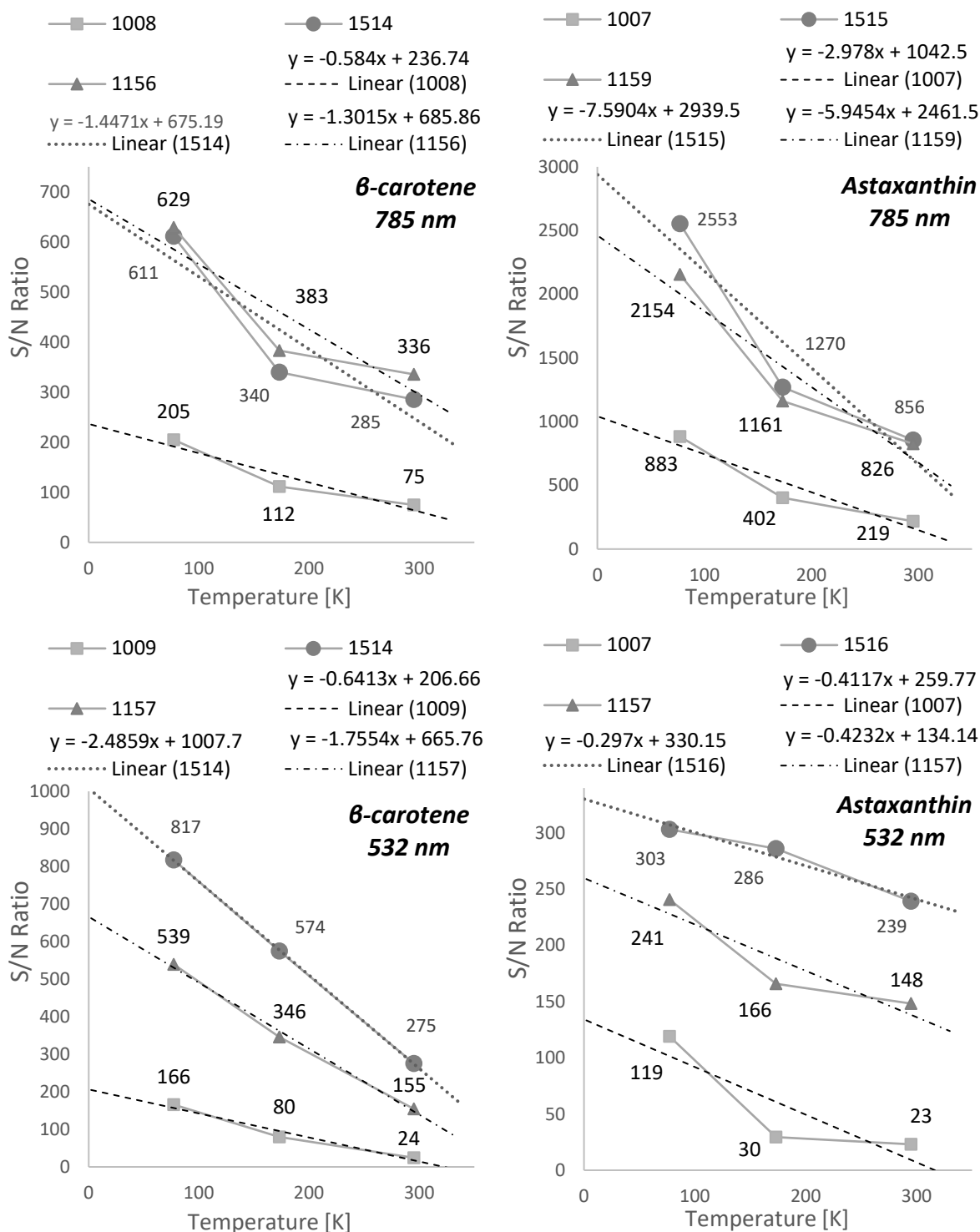


Figure 7-30 SNR change observed at the 3 most dominant carotenoid Raman bands in the spectra of β -carotene and astaxanthin across 22 °C, -100 °C and -196 °C at 785 nm and 532 nm excitation

7.4 Pigments

Apart from carotenoids, which are discussed in the previous section, the two other pigments examined in this study are chlorophyll A and c-phycoyanin. Out of these two pigments, only the spectra of c-phycoyanin at 785 nm excitation could be analysed at cryogenic temperatures as excessive fluorescence prevented any analysis of chlorophyll at both excitations and c-phycoyanin at 532 nm excitation. At 785 nm, the spectra of c-phycoyanin show signs of the molecule's Raman signature, however, only a few barely resolvable Raman bands are visible within the high fluorescence background. This is displayed in Figure 7-31, which compares the spectra of c-phycoyanin at 22 °C, -100 °C and -196 °C.

Unfortunately, the fluorescence interference in the spectra affected the band width and SNR too much to accurately determine its Raman shift. As such, the Raman shift values displayed in Figure 7-31 represent only the best estimate available using the peak-pick (FWHM) algorithm in conjunction with manual FWHM calculations of segments of the data where the automated process failed to recognize the Raman signature.

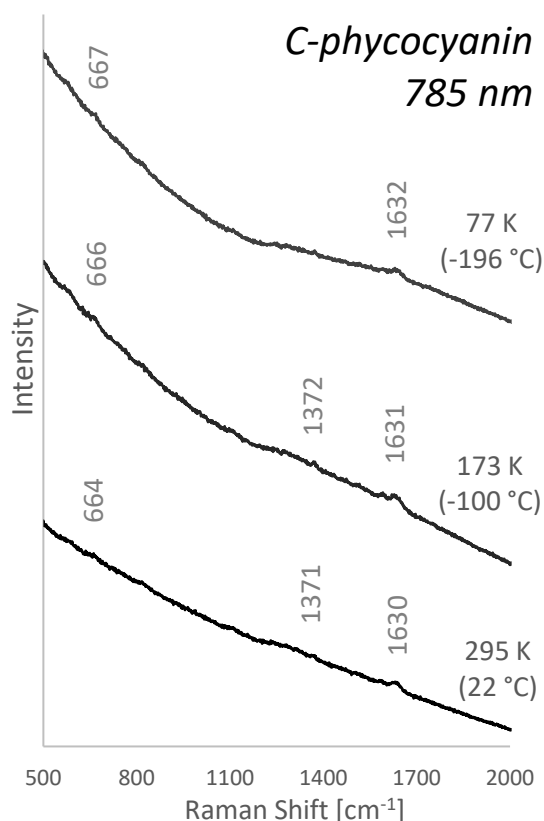


Figure 7-31 Raman spectra of c-phycoyanin at 22 °C, -100 °C and -196 °C at 785 nm excitation

It is important to note that the signature of c-phycoyanin as displayed in Figure 7-31 is not sufficient to fully identify the molecule. However, an analysis of the fluorescence noise tendencies

was attempted nevertheless. This was done predominantly in order to further investigate the SNR change in the spectra of extremely photosensitive molecules at cryogenic temperatures. This is because investigations of other photosensitive molecules discussed in this study revealed SNR rise at cryogenic temperatures, which is contradictory to SNR trends observed in the spectra of other fluorescent molecules.

The SNR trend across the examined temperature range is shown in Figure 7-32. While the SNR change in *c*-phycoerythrin is minor due to the high fluorescence background, an upwards trend similar to the SNR trend observed in the spectra of other photosensitive molecules can be derived from the data. The *c*-phycoerythrin SNR increases by 9.5% from room temperature to -196 °C.

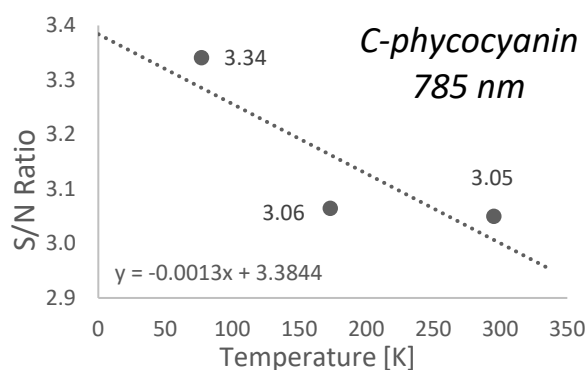


Figure 7-32 SNR of the *c*-phycoerythrin spectra across 22 °C, -100 °C and -196 °C at 785 nm excitation

While an accurate assignment of the band Raman shift was not possible due to the high fluorescence noise, all three resolvable bands shifted to higher frequencies at lower temperatures. The maximum change in the Raman shift was monitored despite possible inaccuracy due to the high fluorescence noise and was determined to be 3.1 cm⁻¹ at the 644 cm⁻¹ band. *C*-phycoerythrin is a relatively complex molecule with multiple functional groups and aromatic rings, as shown in Figure 7-33. As such, the maximum shift of 3.1 cm⁻¹ is in accordance with previously discussed observations as it is just shy of the 5.6 cm⁻¹ maximum change in carotenoids, which are slightly less structurally complex than *c*-phycoerythrin compared to the complexity of other molecules examined in this study.

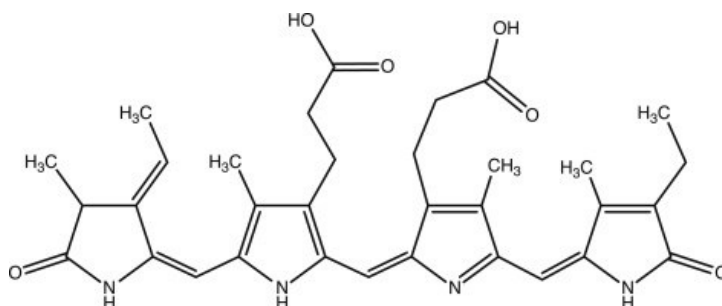


Figure 7-33 Molecular structure of *c*-phycoerythrin

7.5 Natural Mixtures

In order to explore the effect of cryogenic temperatures on pigments in their naturally occurring form, samples of spinach and a carrot root were examined. As shown in Section 6.2, pigments imbedded in a natural tissue matrix were shown to have much higher laser damage thresholds than their raw counterparts. This allowed cryogenic investigations of naturally occurring chlorophyll, which was not detectable in its pure sample form. The spectra of spinach (naturally occurring chlorophyll) and carrot (naturally occurring β -carotene) at 532 nm excitation at room temperature, $-100\text{ }^{\circ}\text{C}$ and $-196\text{ }^{\circ}\text{C}$ are shown in Figure 7-34.

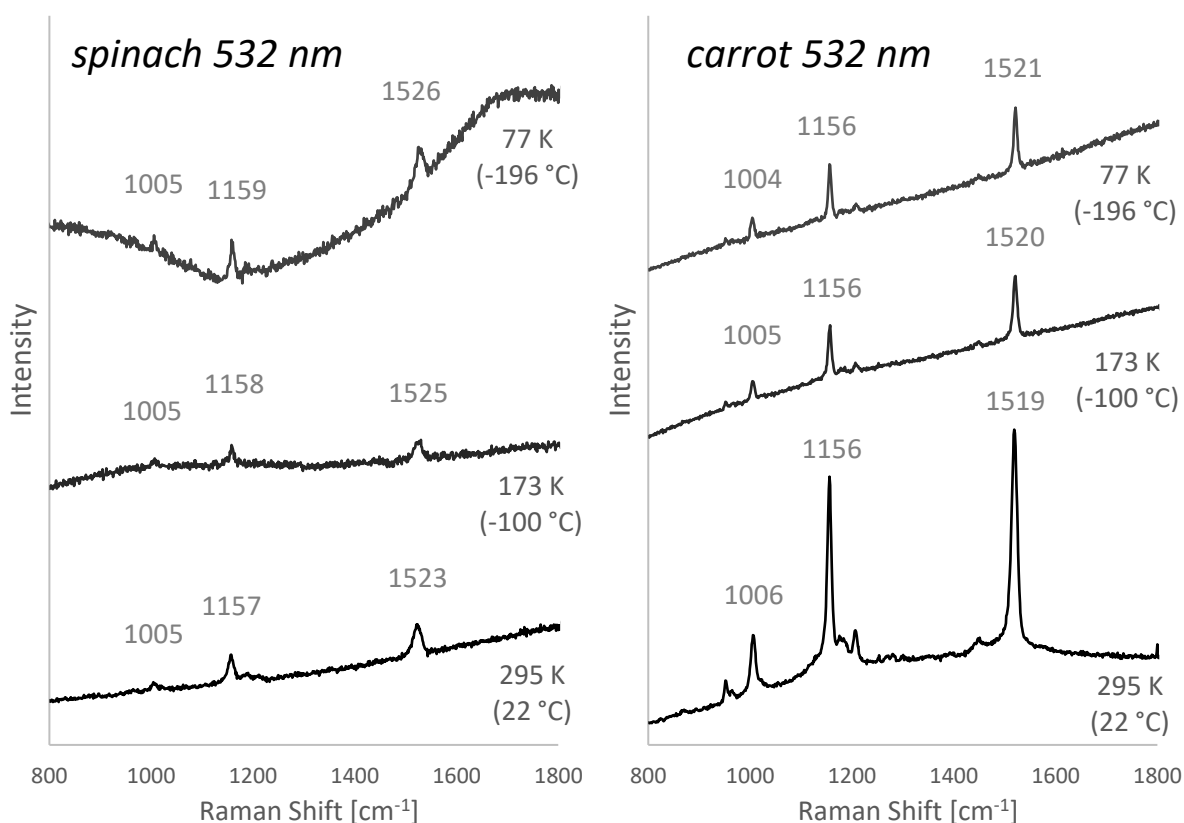


Figure 7-34 Raman spectra of spinach (naturally occurring chlorophyll) and a carrot root (naturally occurring β -carotene) at $22\text{ }^{\circ}\text{C}$, $-100\text{ }^{\circ}\text{C}$ and $-196\text{ }^{\circ}\text{C}$ at 532 nm excitation

Both spinach and carrot spectra show fluorescence at room temperature, which intensifies at decreasing temperatures. The rise in the fluorescence background is quantified in a SNR plot in Figure 7-35, which compares the SNR at the major peak in the spectra at various temperatures. This fluorescence rise is consistent with trends observed in other fluorescent molecules, except for porphyrins and carotenoids, which are mildly fluorescent at 532 nm at room temperature but show a significant increase in the SNR at low temperatures. This is an interesting phenomenon as porphyrin is the base of chlorophyll, which dominates the spectra of spinach, and β -carotene is

the dominant signature in the spectra of a carrot. As such, spinach and carrot spectra should show similar trends at low temperatures as their pure counterparts, which is not the case.

This can be explained by the extreme photosensitivity of both porphyrins and carotenoids in their pure form, as detailed in Section 6.2. As shown in Section 7.2 and 7.3, the SNR increase at low temperatures in the spectra of porphyrins and carotenoids may be attributed to the reduction in photothermal damage of the sample at these temperatures due to the presence of a heat sink. On the contrary, chlorophyll and β -carotene in naturally occurring mixtures are much less photosensitive and the fluorescence background occurring in the spectra is the result of the live tissue matrix interference and naturally occurring impurities rather than sample damage. As such, cryogenic temperatures do not counterbalance the sample damage in their spectra and the SNR decreases.

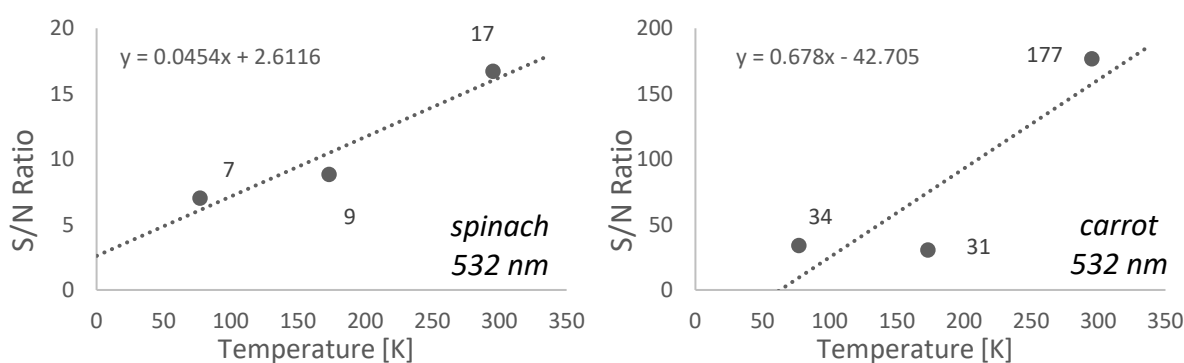


Figure 7-35 SNR change observed at the most dominant Raman bands in the spectra of spinach and carrot (1523 cm^{-1} and 1519 cm^{-1} respectively) across $22\text{ }^{\circ}\text{C}$, $-100\text{ }^{\circ}\text{C}$ and $-196\text{ }^{\circ}\text{C}$ at 532 nm excitation

The largest Raman shift change observed in the spectra of spinach (from room temperature to $-196\text{ }^{\circ}\text{C}$) was 3.28 cm^{-1} at the 1523 cm^{-1} band. This is consistent with the general trend observed across all examined molecules as this is roughly half of the maximum change observed in porphyrins. While porphyrins form the basis of chlorophyll, chlorophyll is structurally more complex due to its long phytol chain attached to the central porphyrin.

The largest change in the Raman shift in the β -carotene signature within the carrot spectra between $22\text{ }^{\circ}\text{C}$ and $-196\text{ }^{\circ}\text{C}$ was 1.94 cm^{-1} , which is less than observed in carotenoids, however, the peaks that shifted the most at low temperatures in carotenoids were not visible in the carrot spectra. Interestingly, the trends observed at cryogenic temperatures in the spectra of carrot did not match the trends observed in the spectra of carotenoids. Namely, the Raman band observed at 1006 cm^{-1} in the spectra of carrot shifted to lower frequencies while in the spectra of pure β -carotene it shifted to higher frequencies. Similarly, the Raman band at 1156 cm^{-1} in the carrot

spectra shift to higher frequencies only by a marginal amount, however, in the spectra of pure β -carotene, it shifts by a considerably higher amount. This implies either that different carotenoids were dominant in each sample or that the interaction of the carotenoid molecule with its natural matrix in the carrot sample affected the cryogenically induced changes in the spectra. While it is impossible to confirm this without further analysis, in both cases, this experiment shows that Raman spectroscopy can potentially and effectively distinguish these very minor differences within a sample when used at two different temperature points. While further investigations of this effect are needed, this could be a very valuable capability in Raman spectroscopy that could be utilized in many scientific areas.

Other effects observed universally across all molecules, i.e. the profile of the shift and width change across temperatures, decrease in the shift variance across different measurements and Raman band narrowing at low temperatures were also observed in the spectra of both spinach and carrot at 532 nm. Additionally, similar results observed at the 532 nm excitation were also observed at 785 nm.

7.6 Nucleic Acids

Unfortunately, excessive fluorescence in the spectra of DNA at both 532 nm and 785 nm excitation as well as RNA at 532 nm prevented any analysis of the thermally induced changes in the spectra of these molecules. The Raman signature of RNA is visible at 785 nm, however, the spectra is plagued by a high fluorescence noise background. This hinders any meaningful analysis of the thermally induced changes beyond basic observations and an investigation of the fluorescence interference trends, which are detailed below.

The Raman spectra of RNA obtained at room temperature, $-100\text{ }^{\circ}\text{C}$ and $-196\text{ }^{\circ}\text{C}$ using a 785 nm Raman system are compared in Figure 7-36. As shown in the figure, the severe fluorescence noise in the RNA spectra obscures the Raman signature and the bands that are visible even despite the fluorescence noise are barely resolvable. As a result of this, the Raman shift corresponding to each distinguishable band at each temperature, as shown in Figure 7-36, may not be sufficiently accurate to draw conclusions. However, based on the data obtained, all bands except for one (723 cm^{-1}) shifted to higher frequencies at lower temperatures. The Raman shift changes were relatively minor in all cases and the largest change observed from room temperature to $-196\text{ }^{\circ}\text{C}$ was 3.3 cm^{-1} at the 1559 cm^{-1} band. This is a relatively small change compared to the changes observed in the spectra of some other molecules, such as amino acids or carotenoids, which are much smaller and less complex than RNA. RNA is a long macromolecule composed of a chain of

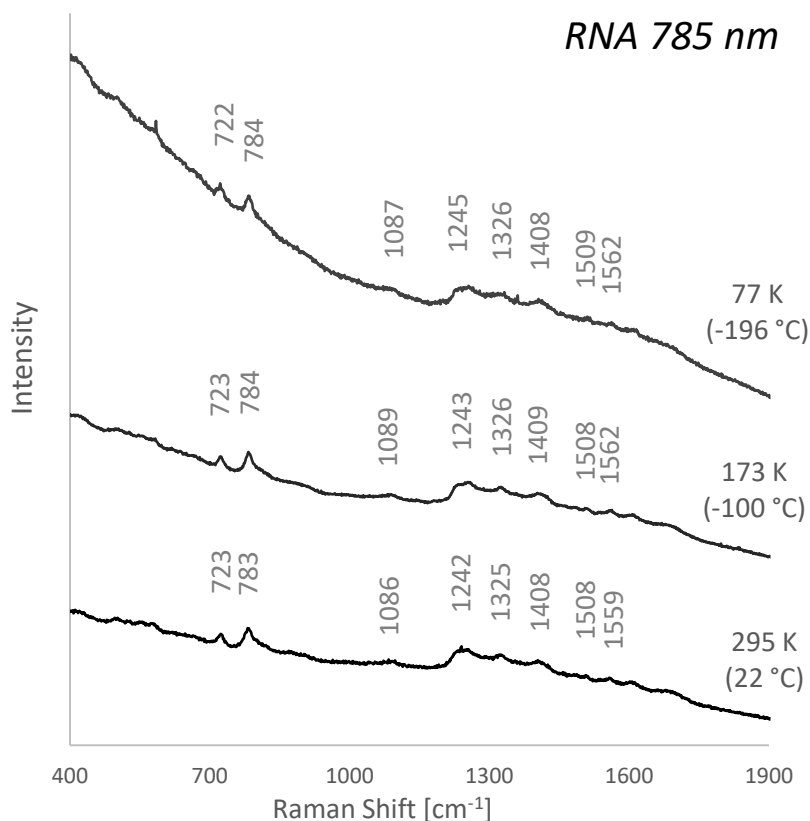


Figure 7-36 Raman spectra of RNA at 22 °C, -100 °C and -196 °C at 785 nm excitation

ribonucleotides where each ribonucleotide is made of a nucleobase, a ribose sugar and a phosphate. While the maximum change observed in RNA may not be entirely accurate due to the fluorescence interference, it is in line with previously discussed results, which indicate that larger and more complex molecules exhibit smaller Raman shift changes at cryogenic conditions. It is also important to note that while Raman shift changes at half of the bands in the spectra of RNA lie in the 1σ error region, which does not indicate high confidence in the results, the 3.3 cm^{-1} maximum shift at the 1559 cm^{-1} band is well beyond the 3σ error threshold. Despite the fluorescence, this provides a relatively good confidence that this is an accurate measurement of the change.

As already observed in other fluorescent molecules, such as some amino acids at 532 nm excitation, the fluorescence noise in the spectra of RNA increases at lower temperatures. This is shown in Figure 7-36 and the corresponding SNR trend across the measured temperature range is detailed in Figure 7-37. The SNR analysis shows a linear downwards trend with approximately a 54.3% decrease in the SNR from room temperature to -196 °C. This has a major impact on the detectability of the molecule as many of the bands in the spectra become hard to distinguish and assign without repeated measurements. While undoubtedly beneficial for many other reasons, multiple measurements may be a luxury not accessible on Europa.

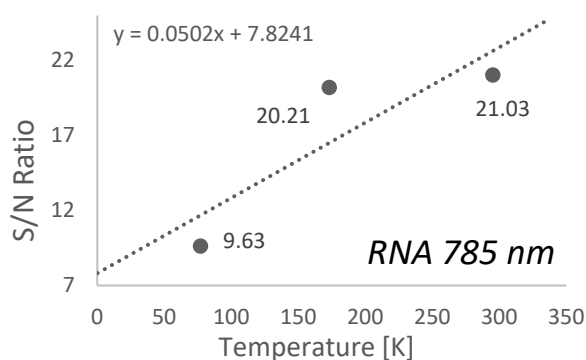


Figure 7-37 SNR change observed in the spectra of RNA across 22 °C, -100 °C and -196 °C at 785 nm

7.7 Carboxylic Acids

The comparison of ectoine spectra at 785 nm excitation collected at room temperature, -100 °C and -196 °C is shown in Figure 7-38. At 532 nm excitation, ectoine is only detectable at high laser power due to severe fluorescence occurring at this wavelength. Due to the cryogenically induced increase in fluorescence, ectoine was not detectable at 532 nm at low temperatures at all, which prevented any meaningful analysis at this wavelength.

While most ectoine Raman bands shifted to higher frequencies, some also shifted to lower frequencies as shown in Figure 7-38. In both cases, the profile of the shift change followed the same trend as described previously (e.g. in Figure 7-2). The highest shift change from room temperature to -196 °C was 11.22 cm⁻¹ at the 113 cm⁻¹ band and the second highest 7.2 cm⁻¹ at the 1637 cm⁻¹ band. This is a similar magnitude of change as observed in histidine, which also happens to be structurally similar to ectoine. As shown in Figure 7-38, similar to histidine, ectoine is also an aromatic molecule with a carboxylic acid group and one side group. The highest negative change was 3.59 cm⁻¹ at the 774 cm⁻¹ band, which is also one of the most dominant bands in the ectoine spectra. Some bands remained relatively stable across all temperatures with the absolute lowest recorded shift being 0.48 cm⁻¹ at 1275 cm⁻¹.

Similar to previous results, significant Raman band width narrowing also occurred in the spectra of ectoine at cryogenic temperatures and the highest decrease in the width between 22 °C and -196 °C was 20.63 cm⁻¹ (79%). Figure 7-39 shows the variability between individual measurements, which decreased at low temperatures as consistent with previous results. The average SNR of the ectoine spectra increased at lower temperatures and the trend is shown in Figure 7-39. Similar to previous results, the higher SNR was accompanied by higher resolution

within the spectra, which also allowed the detection of a few minor bands that were previously unresolvable at room temperature (e.g. 436 cm^{-1} and 458 cm^{-1}).

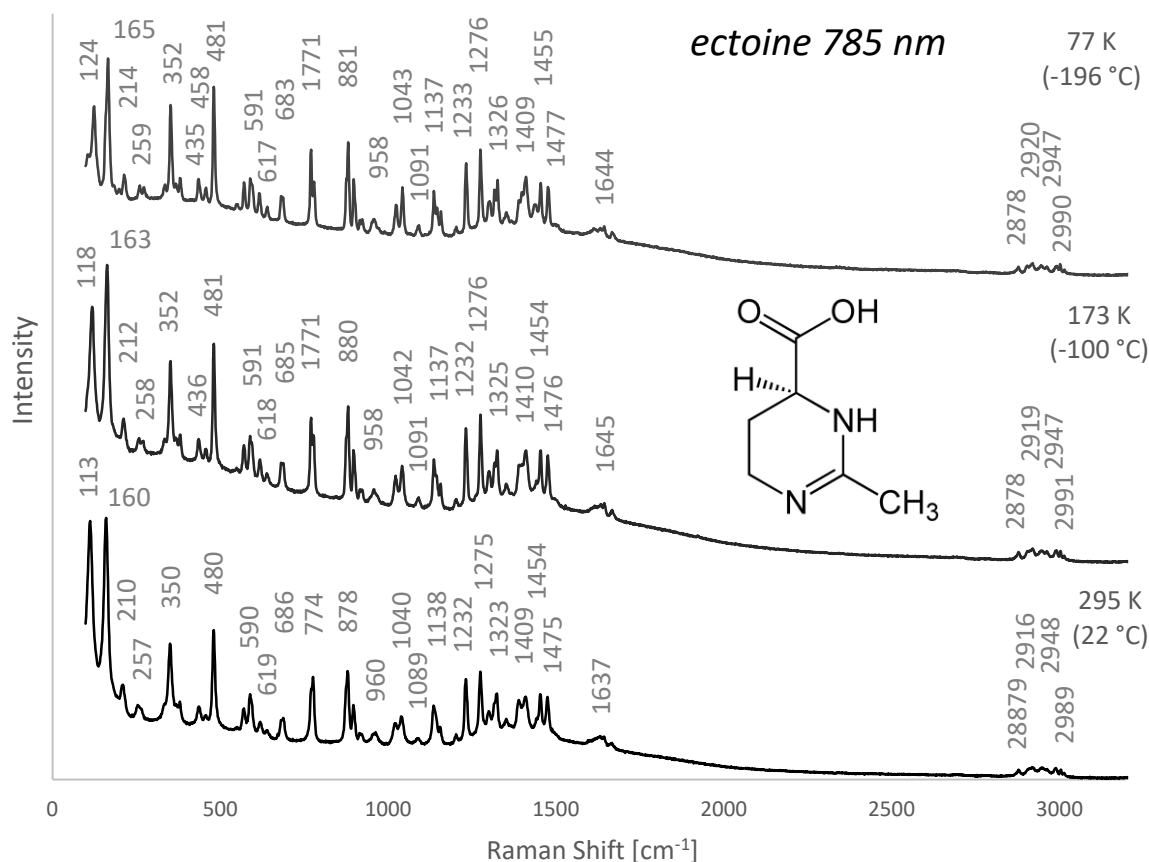


Figure 7-38 Raman spectra of ectoine at 22 °C, -100 °C and -196 °C at 785 nm excitation (6.9 kJ total energy dose and the fluence of 13.79 MJ/cm^2)

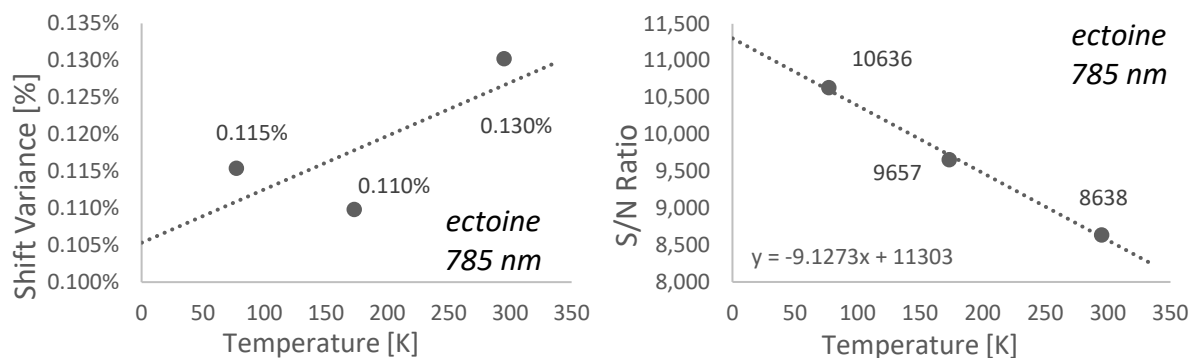


Figure 7-39 Raman shift variance (left) and SNR change (right) recorded in the spectra of ectoine across 22 °C, -100 °C and -196 °C at 785 nm excitation

The minimum peak-to-peak distance in the ectoine spectra was 21.23 cm^{-1} at 22 °C, 21.82 cm^{-1} at -100 °C and 22 cm^{-1} at -196 °C. Similar to some amino acids, the minimum peak-to-peak distance increases at lower temperatures due to bands shifting to higher frequencies.

The spectra of palmitic acid at 22 °C, -100 °C and -196 °C at 785 nm are shown in Figure 7-40, at 532 nm follows the same trends as at 785 nm. Similar to ectoine, some bands in the spectra of palmitic acid move to lower frequencies at lower temperatures, however, the majority moves to higher frequencies. It also follows the same profile of change as already described previously for other samples.

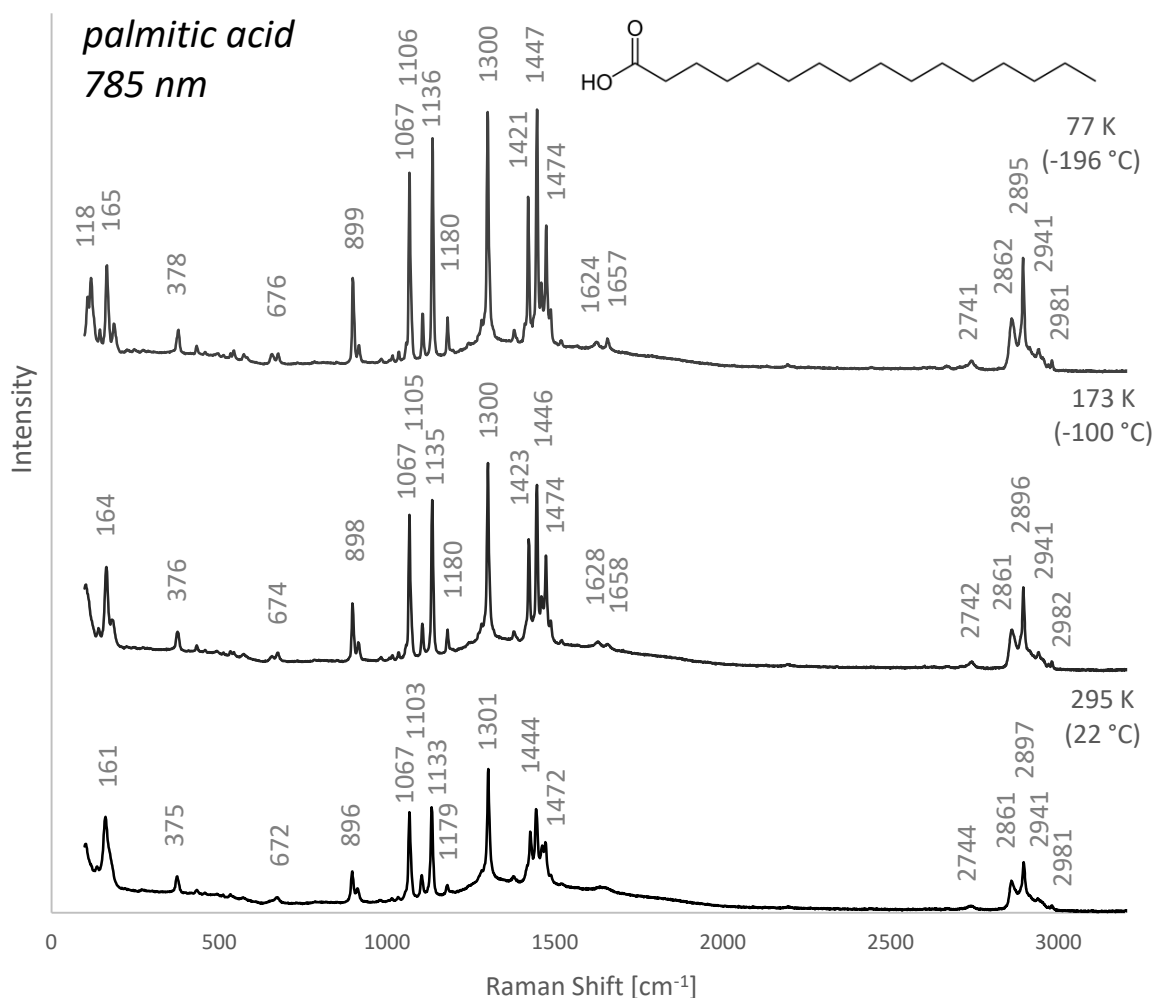


Figure 7-40 Raman spectra of palmitic acid at 22 °C, -100 °C and -196 °C at 785 nm excitation (6.9 kJ total energy dose and the fluence of 13.79 MJ/cm²)

The highest shift change from room temperature to -196 °C was 3.84 cm⁻¹ at the 672 cm⁻¹ band which is comparable to the maximum shift change observed in the spectra of RNA and only slightly less than carotenoids and porphyrins. As shown in Figure 7-40, palmitic acid is a long carbon chain with a carboxylic group and its structural complexity is not far from RNA or carotenoids. The highest negative change was 2.66 cm⁻¹ at the 2744 cm⁻¹ band. Some bands remained relatively stable across all temperatures with shifts as low as 0.11 cm⁻¹ or 0.13 cm⁻¹. While sigma analysis showed that some of these small shifts are the result of an experimental variance, some of these bands were well within or beyond the 2 σ region.

Likewise, significant Raman band width narrowing was also recorded in the spectra of palmitic acid at cryogenic temperatures and the highest decrease in the width between 22 °C and -196 °C was 10.44 cm⁻¹ (59%). As shown in Figure 7-41, the variability between individual measurements decreased at low temperatures and the average SNR increased at lower temperatures as consistent with previous results. Similar to ectoine, the higher definition within the spectra at cryogenic temperatures revealed a few minor bands such as the 1628 cm⁻¹ and 1658 cm⁻¹ bands. The minimum peak-to-peak distance in the spectra of palmitic acid was 28.04 cm⁻¹ at 22 °C, 23.53 cm⁻¹ at -100 °C and 26.17 cm⁻¹ at -196 °C.

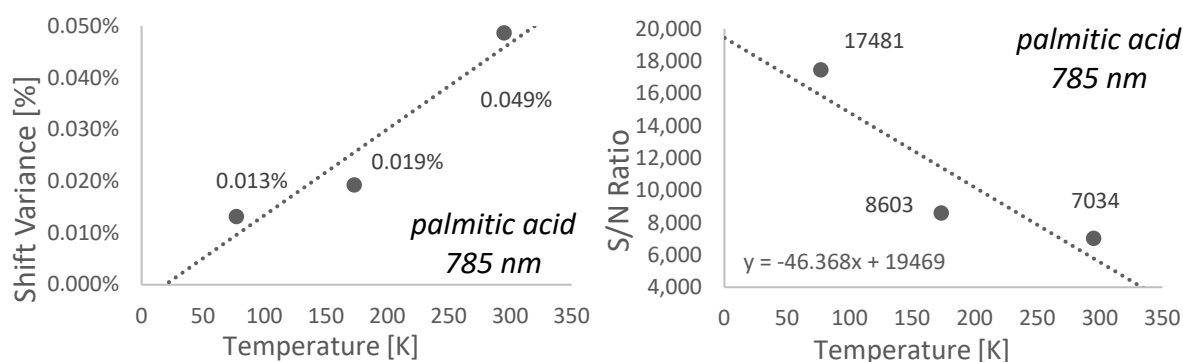


Figure 7-41 Raman shift variance (left) and SNR change (right) recorded in the spectra of palmitic acid across 22 °C, -100 °C and -196 °C at 785 nm excitation

7.8 Carbohydrates

The only carbohydrate examined was trehalose, which is shown at 22 °C, -100 °C and -196 °C at 532 nm in Figure 7-42. While trehalose signature is visible at 785 nm at room temperature, it is not detectable at all at low temperatures, which prevented any analysis at this wavelength. With the exception of a few bands, most trehalose Raman bands shift to higher frequencies at cryogenic temperatures. The profile of the shift change corresponds to the one described previously for other samples.

The highest change in the shift from 22 °C to -196 °C was 3.18 cm⁻¹ at the 540 cm⁻¹ band which is comparable to the maximum shift change observed in the spectra of RNA and palmitic acid. As already discussed, palmitic acid and RNA have similarly complex structures and as shown in Figure 7-42, trehalose is also structurally similar to RNA due to its aromatic base. The highest negative change was 1.78 cm⁻¹ at the 520 cm⁻¹ band. A few bands proved relatively stable across all temperatures with 3 bands shifting by less than 0.5 cm⁻¹. The shift change observed for most trehalose Raman bands was well within or over the 3 σ region.

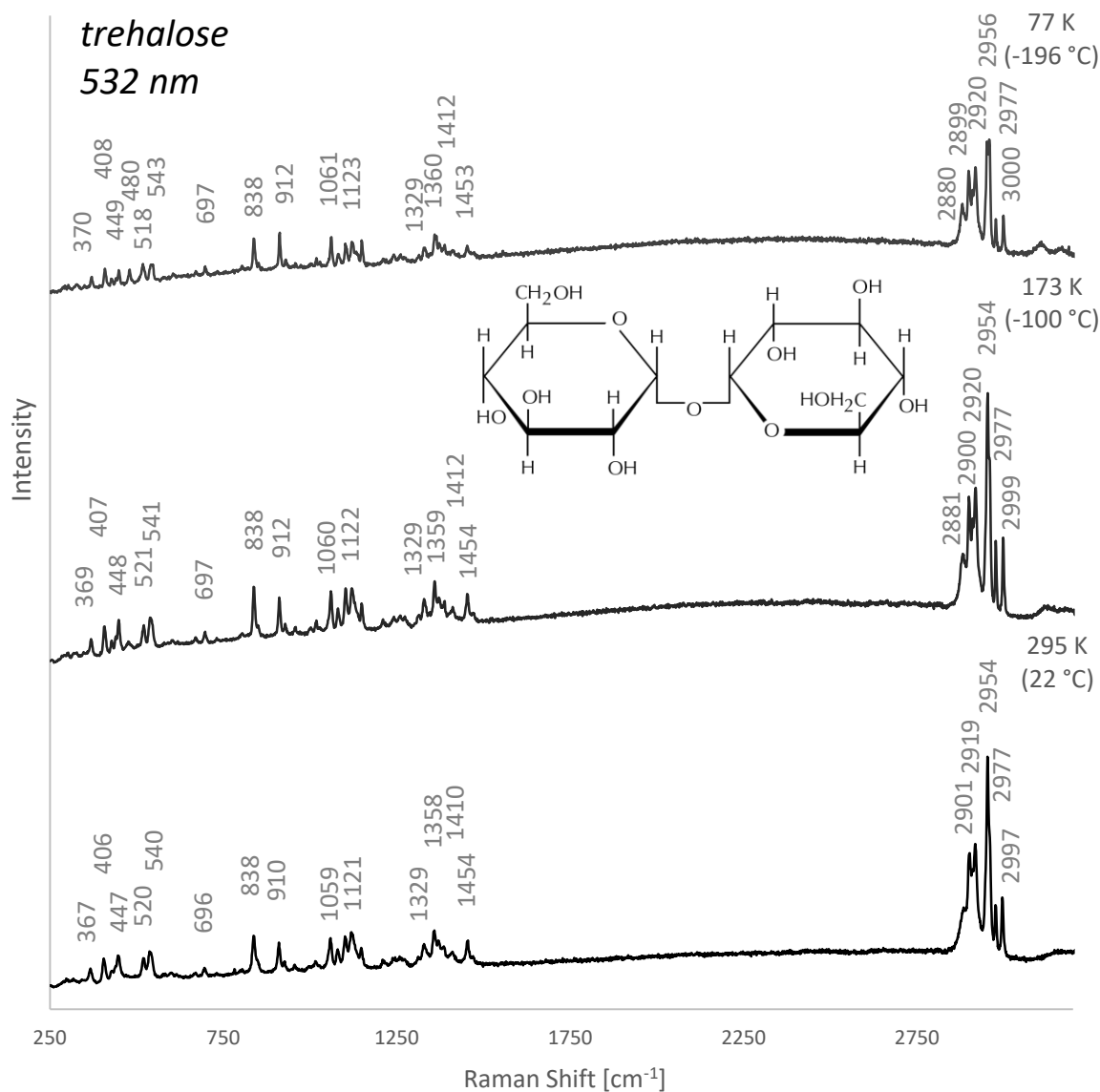


Figure 7-42 Raman spectra of trehalose at 22 °C, -100 °C and -196 °C at 532 nm excitation (538.8 mJ total energy dose and the fluence of 2.35 MJ/cm²)

Trehalose is mildly fluorescent at room temperature and similar to other fluorescent molecules, the SNR of trehalose decreases at low temperatures due to the increase in the fluorescent background. This is quantified in Figure 7-43. The variability between different spectra as well as the Raman band width decreased at low temperatures, which makes the measurement at low temperatures both more accurate and precise. As a result of this, the spectra shown in Figure 7-42 showcase a higher definition at low temperatures even despite the decreased SNR. This also revealed two new bands, 480 cm^{-1} and 2881 cm^{-1} , which were not distinguishable at room temperature.

Overall, the highest decrease in the band width between the temperature extremes was 9.9 cm^{-1} (59%) at the 1121 cm^{-1} band. The minimum peak-to-peak distance in the trehalose spectra was 18.04 cm^{-1} at $22\text{ }^{\circ}\text{C}$, 18.83 cm^{-1} at $-100\text{ }^{\circ}\text{C}$ and 19 cm^{-1} at $-196\text{ }^{\circ}\text{C}$.

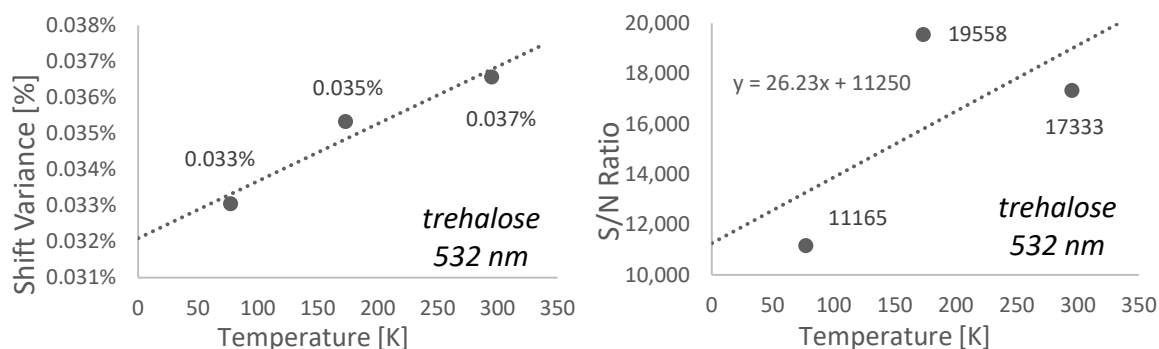


Figure 7-43 Raman shift variance (left) and SNR change (right) recorded in the spectra of trehalose across $22\text{ }^{\circ}\text{C}$, $-100\text{ }^{\circ}\text{C}$ and $-196\text{ }^{\circ}\text{C}$ at 532 nm excitation

7.9 Isoprenoids

Both pristane and squalane are detectable at both 785 nm and 532 nm excitation and tendencies in the cryogenic changes proved similar at both excitations. However, bands between 800 cm^{-1} to 1500 cm^{-1} are proportionally much less visible in the spectra at 532 nm due to the heightened signal of the Raman bands in the region of $2800\text{--}3000\text{ cm}^{-1}$ at this excitation. The results will therefore be shown and discussed using the 785 nm excitation spectra.

The spectra of pristane and squalane at $22\text{ }^{\circ}\text{C}$, $-100\text{ }^{\circ}\text{C}$ and $-196\text{ }^{\circ}\text{C}$ at 785 nm are shown in Figure 7-44 and Figure 7-45 respectively together with their molecular structure. As shown in the figures, the spectra of pristane and squalane are almost identical, which makes studying the spectral changes at cryogenic temperatures a potentially very valuable asset. In both cases, the definition within the spectra visibly improved at lower temperatures. This allowed the detection of previously unresolvable bands, namely 835 cm^{-1} and 871 cm^{-1} , 1170 cm^{-1} in pristane and 835 cm^{-1} , 868 cm^{-1} , 1171 cm^{-1} and 1337 cm^{-1} in the squalane spectra. This higher spectral quality can be attributed to the SNR increase at cryogenic temperatures, which is quantified in Figure 7-46, shifting of Raman band frequencies resulting in a higher peak-to-peak distance and the significant band narrowing. In the spectra of pristane, the highest band width decrease was 45.78 cm^{-1} (78%) and in the squalane spectra 56.96 cm^{-1} (77%). Similar to other examined samples, the variability of the measurements also decreased at lower temperatures as shown in Figure 7-47.

Nevertheless, despite the higher precision and accuracy of the measurements together with the higher spectral quality, distinguishing the two compounds could be challenging. As shown in

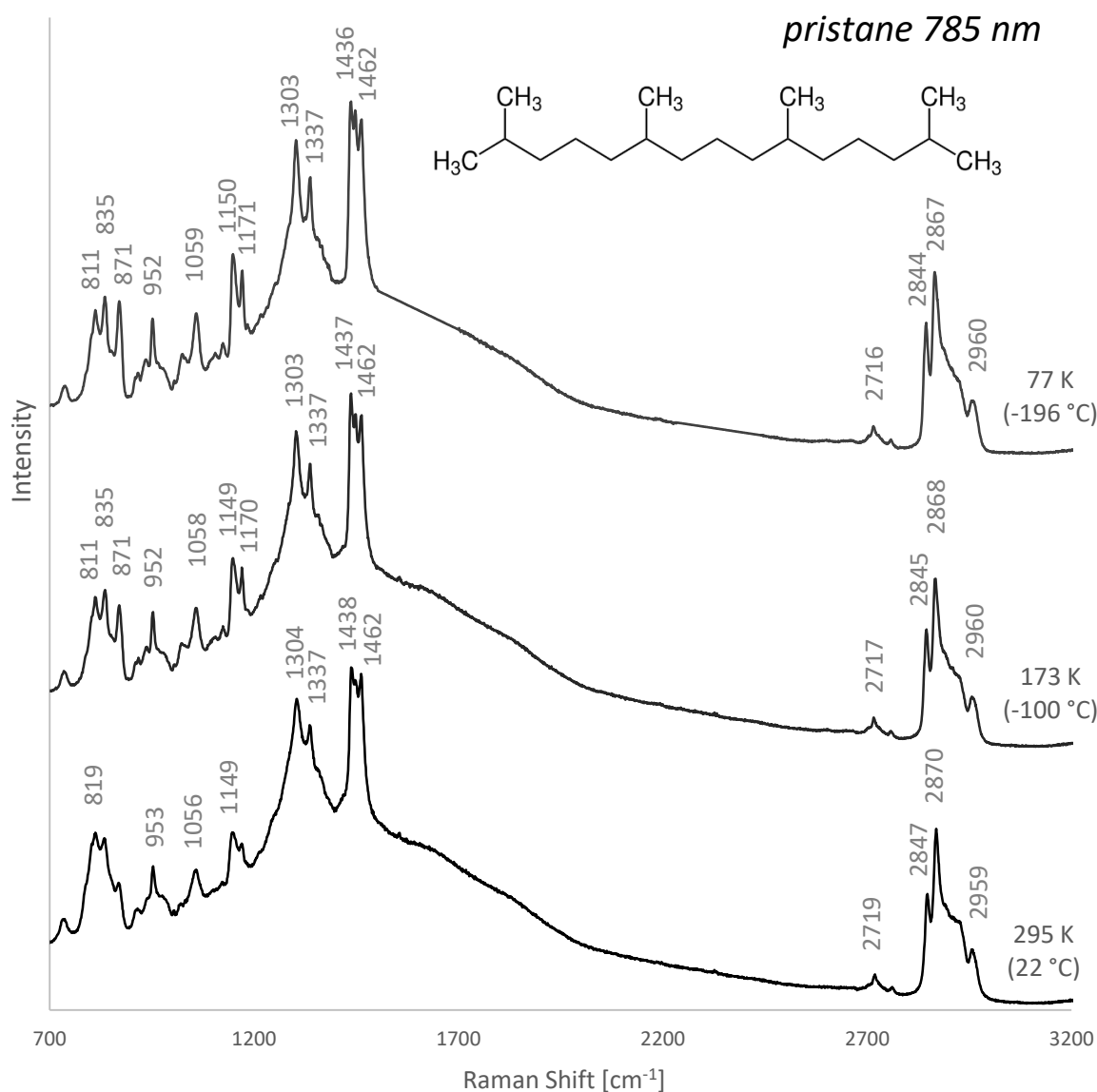


Figure 7-44 Raman spectra of pristane at 22 °C, -100 °C and -196 °C at 785 nm excitation

Figure 7-44 and Figure 7-45, the remarkably similar signatures of the two isoprenoids also display similar tendencies in the band shift changes at low temperatures. Moreover, the minor differences in the spectra of pristane and squalane at room temperature seem to disappear or become less prominent at cryogenic temperatures. Specifically, the Raman band nominally at 819 cm^{-1} in pristane and 816 cm^{-1} in squalane both shift to 811 cm^{-1} at -196 °C. Likewise, 953 cm^{-1} (pristane) and 954 cm^{-1} (squalane) both shift to 952 cm^{-1} and the 1056 cm^{-1} (pristane) and 1058 cm^{-1} (squalane) bands both converge to a higher frequency within 1 cm^{-1} of each other (between 1059 cm^{-1} and 1060 cm^{-1} respectively). Furthermore, one of the most dominant bands at 1442 cm^{-1} at 22 °C in squalane shifts to 1439 cm^{-1} at -196 °C and less than 1 cm^{-1} from the 1438 cm^{-1} band in the spectra of pristane. This could potentially lead to misidentification if cryogenically induced spectral changes are not known or considered. Additionally, bands at 1462 cm^{-1} (pristane) and 1459 cm^{-1} (squalane), which could be used to distinguish the two

compounds at room temperature, converge to a frequency that is within less than 1 cm^{-1} of each other at $-196 \text{ }^{\circ}\text{C}$ (1462 cm^{-1} and 1461 cm^{-1} respectively).

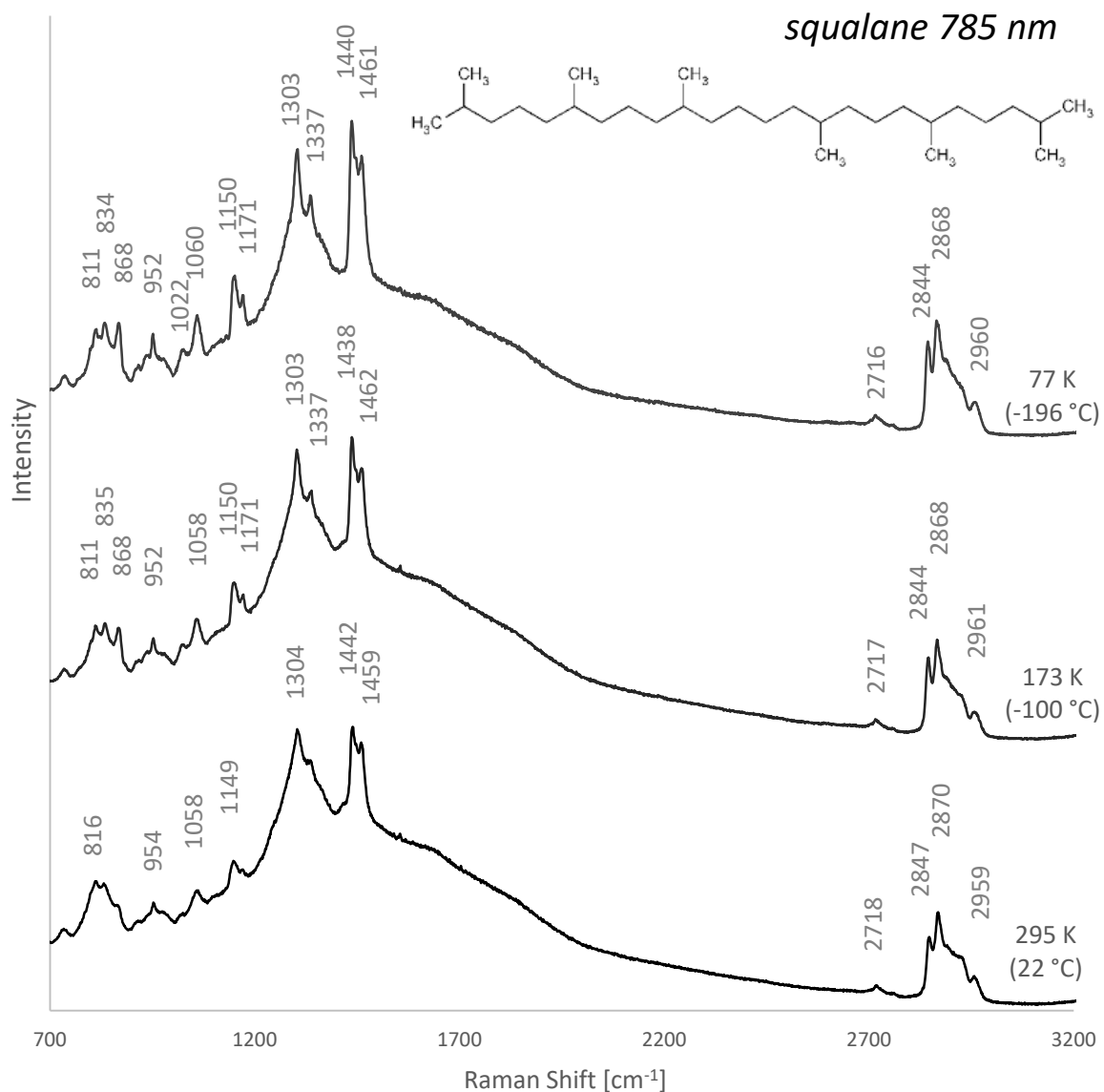


Figure 7-45 Raman spectra of squalane at 22 °C, -100 °C and -196 °C at 785 nm excitation

While these changes make the two compounds much harder to distinguish at low temperatures and could also cause misidentification if only room temperature reference spectra are used, some cryogenically induced changes that could prove to be very useful for differentiating between the two samples have been observed.

Firstly, the maximum change in the Raman shift in the spectra of pristane is a decrease by 8.29 cm^{-1} , which is almost twice as much as the maximum shift change in the spectra of squalane, i.e. decrease by 4.29 cm^{-1} . Both occurred at the same band (819 cm^{-1} and 816 cm^{-1}). Considering previous results from other samples, this variation is expected as squalane is a longer molecule and the general trend indicates that larger and more complex molecules display lower changes in

the Raman shift at low temperatures. With the maximum shift change of 4.29 cm^{-1} , squalane places just below carotenoids, which have similarly long molecular chains but also include an aromatic ring, which is not present in squalane. Likewise, the pristane band nominally at 1462 cm^{-1} seems to be relatively stable and remains at this frequency even at low temperatures while the corresponding 1459 cm^{-1} squalane band at room temperature moves to 1462 cm^{-1} at $-100\text{ }^{\circ}\text{C}$ and 1461 cm^{-1} at $-196\text{ }^{\circ}\text{C}$. Considering the shift change amplitude observed in the spectra of squalane, this is the largest change towards higher frequencies and sigma error bar analysis shows no indication of experimental error or variation for these changes. While this shifts the two bands closer, this variation in the shift change could also be used to distinguish the two molecules provided that measurements at two different temperature points are available. Since the spectral signature of pristane and squalane are almost identical even at room temperature, cryogenic measurements in conjunction with regular room temperature measurements could be helpful in distinguishing these two molecules for many applications besides the exploration of Europa.

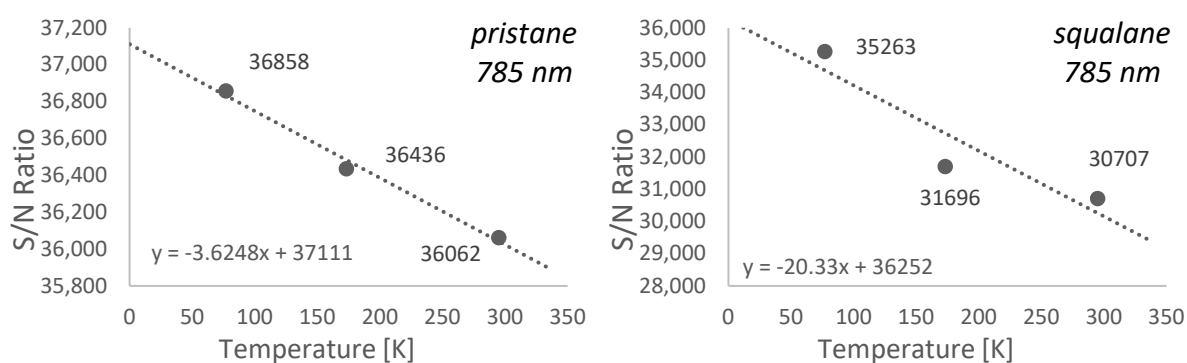


Figure 7-46 SNR change recorded in the spectra of pristane (left) and squalane (right) across $22\text{ }^{\circ}\text{C}$, $-100\text{ }^{\circ}\text{C}$ and $-196\text{ }^{\circ}\text{C}$ at 785 nm excitation

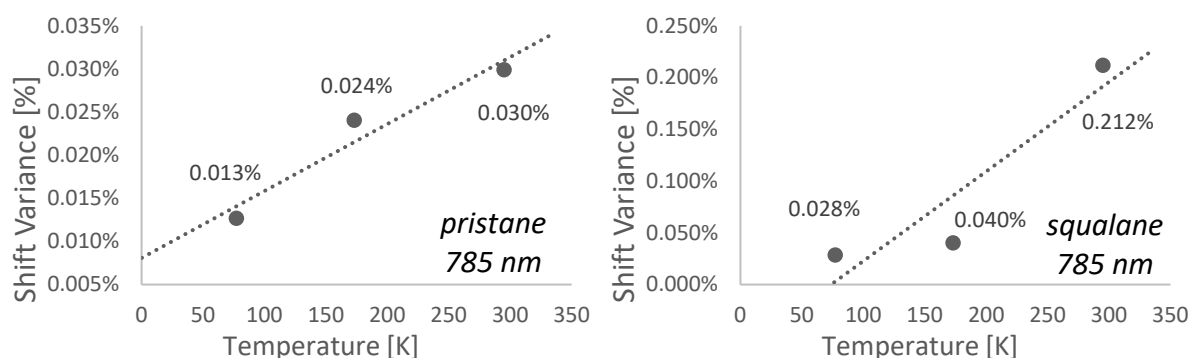


Figure 7-47 Raman shift variance recorded in the spectra of pristane (left) and squalane (right) across $22\text{ }^{\circ}\text{C}$, $-100\text{ }^{\circ}\text{C}$ and $-196\text{ }^{\circ}\text{C}$ at 785 nm excitation

Both isoprenoids followed a similar profile of change as already described for other compounds for both the Raman shift and band width. The minimum peak-to-peak distance in the pristane spectra was 23.09 cm^{-1} at $22\text{ }^{\circ}\text{C}$, 21.18 cm^{-1} at $-100\text{ }^{\circ}\text{C}$ and 20.95 cm^{-1} at $-196\text{ }^{\circ}\text{C}$. For squalane the minimum peak-to-peak distance in the spectra was 17.06 cm^{-1} at $22\text{ }^{\circ}\text{C}$, 21.13 cm^{-1} at $-100\text{ }^{\circ}\text{C}$ and 20.58 cm^{-1} at $-196\text{ }^{\circ}\text{C}$.

7.10 Steranes

The comparison of room temperature spectra of 5 α cholestane and spectra obtained at cryogenic temperatures at 785 nm excitation is shown in Figure 7-48. A good quality spectrum of 5 α cholestane is also obtainable at 532 nm, however, due to the relative enhancement of cholestane bands in the region above 2800 cm^{-1} , lower frequency bands show much lower signals, which makes their comparison across different temperatures less accurate. Since the general trends observed at cryogenic temperatures are similar at both excitations, the 785 nm spectra will be used to show the results of this study.

As shown in Figure 7-48, 5 α cholestane has a very complex Raman signature featuring numerous Raman bands. Similar to other samples, the definition within the spectra rises at low temperatures with many bands becoming more prominent. This also leads to the detection of bands unresolvable at room temperature, e.g. bands at 838 cm^{-1} , 919 cm^{-1} and 1102 cm^{-1} . In many instances, measurements at cryogenic temperatures also show bands splitting into multiple distinct bands. Just like in previous samples, this is the result of significant narrowing of the Raman band width as well as SNR increase and frequency shifts at low temperatures.

Most bands within the spectra of 5 α cholestane remain relatively stable across all temperatures and shifts to both lower and higher frequencies are common. In both cases, the profile of the shift change corresponds to the gradually decreasing rate of change curve described previously (e.g. Section 7.1). The highest change in the shift from $22\text{ }^{\circ}\text{C}$ to $-196\text{ }^{\circ}\text{C}$ was 3.87 cm^{-1} at the 2952 cm^{-1} band. Interestingly, the highest negative change between the temperature extremes (3.65 cm^{-1} at 1455 cm^{-1}) is comparable in magnitude. This was not observed in other samples where the magnitude of the negative changes was typically much lower than the positive change (i.e. shifting to higher frequencies). The highest change in the Raman shift in the spectra of cholestane is very similar to the maximum changes in the shift observed in palmitic acid and just below the magnitude observed in carotenoids. While cholestane is a shorter molecule than both palmitic acid and carotenoids, it also contains a complex aromatic structure, which may be preventing any larger changes to occur.

As clearly visible in Figure 7-48, significant narrowing of the Raman bands was observed at low temperatures with the highest decrease in the band width between 22 °C and -196 °C being as high as 9.2 cm⁻¹ (50%) at the 1174 cm⁻¹ band.

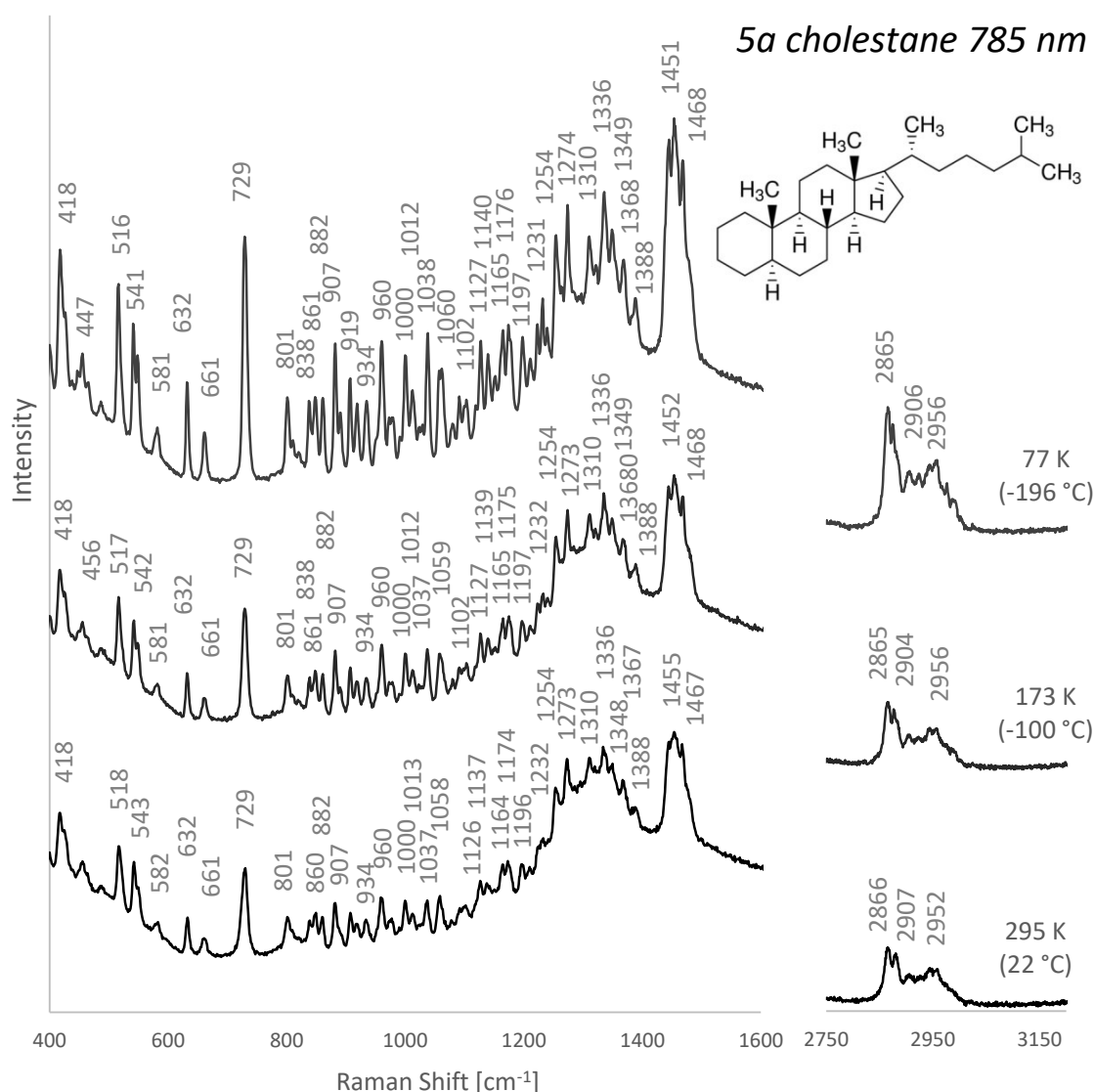


Figure 7-48 Raman spectra of 5 α cholestane at 22 °C, -100 °C and -196 °C at 785 nm excitation, note that there are no Raman bands between 1600 cm⁻¹ and 2750 cm⁻¹ and this region was excluded for clarity

Similar to previous results observed across all examined samples, the variability between individual measurements decreased with decreasing temperature, which is shown in Figure 7-49. The figure also quantifies the SNR increase of the spectra from room temperature to -196 °C, which is also consistent with the results of other non-fluorescent molecules examined in this study.

Due to the numerous Raman bands in the cholestane signature, the minimum peak-to-peak distance is much lower than in most other samples. The minimum peak-to-peak distance in the 5 α cholestane spectra was 9.94 cm⁻¹ at 22 °C, 10.03 cm⁻¹ at -100 °C and 10.9 cm⁻¹ at -196 °C, all occurring between 1164 cm⁻¹ and 1174 cm⁻¹. In this case, both of the bands have comparable signal strength and width, which would result in a wider band with an incorrect frequency. Considering the FWHM width of the bands, which was between 9-11 cm⁻¹, the spectral resolution to resolve the bands would have to be around 4.5-6 cm⁻¹. However, due to the high density of peaks in certain spectral regions, there are a number of other bands with a peak-to-peak distance as low as 11-12 cm⁻¹. Some adjacent bands with this low peak-to-peak distance, such as 1126 cm⁻¹ and 1137 cm⁻¹ or 1000 cm⁻¹ and 1012 cm⁻¹, feature one wider and higher intensity band and another relatively wide but lower intensity band, which requires spectral resolution much higher than the nominal peak-to-peak distance in order to prevent the bands to blend into one very wide band with a skewed frequency measurement. Considering the width and relative signal strength of the bands, the spectral resolution necessary to resolve bands with such a peak-to-peak distance may be as high as 3-6 cm⁻¹.

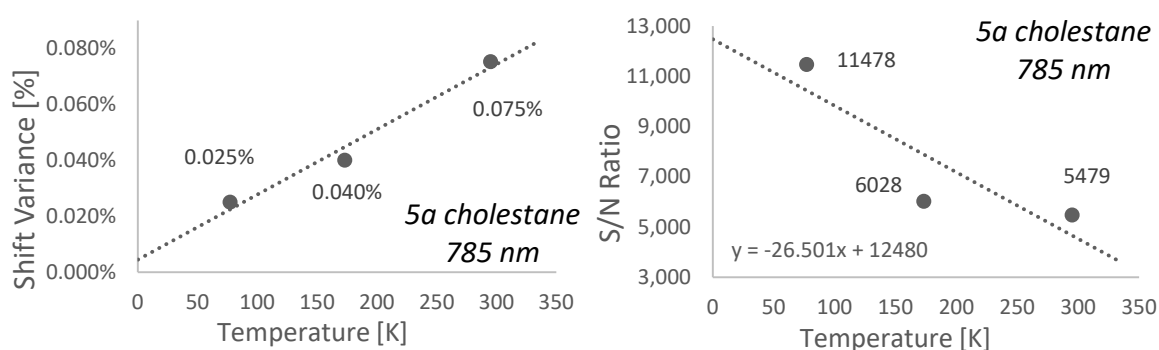


Figure 7-49 Raman shift variance (left) and SNR change (right) recorded in the spectra of 5 α cholestane across 22 °C, -100 °C and -196 °C at 785 nm excitation

7.11 Nucleobases

All examined nucleobases are heavily fluorescent at 532 nm excitation. Similar to other fluorescent molecules, the fluorescence in the spectra of nucleobases increases at low temperatures, which in some cases prevents their detection at these temperatures. Specifically, the adenine Raman signature is visible at room temperature even despite the strong fluorescence background but becomes increasingly overshadowed by the increasing fluorescence at low temperatures and it is completely unresolvable at -196 °C. This is shown in Figure 7-50 and a similar trend was also observed in the spectra of guanine. Similarly, the signature of cytosine, which is resolvable even despite the fluorescence at 22 °C becomes only resolvable to a certain

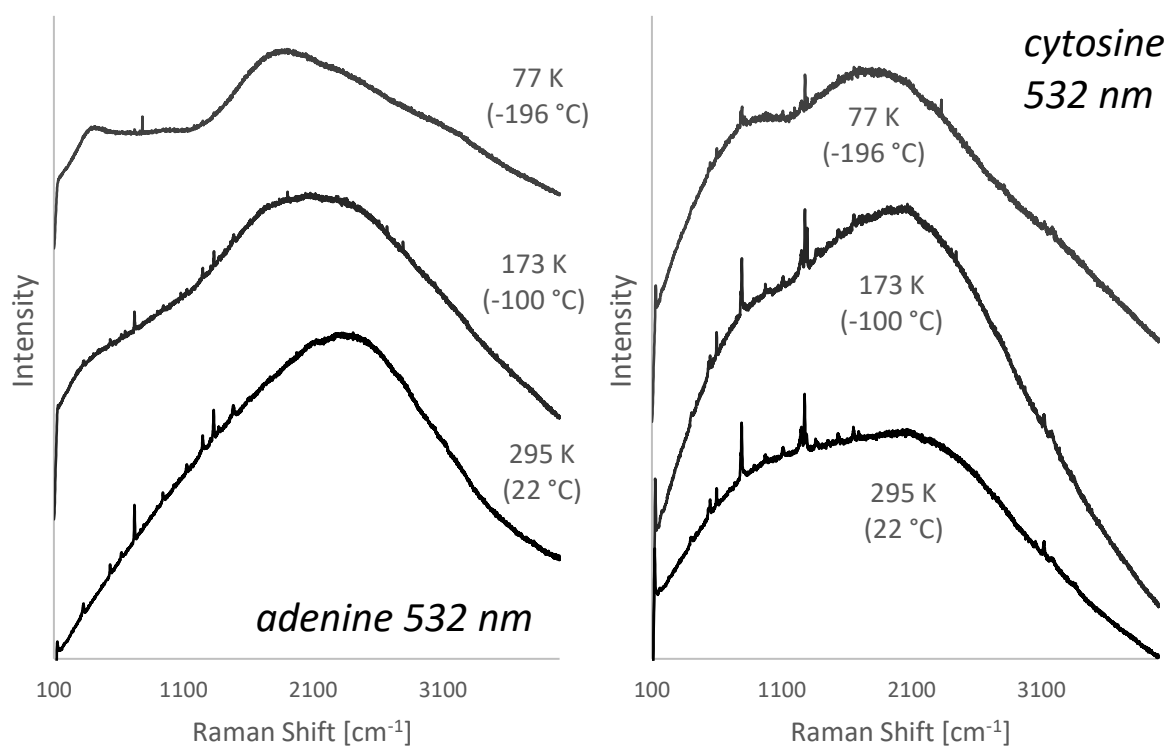


Figure 7-50 Raman spectra of adenine and cytosine at 22 °C, -100 °C and -196 °C at 532 nm excitation

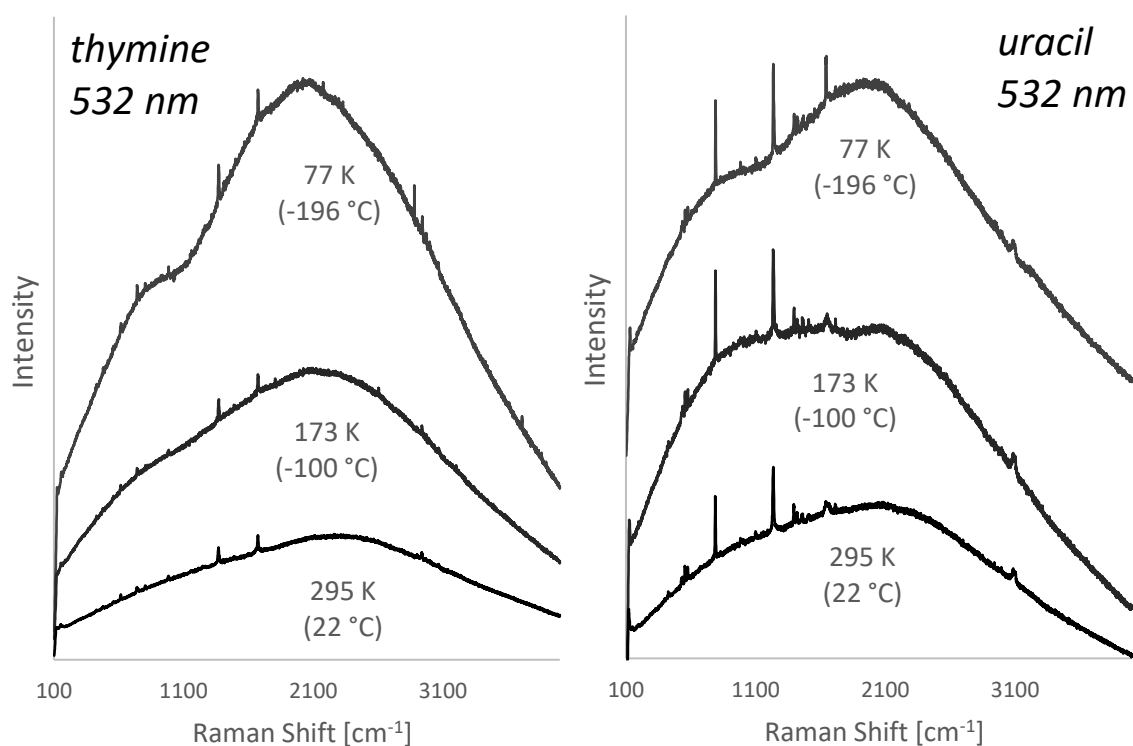


Figure 7-51 Raman spectra of thymine and uracil at 22 °C, -100 °C and -196 °C at 532 nm excitation

extend at $-196\text{ }^{\circ}\text{C}$ as only some major bands remain visible in the spectrum. This is shown in Figure 7-50. Thymine, shown in Figure 7-51, is barely resolvable even at room temperature due to the severe fluorescence background but some major bands in the spectra remain visible and distinguishable even despite the increased fluorescence at cryogenic temperatures. Uracil, the spectrum of which is the least affected by fluorescence even at room temperatures, is the only nucleobase that remains fully identifiable at cryogenic temperatures at 532 nm. This is shown in Figure 7-51.

The SNR comparison of all examined nucleobases at 532 nm at various temperatures is shown in Figure 7-52. The SNR of all nucleobases decreases at lower temperatures with the highest SNR drop between the temperature extremes being full 100% in the spectra of adenine and the lowest only 2.48% in uracil. The SNR of cytosine decreased by 68.42% from $22\text{ }^{\circ}\text{C}$ to $-196\text{ }^{\circ}\text{C}$ and the SNR of guanine and thymine by 31.28% and 29.71% respectively.

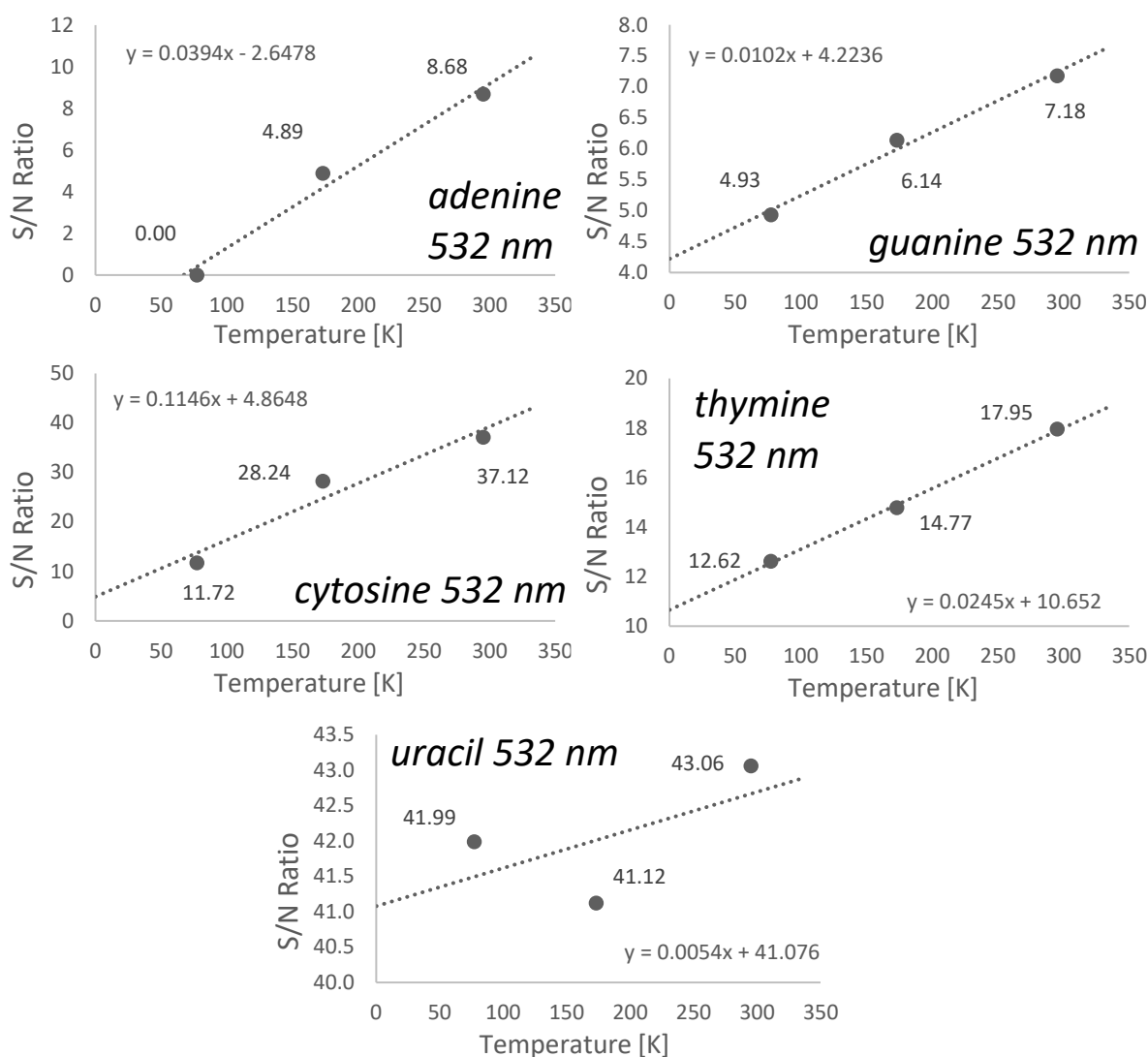


Figure 7-52 SNR change recorded in the spectra of nucleobases across $22\text{ }^{\circ}\text{C}$, $-100\text{ }^{\circ}\text{C}$ and $-196\text{ }^{\circ}\text{C}$ at 532 nm excitation

Due to the severe fluorescence background in the spectra of nucleobases even at room temperatures, the results and comparison of the cryogenic changes will be primarily discussed using the spectra obtained at 785 nm, where only adenine and thymine are mildly fluorescent.

The description of the cryogenically induced changes in the spectra of each nucleobase at 785 nm is provided individually in Sections 7.11.1 to 7.11.5, however, a couple of trends among all the nucleobases are described here.

Similar to other samples examined in this study, most bands within the spectra of nucleobases shift to higher frequencies at low temperatures and the shift change follows the same pattern as

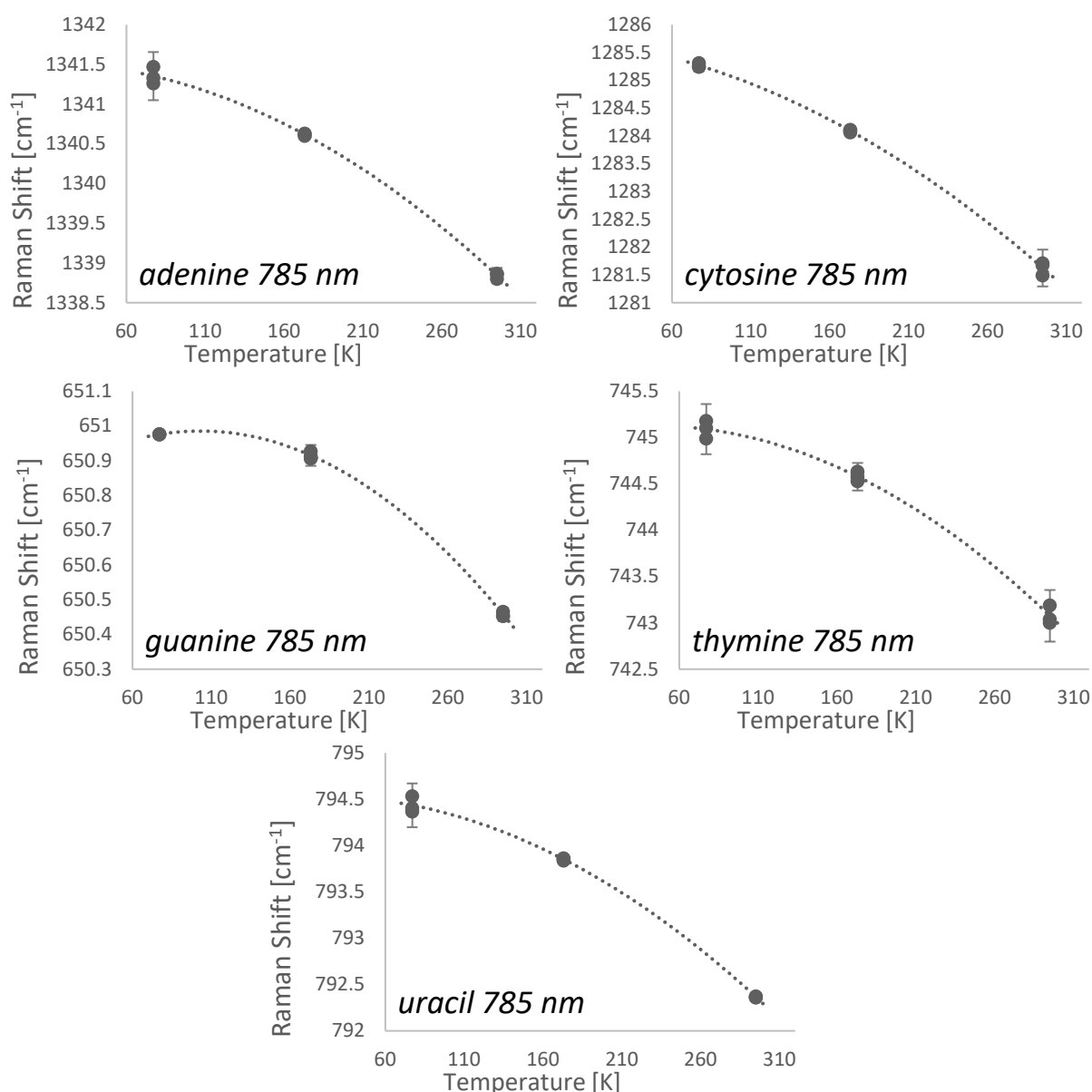


Figure 7-53 Raman shift change from room temperature to $-196\text{ }^{\circ}\text{C}$ in the spectra of nucleobases.

The trend observed at the most dominant Raman band in the spectra is shown together with 2σ error bars.

already described in previous sections. This is shown in Figure 7-53 with 2σ error bars. The figure shows the trend for the most dominant Raman band in the spectra, however, just like in other samples, most other bands follow the same pattern.

Likewise, all bands within the spectra of nucleobases showed significant narrowing at lower temperatures and the change followed a similar gradual pattern but inverse. This has also been shown previously for other samples.

The variability between individual measurements recorded in the spectra of nucleobases at 785 nm is shown in Figure 7-54. As shown in the figure, the variability decreased approximately linearly towards low temperatures for all nucleobases except for adenine, where the variability increased at low temperatures. As adenine is fluorescent at room temperature at 785 nm excitation, this variability increase can be attributed to the effects of the fluorescence

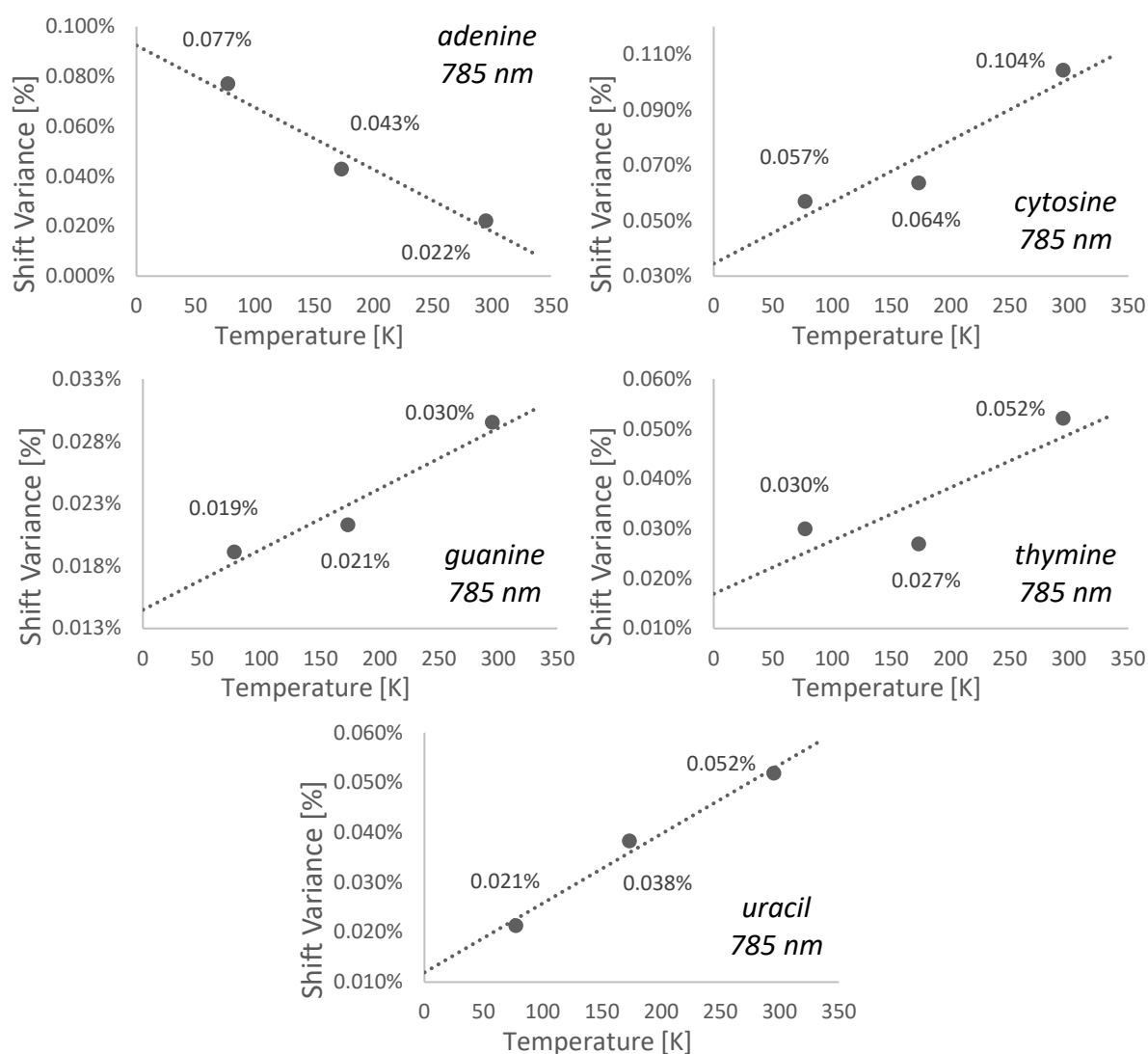


Figure 7-54 Raman shift variance recorded in the spectra of nucleobases across 22 °C, -100 °C and -196 °C at 785 nm excitation

background, which rises at low temperatures. It is important to note that thymine, which is also fluorescent at 785 nm, does not display the same trend as adenine. This may be attributed to the fact that the fluorescence background in thymine is very low and barely detectable, especially compared to the fluorescence in adenine.

This fluorescence rise is also reflected in the adenine SNR change between room temperature and -196 °C. This is shown in Figure 7-55 together with the SNR change of all other nucleobases at 785 nm. Contrary to the SNR trends observed in many other samples, the SNR in nucleobases decreases at lower temperatures even without fluorescence present in the spectra. The only exception to this is uracil, which shows an increase in the SNR at low temperatures. Uracil is the simplest nucleobase and displays a very high SNR spectrum at room temperature compared to other nucleobases. It is also the only nucleobase that contains only one aromatic ring with only

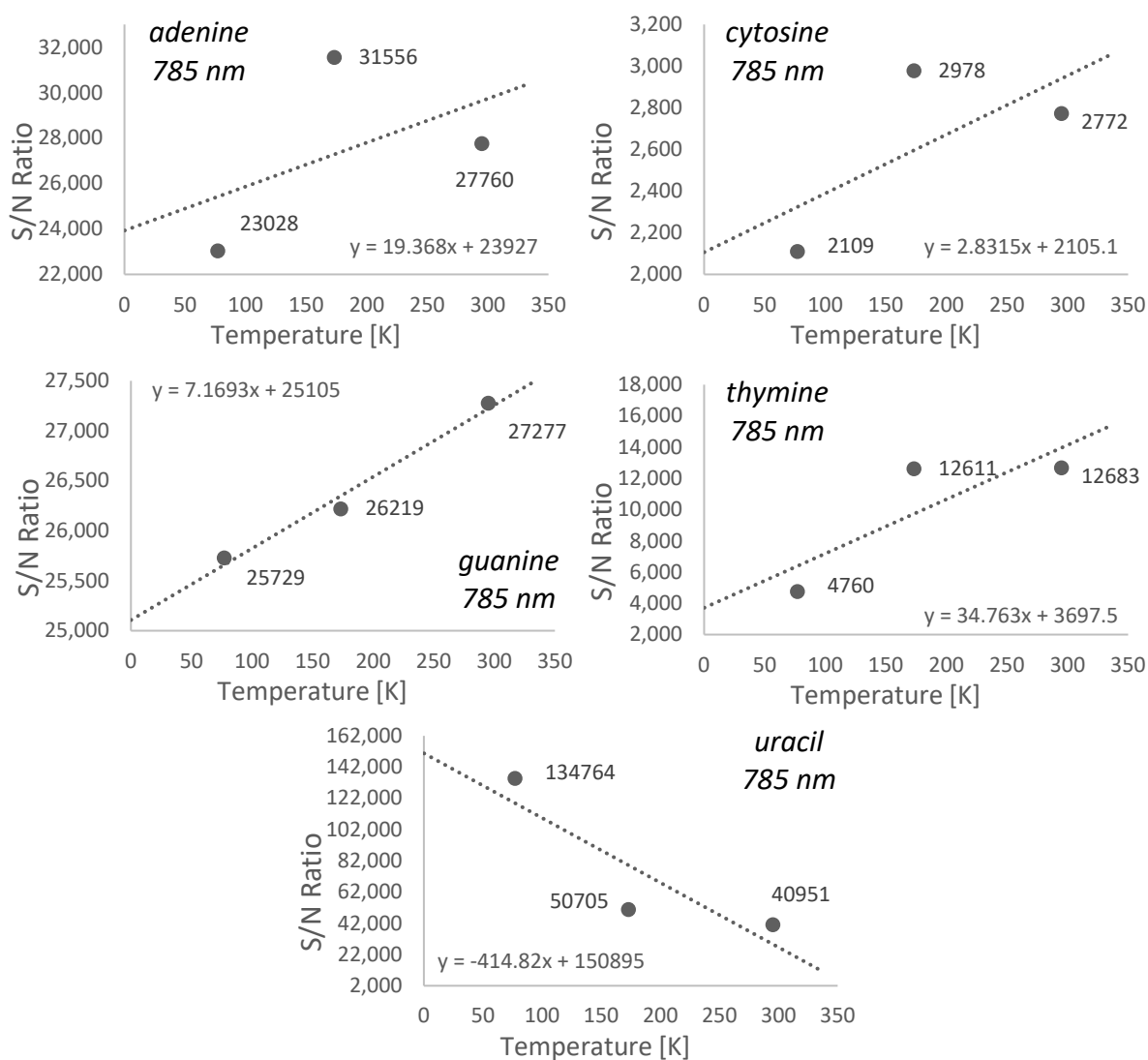


Figure 7-55 SNR change recorded in the spectra of nucleobases across 22 °C, -100 °C and -196 °C at 785 nm excitation

double bonds outside of the ring. All other nucleobases include either two rings or a group outside of the ring attached via a single bond, or both. Double bonds are stronger and harder to break by environmental disturbances. These may all be factors contributing to the cryogenically induced signal increase in the spectra of uracil.

7.11.1 Adenine

The comparison of adenine spectra at 785 nm collected at room temperature, $-100\text{ }^{\circ}\text{C}$ and $-196\text{ }^{\circ}\text{C}$ is shown in Figure 7-56. Adenine is the only nucleobase that is fluorescent at 785 nm. As shown in Figure 7-56, the fluorescence background is only mild at room temperatures but it rises at lower temperatures and visibly decreases the SNR of adenine at $-196\text{ }^{\circ}\text{C}$. The SNR decrease is quantified in Figure 7-55.

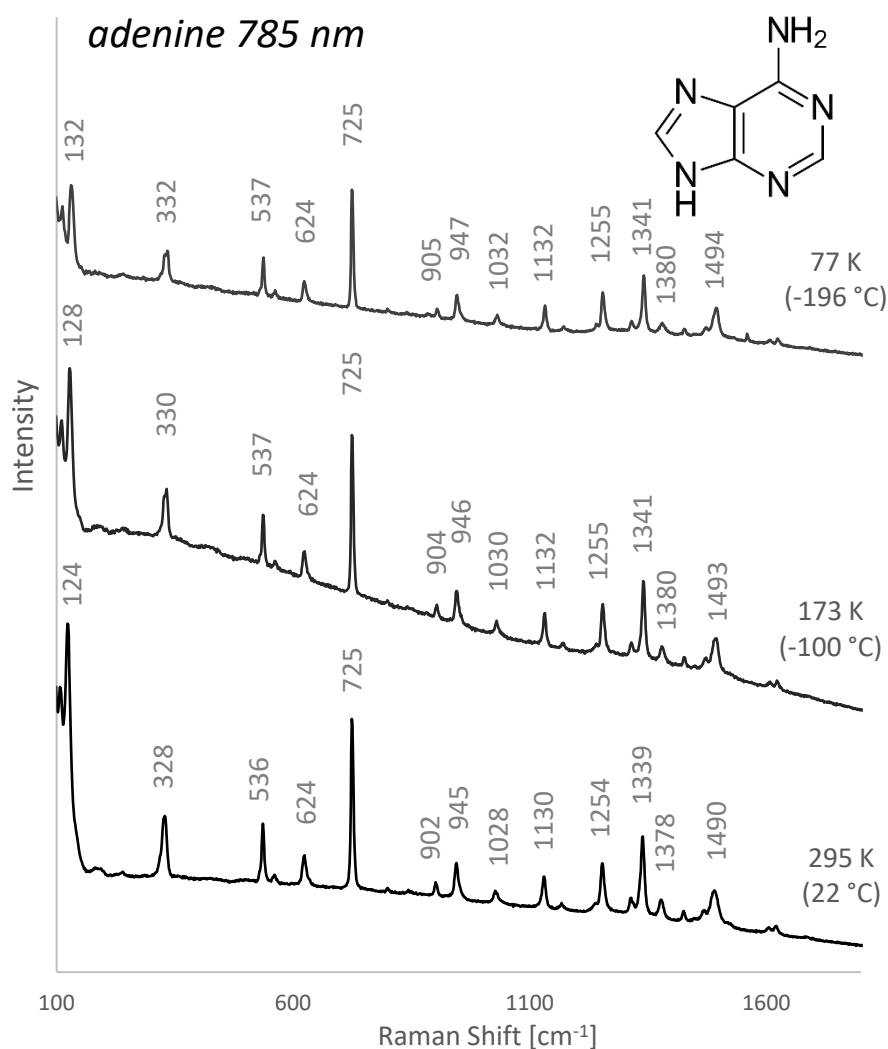


Figure 7-56 Raman spectra of adenine at $22\text{ }^{\circ}\text{C}$, $-100\text{ }^{\circ}\text{C}$ and $-196\text{ }^{\circ}\text{C}$ at 785 nm excitation

As opposed to most other examined samples, all Raman bands within the adenine spectra shift to higher frequencies. While no shifts to lower frequencies were observed, adenine's most dominant

band at 725 cm^{-1} , and the 624 cm^{-1} band remain relatively stable across all temperatures and only shift by less than 0.3 cm^{-1} at $-196\text{ }^{\circ}\text{C}$. Sigma error bar analysis indicates that the shift observed at 624 cm^{-1} is a true shift due to temperature variation as it lies within the 3σ error region. The miniscule shift of 0.13 cm^{-1} observed at the 725 cm^{-1} lies in the 1σ region, which would suggest it may have been the result of variance in the data. However, given that the 2σ threshold is only 0.38 cm^{-1} and the 3σ threshold 0.58 cm^{-1} , it is reasonable to assume that this band is naturally relatively stable regardless. The 725 cm^{-1} band is attributed to ring breathing and the 624 cm^{-1} band to adenine's 6-membered ring deflection [352]. As shown for amino acids in Section 7.1, these vibrational modes typically generate the lowest shifts in frequency. As such, the relative stability of these bands is consistent with previous results. The highest shift from $22\text{ }^{\circ}\text{C}$ to $-196\text{ }^{\circ}\text{C}$ in the spectra of adenine was 8.01 cm^{-1} at the 124 cm^{-1} band. This is a maximum shift magnitude comparable to the one observed in the spectra of tryptophan, which is also an aromatic molecule of similar complexity to adenine that also shows mild fluorescence at 785 nm .

Similar to other samples, the Raman band width within the spectra of adenine decreased significantly at cryogenic temperatures. The highest band width decrease was by as much as 5.48 cm^{-1} (28%). The minimum peak-to-peak distance in the adenine spectra was 39.2 cm^{-1} at $22\text{ }^{\circ}\text{C}$, 39.35 cm^{-1} at $-100\text{ }^{\circ}\text{C}$ and 38.76 cm^{-1} at $-196\text{ }^{\circ}\text{C}$.

7.11.2 Guanine

The spectra of guanine at 785 nm at room temperature, $-100\text{ }^{\circ}\text{C}$ and $-196\text{ }^{\circ}\text{C}$ are shown in Figure 7-57. As already discussed, despite not being fluorescent at 785 nm , the spectra of guanine show a decrease in its SNR at lower temperatures. However, Figure 7-57 shows that despite the SNR drop, measurements at cryogenic temperatures can still provide higher definition spectra. Specifically, the band at 563 cm^{-1} visibly reveals two distinct peaks at lower temperatures, which were not resolvable at room temperature. Similarly, the 166 cm^{-1} band appears as a single peak at $22\text{ }^{\circ}\text{C}$, however, the measurement at $-196\text{ }^{\circ}\text{C}$ clearly shows it may actually be three different peaks. The three bands between 1366 cm^{-1} and 1428 cm^{-1} also show much higher definition at $-196\text{ }^{\circ}\text{C}$ than at room temperature. This is due to the narrowing of the bands at low temperatures and shifts in their frequency.

Shifts to both lower and higher frequencies were observed and the highest shift from $22\text{ }^{\circ}\text{C}$ to $-196\text{ }^{\circ}\text{C}$ was 6.63 cm^{-1} . This is the lowest maximum shift among all nucleobases. This is an expected result as guanine, with its two aromatic rings and two groups ($\text{O}=\text{}$ and $\text{NH}_2\text{-}$) outside of the rings, is the most structurally complex nucleobase. Interestingly, the highest shift to lower frequencies was similar in magnitude to the highest positive shift, i.e. 6.60 cm^{-1} . This band is

associated with ring stretching [352]. Some bands within the spectra of guanine also remained relatively stable across all temperatures, namely bands at 495 cm^{-1} , 562 cm^{-1} , 650 cm^{-1} , 850 cm^{-1} and 1268 cm^{-1} . These bands only shifted by less than 0.55 cm^{-1} . Sigma error bar analysis indicates these shifts are not due to variation in the data except for the 595 cm^{-1} band shift of 0.04 cm^{-1} , which lies in the 1σ error region. Given that the 3σ threshold for this band is only 0.12 cm^{-1} , however, this band may be assumed to be highly stable across all temperatures anyway. The bands are attributed to 6-membered ring deflection (495 cm^{-1} and 562 cm^{-1}), ring breathing (650 cm^{-1}), 5-membered ring deflection (850 cm^{-1}) and ring stretching (1268 cm^{-1}) [352]. These vibrational modes, i.e. stretching and ring deflection, have been previously shown to result in the lowest or negative shift changes and as such the stability of these peaks is in line with previous results.

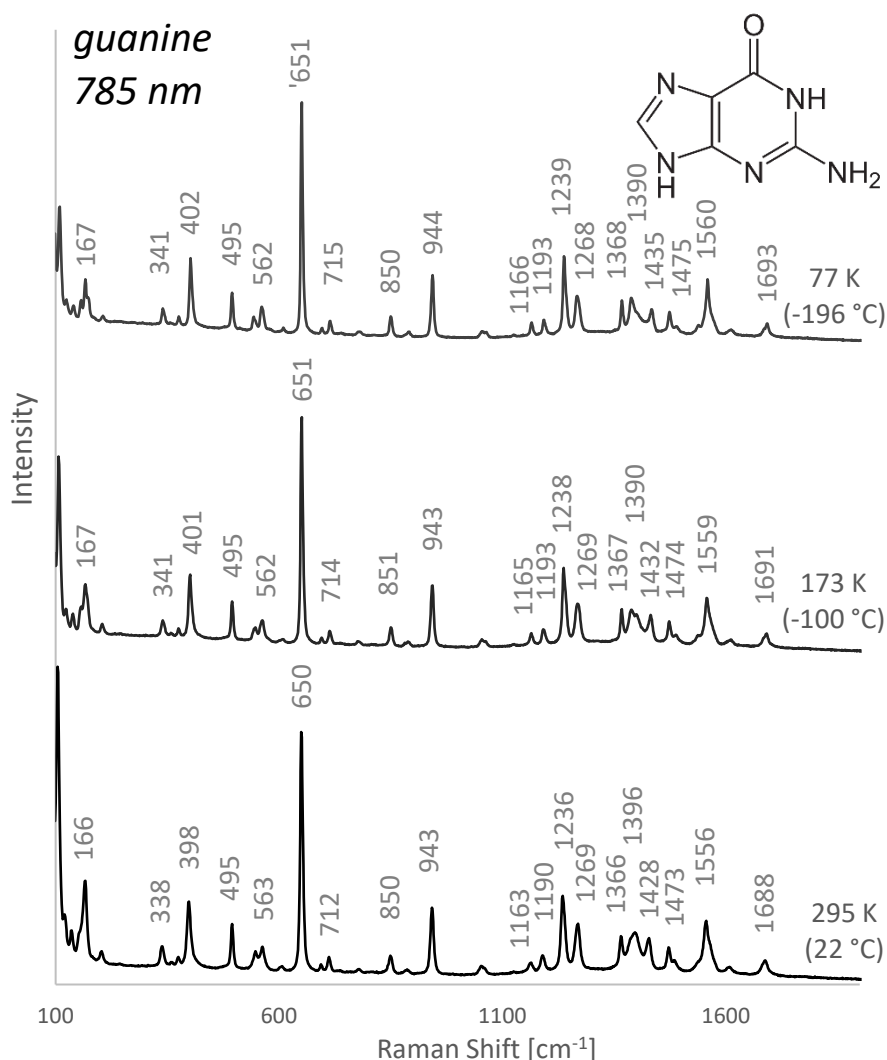


Figure 7-57 Raman spectra of guanine at 22 °C, -100 °C and -196 °C at 785 nm excitation

Similar to other examined molecules, the Raman band width within the spectra of guanine decreased significantly at low temperatures. The highest band width decrease was by 8.85 cm^{-1}

(49%). The minimum peak-to-peak distance in the spectra of guanine was 26.99 cm^{-1} at $22\text{ }^{\circ}\text{C}$ (between 1163 cm^{-1} and 1190 cm^{-1}), 22.77 cm^{-1} at $-100\text{ }^{\circ}\text{C}$ and 21.98 cm^{-1} at $-196\text{ }^{\circ}\text{C}$ (both between 1366 cm^{-1} and 1396 cm^{-1}). In both cases, these adjacent bands have similar signal intensity and could merge into a single very wide band with incorrect frequency measurement if a sufficient resolution was not available. This is especially critical in the region between 1366 cm^{-1} and 1428 cm^{-1} as there are three bands in close vicinity, which could blend together completely.

7.11.3 Cytosine

The spectra of cytosine at 785 nm at room temperature, $-100\text{ }^{\circ}\text{C}$ and $-196\text{ }^{\circ}\text{C}$ are shown in Figure 7-58. While the SNR decreases at cryogenic temperatures (as shown in Figure 7-55), the definition within the spectra is visibly higher compared to measurements at room temperature. This results in three new bands appearing in the spectra at cryogenic temperatures, namely the band at

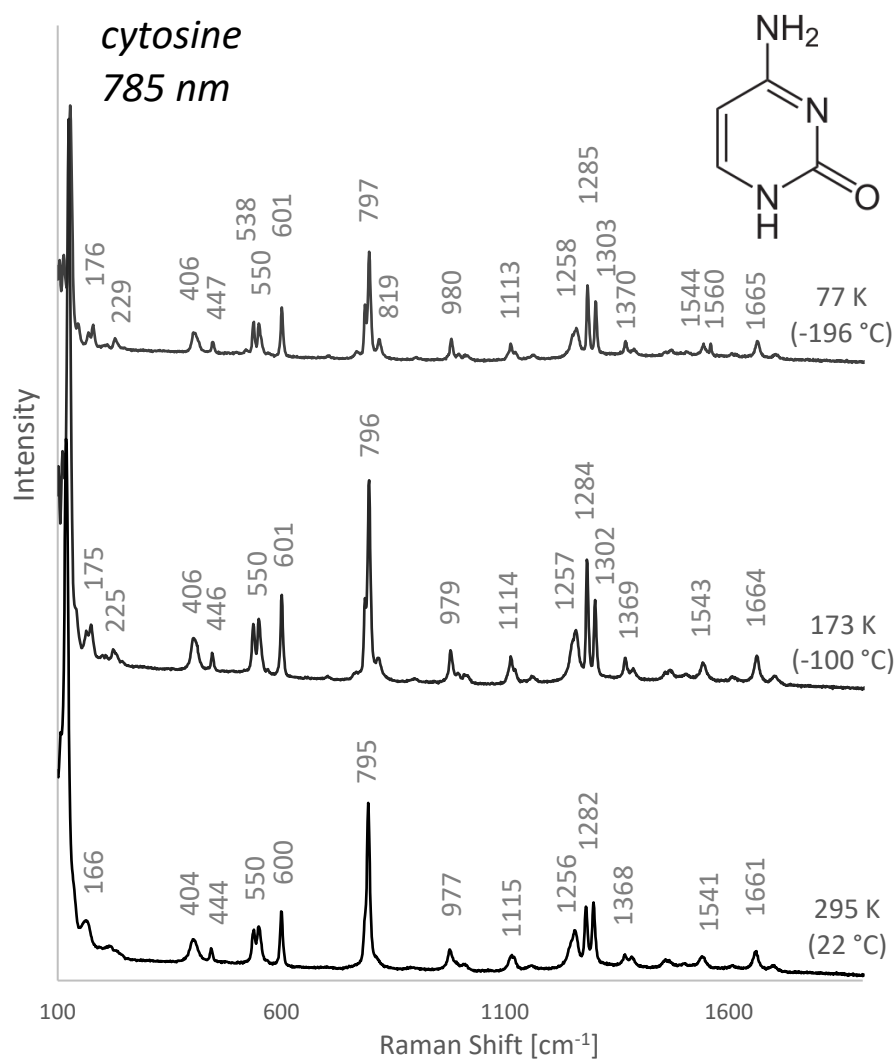


Figure 7-58 Raman spectra of cytosine at $22\text{ }^{\circ}\text{C}$, $-100\text{ }^{\circ}\text{C}$ and $-196\text{ }^{\circ}\text{C}$ at 785 nm excitation

225 cm^{-1} , 819 cm^{-1} and 1544 cm^{-1} , as well as the band at 538 cm^{-1} becoming resolvable from its adjacent band.

Shifts to both lower and higher frequencies were observed and the highest shift from 22 °C to -196 °C was 9.86 cm^{-1} . This is higher than both adenine and guanine. This is in line with previous results as both guanine and adenine are higher complexity molecules containing two rings as opposed to cytosine's single 6-membered ring. The lowest shift in frequency was 0.64 cm^{-1} at the 550 cm^{-1} band, which is associated with ring deflection [352]. This is also a vibrational mode typically associated with lower temperature induced changes in the Raman shift as discussed earlier in this study.

The Raman band width decreased at lower temperatures just as seen in the spectra of other molecules. The highest band width decrease in the spectra of cytosine was 9.92 cm^{-1} (61%) or by percentage 64% (8.53 cm^{-1}).

The minimum peak-to-peak distance in the spectra of cytosine was 26.1 cm^{-1} at 22 °C (between 1156 cm^{-1} and 1182 cm^{-1}), 17.55 cm^{-1} at -100 °C (between 1284 cm^{-1} and 1302 cm^{-1}) and 12.29 cm^{-1} at -196 °C (538 cm^{-1} and 550 cm^{-1}). It is important to note that the 12.29 cm^{-1} minimum clearance between 538 cm^{-1} and 550 cm^{-1} at -196 °C is not as critical for identification as the peak-to-peak distance between 1285 cm^{-1} and 1303 cm^{-1} . These two bands are dominant bands in the cytosine spectra that are important for identification and the distance between these two peaks is 17.74 cm^{-1} at -196 °C.

7.11.4 Thymine

The spectra of guanine at 785 nm at room temperature, -100 °C and -196 °C are shown in Figure 7-59. Despite not being particularly fluorescent at 785 nm at room temperature, the measurement at -100 °C clearly shows a fluorescence background, which intensifies at -196 °C. This fluorescence rise obscures the spectra and renders some bands undetectable, namely bands at 1220 cm^{-1} and 1252 cm^{-1} . The SNR comparison across the measured temperature range is shown in Figure 7-55.

All thymine bands except for 286 cm^{-1} shifted to higher frequencies at lower temperatures. The highest shift from 22 °C to -196 °C was 7.86 cm^{-1} at the 1498 cm^{-1} band, which is associated with NH bending [353]. This is higher than the maximum shift in guanine and less than in cytosine, which corresponds to the relative complexity of these molecules. Thymine only contains one ring, compared to the two-ring structure of guanine, and includes an additional group outside of the ring compared to cytosine, which has the same one-ring base.

Similar to other examined molecules, the Raman band width within the spectra of thymine decreased significantly at low temperatures. The highest band width decrease was by 7.29 cm^{-1} (53%). The minimum peak-to-peak distance in the spectra of guanine was 25.04 cm^{-1} at $22 \text{ }^\circ\text{C}$, 25.28 cm^{-1} at $-100 \text{ }^\circ\text{C}$ and 25.46 cm^{-1} at $-196 \text{ }^\circ\text{C}$, all occurring in the region between 1415 cm^{-1} and 1498 cm^{-1} .

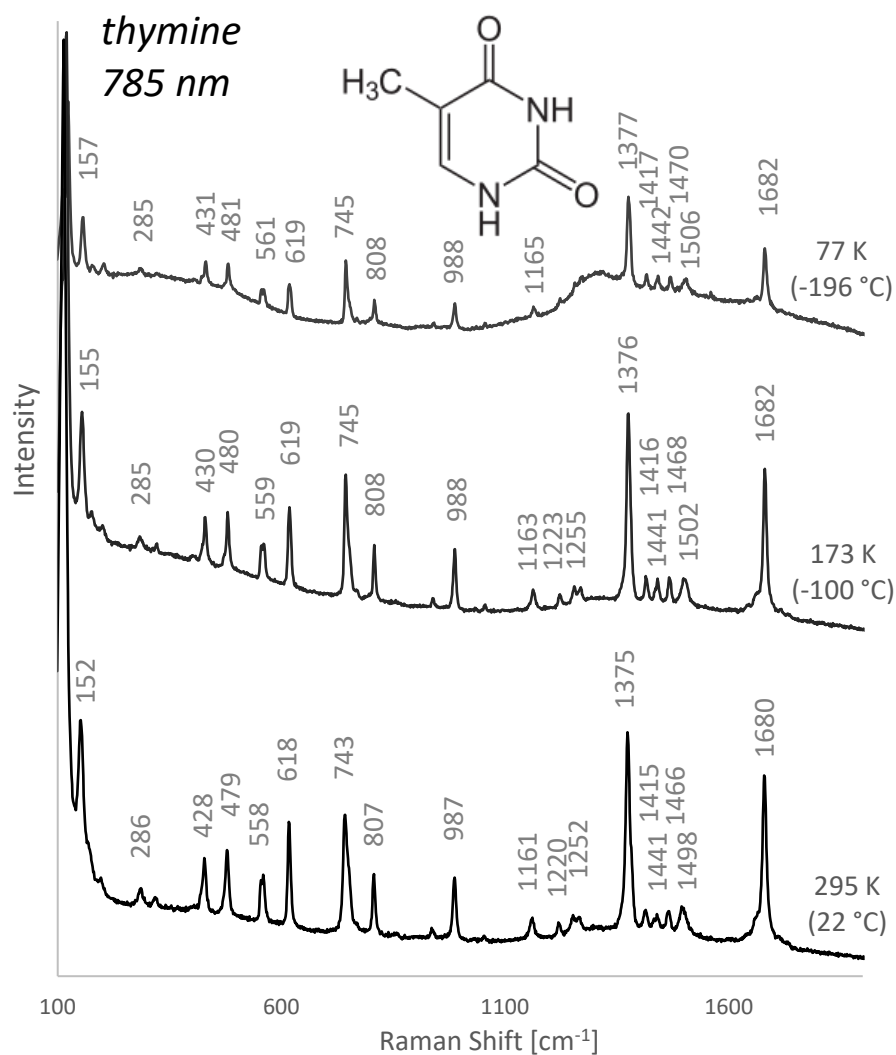


Figure 7-59 Raman spectra of thymine at $22 \text{ }^\circ\text{C}$, $-100 \text{ }^\circ\text{C}$ and $-196 \text{ }^\circ\text{C}$ at 785 nm excitation

7.11.5 Uracil

The spectra of uracil at 785 nm at room temperature, $-100 \text{ }^\circ\text{C}$ and $-196 \text{ }^\circ\text{C}$ are shown in Figure 7-60. Unlike other nucleobases, the spectra show a very visible signal increase at low temperatures, which is also reflected in the SNR comparison in Figure 7-55. This signal increase is accompanied by higher resolution within the spectra, which results in one new minor band at 1615 cm^{-1} that occurs in the spectra at $-100 \text{ }^\circ\text{C}$. Similarly, barely detectable bands at 192 cm^{-1} and 394 cm^{-1} become fully resolvable at lower temperatures.

The vast majority of uracil bands shift towards higher frequencies with decreasing temperature, however, bands at 192 cm^{-1} and 989 cm^{-1} shift to lower frequencies. The 989 cm^{-1} band is also the most stable band in the spectra as it only shifts by 0.8 cm^{-1} between the two temperature extremes. The band is assigned to ring bending [353], which makes its stability in line with previously observed tendencies as ring vibrations seem to display relatively lower changes in the Raman shift. The highest shift from $22\text{ }^{\circ}\text{C}$ to $-196\text{ }^{\circ}\text{C}$ was 10.23 cm^{-1} , which is the highest maximum shift across all nucleobases. This is also in line with previous results as uracil is the simplest nucleobase with only a one-ring structure and two $\text{O}=\text{C}$ groups outside of the ring.

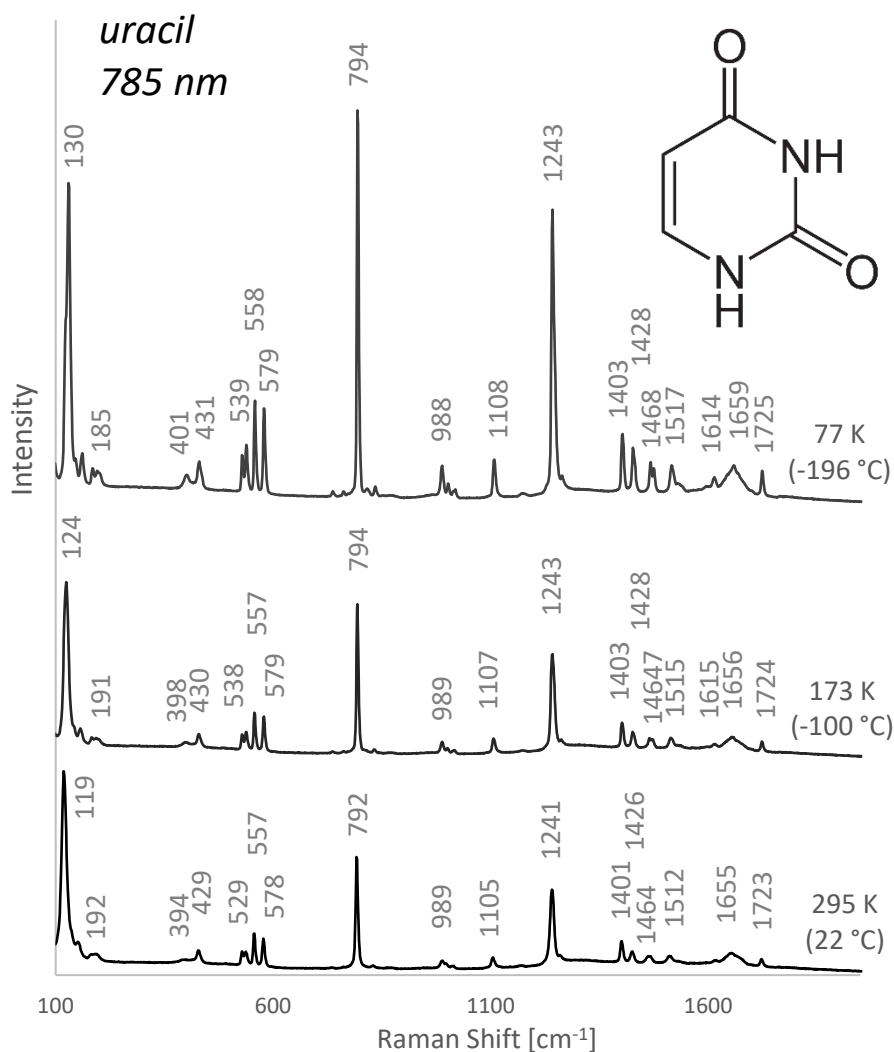


Figure 7-60 Raman spectra of uracil at $22\text{ }^{\circ}\text{C}$, $-100\text{ }^{\circ}\text{C}$ and $-196\text{ }^{\circ}\text{C}$ at 785 nm excitation

Similar to other examined molecules, the Raman band width within the spectra of uracil decreased significantly at low temperatures. The highest band width decrease was by 14.87 cm^{-1} (72%). The minimum peak-to-peak distance in the spectra of guanine was 21.26 cm^{-1} at $22\text{ }^{\circ}\text{C}$ (between 557 cm^{-1} and 578 cm^{-1}), 19.4 cm^{-1} at $-100\text{ }^{\circ}\text{C}$ and 19.38 cm^{-1} at $-196\text{ }^{\circ}\text{C}$ (both between 529 cm^{-1} and 557 cm^{-1}). The 529 cm^{-1} to 578 cm^{-1} region contains three bands that have

comparable signal strength and that are one of the dominant features of the uracil signature. Considering the width of the bands, spectral resolution lower than $12\text{-}14\text{ cm}^{-1}$ could render these bands unresolvable and impact the identifiability of the sample.

7.12 Coenzymes

The comparison of nicotinamide spectra at 785 nm excitation collected at room temperature, $-100\text{ }^{\circ}\text{C}$ and $-196\text{ }^{\circ}\text{C}$ is shown in Figure 7-61. All bands in the spectra of nicotinamide with the only exception of the band at 789 cm^{-1} shifted to higher frequencies at lower temperatures and followed the same profile of change in the Raman shift as previously described for other samples.

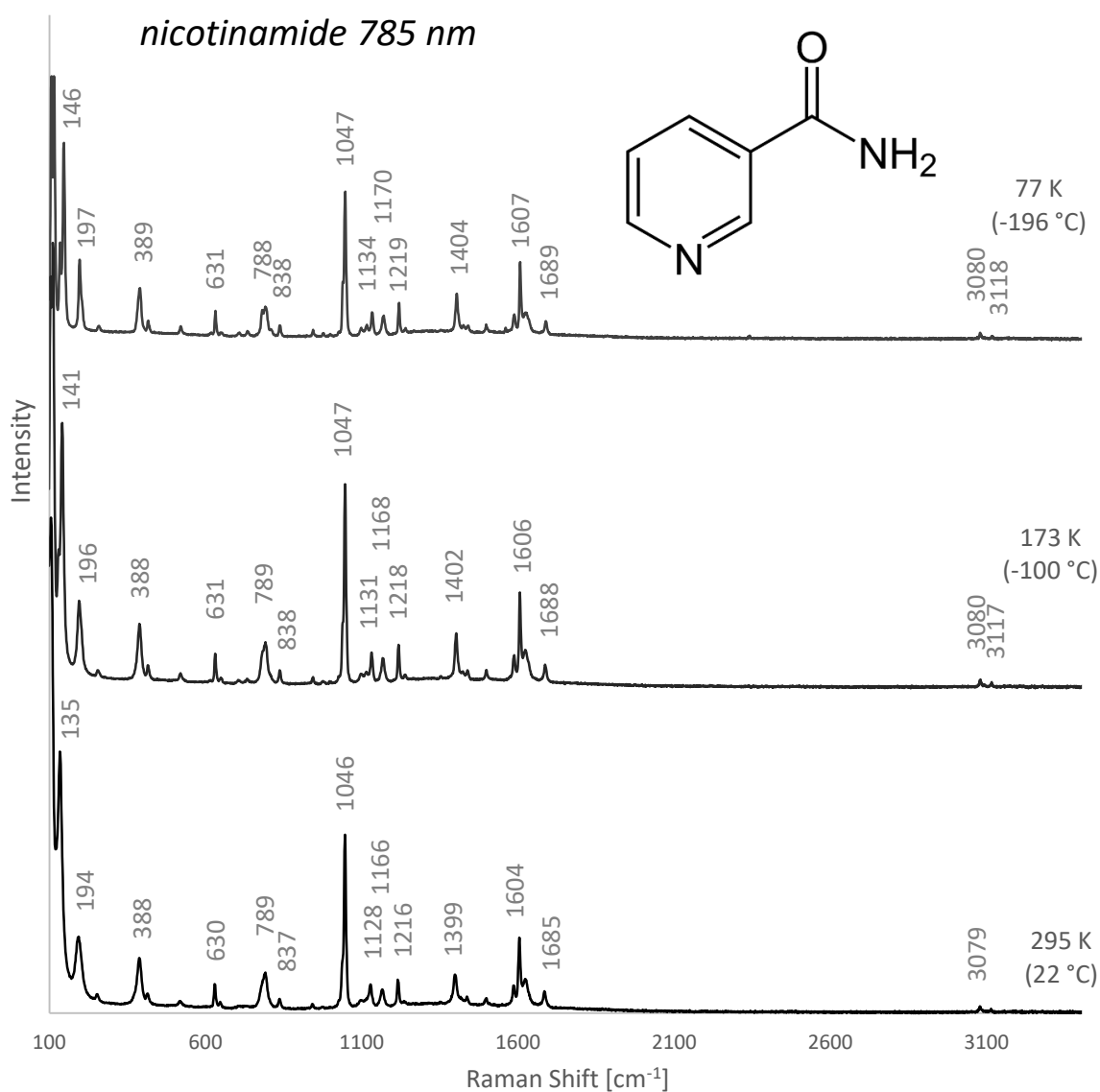


Figure 7-61 Raman spectra of nicotinamide at $22\text{ }^{\circ}\text{C}$, $-100\text{ }^{\circ}\text{C}$ and $-196\text{ }^{\circ}\text{C}$ at 785 nm excitation

The profile of change for the dominant peak of nicotinamide (1046 cm^{-1}) is shown with 2σ error bars in Figure 7-62 and it is in line with previously discussed trends. The 789 cm^{-1} band shifted to a lower frequency but only by 0.68 cm^{-1} .

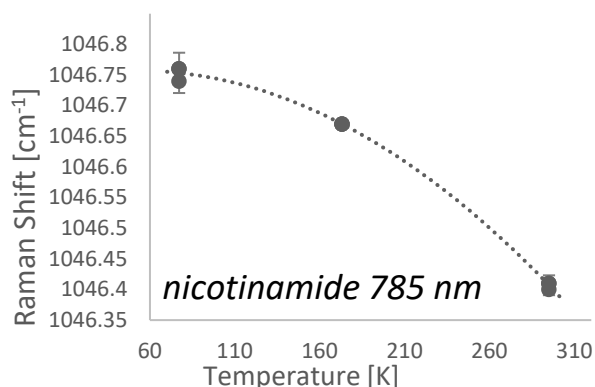


Figure 7-62 Raman shift change from room temperature to $-196\text{ }^{\circ}\text{C}$ observed at the most dominant band in the spectra of nicotinamide (1046 cm^{-1}) including 2σ error bars

The highest shift change from room temperature to $-196\text{ }^{\circ}\text{C}$ was 11.82 cm^{-1} at the 135 cm^{-1} band. This is comparable to the highest shift change in ectoine or uracil, which are both very similar in structure as they are both one-ring aromatic molecules (6-membered ring) containing $\text{O}=\text{}$ groups. On the contrary, the lowest change in the shift between the temperature extremes occurred at the 1046 cm^{-1} band, which is also nicotinamide's most dominant band that is used for its identification. This band only shifts to a higher frequency by 0.35 cm^{-1} . Since this shift lies in the 2σ error region, it is very unlikely to be the result of variance in the data or instrumental error and the band can be assumed to be naturally very thermally stable.

Similar to previous results, significant Raman band width narrowing also occurred in the spectra of nicotinamide at cryogenic temperatures and the highest decrease in the band width between $22\text{ }^{\circ}\text{C}$ and $-196\text{ }^{\circ}\text{C}$ was 11.51 cm^{-1} (58%). The variability between individual measurements also decreased at low temperatures, which is quantified in Figure 7-63 for both Raman shift and Raman band width. Interestingly, while the unaltered nicotinamide spectra in Figure 7-61 display visibly lower intensity at $-196\text{ }^{\circ}\text{C}$, the SNR actually increases towards lower temperatures and peaks at $-196\text{ }^{\circ}\text{C}$. This is shown in Figure 7-64 and can be partly attributed to the narrowing of the bands as well as shifting of the bands towards higher frequencies, which enhances the resolution within the spectra.

The minimum peak-to-peak distance in the nicotinamide spectra was 37.81 cm^{-1} at $22\text{ }^{\circ}\text{C}$, 36.65 cm^{-1} at $-100\text{ }^{\circ}\text{C}$ and 36.15 cm^{-1} at $-196\text{ }^{\circ}\text{C}$, all between 1128 cm^{-1} and 1166 cm^{-1} .

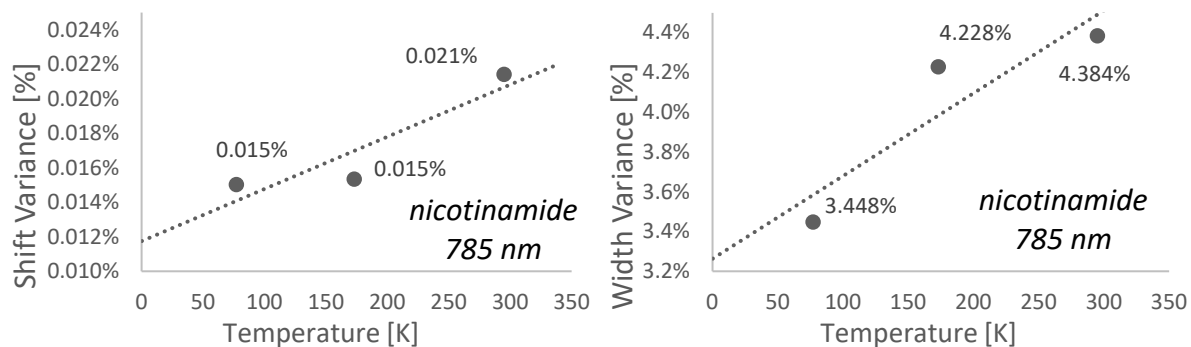


Figure 7-63 Raman shift variance (left) and band width variance (right) recorded in the spectra of nicotinamide across 22 °C, -100 °C and -196 °C at 785 nm excitation

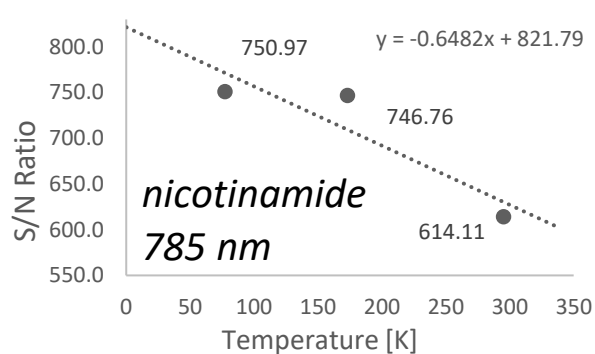


Figure 7-64 SNR change recorded in the spectra of nicotinamide across 22 °C, -100 °C and -196 °C at 785 nm excitation

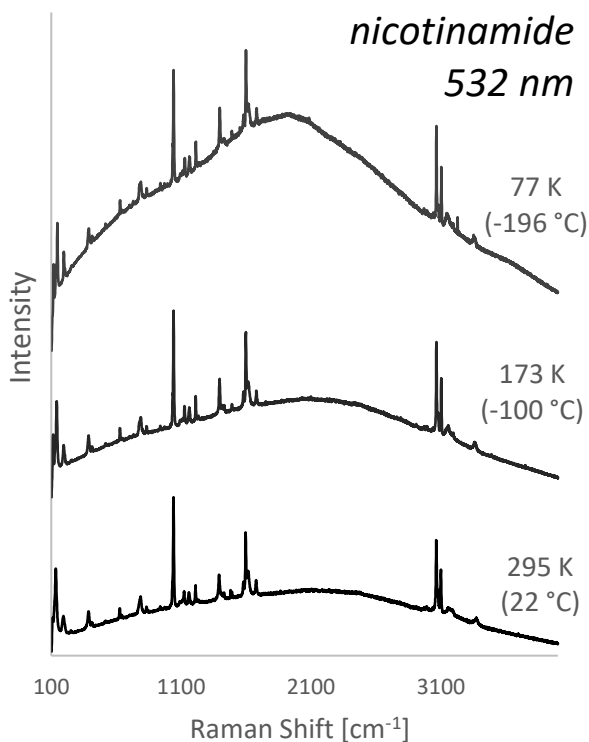


Figure 7-65 Raman spectra of nicotinamide at 22 °C, -100 °C and -196 °C at 532 nm excitation

As opposed to the nicotinamide spectra at 785 nm, the nicotinamide spectrum at 532 nm is fluorescent. Similar to other fluorescent samples, the nicotinamide fluorescence also rises at lower temperatures, which is shown in Figure 7-65. This is also accompanied by a significant decrease in the SNR, as shown in Figure 7-66.

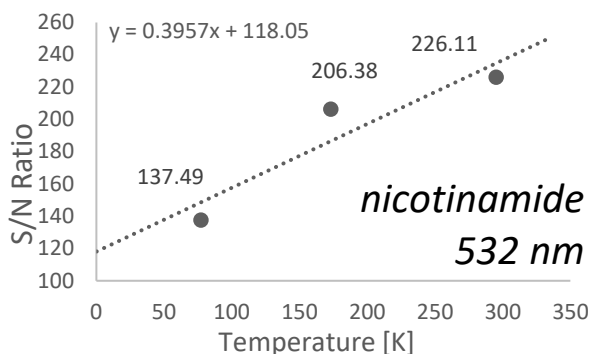


Figure 7-66 SNR change recorded in the spectra of nicotinamide across 22 °C, -100 °C and -196 °C at 532 nm excitation

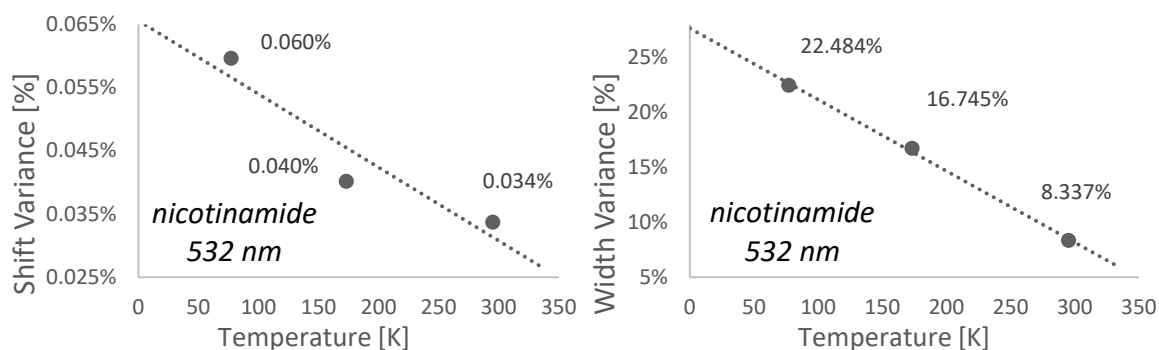


Figure 7-67 Raman shift variance (left) and band width variance (right) recorded in the spectra of nicotinamide across 22 °C, -100 °C and -196 °C at 532 nm excitation

However, the nicotinamide signature remains clearly distinguishable across the measured temperature range even despite the fluorescence background. This offers an opportunity to study the impact of the fluorescence background on the variability of the individual measurements. The variability of the Raman shift between individual measurements of nicotinamide at 22 °C, -100 °C and -196 °C is shown in Figure 7-67, which displays a clear increase towards lower temperatures. This also propagates to the Raman band width variance, which also increases at low temperatures and which is also shown in Figure 7-67. A similar trend was already recorded in the spectra of adenine at 785 nm, which is also fluorescent at this excitation. This naturally leads to the assumption that while cryogenic measurements can provide higher precision measurements, this may not be true for fluorescent molecules as the rising fluorescence also induces higher variability at low temperatures. This may be an important factor in selecting a fluorescence mitigation

technique for the exploration of Europa as some statistics-based computational methods may struggle with the variability of the spectra and increased fluorescence.

7.13 Inorganics

Hawaiian palagonite was examined in order to assess any potential interference of inorganic soil material with biosignature Raman spectra as a result of cryogenically induced changes in the spectra. The spectra of palagonite at 785 nm at 22 °C, -100 °C and -196 °C are shown in Figure 7-68. The figure clearly shows an increase in both the background fluorescence and signal strength. While there were no Raman bands resolvable at 22 °C and -100 °C, new distinct spectral features appear in the spectra at -196 °C. While the SNR and fluorescence change could not be effectively quantified due to the lack of spectral features in the spectra at 22 °C and -100 °C, the figure clearly shows a remarkable rise in the absolute Raman signal intensity. In absolute terms,

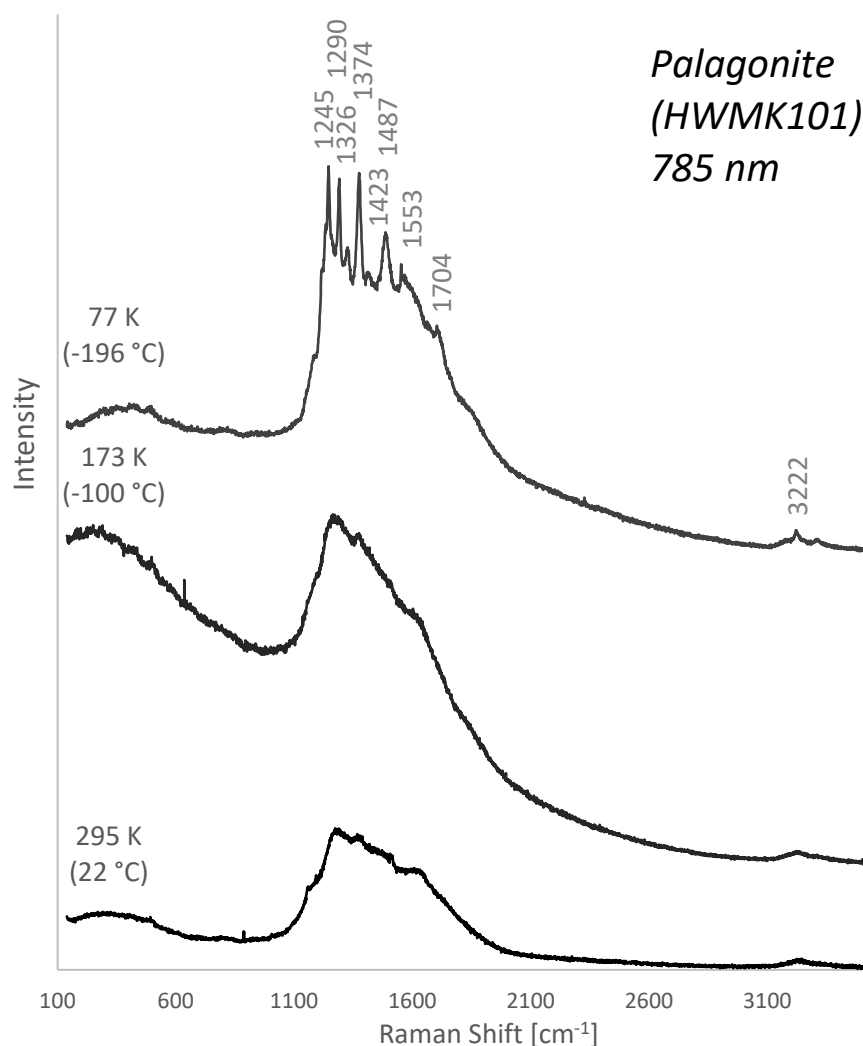


Figure 7-68 Raman spectra of Hawaiian palagonite (HWMK101) at 22 °C, -100 °C and -196 °C at 785 nm excitation

Chapter 7

the intensity changed from just below 7000 counts at room temperature to 18700 counts at -196 °C, which is more than 2.5 higher.

While potentially very useful for the identification of palagonite on Earth, this remarkable enhancement in the palagonite signal may be challenging for the detection of some biosignatures if palagonite is present in the sampled material on Europa. This especially applies to biosignatures, such as nucleobases, which show a decrease in signal strength at low temperatures and could therefore be gradually overshadowed by the signature of palagonite or other inorganic material. Additionally, the new spectral features in the spectra of palagonite could also lead to a serious case of misidentification if reference spectra at cryogenic temperatures are not available. While this is not within the scope of this study, these results prove that further research is necessary to understand the cryogenically induced changes in minerals and inorganic material that could obstruct the detection of biosignatures on Icy Worlds.

Chapter 8 Detection Limits: Sensitivity

This chapter presents the results of the sensitivity experiments aiming to investigate the LODs achievable with various excitation wavelengths for various molecules. This includes quantification of the minimum and maximum laser fluence and total energy dose in Section 8.1.1, which is then used to support the sensitivity study in Section 8.1.2.

8.1.1 Minimum and Maximum Laser Fluence and Total Energy Dose

The minimum and maximum laser power, laser fluence and total energy dose for the identification of the examined set of samples at 532 nm, 633 nm and 785 nm are shown in Figure 8-1, Figure 8-2 and Figure 8-3 respectively. Each figure shows the classification of each measurement taken with a given sample at a given excitation and laser power setting. As detailed in 5.1.2.4, measurements are classified into 5 groups based on the identifiability of the sample: undetectable (U), limited detectability (L), detectable (D), ideal spectral signature and oversaturated detector (O). It is important to note that measurements were taken only up to the maximum laser power of the laser source as described in Section 5.1.2. This is because measurements at higher laser power delivered to the sample would require increasing the exposure time, however, this increases the total energy dose but not the power spectral density. As such, measurements collected in this manner would not be fully comparable to measurements within the laser source nominal power range.

Since the natural maximum laser fluence and total energy dose for full identification are defined by the laser damage threshold or by the oversaturation of the detector, some samples did not reach the maximum within the measured laser power range. Note that laser damage thresholds are discussed in more detail in Section 6.2, this section focuses solely on the detectability of the molecule. Similarly, some molecules denoted as L at a certain laser power and excitation wavelength are only detectable to a limited extent due to the fluorescence background in their spectra at that wavelength. This is discussed in more detail in Section 6.1.

The results at all excitation wavelengths displayed in Figure 8-1, Figure 8-2 and Figure 8-3 show vast differences in the optimal laser power setting among the target molecules. Carotenoids in particular show much lower minimum laser fluence than other molecules, which is particularly pronounced at 785 nm. At this wavelength, most molecules become detectable at least to a limited extent at 137.9 kJ/cm^2 while astaxanthin becomes fully detectable at 2.76 J/cm^2 . Similarly, some molecules at 785 nm also require much higher laser fluence than other molecules for successful detection, namely 5 α cholestane, squalane and RNA. These molecules only become

Chapter 8

Class	Compound	Wavelength	532 nm												
		Power [mW]	2.25E-06	4.49E-06	2.25E-05	4.49E-05	0.0225	0.0449	0.225	0.449	2.245	4.49	22.45	44.9	
		Power Density [W/cm ²]	9.77E-03	1.95E-02	9.77E-02	0.195	97.71	195.4	977.1	1954	9771	1.95E+04	9.77E+04	1.95E+05	
		Fluence [J/cm ²]	1.173	2.345	11.73	23.45	1.17E+04	2.35E+04	1.17E+05	2.35E+05	1.17E+06	2.35E+06	1.17E+07	2.35E+07	
		Total Dose [mJ]	2.69E-04	5.39E-04	2.69E-03	5.39E-03	2.694	5.388	26.94	53.88	269.4	538.8	2694	5388	
Amino Acids	Alanine							L	I	I	I	I	I	I	
	Glutamic Acid				U	U	U	U	U	L	L	O	O		
	Glycine						U	U	L	L	D	D	D	O	
	Histidine						U	U	L	D	D	D	O		
	Tryptophan							U	L	L	D	D	O		
	Tyrosine							U	U	L	D	D	D	D	O
	β-Alanine							U	L	D	I	I	I	I	
Carboxylic Acids	Palmitic Acid				U	U	U	D	I	I	I	I	I	O	
	Ectoine							U	U	U	L	L	O		
Isoprenoids	Pristane							U	L	D	I	I	I	O	
	Squalane				U			L	L	L	L	I	I	I	O
Carotenoids	β-Carotene							U	I	I	I	I	O		
	Astaxanthin							U	L	D	D	I	I	I	I
Steranes	5α-Cholestane							U	U	L	D	I	I	I	
Pigments	C-Phycocyanin		U	U	U	U	U								
	Chlorophyll A								U	U	U	U	U	U	
Nucleic Acids	DNA						U	O				O			
	RNA						U	U	U	U	O				
Nucleobases	Adenine						U	U	U	L	L	O			
	Guanine						U	U	U	L	L	O			
	Cytosine							U	U	L	D	D	D	O	
	Thymine							U	L	L	L	D	O		
	Uracil						U	U	L	D	D	D	D	O	
Carbohydrates	Trehalose							U	L	L	D	I	I	I	
Coenzymes	Nicotinamide							U	L	D	I	I	I	I	O
Porphyrins	Protoporphyrin IX							U	U	L	L	L	U	U	
	Hemin										U	L	U	U	U
Inorganics	Palagonite (HWMK101)										U	U	U	U	O
Natural Mixtures	Carrot Root (natural carotene)							U	U	L	D	D	I	I	O
	Spinach (natural chlorophyll)							U		L	L	L	L	O	

Figure 8-1 Detectability of target molecules at 532 nm at various laser power (O = detector oversaturated due to high intensity signal, U = undetectable, L = limited detectability, D = fully detectable, I = fully detectable with all minor features, i.e. measurement yielding an optimal spectrum)

Class	Compound	Wavelength	633 nm											
		Power [mW]	5.2E-07	1.04E-06	5.2E-06	1.04E-05	0.0052	0.0104	0.052	0.104	0.52	1.04	5.2	10.4
		Power Density [W/cm ²]	1.60E-03	3.20E-03	1.60E-02	3.20E-02	15.99	31.97	159.9	319.7	1599	3197	1.60E+04	3.20E+04
		Fluence [J/cm ²]	0.1918	0.3837	1.918	3.837	1918	3837	19184	38367	1.92E+05	3.84E+05	1.92E+06	3.84E+06
		Total Dose [mJ]	6.24E-05	1.25E-04	6.24E-04	1.25E-03	0.624	1.248	6.24	12.48	62.4	124.8	624	1248
Amino Acids	Alanine							U	L	D	D	I	I	I
	Glutamic Acid							U	U	U	U	L	D	D
	Glycine							U	L	L	I	I	I	I
	Histidine							U	U	U	L	D	I	I
	Tryptophan							U	U	L	D	D	D	D
	Tyrosine							U	U	U	D	D	D	D
	β-Alanine							U	U	L	D	I	I	I
Carboxylic Acids	Palmitic Acid							U	L	D	I	I	I	I
	Ectoine								U	U	L	D	D	D
Isoprenoids	Pristane							U	U	L	D	I	I	I
	Squalane							U	L	L	D	I	I	I
Carotenoids	β-Carotene						U	I	I	I	I	O		
	Astaxanthin						U	D	I	I	I	O		
Steranes	5α-Cholestane								U	U	D	D	I	I
Pigments	C-Phycocyanin		U	U	U	U	O							
	Chlorophyll A							U	U	U	U	U		
Nucleic Acids	DNA						U	U			O			
	RNA						U	U	U	U	U	U	O	
Nucleobases	Adenine							U	U	L	D	D	D	O
	Guanine							U	U	L	D	D	D	O
	Cytosine							U	U	L	D	D	D	O
	Thymine								U	U	L	D	D	D
	Uracil							U	U	L	L	D	D	D
Carbohydrates	Trehalose								U	U	U	L	D	I
Coenzymes	Nicotinamide							U	U	D	I	I	I	O
Porphyrins	Protoporphyrin IX							U	U	U	U	U	U	U
	Hemin										U	U	U	O
Inorganics	Palagonite (HWMK101)										U	U	U	U
Natural Mixtures	Carrot Root (natural carotene)							U	U	U	L	D	D	O
	Spinach (natural chlorophyll)						U	U	O	O	O	O		

Figure 8-2 Detectability of target molecules at 633 nm at various laser power (O = detector oversaturated due to high intensity signal, U = undetectable, L = limited detectability, D = fully detectable, I = fully detectable with all minor features, i.e. measurement yielding an optimal spectrum)

Chapter 8

Class	Compound	Wavelength	785 nm												
		Power [mW]	1.15E-06	5.75E-06	1.15E-05	5.75E-05	1.15E-04	0.0575	0.115	0.575	1.15	5.75	11.5	57.5	115
		Power Density [W/cm ²]	2.30E-03	1.15E-02	2.30E-02	0.1149	0.2299	114.9	229.9	1149	2299	1.15E+04	2.30E+04	1.15E+05	2.30E+05
		Fluence [J/cm ²]	0.2759	1.379	2.759	13.79	27.59	1.38E+04	2.76E+04	1.38E+05	2.76E+05	1.38E+06	2.76E+06	1.38E+07	2.76E+07
Total Dose [mJ]		1.38E-04	6.90E-04	1.38E-03	6.90E-03	0.0138	6.9	13.8	69	138	690	1380	6900	13800	
Amino Acids	Alanine							U	L	I	I	I	I	I	
	Glutamic Acid								U	U	D	I	I	I	
	Glycine							U	L	D	I	I	I	I	
	Histidine							U	L	I	I	I	I	O	
	Tryptophan							U	U	D	I	I	I	I	
	Tyrosine							U	L	L	I	I	I	I	O
	β-Alanine							U	U	I	I	I	I	I	
Carboxylic Acids	Palmitic Acid							U	U	L	I	I	I	I	
	Ectoine							U	L	I	I	I	I	I	
Isoprenoids	Pristane							U	L	D	D	I	I	I	
	Squalane										U	U	U	D	
Carotenoids	β-Carotene							U	U	I	I	I	O		
	Astaxanthin		L	L	D	I	I	O			O	O			
Steranes	5α-Cholestane							U	U	L	L	D	I	I	
Pigments	C-Phycocyanin							U	U	U	U	U			
	Chlorophyll A		U	U	U	U	U	O	O						
Nucleic Acids	DNA							U	U	U	O	O			
	RNA							U	U	U	U	U	L	L	
Nucleobases	Adenine							U	L	D	D	D	D	O	
	Guanine							U	D	I	I	I	I	O	
	Cytosine							U	L	D	I	I	I	O	
	Thymine							U	L	I	I	I	I	I	
	Uracil							U	L	D	I	I	I	O	
Carbohydrates	Trehalose							U	U	L	D	D	D		
Coenzymes	Nicotinamide							U	L	D	I	I	I	O	
Porphyrins	Protoporphyrin IX							U	U	U	U	U			
	Hemin								U	U	U	U	U	O	
Inorganics	Palagonite (HWMK101)							U	L	D	I	I	I	O	
Natural Mixtures	Carrot Root (natural carotene)							U	L	D	D	I	I	I	
	Spinach (natural chlorophyll)							U	U	O	O	O	O		

Figure 8-3 Detectability of target molecules at 785 nm at various laser power (O = detector oversaturated due to high intensity signal, U = undetectable, L = limited detectability, D = fully detectable, I = fully detectable with all minor features, i.e. measurement yielding an optimal spectrum)

detectable at 2.76 MJ/cm² (5 α cholestane) and 13.79 MJ/cm² (squalane and RNA). While this needs to be verified experimentally due to variability in the relative concentration of compounds, these results suggest that a 785 nm instrument may require multiple measurements at various laser power settings in order to ensure the sampled material is scanned for all potential biosignatures. It also indicates that a 785 nm instrument is more likely to be plagued by detector oversaturation or interference due to the presence of high signal molecules or contaminants. While interference due to fluorescence may be mitigated, high intensity molecular interference cannot be extracted from the spectra. Rather, a sample handling mechanism to filter the molecules within the sampled material would be necessary. This is much more complex than fluorescence mitigation.

The number of molecules detectable at each excitation wavelength as well as at each laser power setting is quantified in Table 8-1. Out of the 30 examined samples, 25 are detectable at least to a limited extent at 532 nm, 22 at 633 nm and 24 at 785 nm. This would give the 532 nm excitation an advantage over 633 nm and 785 nm. However, this advantage over 633 nm would be very small and the advantage over 785 nm almost negligible. Additionally, if only fully detectable molecules are considered, the 532 nm only allows the detection of 18 molecules while the 633 nm can detect 22 and 785 nm 24.

Similar tendencies can also be observed when considering the relative priority of the target molecules. Out of the 10 highest priority molecules (class A), 532 nm only allows full detection of 6 while 633 nm and 785 nm can both detect 7. However, if molecules that can be detected only to a limited extent are considered, 532 nm would detect 9 (90%) while both 633 nm and 785 nm remain at 7. Considering the two highest priority classes (A and B), the trend is also similar. Out of the 21 target molecules classified A or B, 532 nm excitation would achieve full detection of 19 and 13 if limited detection is also considered. Both 633 nm and 785 nm allow full detection of 17 A or B class molecules, out of which none would be only detectable to a limited extent.

This leads to the conclusion that any of the excitations would serve fairly well for the detection of most of the target molecular species for the search for life on Europa. However, the NIR excitation is more likely to provide better quality spectra and visible excitations may not be able to provide sufficiently detailed spectra in order to distinguish individual molecules within the species. It is also important to note that this is mainly due to the effects of fluorescence and may be mitigated with a robust fluorescence suppression technique.

Chapter 8

Total no. Target Molecules = 30	Wavelength	532												
	Power [mW]	0.0225	0.0449	0.225	0.449	2.245	4.49	22.45	44.9					
	Power Density [W/cm ²]	97.71	195.4	977.1	1954	9771	1.95E+04	9.77E+04	1.95E+05					
	Fluence [J/cm ²]	1.17E+04	2.35E+04	1.17E+05	2.35E+05	1.17E+06	2.35E+06	1.17E+07	2.35E+07					
	Total Dose [mJ]	2.694	5.388	26.94	53.88	269.4	538.8	2694	5388					
Number of Molecules	L	3	9	13	11	3	1	0	0					
	L [%]	10%	30%	43%	37%	10%	3%	0%	0%					
	D	0	1	5	7	9	6	2	0					
	D [%]	0%	3%	17%	23%	30%	20%	7%	0%					
	I	1	1	3	5	8	10	7	5					
	I [%]	3%	3%	10%	17%	27%	33%	23%	17%					
	D and I	1	2	8	12	17	16	9	5					
	D and I [%]	3%	7%	27%	40%	57%	53%	30%	17%					
	D, I and L	4	11	21	23	20	17	9	5					
	D, I and L [%]	13%	37%	70%	77%	67%	57%	30%	17%					
	Total (D and I)	18												
	Total (D and I) [%]	60%												
	Total (D, I and L)	25												
	Total (D, I and L) [%]	83%												
Total no. Target Molecules = 30	Wavelength	633												
	Power [mW]	0.0052	0.0104	0.052	0.104	0.52	1.04	5.2	10.4					
	Power Density [W/cm ²]	15.99	31.97	159.9	319.7	1599	3197	1.60E+04	3.20E+04					
	Fluence [J/cm ²]	1918	3837	19184	38367	1.92E+05	3.84E+05	1.92E+06	3.84E+06					
	Total Dose [mJ]	0.624	1.248	6.24	12.48	62.4	124.8	624	1248					
Number of Molecules	L	0	0	8	8	3	1	0	0					
	L [%]	0%	0%	27%	27%	10%	3%	0%	0%					
	D	1	0	1	5	13	12	6	4					
	D [%]	3%	0%	3%	17%	43%	40%	20%	13%					
	I	1	2	2	3	3	7	10	9					
	I [%]	3%	7%	7%	10%	10%	23%	33%	30%					
	D and I	2	2	3	8	16	19	16	13					
	D and I [%]	7%	7%	10%	27%	53%	63%	53%	43%					
	D, I and L	2	2	11	16	19	20	16	13					
	D, I and L [%]	7%	7%	37%	53%	63%	67%	53%	43%					
	Total (D and I)	22												
	Total (D and I) [%]	73%												
	Total (D, I and L)	22												
	Total (D, I and L) [%]	73%												
Total no. Target Molecules = 30	Wavelength	785 nm												
	Power [mW]	1.15E-06	5.75E-06	1.15E-05	5.75E-05	1.15E-04	0.0575	0.115	0.575	1.15	5.75	11.5	57.5	115
	Power Density [W/cm ²]	2.30E-03	1.15E-02	2.30E-02	0.1149	0.2299	114.9	229.9	1149	2299	1.15E+04	2.30E+04	1.15E+05	2.30E+05
	Fluence [J/cm ²]	0.2759	1.379	2.759	13.79	27.59	1.38E+04	2.76E+04	1.38E+05	2.76E+05	1.38E+06	2.76E+06	1.38E+07	2.76E+07
	Total Dose [mJ]	1.38E-04	6.90E-04	1.38E-03	6.90E-03	0.0138	6.9	13.8	69	138	690	1380	6900	13800
Number of Molecules	L	1	1	0	0	0	5	7	4	1	2	1	0	0
	L [%]	3%	3%	0%	0%	0%	17%	23%	13%	3%	7%	3%	0%	0%
	D	0	0	1	0	0	1	4	3	6	4	3	2	1
	D [%]	0%	0%	3%	0%	0%	3%	13%	10%	20%	13%	10%	7%	3%
	I	0	0	0	1	1	1	2	12	13	15	16	19	13
	I [%]	0%	0%	0%	3%	3%	3%	7%	40%	43%	50%	53%	63%	43%
	D and I	0	0	1	1	1	2	6	15	19	19	19	21	14
	D and I [%]	0%	0%	3%	3%	3%	7%	20%	50%	63%	63%	63%	70%	47%
	D, I and L	1	1	1	1	1	7	13	19	20	21	20	21	14
	D, I and L [%]	3%	3%	3%	3%	3%	23%	43%	63%	67%	70%	67%	70%	47%
	Total (D and I)	24												
	Total (D and I) [%]	80%												
	Total (D, I and L)	24												
	Total (D, I and L) [%]	80%												

Table 8-1 The number of molecules detectable at each excitation wavelength and each laser power setting (L = limited detectability, D = fully detectable, I = fully detectable with all minor features, i.e. measurement yielding an optimal spectrum)

8.1.2 Sensitivity

The sensitivity of an instrument to different molecules determines the lowest detectable concentration (LOD) of the molecule. This is an important detection limit on Europa as the concentration of biomolecules in its icy shell is predicted to be very low. The minimum and maximum laser fluence data shown in the previous section were used alongside measurements of control molecules at various low concentrations in water in order to determine the LOD of the target molecules at different excitation wavelengths.

Among the control molecules examined at various concentrations between 100 wt% and 0.01 wt% in water, only adenine was detectable at a concentration below 5 wt%. At 532 nm adenine was successfully detected at 0.1 wt%. At 785 nm, the spectral signature of the control molecule nicotinamide was only detectable at and above 5 wt%. The secondary control molecule, glycine, was not detectable at 5 wt% at 785 nm but was detectable at this concentration at 532 nm. This is summarised in Table 8-2, which compares the experimentally obtained LOD data of the control molecules to the predicted values obtained as described in Section 5.1.2.5.

Control molecule	LOD at 532 nm [wt%]		LOD at 785 nm [wt%]	
	experimental	predicted	experimental	predicted
Primary: adenine	0.1			
Primary: nicotinamide			5	
Secondary: glycine	<5	2.5	>>5 <<50	25

Table 8-2 Theoretical and experimental LODs of the control molecules

A comparison of glycine spectra at 100 wt% and 5 wt% at 532 nm is shown in Figure 8-4. As shown in the figure, the major bands of glycine are still visible, and the molecule could be detectable at a slightly lower concentration than the nominal 5 wt%. Therefore, the predicted 2.5 wt% LOD for glycine at 532 nm appears to be an accurate estimate. Similarly, the predicted LOD for glycine at 785 nm was 25 wt% which is a good estimate considering the experimental results as no sign of the glycine signature was detectable in the spectra collected at 5 wt% at 785 nm but the molecule was fully detectable at 50 wt%. While these are rough estimates resulting in a relatively high absolute margin of error, it is important to note that the concentration of biomolecules on Europa is measured in the order of parts per billion (ppb). As such, these estimates are more than sufficient for the purposes of this study.

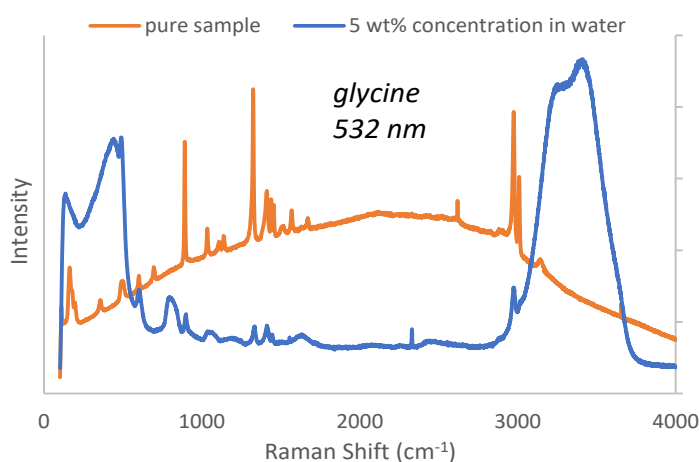


Figure 8-4 Raman spectra of a pure glycine sample compared to a 5 wt% solution in water at 532 nm

The theoretical estimate of the lowest detectable concentration of each target molecule at 532 nm and 785 nm is shown in Table 8-3. As clearly visible in the table, all molecules at 532 nm have much lower LODs than at 785 nm. This was expected as the Raman scattering intensity is proportional to λ^{-4} . However, neither 532 nm nor 785 nm can detect any of the target molecules at a sufficiently low concentration for in-situ exploration of Europa. The estimated concentration of biomolecules in the European ice could be in the order of ppb and as low as 0.01 ppb [9], [19], [23], which is 3 orders of magnitude lower than even the lowest theoretical LOD among the examined target molecules. The lowest concentration detectable was 5 ppm for astaxanthin at 785 nm. However, it is important to note that apart from astaxanthin, all other molecules have much higher LODs at 785 nm than at 532 nm. While no molecule is detectable at concentrations as low as 5 ppm at 532 nm, a number of molecules could be detected at 100-200 ppm, namely β -carotene, protoporphyrin, nicotinamide and natural chlorophyll. Many other molecules at 532 nm could be detected at 1000-2000 ppm, which is still roughly 2 orders of magnitude better than most molecules at 785 nm.

Furthermore, while these LODs are vastly inadequate for the exploration of Europa, it may be sufficient for in-situ biosignature detection on Mars. Research conducted to date using data from Mars analogue sites and predictions estimate the concentration of biomolecules to be from as low as 0.0001 wt % (i.e. 1 ppm) to 0.36 wt % in the regolith and in the order of 1 ppb or lower in the Martian Ice [61]–[64]. While the LOD required for the exploration of Martian ice is clearly also out of reach for traditional Raman instruments at 532 nm and 785 nm, most examined target molecules could be theoretically detectable at concentrations required for detection in the Martian regolith. This is a reassuring result as most state-of-the-art Raman instruments have been designed for bulk detection of minerals on Mars but could in theory also allow biosignature detection as well given that 2 out of the 3 flown or soon-to-be flown Raman instruments for extraterrestrial exploration are 532 nm Raman systems.

It is also important to note that these results are based on room temperature data, while experiments at cryogenic temperatures analogous to Europa revealed that the signal intensity may change with decreasing temperature. Some molecules, such as nucleobases, show lower SNR at decreased temperatures, which would inevitably also decrease the LOD. Depending on the specific molecules, data indicates that the SNR of nucleobases can decrease by very little to over 50% at 785 nm. At 532 nm the SNR decrease is even higher due to fluorescence interference. This decrease could thus result in LODs much higher than stated in Table 8-3 .

Class	Compound	Lowest Detectable Concentration (LOD)					
		532 nm			785 nm		
		wt%	ppm	ppth	wt%	ppm	ppth
Amino Acids	Alanine	0.1%	1000	1	25%	250000	250
	Glutamic Acid	1%	10000	10	50%	500000	500
	Glycine	1%	10000	10	25%	250000	250
	Histidine	0.2%	2000	2	25%	250000	250
	Tryptophan	1%	10000	10	25%	250000	250
	Tyrosine	0.2%	2000	2	25%	250000	250
	β-Alanine	0.2%	2000	2	25%	250000	250
Carboxylic Acids	Palmitic Acid	0.1%	1000	1	25%	250000	250
	Ectoine	0.2%	2000	2	25%	250000	250
Isoprenoids	Pristane	0.1%	1000	1	50%	500000	500
	Squalane	1%	10000	10	2500%	25000000	25000
Carotenoids	β-Carotene	0.01%	100	0.1	2.5%	25000	25
	Astaxanthin	0.1%	1000	1	0.00050%	5	0.005
Steranes	5α-Cholestane	1%	10000	10	500%	5000000	5000
Pigments	C-Phycocyanin	U	U	U	U	U	U
	Chlorophyll A	U	U	U	U	U	U
Nucleic Acids	DNA	U	U	U	U	U	U
	RNA	U	U	U	2500%	25000000	25000
Nucleobases	Adenine	0.1%	1000	1	5%	50000	50
	Guanine	0.1%	1000	1	2.5%	25000	25
	Cytosine	0.2%	2000	2	5%	50000	50
	Thymine	1%	10000	10	25%	250000	250
	Uracil	0.1%	1000	1	5%	50000	50
Carbohydrates	Trehalose	1%	10000	10	50%	500000	500
Coenzymes	Nicotinamide	0.02%	200	0.2	5%	50000	50
Porphyrins	Protoporphyrin IX	0.02%	200	0.2	U	U	U
	Hemin	1%	10000	10	U	U	U
Inorganics	Palagonite (HWMK101)	U	U	U	50%	500000	500
Natural Mixtures	Carrot Root (natural carotene)	0.1%	1000	1	50%	500000	500
	Spinach (natural chlorophyll)	0.01%	100	0.1	U	U	U

Table 8-3 Estimated lowest detectable concentration of target biosignatures for the exploration of Europa at 532 nm and 785 nm (U = molecule undetectable)

Chapter 8

On the contrary, some other molecules show an increase in their SNR at low temperatures. Most notably, the SNR of carotenoids can increase 2-3 fold at cryogenic temperatures at either excitation and depending on the band, the SNR of porphyrins can increase up to 310% at 532 nm. While this would still not accomplish the LODs required for the general detection of biosignatures on Europa, it could greatly enhance the chances of detection in case a localized higher density deposit of biomolecules was found and targeted.

Chapter 9 Detection Limits: Overall Detectability and Instrument Design Considerations

Important limitations associated with the detection of biosignatures on Europa were explored and their impact was described in detail in previous chapters, however, a couple of overarching principles and trends need to be considered. Please note that some of these results have been presented and discussed in peer reviewed journal articles arising from this research work, the references are provided here [310], [311].

Fluorescence is a notorious challenge for the detection of biogenic material using Raman spectroscopy and is a critical factor for the excitation wavelength selection, however, many high importance target molecules are identifiable across all excitation wavelengths tested in this study (from UV to NIR). The 785 nm excitation clearly outperforms visible and UV excitations in reducing the fluorescence interference in the spectra, nevertheless, it also generates a much lower Raman signal. While theoretical estimates show that neither one of the tested excitations could detect molecules at a concentration required for the detection of life on Europa, the NIR excitation would struggle to detect biomolecules even at the much higher concentration predicted for the Martian regolith [61]–[64]. At 532 nm, many of the examined target molecules could be detectable in the Martian regolith, if not on Europa. For biosignature detection on Europa or other Icy Worlds, both 532 nm and 785 nm would need to be used in conjunction with SERS.

While calculations of the theoretical lowest concentration detectable at DUV or UV excitations were not within the scope of this study and this needs to be confirmed in future work, it is unlikely that DUV or UV excitation alone would be capable of detection at such low concentrations as required on Europa. It is also important to note that theoretical predictions of the lowest detectable concentrations of the target molecules indicate that resonance experienced by some molecules, such as carotenoids, is also not sufficient to achieve the required LOD for life detection on Europa.

Only a couple of very photosensitive molecules such as pigments and porphyrins showed susceptibility to laser damage, another limitation of Raman spectroscopy, at visible and NIR excitations. At the UV 325 nm excitation, most molecules yield to laser damage at higher power, however, the effects of the sample degradation due to the laser damage were not as severe as expected. While a full dataset at 325 nm could not be obtained, measurements at this excitation allowed the detection of most traditional biosignatures for life detection, e.g. amino acids, in many cases even despite the laser damage.

Furthermore, it was shown that for photosensitive samples, the laser damage threshold increases significantly at cryogenic temperatures thus allowing either a much higher Raman signal or even identification of previously unresolvable molecules. This could be a very desirable side effect of the extreme low temperatures on Europa as it could potentially allow the detection of very sensitive molecules or intensify the Raman signature. Likewise, it is possible that the destructive nature of DUV and UV excitations could be mitigated at least to a certain extent by the extremely low temperatures on Europa, which could enable the detection of molecules not resolvable at visible or NIR excitation as well as a better LOD.

In general, cryogenically induced changes in the spectra of molecules could be critical for the detectability of the molecules. While the profile of the Raman shift change as well as the change in the Raman band width proved to be fairly consistent among most molecules and most Raman bands, there were also numerous exceptions and many other effects were found to be highly specific to each molecule. The occurrence of new bands or diminishing of existing bands as well as changes in the Raman signal strength were particularly unpredictable and no common trend was found. This is particularly concerning as all of these effects could greatly impact the detectability and identifiability of the target molecules. Particularly, while most molecules showed an exceptional increase in the signal strength at low temperatures, some others, such as nucleobases, showed a significant decrease in the signal strength.

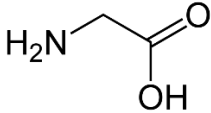
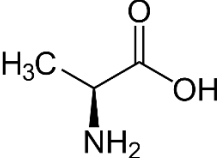
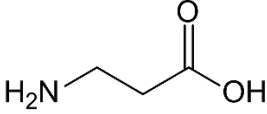
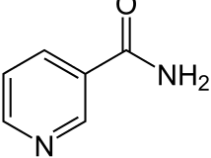
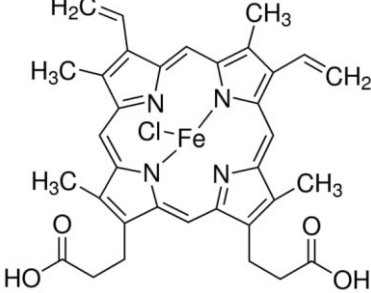
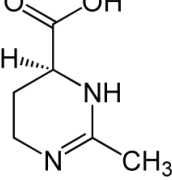
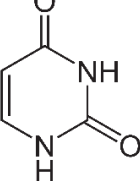
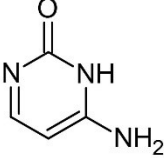
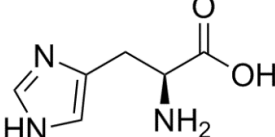
It is important to note that similar effects such as observed at cryogenic temperatures, e.g. shifting of Raman bands and variable signal strength, can also be caused by other factors. Similar effects can be the result of partial degradation of molecules, as shown in the data monitoring laser damage, or the interaction with a matrix or a solution that examined molecules are imbedded in, as observed in Raman spectra of naturally occurring carotenoids and chlorophyll.

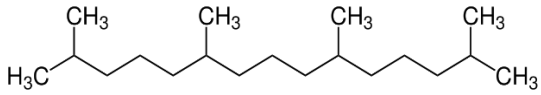

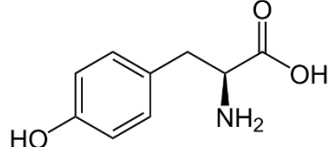
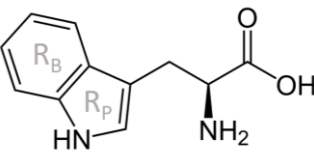
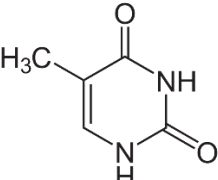
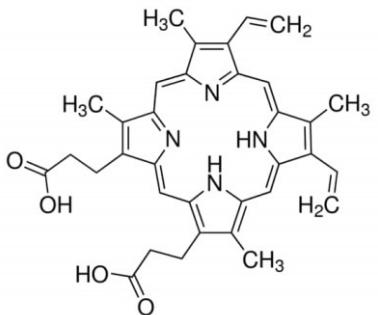
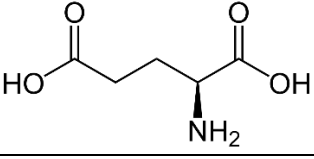
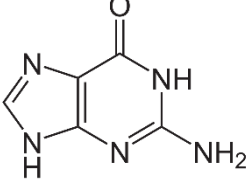
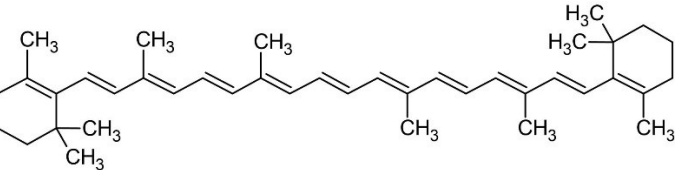
On the other hand, some effects of the cryogenic temperatures proved to be highly ubiquitous. Namely, a significant decrease in the Raman band width as well as in the variance between individual measurements was recorded in the spectra of all target molecules. This makes measurements at cryogenic temperatures both more precise and more accurate, which could be useful for many other applications besides the exploration of Icy Worlds. The only exception to this rule were fluorescent molecules, which showed an increase in the measurement variability at low temperatures. This is partly associated with the significant increase in the fluorescent background in fluorescent molecules which occurred in all fluorescent molecules except for highly photosensitive molecules. The SNR of photosensitive molecules increased at low temperatures even despite being fluorescent. This is the result of the higher signal at low temperatures due to laser damage reduction counter balancing and outperforming the cryogenically induced increase

in the fluorescence. Nevertheless, while some photosensitive molecules, such as porphyrins or carotenoids, are somewhat immune to this effect, the rise in the fluorescent at low temperatures can pose a serious issue for life detection on Europa. Not only because in many cases the much higher fluorescence overshadows the Raman signal of a molecule all together but also because it seems to introduce higher variability in the measurements. This makes many computational fluorescence mitigation techniques either less reliable or completely ineffective, e.g. any baseline subtraction techniques or methods based on statistical data analysis.

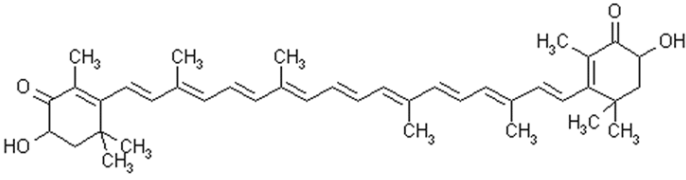
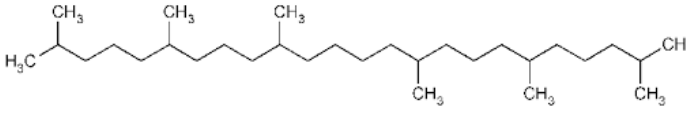
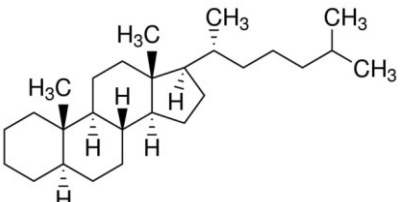
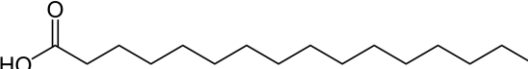
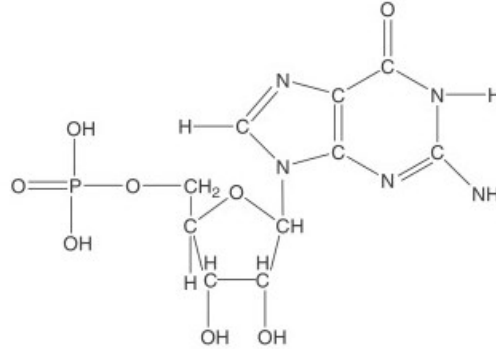
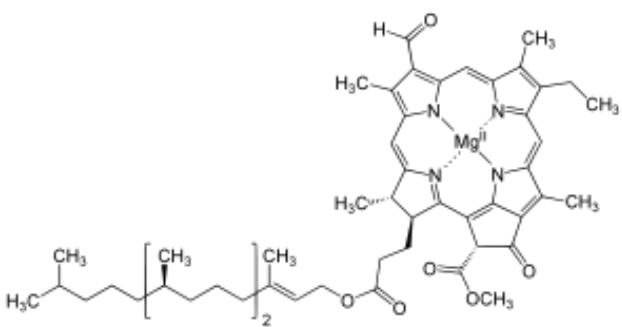
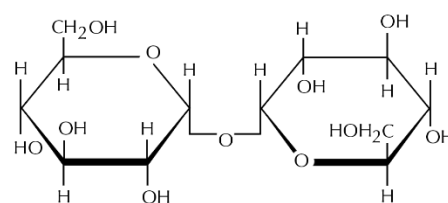
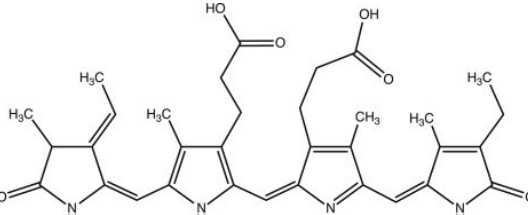
Another common and potentially very helpful trend observed in the data was the link between the absolute maximum change in the Raman shift from room temperature to cryogenic temperatures and the complexity of the molecule. The results indicate that Raman measurements of smaller, shorter or otherwise structurally less complex molecules generate much higher changes in the Raman shift at cryogenic temperatures. This is quantified in Table 9-1 for the set of target molecules examined in this study. The table shows the Raman shift change from 22 °C to -196 °C in descending order together with the molecular structure of each target molecule. It is evident from the table that molecules with longer chains, a higher number of side chains or groups or aromatic molecules induce much lower changes in the Raman shift. Interestingly, Table 9-1 also suggests that while aromatic molecules generate lower changes than non-aromatic molecules, this only applies for molecules of a similar count of atoms, i.e. chain length. Non-aromatic molecules with longer molecular chains seem to rank lower than aromatic molecules with a similar number of atoms. The only exception to the observed trend is hemin, which ranks rather high despite being a complex aromatic molecule. As already discussed in 7.2, this is most likely the result of the low quality room temperature spectra, which may have not allowed accurate quantification of the absolute maximum change in the Raman shift at cryogenic temperatures.

This trend may be potentially a very useful tool for the identification of molecules on Europa, provided that two measurements at two different temperature points are taken, as it could provide more information on the molecule's overall structure and structural complexity. However, as shown in Table 9-1, shifts in the spectrum of up to 25 cm^{-1} are to be expected for simple molecules at cryogenic temperatures. This is a significant change in the position of the Raman band and could severely affect the identifiability of the molecule. Particularly, these radical changes in the spectra could lead to misidentification if reference spectra collected at temperatures analogous to Europa are not available. Unfortunately, some of the most important high priority biosignatures are relatively very simple molecules, e.g. amino acids and nucleobases.

Rank	Maximum Change in the Raman Shift from 22 °C to -196 °C [cm ⁻¹]	Molecule	Molecular Structure
1	24.97	Glycine	
2	18.78	Alanine	
3	13.66	β-Alanine	
4	11.82	Nicotinamide	
5	11.26	Hemin	
6	11.22	Ectoine	
7	10.23	Uracil	
8	9.86	Cytosine	
9	8.79	Histidine	

10	8.29	Pristane	
11	8.01	Adenine	
12	7.99	Tyrosine	
13	7.95	Tryptophan	
14	7.86	Thymine	
15	7.32	Protoporphyrin IX	
16	6.81	Glutamic Acid	
17	6.63	Guanine	
18	5.67	β -Carotene	

Chapter 9

19	5.63	Astaxanthin	
20	4.29	Squalane	
21	3.87	5 α -Cholestane	
22	3.84	Palmitic Acid	
23	3.3	RNA	 <p>* Example with guanine</p>
24	3.28	Spinach Leaf (natural chlorophyll)	 <p>*in a tissue matrix</p>
25	3.18	Trehalose	
26	3.1	C-Phycocyanin	

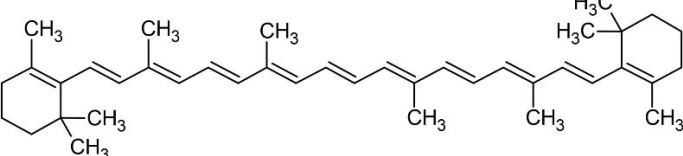
27	1.94	Carrot Root (natural carotene)	 <p>*in a tissue matrix</p>
----	------	--------------------------------------	---

Table 9-1 The maximum change in the Raman shift observed in the spectra of the examined target molecules from room temperature to -196 °C ranked in descending order and including the molecular structure

Likewise, a link between the type of vibrational modes associated with Raman bands and the change in their Raman shift at extreme low temperatures was identified. Bands associated with stretching vibrations, out of plane deformation of a ring or vibrations including inner atoms of a molecule were found to be more likely to shift to lower frequencies at low temperatures or shift to higher frequencies by only a small amount compared to bands assigned to other vibrational modes. On the contrary, bands that shift to a significantly higher frequency at lower temperatures are more likely to be associated with vibrations that are relatively less constrained within the molecule, that is, vibrational modes including the extremities of a molecule, such as its side chains, outer atoms and groups, or vibrations including most or all of the molecule's main chain and in plane bending within a ring.

This link offers an exciting new method of molecule identification solely based on the comparison of spectra collected at two different temperatures, and could greatly improve the identification capabilities in Raman spectroscopy for a wide array of applications besides the exploration of Europa. This also indicates that taking two separate Raman measurements of the same sample at two different temperature points could offer very valuable information for the exploration of Europa and analysis of samples with an unknown composition. Indeed, this study shows that the relative change in the Raman shift between measurements at different temperatures could also help distinguish between two very similar molecules, such as isoprenoids or carotenoids, that otherwise yield very similar spectra. The results also indicate that the relative difference between the cryogenically induced changes in the Raman shift could potentially provide more information on the solution or matrix that the examined molecules are imbedded in, potentially even the orientation or bonding of the atoms. This could be a very valuable tool for the identification of molecules and characterisation of samples in general, not just for life detection on other planets.

Another very important parameter to consider for a design of a Raman instrument is the peak-to-peak distance between Raman bands in the spectra of target molecules, particularly for bands that are important for the identification of the molecule. This has a direct impact on the required

spectral resolution. A summary of the minimum peak-to-peak distance recorded in the spectra of the target molecules at 22 °C, -100 °C and -196 °C is provided in Table 9-2.

	Compound	Priority	Minimum Peak-to-Peak Distance [cm ⁻¹]		
			22 °C	-100 °C	-196 °C
Amino Acids	Alanine	B	21.1	21.5	22.4
	Glutamic Acid	B	20.9	19.3	17.6
	Glycine	A	16.0	17.1	16.8
	Histidine	A	12.4	13.9	14.8
	Tryptophan	C	18.8	17.4	16.6
	Tyrosine	C	17.6	17.9	16.8
	β-Alanine	D	14.2	13.2	12.6
Carboxylic Acids	Palmitic Acid	A	28.0	23.5	26.2
	Ectoine	A	21.2	21.8	22
Isoprenoids	Pristane	B	23.1	21.2	21
	Squalane	C	17.1	21.1	20.6
Carotenoids	β-Carotene	A	21.0	21.0	22.0
	Astaxanthin	B	29.8	29.0	24.3
Steranes	5α-Cholestane	B	9.9	10	10.9
Pigments	C-Phycocyanin	C	259.3*	258.5*	260*
	Chlorophyll A	B	U	U	U
Nucleic Acids	DNA	A	U	U	U
	RNA	C	51.3*	53.7*	53.7*
Nucleobases	Adenine	B	39.2	39.4	38.8
	Guanine	B	27.0	22.8	22.0
	Cytosine	B	26.1	17.6	12.3
	Thymine	B	25.0	25.3	25.5
	Uracil	B	21.3	19.4	19.4
Carbohydrates	Trehalose	A	18	18.8	19
Coenzymes	Nicotinamide	A	37.8	36.7	36
Porphyrins	Protoporphyrin IX	A	24.8	20.8	18.1
	Hemin	A	30.9	14.1	12.7
Inorganics	Palagonite (HWMK101)	NA	NA	NA	NA
Natural Mixtures	Carrot Root (natural carotene)	NA	149.5*	151.2*	152.1*
	Spinach Leaf (natural chlorophyll)	NA	152.4*	153.8*	154.1*

Table 9-2 Minimum peak-to-peak distance in the spectra of the examined biosignatures at various temperatures. The values are similar for 532 nm and 785 nm and the lower value was chosen in this table. U denotes molecules that were undetectable and the minimum peak-to-peak distance could not be determined. * denotes molecules where high fluorescence may have restricted the number of visible peaks and the shown value is only based on the detectable bands in the spectra.

The table shows that the peak-to-peak distance may not always change to any significant extent at cryogenic temperatures and in many cases may even increase due to the band frequency shifts. However, the results also show that the required spectral resolution for some target biomolecules may be much higher than the previously estimated 16 cm^{-1} [46]. As discussed prior in this study, the resolution required for the identification of some molecules may be as high as $3\text{-}6\text{ cm}^{-1}$. Furthermore, much higher spectral resolution may be necessary to resolve molecules in mixtures. This specifically applies to molecules that routinely occur in nature in mixtures of other molecules

	Compound	Required Spectral Range [cm^{-1}]
Amino Acids	Alanine	130-1630
	Glutamic Acid	150-1700
	Glycine	150-1600
	Histidine	120-1600
	Tryptophan	100-1640
	Tyrosine	100-1650
	β -Alanine	120-1680
Carboxylic Acids	Palmitic Acid	140-3000
	Ectoine	100-3000
Isoprenoids	Pristane	800-2980
	Squalane	800-2980
Carotenoids	β -Carotene	990-1600
	Astaxanthin	950-1550
Steranes	5 α -Cholestane	400-2980
Pigments	C-Phycocyanin	200-1700 *[354]
	Chlorophyll A	700-1700 *[355], [356]
Nucleic Acids	DNA	400-1800 *[357], [358]
	RNA	600-1800 *[359]
Nucleobases	Adenine	100-1650
	Guanine	150-1700
	Cytosine	100-1680
	Thymine	130-1700
	Uracil	100-1750
Carbohydrates	Trehalose	340-3020
Coenzymes	Nicotinamide	100-1700
Porphyrins	Protoporphyrin IX	700-1700
	Hemin	700-1700
Inorganics	Palagonite (HWMK101)	1000-2500
Natural Mixtures	Carrot Root (natural carotene)	950-1550
	Spinach Leaf (natural chlorophyll)	700-1700 *[355], [356]

Table 9-3 Spectral range required for the identification of the examined target molecules,

* denotes molecules where the required spectral range could not be determined from the experimentally obtained spectra and literature available to date was used instead

Chapter 9

of the same molecular species and with a similar molecular structure, such as nucleobases or amino acids. In this case, the required spectral resolution may be as high as 2 cm^{-1} . Considering the spectral resolution of the state-of-the-art instruments as described in 2.3.4, this may prove to be an important engineering challenge for the development of a Raman instrument for life detection on Icy Worlds.

Lastly, the Raman signature of the target molecules also directly translates into the required spectral range, which is another important instrument design parameter. The spectral range required for the identification of the examined target molecules is shown in Table 9-3. For molecules that were undetectable or where the experimentally obtained spectra was severely affected by fluorescence or laser damage, data available in literature published to date were used to determine the required spectral range.

Chapter 10 Instrument Design and Requirements

Based on the experimental results from Chapter 6 to Chapter 9 as well as the mission constraints, requirements and goals outlined by the Europa Lander Report [19], [26] and other limitations discussed in literature to date, this chapter summarises the key instrument design requirements for a Raman spectrometer adapted for the exploration of Europa. The design requirements are then discussed in terms of the available technology and Raman techniques in Section 10.2, which highlights the critical design parameters that need to be considered for the development of a Raman instrument compatible with a landed mission to Europa and its scientific goals.

Based on the assessment of the key design parameters, potential instrument designs that meet the identified requirements are derived and discussed in Section 10.3. The experimental results defining the detection limits together with the assessment of target molecules and mission constraints are also used to discuss and identify the optimal measurement method for Raman instruments aiming to explore Europa, as discussed in Section 10.4.

The assessment of the key design parameters, as well as the optimal instrument design and measurement method, alongside a review of the available technology and technology readiness level of contemporary Raman spectroscopy techniques form the basis of Section 10.5. The section highlights the key enabling technology and limitations in contemporary Raman spectroscopy critical for the development of a Raman instrument for the detection of biosignature on Europa, and identifies areas for future research and development.

10.1 Requirements

This section outlines the design requirements for a Raman spectrometer optimised for the detection of biosignatures on Europa. Mission goals and constraints derived from the NASA's Europa Lander mission concept [19], [26] and other limitations discussed in literature to date are considered alongside the results of the experimental study described in Chapter 6 to Chapter 9.

Please note that high level mission requirements or qualification requirements, such as the mechanical loads or the radiation environment, are not within the scope of this work. While equally important, only key instrument design requirements derived from the scientific goals and objectives of the mission are discussed here.

10.1.1 Detectable Molecules

A rough outline of the target molecular species for the Europa Lander is provided in the Europa Lander Report and includes amino acids, carboxylic acids, lipids, and other molecules of potential biological origin (biomolecules and metabolic products) [19], [26]. In this study, a detailed assessment of potential target molecules for the detection of life on Europa and their relative priority is provided in Chapter 4. A comprehensive overview of the target molecules and their priority is shown in Table 4-2, Table 4-3, Table 4-4 and Table 4-5 in Section 4.3.

10.1.2 Mass & Size

Perhaps the most important requirement for an instrument aiming to explore the distant moon Europa is the size and mass. According to the design of the Europa Lander that is currently under development by NASA, which would carry the scientific instruments, an approximate instrument mass allocation of 5.4 kg has been assigned to smaller analytical instruments, including the baselined vibrational spectrometer [22], [26]. The preliminary example volumes and locations assigned to individual instruments inside the lander vault are shown in Figure 10-1. Instrument

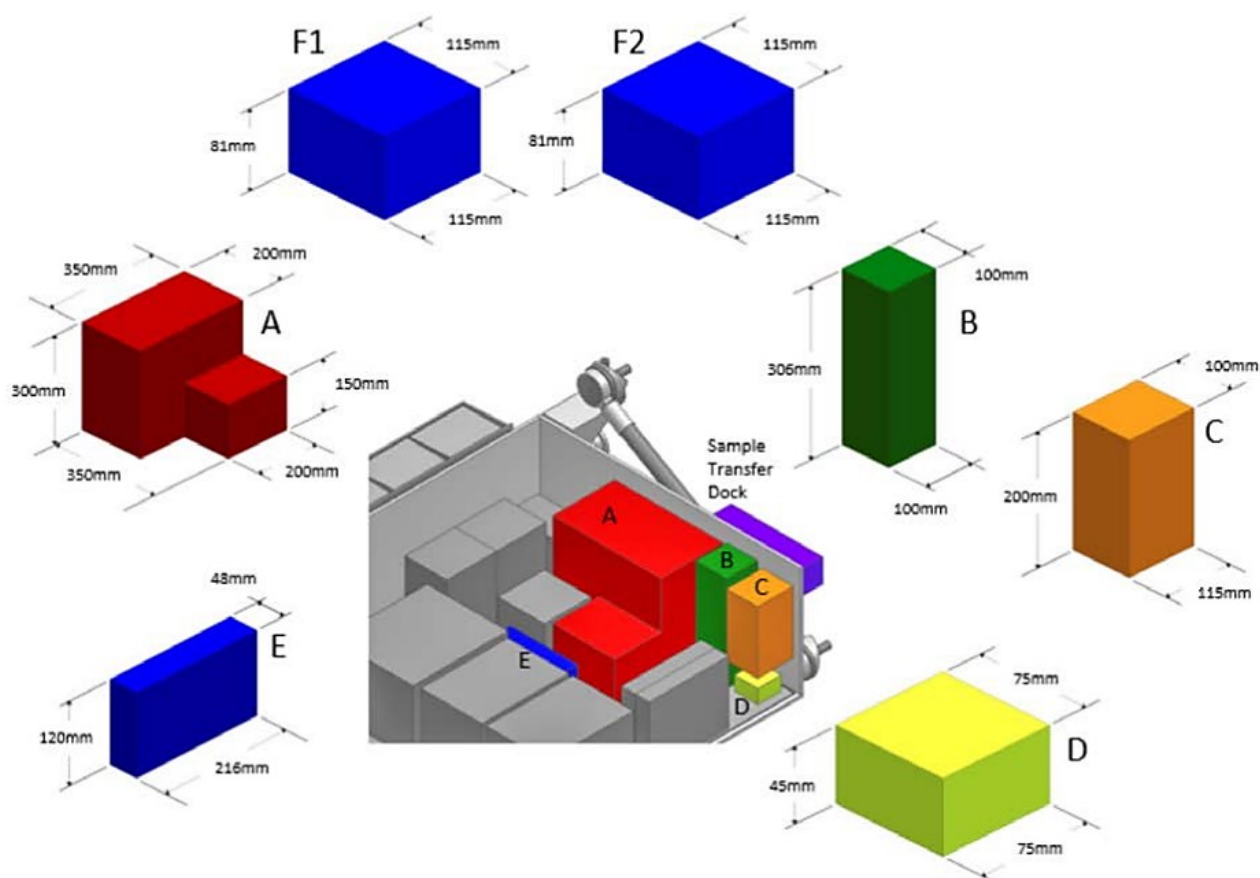


Figure 10-1 Instrument volume example allocation according to the Europa lander concept study [22]

boxes B and C correspond to smaller analytical instruments such as a Raman spectrometer. These values only serve as an approximate guidance as the final allocations will be to a certain degree dependent on the chosen instruments [22]. However, it is unlikely that these requirements can be relaxed by a significant amount.

10.1.3 Sensitivity (Limit of Detection)

The Europa Lander mission study proposes the required detection limit for organics in the European soil of 1 picomole per gram of the sampled material and LOD for vibrational spectroscopy as low as 1 nM (i.e. 0.1 ppb) [19]. For vibrational spectroscopy specifically, the Europa Lander LOD minimum requirement is a concentration by mass at least in the order of parts per thousand (ppth) [26]. Considering that the high-level science goal of the mission is “the detection of biomolecules at compound concentrations as low as 1 picomole in a 1 gram sample” (i.e. 1 nM or 0.1 ppb) [26], this is a practical requirement relaxation resulting from the LOD limitations of currently available instruments. As already discussed in Section 2.3.3 and 2.3.4, traditional Raman spectroscopy is not capable of 0.1 ppb detection and neither are any of the current state-of-the-art Raman instruments for planetary exploration.

However, research conducted to date indicates that the concentration of organics in the European ice is in the order of ppb and as low as 0.01 ppb [9], [19], [23]. As such, instruments with a ppth LOD, as recently proposed by the Europa Lander study [26], may not be able to detect biosignatures on Europa at all unless a specific higher concentration deposit or colony is found and targeted. While this is a potentially viable detection method, it relies on the presence of these higher concentration deposits of biogenic materials, which is a noteworthy challenge of its own. Thus, in order to ensure successful detection of any biogenic material that may be present in the European ice, the instrument LOD must be in the order of ppb as suggested by research conducted to date.

10.1.4 Spectral Resolution

The Europa Lander mission guidelines state that the model vibrational spectrometer should have a spectral resolution of at least 6 cm^{-1} [26]. Previous studies estimated the required spectral resolution for unambiguous identification at ambient temperature to be 16 cm^{-1} for organic compounds and for most minerals 8 cm^{-1} [46]. Other sources cite a spectral resolution of up to 30 cm^{-1} as sufficient for planetary mineralogy and microbiology [360]. No sources available to date discuss how the spectral resolution requirement may change at cryogenic temperatures.

However, as shown in this study, much higher spectral resolution may be needed for unambiguous identification of the target biosignatures, especially if present in a mixture of compounds with potentially interfering Raman bands.

Table 9-2 in Chapter 9 shows the minimum peak-to-peak distance at 22 °C, -100 °C and -196 °C in the spectra of the target molecules examined in this study. The peak-to-peak distance in the spectra of the target molecules drives the spectral resolution requirement and can be an approximate measure to compare the required spectral resolution between individual molecules. However, other factors further to the minimum peak-to-peak distance between adjacent bands need to be considered to determine the required spectral resolution. These factors include the importance of the bands for the identification of the molecules and presence of other signature bands that may be used for identification instead, as well as the relative Raman band width and intensity of the adjacent bands. Please note that Table 9-2 only includes the minimum peak-to-peak distance between bands that may be important for the identification of the molecule, minor bands or bands that do not affect the identifiability of the molecule were excluded. As shown in the table, the minimum distance between bands in most of the target molecules is between 15-26 cm^{-1} . Considering the relative width and signal strength of the bands, this may translate to an average required spectral resolution of 7-17 cm^{-1} . However, the minimum peak-to-peak distance in the spectra of many important biosignatures, such as amino acids, nucleobases or steranes, is much lower and, as already discussed in Chapter 9, would require the spectral resolution of 3-6 cm^{-1} . Likewise, some molecules are very likely to occur in nature alongside other molecules of the same molecular species with a similar molecular structure and Raman signature. This unfortunately applies to some of the most important biosignatures such as amino acids and nucleobases. As discussed in Section 7.1, the required spectral resolution in such a case would be much higher as many bands important for the identification of the molecules may be very close to one another or overlap. As shown in this study, unless a very high spatial resolution is available, the spectral resolution required to identify amino acids in mixtures could be as high as 2 cm^{-1} . Considering these results, the spectral resolution required to ensure maximum science return for an astrobiology mission to Europa is closer to 2-3 cm^{-1} than the proposed 6 cm^{-1} .

Table 9-2 also shows that there are variations across the temperature range, however, there is no clear pattern in these variations. While the significant narrowing of the Raman bands observed at low temperatures leads to a higher required spectral resolution and relaxes the requirement, shifting of the band frequency may increase the spectral resolution requirement (i.e. lower required spectral resolution) as adjacent bands move closer to one another. In general, the differences in the spectral resolution required for full identification may be 0.5-2 cm^{-1} across temperatures from ambient temperature to -196 °C. This is a relatively small change, however, it

should not be neglected, especially if the nominal spectral resolution requirement is already very high, e.g. 2-3 cm^{-1} , as required for the identification of biosignatures on Europa.

10.1.5 Spectral Range

The Europa Lander mission baselines the required spectral range of 150-3800 cm^{-1} . However, results summarised in Table 9-3 in Chapter 9 suggest that many biomolecules may not require the full 150-3800 cm^{-1} spectral range for successful identification. Many important target molecules for the search for life on Europa are fully identifiable within the spectral range of 150-1800 cm^{-1} . While the full spectral range may be necessary for the detection of water, minerals and some other biogenic molecules, which are all also important detection targets for the exploration of Europa, the possibility of a reduced spectral range may be an attractive option in case a compromise is required.

10.2 Key Design Parameters

The following sections discuss the key instrument design parameters for biosignature detection on Europa using Raman spectroscopy. The design requirements introduced in Section 10.1 are discussed in terms of the available technology and methods as well as key detection limits. The results of the detection limits experiments and analysis described in Chapter 6 to Chapter 9 are then used to assess the available options and identify the optimal approach.

10.2.1 Wavelengths Selection

The laser source excitation wavelength is easily the most important design parameter as it drives the design of the entire instrument as well as the detectability of the target molecules with implications on the fluorescence mitigation technique and the miniaturization potential of the instrument.

As already discussed in Section 2.3.2, NIR wavelengths are often preferred for the detection of biological samples due to the high fluorescence interference typically occurring in the spectra of organics at visible excitation. However, this study shows that many of the target molecules are also detectable at visible excitations, albeit some only to a limited extent without a suitable fluorescence mitigation mechanism. While the results of this study show that fluorescence interference as well as its variability increase at cryogenic temperatures, this may not be the primary concern for an instrument aiming to detect biosignatures on Europa. The increased and more unpredictable fluorescence background call for a robust fluorescence mitigation technique, however, a range of potentially suitable and effective techniques is available. This is described in

more detail in Section 2.3.2 and 10.2.3. While verification of these techniques is necessary to account for the higher fluorescence with higher variability, this may be a minor effort compared to raising the LOD of the instrument.

As shown in this study, the lowest concentration of target molecules that is achievable using either visible or NIR excitation is significantly higher than the LOD required for the detection of life on Europa. While NIR excitation typically outperforms visible excitations in terms of lower fluorescence interference, which was also confirmed in this study, its sensitivity to target molecules is much lower than at visible excitation. The predicted lowest concentration detectable using a 785 nm excitation shown in this study is much higher than the ppt LOD required by the Europa Lander mission [26] for most of the target molecules and only reaches the ppt order for astaxanthin. Considering that the ppt concentration requirement may be wildly insufficient as the concentration of biomolecules on Europa is estimated to be in the order of ppb or even lower [9], [19], [23], the NIR excitation is utterly unsuitable for such a mission unless paired with the SERS technique. Furthermore, the SERS signal of most target molecules at NIR would need to be enhanced by at least 10^8 and potentially up to 10^{11} . While such enhancement is possible with SERS, it could still be challenging to achieve such enhancement, especially for most of the target molecules. This is due to the dependency of the SERS enhancement on the coupling of the molecule's size to the SERS substrate, which may be difficult to achieve for all target molecules [149], [150]. Additionally, the SERS signal enhancement at NIR excitations tends to be lower than at visible excitation [361], which further restricts the LOD capabilities of NIR Raman systems.

On the other hand, a visible excitation at 532 nm could potentially detect most target molecules at the concentration in the order of ppt, as required by the Europa Lander mission [26], however, it is not capable of detection at the ppb level predicted for biomolecules on Europa either. However, in this case, the SERS enhancement necessary for the detection of most of the target molecules would be only 10^5 to 10^8 . These are enhancement factors well within the capabilities of SERS and could be more achievable across a wider set of molecules than the enhancement necessary at NIR. It is also important to note that based on the results of this study, the 633 nm excitation offers little to no benefits in terms of molecule detection and fluorescence mitigation compared to the shorter 532 nm excitation, which generates a higher Raman signal and is thus a better choice.

While a full experimental study including UV and DUV excitations was not within the scope of this research work, the results that were obtained indicate that a DUV excitation may be a suitable alternative to the more traditional and widely used visible and NIR excitation. Experiments at 325 nm presented in this work show that sample laser damage, which is one of the main drawbacks of

UV excitation wavelengths, may not be a critical problem, provided that an appropriate laser power setting is selected. This may, however, require further research into the laser damage thresholds at DUV excitation for solutions of target molecules in an European analogue. Furthermore, the results of this study also show that sample damage due to photothermal degradation is significantly reduced in solutions or a live tissue matrix as well as at cryogenic temperatures. This may significantly increase the sample degradation thresholds of target molecules in the European ice and allow DUV Raman measurements without significant laser damage concerns. However, it is important to note that photodamage, as opposed to photothermal damage, could not be investigated in this study and is likely to be a component in the sample degradation process at UV excitations. However, while sample degradation concerns at UV excitations may not be completely avoided due to photodamage, this study shows that photothermal degradation is a significant component of the laser damage observed in Raman spectra and can be significantly reduced through cryogenic measurements or in solutions.

The effect of laser damage at cryogenic temperatures and in low concentrations in water/ice needs to be verified experimentally at DUV, however, this may be a relatively minor effort considering the benefits of a DUV Raman system. Since the fluorescence and Raman scattering signals are well separated below the excitation of 250 nm, DUV excitation allows fluorescence-free Raman measurements for most organics. Due to the inverse dependence of the Raman signal on the excitation wavelength, DUV excitation also yields very strong Raman signals compared to visible and NIR excitation. As shown in Section 8.1.2, this is particularly important for the detection of biosignatures on Europa, especially since neither NIR nor visible excitations can achieve the required LOD. While this could not be confirmed experimentally in this study, the lowest detectable concentration of the target molecules is bound to be lower at DUV than at visible excitation as the Raman scattering intensity is proportional to λ^{-4} . Additionally, many important biosignatures, such as aromatic amino acids, nucleic acids and polyaromatic hydrocarbons (PAHs), are resonant in the DUV region, which increases the Raman signal intensity even further [130]. Considering the LOD trend at visible and NIR excitation in this study, a DUV Raman system should be capable of detection at the concentration of 1 ppt and even much lower. For some molecules, detection at concentrations in the order of ppm or even ppb as required for life detection on Europa may also be possible even without the use of SERS. However, this enhancement may be very specific to molecules resonant in the DUV region, particularly those that may also benefit from a signal enhancement at cryogenic temperatures. This needs to be experimentally verified, however, considering that any higher excitation wavelength would need to be used in a SERS system at the cost of immense additional complexity, it may be an effective solution. Additionally, even if the use of SERS is required at

DUV, only a relatively minor enhancement will be necessary. However, it is also important to state that DUV SERS has not been studied as extensively as visible or NIR SERS and the enhancement factors reported to date are lower [132].

10.2.2 Sensitivity (Limit of Detection)

As already mentioned in the previous Section, the sensitivity of the instrument may be the highest priority constraint for the design of a Raman instrument aiming to detect biosignatures on Europa. This is due to the limited options available for enhancing the instrument's sensitivity and the extremely low concentrations of biomolecules predicted in the European ice [9], [19], [23].

There are only three viable methods of enhancing the Raman signal intensity and thus reducing the LOD of the instrument. These methods include the cryogenically induced signal enhancement described in this study, using short wavelength excitation and SERS.

Firstly, this study reports and describes a significant cryogenically induced enhancement of the Raman scattering signal. This is discussed in detail in Chapter 7. However, it only applies to some of the target molecules and some other molecules may also show a decrease in the Raman signal at cryogenic temperatures. Likewise, the enhancement achievable via cryogenic measurements is variable across different molecules and individual bands and it is unlikely to be more than a factor of 10. While this is a significant enhancement, it is not enough to reach the ppb level of detection required for the exploration of Europa on its own. Having said that, due to the extremely low temperatures on Europa, any Raman instrument on Europa will benefit from this signal enhancement provided that the sample is presented to the instrument at its native temperature.

An alternative method of increasing the signal intensity is using a short excitation wavelength. Raman scattering intensity is proportional to λ^{-4} , which makes the Raman signal at UV excitations much stronger than at visible or NIR excitation. As already mentioned in Chapter 9, this natural enhancement of the Raman signal allows DUV Raman systems to detect molecules at much lower concentrations than the more traditional visible or NIR excitations. DUV Raman systems should be easily capable of detection at the ppb concentration required by the Europa Lander mission and for many target molecules for the detection of life on Europa, LODs in the order ppm should also be possible. Resonant molecules, especially those that also experience cryogenically induced Raman signal enhancement as shown in this study, may even be detectable at a concentration in the order of ppb, which is the estimated concentration of biomolecules on Europa [9], [19], [23]. However, this applies only to a few target molecules and may still fall short of the required LOD as studies show that the concentration of molecules on Europa may be as low as 0.01 ppb [9], [19], [23]. Nevertheless, depending on the goals of the mission, a DUV Raman instrument may be an

effective solution and a good compromise compared to the alternative SERS approach, which is much more complex and requires further technology development. If targeting only a selected number of resonant biosignatures is sufficient to fulfil the mission's goals or if higher concentration biosignature deposits are found and targeted instead, a DUV Raman may be a very good option to consider.

Any Raman system with longer excitation wavelengths will need to use SERS in order to achieve the required LOD in the order of ppb. The SERS technique and most recent SERS technology advances in terms of planetary exploration have already been discussed in Section 2.3.3. SERS is the only Raman signal enhancement method that allows enhancements by a factor of 10^7 to 10^{11} [132], [133] as is potentially required to detect biosignature on Europa at the visible to NIR excitations. As already mentioned in the Section 2.3.3, traditional SERS substrates, although allowing SERS instruments to collect Raman spectra at very low concentrations and without fluorescence interference, are not compatible with long duration spaceflight and planetary applications. This is due to the short shelf-life of SERS substrates but also due to the inherent variability of SERS spectra depending on the material and surface geometry of the substrate as well as the location within the substrate and the size coupling of the target molecule to the surface geometry [132], [133], [138], [139], [141], [146]–[150]. However, recent advances in the SERS technology previously described in Section 2.3.3 could allow this technique to be considered for future planetary missions.

Particularly, the proposed in-situ activated SERS substrate concept [146], [158] in a combination with a nanostructured SERS substrate could be a very powerful solution capable of highly consistent and reproducible Raman measurements even years after manufacture [143], [152], [153]. Nanostructured SERS substrates can be designed with an extremely even and controlled surface geometry and thus produce more consistent Raman spectra [152], [153]. Furthermore, a nanostructured quartz or sapphire substrate would be much less prone to degradation over time in vacuum than traditional silver or gold nanoparticle substrates. However, it is important to note that nanostructuring glassy materials, such as quartz or sapphire, is not a trivial task as the surface is too smooth for direct writing lithography methods such as electron beam [362]. A more sophisticated lithography process including multiple-step methods such as the reactive ion etching technique will be necessary. An example of a reactive ion etching lithography process for high aspect ratio nanostructuring of glass surfaces is shown in Figure 10-2 [362].

The layer of precursor AgCl nanoparticles can be either coated directly onto the nanostructured surface or imbedded in a sol-gel matrix [363], which would provide further protection from the outside environment. Although not tested as a nanostructured substrate, in-situ activated sol-gel

substrates impregnated with AgCl nanoparticles have shown promising results and could also be re-activated multiple times [363]. The AgCl impregnated sol-gel matrix can be either coated onto an already nanostructured substrate or coated on a smooth substrate and nanostructured directly. This is shown in Figure 10-2. The precursor AgCl particles are then activated in-situ either via a LED source or the Raman laser itself [146], [158], which does not require any additional equipment or mechanisms.

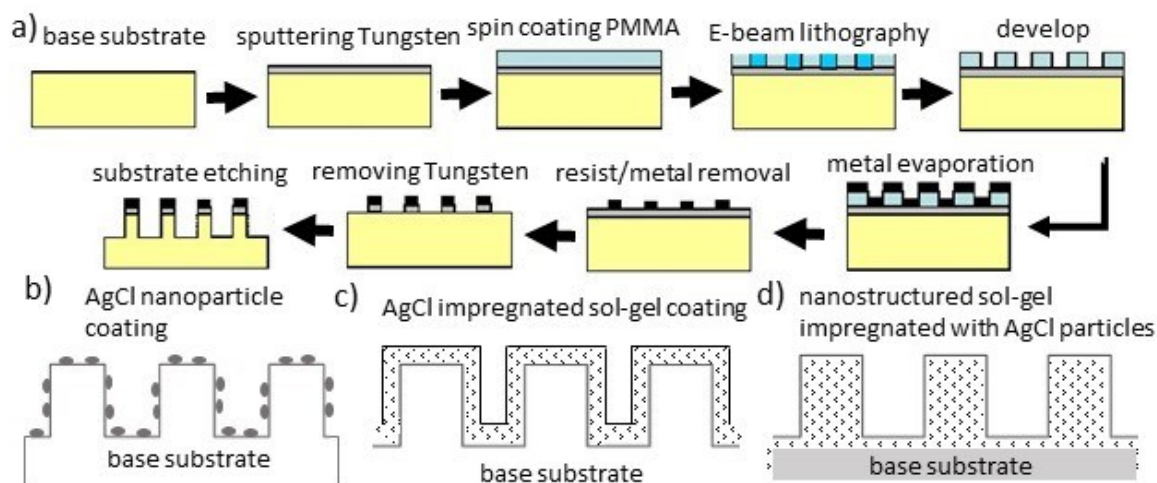


Figure 10-2 Lithography process for high aspect ratio nanostructuring of glassy substrate material [362]. (b), (c) and (d) show cross section of the three proposed methods of combining AgCl in-situ activated SERS with a nanostructured substrate surface

However, this method requires throughout testing and verification in order to achieve the required TRL and further development is needed to optimize the method for life detection on Europa. Firstly, the in-situ activated SERS substrates have not been used in combination with a nanostructured SERS substrate to date and optimisation of the surface geometry and nanoparticle size is a critical step towards TRL 4. Specifically, optimisation of the geometry and nanoparticle size to the target molecules for the search for life on Europa is critical to ensure successful detection. Likewise, the lifetime of glass/fused silica nanostructured SERS substrates has not been experimentally verified yet. The impact of prolonged storage of AgCl coated substrates in vacuum has also not been defined. Further research is also necessary to confirm the ideal activation exposure.

It is also important to note that this concept is best tailored to a Raman system with an excitation at 532 nm. The signal enhancement using silver nanoparticles is less efficient at NIR excitations [361]. Likewise, SERS active materials such as silver or gold in the visible to NIR region are not SERS active in the UV region [132]. In fact, adapting SERS to UV Raman spectroscopy has been particularly challenging due to issues with finding materials that are SERS active in the UV excitation [132]. Among the materials tested to date, Al substrates show promising results [132],

[143]–[145], however, further research is necessary to optimise the signal enhancement in the UV region.

Lastly, while reproducible and consistent measurements are potentially possible with nanostructured in-situ activated SERS substrates, SERS spectra may still differ significantly to traditional Raman spectra of the same molecule. As such, reference SERS spectra of target molecules collected using the nanostructured in-situ activated SERS method described above are necessary to allow full and unambiguous data analysis.

10.2.3 Fluorescence Mitigation

A wide range of fluorescence mitigation techniques has been proposed to date and a summary of the available techniques is provided in Section 2.3.2.

Based on the results of this study that show increased fluorescence background and its variability at cryogenic temperatures, it becomes obvious that any computational methods relying on baseline subtraction, such as baseline estimation using wavelet transformation [105], principal component analysis [106], and polynomial curve-fitting [107], would be ineffective for a mission to Europa or any other Icy World. The fluorescence increase and higher variability of the fluorescent background require a robust fluorescence mitigation technique that does not rely solely on statistical calculations of the baseline or repeated measurements without changing any physical parameters.

Time-gating, or fluorescence quenching as implemented on the RLS instrument [51], could be a powerful fluorescence elimination tool for biosignature detection even at very low temperatures analogous to Europa. As already described in Section 2.3.2, time-gating exploits the instantaneous character of Raman scattering as opposed to fluorescence, which occurs in picoseconds to milliseconds after the Raman signal [90], [112], [113]. While temporal dependence of the fluorescence effect on cryogenic temperatures was not within the scope of this study and is yet to be confirmed experimentally, no significant changes are expected. This is because the source of the fluorescence increase is the reduction of radiationless decay and extra energy heat loss due to the reduced number of collisions as the movement of molecules is impeded at lower temperatures, which is not a temporal effect.

Furthermore, compact single photon avalanche diode arrays (SPAD arrays) are capable of nanosecond time gating, which allows the use of time-gating in planetary sciences where traditional streak cameras used for the purpose do not meet the mass and size requirements [90], [100], [101]. Nevertheless, while time-gating could be a highly effective method, it has not been

able to completely avoid fluorescence. This is because organics, where fluorescence occurs after sub-nanosecond intervals from the excitation, have proven to be problematic to resolve with current SPAD arrays [90], [112]. It is important to note that this is a relatively minor issue compared to the benefits of time-gated Raman instruments, however, further development is necessary to enable fluorescence elimination for all molecules.

Alternatively, the SSE fluorescence mitigation technique, although based on computational subtraction of the fluorescence background which relies on repeated measurements and statistics to a certain extent, has shown to be very effective in eliminating the fluorescence effect [108], [109]. This technique was already introduced in Section 2.3.2. It relies on processing a set of raw spectra of a sample collected repeatedly over a number of slightly shifted excitation frequencies, e.g. 1 cm^{-1} apart [108], [109]. Most recently, the technique was also shown to be effective even at low temperatures [364]. This makes SSE a very capable fluorescence mitigation technique for the exploration of Europa. However, it is also important to note that this method requires a precise control of the laser source wavelength, which requires the use of tunable laser sources with a sufficiently narrow spectral linewidth. This introduces additional complexity to the instrument design and may be restricted by the currently available laser source technology.

An alternative approach to fluorescence elimination is a multiline Raman system. This method combines two or more excitation wavelengths in order to collect spectra without fluorescence noise. This method is also described in more detail in Section 2.3.2. One of the main advantages of this method is that it enables the collection of spectra at multiple excitations, which could, besides fluorescence mitigation, also provide more information on the composition of the sample. This could be particularly beneficial for complex samples with many unknown constituents. However, while multi-line Raman systems could be very effective, the technology is significantly more complex and at much lower TRL compared to other fluorescence mitigation techniques. As such, a significant level of further development is necessary for multiline Raman systems to be considered for planetary exploration.

Lastly, it is also important to mention that SERS, which was already discussed in Section 10.2.2, also reduces the effect of fluorescence in Raman spectra as it enhances the signal strength beyond the fluorescence baseline. Implementation of SERS for a mission to Europa as well as its drawbacks and any required future development were already discussed in the previous section (Section 10.2.2). Likewise, fluorescence can also be eliminated by using a DUV excitation, at which the Raman signal and fluorescence are well separated. The use of DUV excitation has also already been discussed in terms of biosignature detection on Europa in Section 10.2.1 and 10.2.2.

10.2.4 Miniaturization

The allocated volume and mass as described in Section 10.1.2 is a rather challenging constraint considering the size of the state-of-the-art instruments for planetary exploration. According to the official NASA records, SHERLOC, a DUV Raman spectrometer recently launched on the Perseverance rover, has the volumetric envelope of 26.0 x 20.0 x 6.7 cm, and SuperCam, a visible excitation Raman spectrometer also launched with the Perseverance rover, 38 x 24 x 19 cm. While the total mass of SHERLOC is 4.72 kg, which would fit the allocated mass budget, the instrument is still much larger in size than the allocated volume. The total mass of SuperCam is 10.6 kg and while the SuperCam instrument suite includes multiple integrated instrumental techniques, it is much larger and heavier than the allocated budget for a mission to Europa. It is also important to note that both of these instruments are flown space grade instruments that have already been miniaturized for the use in space. Nevertheless, considering the strict requirements of the Europa Lander mission and the mass and size parameters of the current state-of-the-art Raman instruments for planetary exploration, further miniaturization is necessary to enable the exploration of Icy Worlds using Raman spectroscopy. Naturally, this is not a trivial task as miniaturization of Raman instruments typically involves a trade-off between the size and the performance of the instrument, i.e. spectral resolution, spectral range and the throughput, which affects the signal strength.

The mass and size of Raman instruments are driven by a number of factors including the size of the laser source, the spectrometer itself, as well as the individual optical components within the spectrometer. The miniaturization potential of the laser source depends on the required excitation wavelength. While compact microchip diode lasers are commercially available in the visible to NIR spectrum and have been widely used for miniaturized Raman instruments, UV laser technology has not quite caught up with the more widely used visible and NIR sources. UV lasers tend to be bulkier and more expensive, which makes visible and NIR excitations more favourable for planetary exploration. However, it is also important to note that the UV laser technology is a fast-paced industry and recent advances now allow the development of much smaller UV lasers with sufficiently narrow linewidth and Raman-compatible stability. Compact microchip DUV lasers that could be used as a Raman excitation source are now also available, although still at a steep cost.

The size of the spectrometer is a much more complex issue as it involves physical constraints associated with the optical path of the instrument. One of the key parameters in the design of the spectrometer is the focal length of the mirrors or lenses. The focal length can be minimized by either decreasing the length of the detector or increasing the gratings groove density. Increasing

the groove density of the grating also increases the spectral resolution. However, higher grating groove density also decreases the spectral range, which is a high-level design parameter that is not variable as it stems from the scientific goal of the instrument. As such, the spectral range limits the highest allowable groove density of the gratings and the miniaturization potential of the instrument.

On the other hand, decreasing the length of the detector also decreases the number of pixels, which in turn decreases the spectral resolution. The spectral resolution is also a high-level design parameter that is not variable and thus drives the number of pixels required and the detector width. It is also important to note that the required spectral resolution also limits the focal length as a longer focal length allows a wider separation of light, which leads to higher spectral resolution.

The spectral resolution is also driven by the slit size with smaller slit sizes providing higher spectral resolution. On the other hand, a small aperture also limits the throughput which in turn leads to a lower Raman signal. However, shorter excitation wavelengths can be coupled with smaller apertures as they naturally produce a much higher Raman signal. This can be to a certain extent used to compensate for shorter focal length and its impact on the spectral resolution. However, the signal strength is one of the most important parameters for the detection of biosignatures on Europa and as such, a trade-off between the spectral resolution and signal strength as well as the size of the instrument is necessary. This somewhat restricts the miniaturization potential of Raman instruments.

Alternatively, a less traditional spectrometer design can be used to achieve a highly compact Raman instrument with high spectral resolution, sufficiently wide spectral range, as well as high throughput. One such design is a Spatial Heterodyne Spectrometer (SHS). The SHS evolved from the Michelson interferometer but the scanning and fixed mirrors are replaced by stationary diffraction gratings in the SHS. A basic design of a Spatial Heterodyne Raman Spectrometer is shown in Figure 10-3. The scattered light from the sample is split into two beams by a beam splitter. The two beams are then dispersed onto two diffraction gratings. Dispersed from the gratings, the two beams interfere and produce an interferogram, which is then analysed using Fourier transform. This retrieves the original signal that enters the SHS.

While the technology is relatively young and mostly restricted to research centres with no wide commercial availability yet, it has been successfully demonstrated a number of times with very promising results [333], [365]–[370]. SHS Raman instruments do not include any moving parts, which makes the design very robust. The SHS design also allows a much wider aperture than in traditional spectrometers, which allows high throughput and consequently much higher signal

strength. Simultaneously, SHS also offers high spectral resolution and spectral range without limiting the throughput. The spectral resolution in a Spatial Heterodyne Raman Spectrometer (SHRS) is only limited by the gratings and the spectral range by the number of pixels on the CCD [370]. This makes SHRS much smaller compared to traditional Raman instruments with similar parameters.

For its many merits, SHRS is ideal for planetary exploration and could enable the development of a highly miniaturized Raman instrument at no cost of spectral resolution, spectral range nor signal strength. Nevertheless, it is also important to note that there are also a few drawbacks of the SHRS method that need to be considered. Namely, apart from the lower TRL compared to traditional Raman instruments, SHS Raman systems are demanding instruments in terms of data processing due to the interferometer data conversion required to retrieve the original signal.

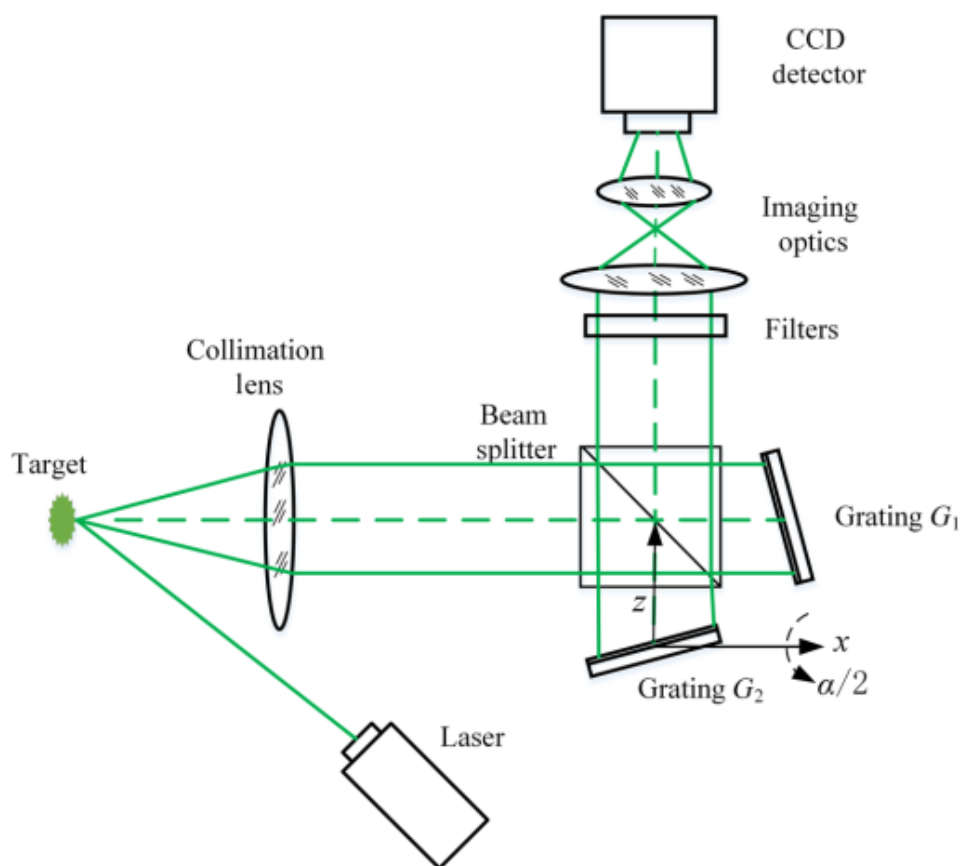


Figure 10-3 Working principle of a Spatial Heterodyne Raman Spectrometer [366]

10.3 Design

Based on the experimental results of this study, mission requirements based on the NASA Europa Lander study and instrument considerations discussed in Section 10.2, the following section identifies two promising instrument designs compatible with a lander mission to Europa. The proposed instrument designs are described in detail and compared in Table 10-1. The table

includes a description of the main design features and parameters, technology readiness level assigned, limitations, as well as the advantages and disadvantages and areas for future development. Note that these instrument designs are based on technology and methods at various levels of maturity and as such, the technology readiness level was assigned based on the maturity of the individual key technological components as well as the level of development necessary for an integrated system. The two instrument designs are:

- 1. Green Excitation Time-Gated Surface Enhanced Raman Spectrometer using In-Situ Activated AgCl Nanostructured SERS Substrate Technology**
- 2. DUV Spatial Heterodyne Raman Spectrometer**

While the green excitation cannot detect molecules at LODs required for the exploration of Europa, it could be a very powerful tool in combination with SERS technology. Novel emerging technology based on in-situ activation of precursor AgCl nanoparticles and SERS substrate nanostructuring, described in Section 10.2.2, could enable highly reproducible and consistent SERS measurements even after years of storage during planetary transfer. The LOD of such an instrument would be in the order of ppb or even lower, which comfortably meets the LOD requirement for the detection of biosignatures on Icy Worlds.

Due to the high fluorescence experienced by most organics in the green wavelength region, the instrument requires a robust fluorescence mitigation method. While a number of fluorescence mitigation techniques are available, time-gating is a highly efficient method that does not require much additional mass and size allocation. Time-gating also uses technology that is readily available and does not restrict the instrument's TRL. While some sub-nanosecond fluorescence may not be completely eliminated by time-gating, SERS enhancement of the signal may limit the impact of the residual fluorescence on the resulting Raman spectra.

If the fluorescence mitigation is successful, the proposed green Raman spectrometer, as described in Table 10-1, should be able to detect and identify most molecules of interest to astrobiology, including most minerals. Green excitation Raman spectrometers are also widely used and the plentiful availability of compact green lasers compatible with Raman spectroscopy makes them relatively easy to miniaturize. With compact laser sources being readily available, the major size constraint is the focal length and spectral resolution trade off. While an instrument within the size and mass budget of a mission to Europa and with sufficient spectral range and the spectral resolution of 4.5 cm^{-1} should be feasible, a SHS design may be necessary if a higher spectral resolution is required.

However, while a green Raman on its own is a heritage instrument, the addition of SERS lowers the TRL of the concept significantly. SERS technology compatible with planetary exploration is the primary limitation of this design in terms of technology availability as well as the TRL. Both the AgCl in-situ activated substrate technology and nanostructured SERS substrates have been verified experimentally, however, they have not been combined as of yet and further development is necessary to optimise this technology. Reference spectra obtained using this SERS method will also be required to enable effective data analysis. Other areas for future development also include verification of the shelf-life of the substrates or optimisation for various sizes of molecules. Lastly, the method of sample deposition and coupling to the substrate cannot be neglected as it drives the SERS enhancement and may require an additional complex mechanism.

On the other hand, a DUV SHS Raman instrument could be a relatively simple instrument that does not require the complex and underdeveloped SERS technology for the detection of biosignatures at low concentrations. The SHS design allows high spectral resolution and range at high throughput and in combination with the natural signal enhancement at short excitation and resonance signal enhancement for some molecules that are resonant in the DUV region, the instrument could be capable of LODs in the order of ppm. For some molecules, LODs in the order of ppb may also be possible. While this may not allow the detection of all the target molecules at the required concentration for life detection on Europa, many high importance biosignatures such as amino acids or nucleobases could be detectable at the required ppb LOD. Furthermore, the natural separation of the Raman signal and the fluorescence signal at excitations below 244 nm completely eliminates the impact of the fluorescence noise on the spectra without any additional fluorescence mitigation mechanisms. Recent advances in the DUV laser technology and the resulting compact DUV laser sources in combination with the SHS concept also allow a DUV SHS Raman design to meet the required mass and size requirements of a mission to Icy Worlds.

While the availability of Raman compatible compact DUV sources is still one of the major TRL limitations of this instrument design that may also have an impact on the achievable spectral resolution of the instrument, the SHS design should allow a very high spectral resolution, potentially even as low as 2 cm^{-1} , and the full spectral range of $150\text{-}3800\text{ cm}^{-1}$. Furthermore, despite limited availability of compatible compact Raman sources, DUV laser sources compatible with spaceflight are available. While further miniaturisation for Europa is necessary, SHERLOC, one of the Raman instruments on the Perseverance rover, uses a DUV laser source for Raman measurements on Mars.

However, the high energy DUV laser could also lead to sample damage and further research into the laser damage thresholds is necessary. Furthermore, while DUV hardened optics and detectors are becoming increasingly more available, they could still represent a challenge in the near future. The higher complexity of the data processing in order to retrieve the original signal entering the SHS also needs to be considered. Lastly and most importantly, the DUV SHS Raman instrument may still require SERS to achieve the very low LOD required for biosignature detection on Europa, which would be a whole new challenge to be addressed.

	Green Excitation Time-Gated SERS Instrument using In-Situ Activated AgCl Nanostructured SERS Substrate Technology	DUV Spatial Heterodyne Raman Spectrometer
Excitation Wavelength	~532 nm	<250 nm
Signal Enhancement Method	SERS using an in-situ activated AgCl nanostructured SERS substrate concept	<ul style="list-style-type: none"> • natural signal enhancement at a short excitation wavelength • SHS design allowing a high throughput at high spectral resolution and range • resonance (for some target molecules only)
Achievable LOD	ppb	ppm, potentially ppb for some molecules including high importance biosignatures such as amino acids and nucleobases
Fluorescence Mitigation Method	time-gating/SERS	natural wavelength separation
Fluorescence Mitigation Limitations	Organics, where fluorescence takes place after sub-nanosecond intervals, may not be resolved with currently available SPAD arrays, however, SERS may be able to mitigate the effect of any fluorescence that is not eliminated via time-gating	none, however, for the best separation of the autofluorescence, the laser excitation wavelength should be <244 nm
Mass and Size Compatibility to the Requirements of a Mission to Europa	yes	yes
Main Mass and Size Constraint	focal length/spectral resolution trade-off	laser source size
Molecule Detectability	provided that fluorescence mitigation is successful in most cases, most target molecular species should be detectable, although sub-nanosecond	molecules resonant in DUV (e.g. aromatic amino acids, nucleic acids and PAHs) at ppb LOD, other target molecules at

	fluorescence may cause detectability issues if present and not mitigated by SERS	higher LODs (but still in the order of ~ppm)
Technology Availability Limitations	SERS substrates compatible with planetary exploration	<ul style="list-style-type: none"> • compact DUV laser source • DUV compatible optics and detector
Complexity	while the green excitation Raman system on its own is a widely used system with space heritage, the time-gated system including SERS is a relatively complex instrument, potentially requiring sample handling to ensure the sample is coupled to the substrate to allow SERS measurements	relatively simple design is possible without any moving parts or additional fluorescence mitigation mechanisms
Spectral Resolution	potentially 4.5 cm^{-1} [364], higher resolution is potentially possible with SHS	$\sim 2 \text{ cm}^{-1}$ potentially possible
Spectral Resolution Limiting Factor	focal length/spectral resolution trade-off	availability of DUV compatible detector and optics
Spectral Range	full $150\text{-}3800 \text{ cm}^{-1}$ range possible	full $150\text{-}3800 \text{ cm}^{-1}$ range possible
TRL	TRL 2-3 – nanostructured and in-situ activated SERS substrate concepts have been tested separately, a system integrating both only conceptualized	TRL 3-4 – not tested with a miniaturized laser source but SHS Raman instruments in the UV region have been successfully built and tested
TRL Limitation	in-situ activated AgCl nanostructured SERS	compact DUV laser source and SHS design
Main Advantages	<ul style="list-style-type: none"> • very low LOD • use of widely available 532 nm laser technology which does not require custom optics • compact laser sources available • wide heritage of green excitation Raman systems 	<ul style="list-style-type: none"> • very low LOD without the use of SERS • simple fluorescence mitigation via natural wavelength separation - no need for additional mechanisms or processing
Main Drawbacks	<ul style="list-style-type: none"> • low TRL of SERS technology compatible with planetary exploration • variability of SERS enhancement depending on the target molecule size • lack of SERS reference spectra • SHS design potentially necessary for higher spectral resolution • requires robust fluorescence mitigation technique as most 	<ul style="list-style-type: none"> • The high energy DUV laser could lead to sample damage and further research into the laser damage thresholds is necessary • availability of DUV compatible optics and detectors • availability of compact DUV lasers compatible with Raman spectroscopy – DUV microchip lasers available but not used in Raman spectroscopy to date

	<ul style="list-style-type: none"> organics are heavily fluorescent at 532 nm • not all fluorescence may be eliminated by time-gating 	<ul style="list-style-type: none"> • complexity of data processing to retrieve the original signal • may still require SERS to achieve the very low LOD required for biosignature detection on Europa
Areas for Further Development	<ul style="list-style-type: none"> • in-situ activated AgCl nanostructured SERS substrates and their performance <ul style="list-style-type: none"> ○ SERS reference spectra ○ characterisation of the SERS enhancement relative to the molecule size ○ characterisation and optimisation of sample deposition onto the substrate ○ verification of the shelf-life and degradation over long periods of time • SPAD arrays for sub-nanosecond fluorescence elimination 	<ul style="list-style-type: none"> • identification of laser damage thresholds for target molecules in European analogue • compact DUV lasers for Raman spectroscopy • DUV compatible detectors and optics • characterisation of the LOD achievable for target molecules • DUV SERS

Table 10-1 A description of two promising Raman instrument designs for the detection of biosignatures on Europa including the main design features, techniques, limitations as well as the advantages and areas for further development

10.4 Measurement Method

There are no specific requirements for the measurement method defined by the Europa Lander mission. The mission baselines 3 samples of approximately 10 cm³ of surface material to be collected from the depth of at least 10 cm and presented to the instruments [19], [26]. The lander sample collection system is to maintain the samples' scientific integrity including keeping the sample's temperature below 150 K (<-123.15 °C) or at the surface temperature of the excavation site [26].

The surface temperature on Europa varies between -233 to -168 °C depending on the location and time of day [24], [71], which makes the -123.15 °C sample temperature upper limit rather high to maintain the sample's integrity. At best, this would be 45 °C above the native surface temperature and only if collected near the equator and at the hottest time of the European cycle. Considering that the average temperature at 10 cm below the surface is estimated to be between -175 to -200 °C [24], [71], it would also exceed the sample's native temperature by at least 52 °C. This is a considerable temperature difference, which may affect the sample's integrity, especially if temperature sensitive molecules or organisms are present in the sample. While the -123.15 °C sample temperature limit is a practical limit resulting from the engineering challenges of keeping

the sample cold as it is being transferred through the sample handling system to the instruments, it is critical to ensure that the temperature is kept either equal to or as similar to the native sample temperature as possible.

Furthermore, this study provides evidence that in order to maximise the science return of the mission, two measurements at two different temperatures as far from each other as possible should be taken. This is described in detail in Chapter 7 and Chapter 9. This enables investigations of the cryogenically induced changes in the spectra, which provides further information about the sample's composition as well as any molecular or phase changes and could greatly improve the identifiability of the sample. Furthermore, some target molecules such as heat-shock or cold-shock proteins may be expressed in higher quantities at various temperatures compared to their native state as described in Section 4.3.6.

Notably, the two measurement temperature points do not necessarily need to include a measurement at room temperature or any other relatively high temperature that would require sample heating and thus an additional power budget allocation. Rather, a measurement at the native sample temperature could be taken, together with a subsequent measurement at the highest temperature the sample spontaneously heats up to, as it rests in the sample delivery system. Considering that the Allowable Flight Temperature (AFT) in the vault of the Europa Lander is $-40/+50$ °C at the vault-wall interfaces and the instruments are advised to qualify for the temperature range of -55 °C to $+70$ °C [19], the sample may not require an additional power budget allocation in order to heat up to a considerably higher temperature than its native temperature. In fact, this spontaneous heating may be a very useful resource as the power budget for a mission to such a distant planetary target such as Europa or other Icy Worlds is one of the key constraints due to the limited power raising capabilities of the spacecraft. Nevertheless, in order to ensure that the measurement temperatures are fully defined and thus allow full analysis of the data, the sample temperature should be monitored and recorded throughout the experiments.

10.5 Future Directions

The results of this study, as well as information available in literature published to date, showcase that the detection of biosignatures on Icy Worlds is well beyond the capabilities of current state-of-the-art Raman instruments for planetary exploration. Significant levels of further research and development are necessary in order to progress the TRL of the Raman spectroscopy technology that may one day enable the detection of life on Europa or Enceladus. The key technology

required for the detection of biosignatures on Icy Worlds using Raman spectroscopy, as well as areas for further development, are highlighted below.

Firstly and most importantly, it is clear that Raman spectroscopy for the detection of biosignatures on Icy Worlds requires SERS in order to achieve the extremely low LOD required for such a mission. Since Icy Worlds were identified as high priority targets for future planetary exploration by both NASA and ESA [14], [18], the future of Raman spectroscopy for planetary exploration thus relies on the development of SERS compatible with long duration spaceflight. While recent advances in the SERS technology cover the basic concepts that are required to enable SERS measurements on Icy Worlds and critical processes and methods have been verified experimentally, the technology is yet to be fully developed and optimised. Specifically, the method of activating AgCl nanoparticle coated substrates in-situ represents a key enabling concept for the use of SERS in planetary sciences and requires much more attention. While the main principles of this method were experimentally verified and the concept shows very promising results [146], [158], [363], further research is necessary to fully characterise the degradation profile of these substrates over long periods of time and in vacuum. Other variables in the manufacturing process such as the optimal nanoparticle density, the coating process or duration of the activation exposure need to be explored in more detail. The achievable signal enhancement and LOD for molecules of varying size also need to be defined.

Similarly, nanostructured SERS substrates have been discussed in literature in many shapes, materials and forms [132], [134], [140], [141], [143], [147], [151], [153], [371], [372], however, they have not been combined with a layer of in-situ activated AgCl nanoparticles coating. The optimal geometry for the detection of biosignatures on Europa will need to be defined, which requires further research into the SERS enhancement dependence on the molecular size. The method of sample deposition and coupling to the substrate in Europa's lower gravity also needs to be addressed as it drives the SERS enhancement and may require an additional complex mechanism.

Additionally, reference SERS spectra of the target molecules together with their experimentally defined LODs are necessary in order to allow full analysis of the data. This is because SERS enhanced spectra can differ to spectra collected using traditional Raman spectrometers. The spectra can also differ depending on the specific SERS substrate design and as such, reference spectra of astrobiologically significant samples collected using the final optimised SERS substrates will be required.

It is also important to note that both the in-situ activated SERS substrate design and nanostructured SERS substrates individually as well as the combination of the two technologies

represent a significant advancement in Raman spectroscopy in general, not just for the exploration of Europa. A long shelf-life SERS substrate that allows reproducible and consistent SERS measurements would be an invaluable asset in many areas of science besides planetary exploration. To name a few, SERS is used in medicine and biomedical research for diagnostics and drug development as well as in analytical chemistry for many applications including environmental pollutant detection, forensic science or even for the restoration of original pigments in art works [132].

Similarly, further research into UV SERS active materials is necessary to enable UV SERS measurements. While UV Raman spectroscopy has been somewhat less popular than the more widely available visible and NIR Raman systems, this is primarily due to the less advanced UV laser and optics technology. As a result of this, UV SERS has also not been fully explored to date and there are many gaps to fill in now that advanced UV laser sources, detectors and optics are becoming increasingly more available.

As demonstrated in this study, another critical gap in the knowledge and technology required for the development of life-detection instruments compatible with a mission to Icy Worlds is the effect of the cryogenic temperatures on the instrumentation, as well as the science output. The results of this study show that the cryogenic temperatures on Icy Worlds will have a significant impact on Raman spectra and further studies are required to prepare for upcoming missions. This study provides an outline of some of the most important considerations for cryogenic Raman measurements derived from a relatively broad spectrum of molecules and molecular species. However, it also highlights the lack of data on cryogenic Raman measurements at temperatures analogous to Europa and other Icy Worlds. While some of the gaps have been filled by the results of this study, there is much more work to be done. Particularly, a complete database of Raman spectra of all target molecules and other molecules significant for astrobiology at various temperatures ranging to cryogenic temperatures analogous to Icy Worlds will be required to allow full analysis of samples collected on Icy Worlds. This is critical to avoid misidentification due to the cryogenically induced changes as traditional Raman spectra collected at room temperature could be very different to those collected on Europa and other Icy Worlds.

It is also important to note that a complete Raman spectra database including measurements at various temperatures would be an incredibly valuable asset for many other applications beyond planetary sciences. As shown in this study, the cryogenically induced changes can be used to identify molecules based on the severity of the Raman shift change as this is linked to the vibrational modes of Raman bands. While further research into the relationship between the vibrational modes and the cryogenically induced changes is necessary, this method of

identification could be very helpful for molecules with similar Raman signatures or in samples containing multiple compounds with interfering bands. Further research into the cryogenically induced changes in Raman spectra together with a database summarising the results could thus greatly improve the scientific capabilities of Raman spectroscopy.

While this was not within the scope of this study, the results also show that further research is necessary to understand the cryogenically induced changes in minerals and inorganic material that could obstruct the detection of biosignatures on Icy Worlds. Particularly, soil simulants and analogues should be used at analogue concentrations in order to define the potential interference. This is especially important for SERS measurements as inorganic interferants could obstruct the SERS signal enhancement.

Lastly, while fluorescence mitigation techniques are relatively well defined and very effective solutions are available, further work may be needed to evaluate and potentially mitigate the effect of the cryogenically enhanced fluorescence noise.

Chapter 11 Conclusions & Future Work

Jupiter's moon Europa is a high priority target for future planetary exploration and was specifically named in both NASA's most recent Decadal Survey as well as ESA's Voyage 2050 plan as a potential candidate for their future interplanetary missions [14], [18]. This is due to its vast saline ocean underneath its icy shell, which could provide an ideal chemical environment for the emergence of life [19]. However, Europa is a very different world to the environment on Mars, which has been the primary planetary target for the past few decades and which shaped the design of current state-of-the-art instruments for planetary exploration. A new generation of scientific instruments will be necessary for the exploration of Icy Worlds.

As an exceptionally versatile non-destructive compositional analysis technique, Raman spectroscopy has gained popularity in planetary exploration over the last decade. It can identify a vast spectrum of molecules including both minerals and biomolecules, as well as provide information on the molecular structure, material phase and atom arrangements. For its many merits, Raman spectroscopy was also identified as one of the instruments in the model payload of the Europa Lander mission, which is currently under development at NASA [19], [26].

This study provides an overview of the key limitations of contemporary Raman spectroscopy for the detection of biosignatures on Europa and identifies critical design parameters and requirements for the development of a Raman instrument optimised for such a mission. In order to effectively evaluate the capabilities and limits of Raman spectroscopy, high priority molecular targets specific for the search for life on Europa were discussed and identified. Based on the likelihood of occurrence, biogenicity, abundance, uniformity across the 3 domains of life, stability in extreme environments, representation in extremophile organisms and uniqueness to terrestrial life, the identified target molecules were assigned relative priority for the search for life on Europa.

While many traditional biosignatures used for the search for life on Mars are also high priority detection targets for the exploration of Europa, other molecules could also signal the presence of life on Icy Worlds. For instance, Europa's extremely cold icy shell could help preserve molecules that could not survive on the rocky surface of Mars. Besides traditional biosignatures such as amino acids, nucleobases and carboxylic acids, uniquely biogenic molecules associated with crucial protectant capabilities such as ectoine, trehalose, scytonemin and carotenoids were also identified as high confidence and high priority biosignatures for the search of life on Europa. Other suitable target molecules include isoprenoid biomarkers, for instance hopanes or steranes, and biomolecules such as porphyrins, nicotinamide and organosulfur metabolic products.

A selection of the identified high priority target molecules was used to study the key limits of Raman spectroscopy for the exploration of Europa. The detection limits explored in this study were the thermally induced changes and fluorescence interference in Raman spectra of the target molecules, laser induced sample degradation, and sensitivity to relevant molecules at low concentrations analogous to Europa.

Laser damage thresholds were identified for the selected target molecules at UV excitation of 325 nm, visible excitation of 532 nm and 633 nm and NIR excitation of 785 nm. While laser induced sample damage is a commonly cited concern for studies of biological samples using Raman spectroscopy, only a couple of very photosensitive molecules such as pigments and porphyrins showed susceptibility to laser damage at visible and NIR excitations. At the UV 325 nm excitation, most molecules yield to laser damage at higher power, however, the effects of the sample degradation due to the laser damage were not as severe as expected. While a full dataset at 325 nm could not be obtained, measurements at this excitation still allowed the detection of most traditional biosignatures for life detection such as amino acids.

Fluorescence is a notorious challenge for the detection of biogenic material using Raman spectroscopy and a critical factor for the selection of the excitation wavelength for various applications of Raman spectroscopy. However, this study showed that many high importance target molecules are identifiable across excitation wavelengths from UV to NIR. As expected, the NIR 785 nm excitation reduced the effect of fluorescence in the spectra of most of the tested target molecules compared to measurements at UV and visible excitations. However, it also generated much lower Raman signal and the sensitivity to target molecules at low concentrations is considerably lower than at visible excitation.

While theoretical estimates showed that neither visible nor NIR excitation could detect molecules at a concentration required for the detection of life on Europa, the NIR excitation would struggle to detect biomolecules even at the much higher concentration predicted for the Martian regolith [61]–[64]. On the other hand, at 532 nm, many of the examined target molecules could be detectable in the Martian regolith, if not on Europa. Notably, the visible 532 nm excitation could also meet the LOD requirement of the Europa Lander mission, which is only in the order of ppt. However, considering that research conducted to date indicates that the concentration of organics in the European ice is in the order of ppb and as low as 0.01 ppb [9], [19], [23], this is unlikely to be enough unless a specific higher concentration deposit or colony is found and targeted. For biosignature detection on Europa or other Icy Worlds at these extremely low concentrations, both 532 nm and 785 nm would need to be used combined with SERS.

An alternative method of increasing the signal intensity is using a short excitation wavelength. While DUV measurements at low concentrations were not within the scope of this study, based on the results at higher excitation wavelengths DUV Raman systems should be easily capable of detection at the ppt concentration required by the Europa Lander mission. For many target molecules for the detection of life on Europa, LODs in the order ppm should also be possible. Resonance of some high priority biosignatures such as amino acids, nucleobases or PAHs in the UV region could also contribute to even lower LODs. While the achievable LODs at DUV excitation fall short of the required LOD for most molecules, the signal enhancement for detection at very low concentrations of ppm or lower does not rely on SERS, which is the main advantage of using a DUV Raman system. In comparison, SERS is a complex method that is still poorly understood and that requires a significant amount of further development to be adapted to planetary exploration.

Besides the extremely low concentrations in ice, biosignatures on Europa would also be exposed to extremely low temperatures unparalleled on Earth, ranging down to $-233\text{ }^{\circ}\text{C}$. However, there is very limited data on the spectra of molecules at these extremely low temperatures, especially for molecules important for astrobiology. The results of this study showed that cryogenically induced changes in the spectra of molecules could be critical for the detectability of the molecules. Spectral changes induced by the extreme low temperatures include shifting of Raman bands to higher or lower frequencies, narrowing of the Raman band width, decrease in the variance between individual spectra, the emergence of new bands or the diminishing of existing Raman bands as well as changes in the signal intensity and increasing fluorescence background.

While the profile of the Raman shift change as well as the change in the Raman band width proved to be fairly consistent among most molecules and most Raman bands, there were also numerous exceptions and many other effects were found to be highly specific to each molecule. The occurrence of new bands or diminishing of existing bands as well as changes in the Raman signal strength were particularly unpredictable and no common trend was found. This is particularly concerning as these effects could greatly impact the detectability and identifiability of the target molecules. Particularly, while most molecules showed an exceptional increase in the signal strength at low temperatures, some others, such as nucleobases, showed a significant decrease in the signal strength.

Perhaps one of the most critical effects of the cryogenic temperatures is the increase in the fluorescence noise, which is also accompanied by a higher variability between individual measurements. This cryogenically induced fluorescence increase was shown to significantly decrease the SNR in the spectra or, in many cases, completely overshadow the Raman signature. This makes many computational fluorescence mitigation techniques either less reliable or

completely ineffective as it requires a very robust fluorescence mitigation method that does not rely on statistics or baseline subtraction.

On the other hand, some of the cryogenically induced changes in the spectra could be advantageous for the detection of biosignatures on Icy Worlds. It was shown that for photosensitive samples, the laser damage threshold increases significantly at cryogenic temperatures. This allowed either a much higher Raman signal or even the identification of previously unresolvable molecules. Furthermore, it also rendered highly photosensitive fluorescent molecules, such as porphyrins or carotenoids, immune to the cryogenically induced fluorescence increase. The SNR of photosensitive molecules increased at low temperatures as the reduction in the laser damage allowed higher Raman signal intensity. This counterbalanced and, in many cases, outperformed the fluorescence increase. This could be a very desirable side effect of the extreme low temperatures on Europa as it could potentially allow the detection of very photosensitive molecules or intensify the Raman signature. Likewise, it is possible that the destructive nature of DUV and UV excitations could be mitigated at least to a certain extent by the extremely low temperatures on Europa.

Likewise, a significant decrease in the Raman band width as well as in the variance between individual measurements was recorded in the spectra of all target molecules. This makes measurements at cryogenic temperatures both more precise and more accurate, which could be useful for many other applications beyond the exploration of Icy Worlds.

Another common and potentially very helpful trend observed in the data was the link between the absolute maximum change in the Raman shift between the temperature extremes and the complexity of the molecule. The results indicate that Raman measurements of smaller, shorter or otherwise structurally less complex molecules generate much higher changes in the Raman shift at cryogenic temperatures. Nevertheless, it is also important to note that many important biosignatures are simple molecules and the changes in the band shift observed on Europa may thus be up to 25 cm^{-1} . This is a significant change that may obstruct the identification of target molecules. It also highlights the need for a database of reference spectra collected at temperatures analogous to Europa, which will be necessary for the full analysis of samples on Europa in order to avoid misidentification.

Likewise, a link between the type of vibrational modes associated with Raman bands and the change in their Raman shift at extreme low temperatures was identified. Bands associated with stretching vibrations, out of plane deformation of a ring or vibrations including inner atoms of a molecule were found to be more likely to shift to lower frequencies at low temperatures or shift to higher frequencies by only a small amount compared to bands assigned to other vibrational

modes. On the contrary, bands that shift to a significantly higher frequency at lower temperatures are more likely to be associated with vibrations that are relatively less constrained within the molecule, that is, vibrational modes including the extremities of a molecule, such as its side chains, outer atoms and groups, or vibrations including most or all of the molecule's main chain and in plane bending within a ring.

This link offers an exciting new method of molecule identification solely based on the comparison of spectra collected at two different temperatures and could greatly improve the identification capabilities in Raman spectroscopy for a wide array of applications beyond the exploration of Europa. This also suggests that taking two separate Raman measurements of the same sample at two different temperature points could be a very advantageous strategy for spectra collection on Europa as it could provide much more information on the composition of the sample or help distinguish between compounds with very similar Raman signatures.

The investigations of the key detection limits together with data available in previously published literature were used to derive critical instrument design requirements. The results showed that the spectral resolution required to ensure maximum science return for an astrobiology mission to Europa is 2-3 cm^{-1} . This is much higher than the spectral resolution of contemporary state-of-the-art Raman instruments for planetary exploration. More importantly, it may be particularly challenging for miniaturized instruments as miniaturization of Raman instruments typically relies on a trade-off between the size and the performance of the instrument, i.e. spectral resolution, spectral range and the throughput, which affects the signal strength. Furthermore, despite being highly miniaturized instruments, contemporary state-of-the-art Raman spectrometers for planetary exploration, do not meet the strict size and mass requirements of a mission to Europa and further miniaturization will be necessary.

Based on the requirements of a mission to Europa and requirements derived from the experimental study of the detection limits of Raman spectroscopy, key design parameters were identified and discussed in terms of the available technology. Two promising instrument designs compatible with a lander mission to Europa were identified:

- 1. Green Excitation Time-Gated Surface Enhanced Raman Spectrometer using In-Situ Activated AgCl Nanostructured SERS Substrate Technology**
- 2. DUV Spatial Heterodyne Raman Spectrometer**

While the green excitation cannot detect molecules at LODs required for the exploration of Europa, it could be a very powerful tool in combination with SERS technology. Novel emerging technology based on in-situ activation of precursor AgCl nanoparticles and SERS substrate

nanostructuring could enable highly reproducible and consistent SERS measurements even after years of storage during planetary transfer. This would allow the instrument to meet the ppb LOD requirement for a mission to Europa. Furthermore, the combination of SERS and time-gating would effectively mitigate the effects of fluorescence noise without requiring additional mass and size allocation. This would allow the instrument to detect and identify most molecules of interest to astrobiology, including most minerals. With compact laser sources being readily available, the major constraint would be the size and spectral resolution trade-off. While an instrument within the size and mass budget of a mission to Europa and with sufficient spectral range and the spectral resolution of 4.5 cm^{-1} should be feasible, a SHS design may be necessary if a higher spectral resolution is required.

On the other hand, a DUV Raman instrument based on the SHS design could be a relatively simple instrument that does not require the complex and underdeveloped SERS technology for the detection of biosignatures at low concentrations. The SHS design allows high spectral resolution and range at high throughput. In combination with the natural signal enhancement at short excitation and resonance signal enhancement for some molecules that are resonant in the DUV region, the instrument could be capable of LODs in the order of ppm. For some molecules, LODs in the order of ppb may also be possible. While this may not allow the detection of all the target molecules at the required concentration for life detection on Europa, many high importance biosignatures such as amino acids or nucleobases could be detectable at the required ppb LOD. Furthermore, the natural separation of the Raman signal and the fluorescence signal at excitations below 244 nm completely eliminates the impact of the fluorescence noise on the spectra without any additional fluorescence mitigation mechanisms. Recent advances in the DUV laser technology and the resulting compact DUV laser sources in combination with the SHS concept also allow a DUV SHS Raman design to meet the required mass and size requirements of a mission to Icy Worlds. While the availability of Raman compatible compact DUV sources may still have an impact on the achievable spectral resolution of the instrument, the SHS design allows very high spectral resolution without affecting the size of the instrument, potentially even as low as 2 cm^{-1} .

Nevertheless, a significant amount of further development is necessary in order to progress the TRL of the two proposed instruments past the conceptual stage and allow biosignature detection on Europa using Raman spectroscopy. Particularly, SERS was identified as a key enabling technology for future planetary exploration. It is critical for effective investigations of Icy Worlds and their surface and sub-surface material and may also be highly beneficial, if not crucial, for the exploration of other planetary targets, such as the Martian polar regions. This makes a Surface Enhanced Raman Spectrometer the instrument of the future and a key technology to focus on.

SERS techniques that are compatible with long duration space flight have been proposed and show promising results. Particularly, in-situ activated AgCl SERS substrates [146], [158], [363] combined with nanostructuring of SERS substrates could provide highly reproducible and consistent Raman measurements years after manufacture. While the main principles of this method were experimentally verified and the concepts show very promising results, they have not been combined as of yet and further research and development is necessary to achieve a fully integrated and verified system optimised for the detection of biosignatures on Icy Worlds.

11.1 Future Work

First and foremost, a SERS technique compatible with planetary exploration is a critical enabling technology that will be a necessary key component of future Raman instruments for planetary exploration. Particularly, a SERS technique combining in-situ activated AgCl SERS substrates [146], [158], [363] and nanostructuring of SERS substrates offers a solution that is compatible with long-duration spaceflight and that could provide highly reproducible and consistent Raman measurements. However, both the in-situ activated AgCl SERS method and nanostructured SERS substrate method need to be optimised and an integrated system combining the two methods is yet to be developed and verified experimentally. Furthermore, further research is necessary to progress the TRL of the proposed method and to optimise the technique for the detection of biosignatures on Europa. Issues such as the optimal nanostructure geometry, the LOD for molecules of varying sizes, optimal nanoparticle density, the profile of the performance degradation over time and in vacuum as well as the activation exposure time or coupling of molecules to the SERS surface are yet to be fully addressed. Furthermore, a database of SERS spectra of relevant molecules will be necessary as SERS measurements often differ to traditional Raman spectra and could also change depending on the specific SERS method or substrate.

As demonstrated in this study, another critical gap in the knowledge and technology required for the development of life-detection instruments compatible with a mission to Icy Worlds is the effect of the cryogenic temperatures on the instrumentation and the science output. The results of this study showed that the cryogenic temperatures on Icy Worlds will have a significant impact on the Raman spectra and further studies are required to prepare for the upcoming missions. While some of the gaps in the knowledge were filled in this work, further research is necessary. Particularly, a complete database of Raman spectra of all target molecules and other molecules significant for astrobiology at various temperatures ranging to cryogenic temperatures analogous to Icy Worlds will be required to allow full analysis of samples collected on Icy Worlds. This is critical to avoid misidentification due to the cryogenically induced changes as traditional Raman

Chapter 11

spectra collected at room temperature could be very different to those collected on Europa and other Icy Worlds.

Lastly, further research into the relationship between the vibrational modes and the cryogenically induced changes would be a potentially invaluable contribution to science in general. As demonstrated in this study, the cryogenically induced changes can be used to identify molecules based on the severity of the Raman shift change as this is linked to the vibrational modes of Raman bands. This offers a completely new method of identification that could greatly improve the scientific capabilities of Raman spectroscopy, especially if a complete database of molecules at various temperatures is available. This could also be an incredibly valuable asset for many other applications beyond planetary sciences.

List of References

- [1] S. J. Dick, "NASA and the search for life in the universe," *Endeavour*, vol. 30, no. 2, pp. 71–75, 2006, doi: 10.1016/j.endeavour.2006.02.005.
- [2] D. J. Des Marais *et al.*, "The NASA Astrobiology Roadmap," *Astrobiology*, vol. 8, no. 4, pp. 715–730, 2008, doi: 10.1089/ast.2008.0819.
- [3] G. Horneck and C. Baumstark-Khan, Eds., *Astrobiology: The Quest for the Conditions of Life*. Springer Science & Business Media, 2012.
- [4] N. A. Cabrol and E. A. Grin, Eds., *Lakes on Mars*. Elsevier, 2010.
- [5] M. Neveu, L. E. Hays, M. A. Voytek, M. H. New, and M. D. Schulte, "The Ladder of Life Detection," *Astrobiology*, vol. 18, no. 11, pp. 1375–1402, 2018, doi: 10.1089/ast.2017.1773.
- [6] Harold P. Klein, "The Viking Biological Experiments on Mars," *Icarus*, vol. 34, no. 3, pp. 666–674, 1978, Accessed: May 12, 2019. [Online]. Available: [https://pdf.sciencedirectassets.com/272593/1-s2.0-S0019103500X01819/1-s2.0-0019103578900532/main.pdf?x-amz-security-token=AgoJb3JpZ2luX2VjEK3%2F%2F%2F%2F%2F%2F%2F%2F%2FwEaCXVzLWVhc3QtMSJGMEQCIGwg2koXYUGflk0FnSILAprvCgqf80J7xInzfkawvsdAiBAGBtjW05KDbrfj](https://pdf.sciencedirectassets.com/272593/1-s2.0-S0019103500X01819/1-s2.0-0019103578900532/main.pdf?x-amz-security-token=AgoJb3JpZ2luX2VjEK3%2F%2F%2F%2F%2F%2F%2F%2F%2F%2FwEaCXVzLWVhc3QtMSJGMEQCIGwg2koXYUGflk0FnSILAprvCgqf80J7xInzfkawvsdAiBAGBtjW05KDbrfj)
- [7] S. A. Benner, K. G. Devine, L. N. Matveeva, and D. H. Powell, "The missing organic molecules on Mars," *Proc. Natl. Acad. Sci.*, vol. 97, no. 6, pp. 2425–2430, Mar. 2000, doi: 10.1073/PNAS.040539497.
- [8] J. D. Anderson, E. L. Lau, W. L. Sjogren, G. Schubert, and W. B. Moore, "Europa's Differentiated Internal Structure: Inferences from Two Galileo Encounters," *Science (80-.)*, vol. 276, no. 5316, pp. 1236–1239, 1997, doi: 10.1126/science.276.5316.1236.
- [9] C. F. Chyba and C. B. Phillips, "Possible ecosystems and the search for life on Europa," *Proc. Natl. Acad. Sci.*, vol. 98, no. 3, pp. 801–804, Jan. 2001, doi: 10.1073/PNAS.98.3.801.
- [10] A. Coustenis *et al.*, "TandEM: Titan and Enceladus mission," *Exp. Astron.*, vol. 23, no. 3, pp. 893–946, 2009, doi: 10.1007/s10686-008-9103-z.
- [11] C. D. Parkinson *et al.*, "Enceladus : Cassini observations and implications (Research Note)," *J. Astron. Astrophys.*, vol. 357, pp. 353–357, 2007, doi: 10.1051/0004-6361.

List of References

- [12] J. H. Waite *et al.*, "Liquid water on Enceladus from observations of ammonia and ^{40}Ar in the plume," *Nature*, vol. 460, no. 7254, pp. 487–490, 2009, doi: 10.1038/nature08153.
- [13] J. A. Hiscox, "Outer solar system, Europa, Titan and the possibility of life," 2000. doi: 10.1046/j.1468-4004.2000.41523.x.
- [14] Committee on the Planetary Science Decadal Survey, "Vision and Voyages for Planetary Science in the Decade 2013-2022," The National Academies Press, Washington D.C., 2011.
- [15] G. Mitri *et al.*, "Exploration of Enceladus and Titan: investigating ocean worlds' evolution and habitability in the Saturn system," *Exp. Astron.*, vol. ESA Voyage, 2021, doi: 10.1007/s10686-021-09772-2.
- [16] G. Choblet *et al.*, "Enceladus as a potential oasis for life: Science goals and investigations for future explorations," *Exp. Astron.*, vol. ESA Voyage, 2021, doi: 10.1007/s10686-021-09808-7.
- [17] A. H. Sulaiman *et al.*, "Enceladus and Titan: emerging worlds of the Solar System," *Exp. Astron.*, vol. ESA Voyage, 2021, doi: 10.1007/s10686-021-09810-z.
- [18] L. J. Tacconi *et al.*, "ESA: Voyage 2050 Plan Final Recommendations," 2021.
- [19] K. P. Hand *et al.*, "Europa Lander Mission - Europa Lander Study 2016 Report," Jet Propulsion Laboratory, NASA, 2017.
- [20] B. Buffington, S. Campagnola, and A. Petropoulos, "Europa Multiple-Flyby Trajectory Design," 2012.
- [21] J. Rask, W. Vercootere, B. J. Navarro, and A. Krause, "The Radiation Challenge," in *An Interdisciplinary Guide on Radiation and Human Space Flight*, vol. Radiation, National Aeronautics and Space Administration, 2008. [Online]. Available: http://www.nasa.gov/audience/foreducators/topnav/materials/listbytype/Space_Faring_Radiation.html
- [22] J. Krajewski, K. Hand, R. Gibbs, J. Doodley, G. Tan-Wang, and P. Danesh, "Europa Lander Science Payload - Draft Proposal Information Package," Jet Propulsion Laboratory, NASA, 2018.
- [23] O. Prieto-Ballesteros, E. Vorobyova, V. Parro, J. A. Rodriguez Manfredi, and F. Gó Mez, "Strategies for detection of putative life on Europa," *Adv. Sp. Res.*, vol. 48, pp. 678–688, 2011, doi: 10.1016/j.asr.2010.11.010.

- [24] Y. Ashkenazy, "The surface temperature of Europa," 2016.
- [25] F. Nimmo, P. C. Thomas, R. T. Pappalardo, and W. B. Moore, "The global shape of Europa: Constraints on lateral shell thickness variations," *Icarus*, vol. 191, no. 1, pp. 183–192, 2007, doi: 10.1016/j.icarus.2007.04.021.
- [26] K. P. Hand *et al.*, "Science Goals and Mission Architecture of the Europa Lander Mission Concept," *Planet. Sci. J.*, vol. 3, no. 22, 2022, doi: 10.3847/psj/ac4493.
- [27] K. P. Hand, R. W. Carlson, and C. F. Chyba, "Energy, chemical disequilibrium, and geological constraints on Europa," *Astrobiology*, vol. 7, no. 6, pp. 1006–1022, 2007, doi: 10.1089/ast.2007.0156.
- [28] S. D. Vance, K. P. Hand, and R. T. Pappalardo, "Geophysical controls of chemical disequilibria in Europa," *Geophys. Res. Lett.*, vol. 43, no. 10, pp. 4871–4879, 2016, doi: 10.1002/2016GL068547.
- [29] W. Zimmerman, R. Bonitz, and J. Feldman, "Cryobot: an ice penetrating robotic vehicle for Mars and Europa," 2001.
- [30] J. Biele, S. Ulamec, M. Hilchenbach, and N. I. Kömle, "In situ analysis of Europa ices by short-range melting probes," *Adv. Sp. Res.*, vol. 48, no. 4, pp. 755–763, 2011, doi: 10.1016/j.asr.2010.02.029.
- [31] P. Weiss, K. L. Yung, N. Kömle, S. M. Ko, E. Kaufmann, and G. Kargl, "Thermal drill sampling system onboard high-velocity impactors for exploring the subsurface of Europa," *Adv. Sp. Res.*, vol. 48, no. 4, pp. 743–754, 2011, doi: 10.1016/j.asr.2010.01.015.
- [32] NASA, *SP-349/396 PIONEER ODYSSEY*. 1974. [Online]. Available: <https://history.nasa.gov/SP-349/ch6.htm>
- [33] S. W. Squyres, R. T. Reynolds, P. M. Cassen, and S. J. Peale, "Liquid water and active resurfacing on Europa," *Nature*, vol. 301, no. 5897, pp. 225–226, 1983, doi: 10.1038/301225a0.
- [34] A. Liptak, "Europa changed how we saw the Solar System," *The Verge*, Sep. 25, 2016. [Online]. Available: <https://www.theverge.com/2016/9/25/13038486/europa-solar-system-moon-discovery-water-nasa>
- [35] C. B. Pilcher, S. T. Ridgway, and T. B. Mccord, "Galilean Satellites : Identification of Water Frost," *Science (80-.)*, vol. 178, no. 4065, pp. 1087–1089, 1972.

List of References

- [36] National Aeronautics and Space Administration, "Galileo End of Mission Press Kit," 2003.
- [37] Jet Propulsion Laboratory, "Photojournal," 2014.
<https://photojournal.jpl.nasa.gov/jpeg/PIA19048.jpg>
- [38] T. A. Nordheim, K. P. Hand, and C. Paranicas, "Preservation of potential biosignatures in the shallow subsurface of Europa," *Nat. Astron.*, no. 2, pp. 673–679, 2018.
- [39] D. C. Niebur, "First Community Announcement Regarding Europa Lander Instrument Investigation Program Element Appendix," *SOMA Europa Lander Investigation Acquisition Homepage*, 2017.
<https://soma.larc.nasa.gov/europalander/announcements.html#ca05242017> (accessed Nov. 29, 2018).
- [40] A. M. Rymer *et al.*, "Pioneering Outer Planet Ocean Exploration at Europa and Beyond," 2017. Accessed: Nov. 19, 2018. [Online]. Available:
<https://astrobiology.nasa.gov/research/life->
- [41] P. Vernazza *et al.*, "Sample return of primitive matter from the outer Solar System," *Exp. Astron.*, 2021, doi: 10.1007/s10686-021-09811-y.
- [42] V. Stamenković *et al.*, "The Quest for Life Leads Underground: Exploring Modern-Day Subsurface Habitability & Extant Life on Mars," *ESA Voyag. 2050*, 2021.
- [43] J. Parnell *et al.*, "Searching for Life on Mars: Selection of Molecular Targets for ESA's Aurora ExoMars Mission," *Astrobiology*, vol. 7, no. 4, pp. 578–604, 2007, doi: 10.1089/ast.2006.0110.
- [44] National Research Council, *An Astrobiology Strategy for the Exploration of Mars*. Washington DC: National Academies Press, 2007. doi: 10.17226/11937.
- [45] J. H. Hooijschuur, M. F. C. Verkaaik, G. R. Davies, and F. Ariese, "Raman spectroscopy for future planetary exploration: Photodegradation, self-absorption and quantification of carotenoids in microorganisms and mineral matrices," *J. Raman Spectrosc.*, vol. 46, no. 10, pp. 856–862, 2015, doi: 10.1002/jrs.4647.
- [46] S. E. J. Villar and H. G. M. Edwards, "Raman spectroscopy in astrobiology," *Anal. Bioanal. Chem.*, vol. 384, no. 1, pp. 100–113, 2006, doi: 10.1007/s00216-005-0029-2.
- [47] I. Weber, U. Böttger, S. G. Pavlov, E. K. Jessberger, and H. W. Hübers, "Mineralogical and Raman spectroscopy studies of natural olivines exposed to different planetary

- environments," *Planet. Space Sci.*, vol. 104, pp. 163–172, 2014, doi: 10.1016/j.pss.2014.08.016.
- [48] K. A. Farley *et al.*, "Mars 2020 Mission Overview," *Space Sci. Rev.*, vol. 216, p. 142, 2020, doi: 10.1007/s11214-020-00762-y.
- [49] L. W. Beegle *et al.*, "SHERLOC: scanning habitable environments with Raman & luminescence for organics & chemicals, an investigation for 2020," 2014.
- [50] S. Maurice *et al.*, *The SuperCam Instrument Suite on the Mars 2020 Rover: Science Objectives and Mast-Unit Description*, vol. 217, no. 3. The Author(s), 2021. doi: 10.1007/s11214-021-00807-w.
- [51] F. Rull *et al.*, "The Raman Laser Spectrometer for the ExoMars Rover Mission to Mars," *Astrobiology*, vol. 17, no. 6 and 7, pp. 627–654, 2017, doi: 10.1089/ast.2016.1567.
- [52] G. B. B. M. Sutherland, "Experiments on the raman effect at very low temperatures," *Proc. R. Soc. London A Math. Phys. Eng. Sci.*, vol. 141, no. 845, pp. 535–549, 1933, doi: 10.1098/rspa.1933.0137.
- [53] H. G. M. Edwards, I. B. Hutchinson, R. Ingley, and J. Jehlička, "Biomarkers and their Raman spectroscopic signatures: a spectral challenge for analytical astrobiology," *Philos. Trans. R. Soc. A*, vol. 372, no. 2030, 2014, doi: 10.1098/rsta.2014.0193.
- [54] J. Toporski and A. Steele, "The relevance of bacterial biomarkers in astrobiological research," in *Proceedings of the Second European Workshop on Exo/Astrobiology*, 2002, no. 518, pp. 239–242.
- [55] A. F. Davila and C. P. McKay, "Chance and Necessity in Biochemistry: Implications for the Search for Extraterrestrial Biomarkers in Earth-like Environments," *Astrobiology*, vol. 14, no. 6, pp. 534–540, 2014, doi: 10.1089/ast.2014.1150.
- [56] S. Pizzarello, Yo. Huang, and M. Fuller, "The carbon isotopic distribution of Murchison amino acids," *Geochim. Cosmochim. Acta*, vol. 68, no. 23, pp. 4963–4969, 2004, doi: 10.1016/j.gca.2004.05.024.
- [57] J. Aerts, W. Röling, A. Elsaesser, and P. Ehrenfreund, "Biota and Biomolecules in Extreme Environments on Earth: Implications for Life Detection on Mars," *Life*, vol. 4, no. 4, pp. 535–565, 2014, doi: 10.3390/life4040535.
- [58] I. B. Hutchinson *et al.*, "Raman spectroscopy on Mars: identification of geological and bio-

List of References

- geological signatures in Martian analogues using miniaturized Raman spectrometers,” *Philos. Trans. R. Soc. A*, vol. 372, no. 2030, 2014, doi: 10.1098/rsta.2014.0204.
- [59] M. Zolotov, E. L. Shock, and M. Y. Zolotov, “A model for low-temperature biogeochemistry of sulfur, carbon, and iron on Europa,” *J. Geophys. Res.*, vol. 109, p. 6003, 2004, doi: 10.1029/2003JE002194.
- [60] R. T. Pappalardo *et al.*, “Geological evidence for solid-state convection in Europa’s ice shell,” *Nature*, vol. 391, no. 6665, pp. 365–368, 1998, doi: 10.1038/34862.
- [61] L. E. Hays *et al.*, “Biosignature Preservation and Detection in Mars Analog Environments,” *Astrobiology*, vol. 17, no. 4, pp. 363–400, 2017, doi: 10.1089/ast.2016.1627.
- [62] C. P. McKay *et al.*, “The icebreaker life mission to mars: A search for biomolecular evidence for life,” *Astrobiology*, vol. 13, no. 4, pp. 334–353, 2013, doi: 10.1089/ast.2012.0878.
- [63] L. Becker, D. P. Glavin, and J. L. Bada, “Polycyclic aromatic hydrocarbons (PAHs) in Antarctic Martian meteorites, carbonaceous chondrites, and polar ice,” *Geochim. Cosmochim. Acta*, vol. 61, no. 2, pp. 475–481, 1997, doi: 10.1016/S0016-7037(96)00400-0.
- [64] J. L. Vago *et al.*, “Habitability on Early Mars and the Search for Biosignatures with the ExoMars Rover,” *Astrobiology*, vol. 17, no. 6–7, pp. 471–510, 2017, doi: 10.1089/ast.2016.1533.
- [65] R. D. Kidd, A. Noell, G. Kazarians, A. D. Aubrey, N. Scianmarello, and Y.-C. Tai, “Ion Chromatography-on-a-Chip for Water Quality Analysis,” 2015. Accessed: May 12, 2019. [Online]. Available: https://trs.jpl.nasa.gov/bitstream/handle/2014/45830/15-2353_A1b.pdf?sequence=1&isAllowed=y
- [66] V. Craige Trenerry and S. J. Rochfort, “Natural Products Research and Metabolomics,” *Compr. Nat. Prod. II*, vol. 9, pp. 595–628, Jan. 2010, doi: 10.1016/b978-008045382-8.00211-2.
- [67] T. M. Annesley, “Ion Suppression in Mass Spectrometry,” *Clin. Chem.*, vol. 49, no. 7, pp. 1041 LP – 1044, Jul. 2003, doi: 10.1373/49.7.1041.
- [68] M. Moreno-Paz *et al.*, “Detecting Nonvolatile Life- and Nonlife-Derived Organics in a Carbonaceous Chondrite Analogue with a New Multiplex Immunoassay and Its Relevance for Planetary Exploration,” *Astrobiology*, vol. 18, no. 8, pp. 1041–1056, 2018, doi: 10.1089/ast.2017.1747.

- [69] N. Thomas, P. Becerra, and I. B. Smith, "Mars and the ESA Science Programme - the case for Mars polar science," *Exp. Astron.*, 2021, doi: 10.1007/s10686-021-09760-6.
- [70] R. Bhartia *et al.*, "The WATSON Project: Biosignature Mapping in Subsurface Ice," 2018. Accessed: Dec. 15, 2018. [Online]. Available: <http://adsabs.harvard.edu/abs/2018cosp...42E.321B>
- [71] F. Nimmo and M. Manga, "Geodynamics of Europa's Icy Shell," in *Europa*, K. K. Robert T. Pappalardo, William B. McKinnon, Ed. 2004, pp. 381–404.
- [72] T. A. Scambos *et al.*, "Ultralow Surface Temperatures in East Antarctica From Satellite Thermal Infrared Mapping: The Coldest Places on Earth," *Geophys. Res. Lett.*, vol. 45, no. 12, pp. 6124–6133, 2018, doi: 10.1029/2018GL078133.
- [73] G. Tobie, G. Choblet, and C. Sotin, "Tidally heated convection : Constraints on Europa ' s ice shell thickness," *Journal Geophys. Res.*, vol. 108, pp. 1–15, 2003, doi: 10.1029/2003JE002099.
- [74] P. Fretwell *et al.*, "Bedmap2: Improved ice bed, surface and thickness datasets for Antarctica," *Cryosphere*, vol. 7, no. 1, pp. 375–393, 2013, doi: 10.5194/tc-7-375-2013.
- [75] A. Clarke, G. J. Morris, F. Fonseca, B. J. Murray, E. Acton, and H. C. Price, "A Low Temperature Limit for Life on Earth," *PLoS One*, vol. 8, no. 6, p. e66207, 2013, doi: 10.1371/journal.pone.0066207.
- [76] L. Paganini *et al.*, "A measurement of water vapour amid a largely quiescent environment on Europa," *Nat. Astron.*, 2019, doi: 10.1038/s41550-019-0933-6.
- [77] Huayan Yang, Shouning Yang, Jilie Kong, Aichun Dong, and Shaoning Yu, "Obtaining information about protein secondary structures in aqueous solution using Fourier transform IR spectroscopy," *Nat. Protoc.*, vol. 10, no. 3, pp. 382–396, 2015, doi: 10.1038/nprot.2015.024.
- [78] A. Nathues and U. Mall, "Near Infrared Spectrometry with SIR on SMART-1," 2014.
- [79] O. I. Korablev *et al.*, "ExoMars Rover Mission Infrared Spectrometer for ExoMars: A Mast-Mounted Instrument for the Rover," *Astrobiology*, vol. 17, no. 6–7, pp. 542–564, 2017, doi: 10.1089/ast.2016.1543.
- [80] O. Korablev *et al.*, "Development of a mast or robotic arm-mounted infrared AOTF spectrometer for surface Moon and Mars probes," *Infrared Remote Sens. Instrum. XXIII*,

List of References

- vol. 9608, no. September, p. 960807, 2015, doi: 10.1117/12.2190450.
- [81] C. S. Rix, M. R. Sims, and D. C. Cullen, "Immunological Detection of Small Organic Molecules in the Presence of Perchlorates: Relevance to the Life Marker Chip and Life Detection on Mars," *Astrobiology*, vol. 11, no. 9, pp. 839–846, 2011, doi: 10.1089/ast.2011.0662.
- [82] R. W. Carlson *et al.*, *Europa*. The University of Arizona Press, 2009. Accessed: Apr. 11, 2019. [Online]. Available: https://books.google.co.uk/books?hl=cs&lr=&id=bxNDDwAAQBAJ&oi=fnd&pg=PA283&dq=europas+surface+composition+&ots=qk-bJGeo6m&sig=HlwZPV3JHeoRFi3Jj_ZGdurbnr4#v=onepage&q=europas+surface+composition&f=false
- [83] J. S. Kargel *et al.*, "Europa's Crust and Ocean: Origin, Composition, and the Prospects for Life," *Icarus*, vol. 148, pp. 226–265, 2000, doi: 10.1006/icar.2000.6471.
- [84] R. Horn, "Raman Spectroscopy," in *Lecture Series: Modern Methods in Heterogeneous Catalysis*, Fritz-Haber-Institute of the MPG, 2009, pp. 1–42. [Online]. Available: http://www.fhi-berlin.mpg.de/acnew/departement/pages/teaching/pages/teaching__wintersemester__2008_2009/raimund_horn__raman_spectroscopy__090123.pdf
- [85] M. Skulinova *et al.*, "Time-resolved stand-off UV-Raman spectroscopy for planetary exploration," *Planet. Space Sci.*, vol. 92, pp. 88–100, 2014, doi: 10.1016/j.pss.2014.01.010.
- [86] R. Lewandowska, "Raman Microscopy: Analysis of Nanomaterials," in *Encyclopedia of Materials: Science and Technology*, 2nd ed., 2010, pp. 1–6. doi: 10.1016/b978-008043152-9.02247-8.
- [87] A. J. Thompson and G. Yang, "Tethered and Implantable Optical Sensors," in *Implantable Sensors and Systems*, G. Yang, Ed. Springer, 2018, pp. 439–505. doi: 10.1007/978-3-319-69748-2.
- [88] S. M. Angel, N. R. Gomer, S. K. Sharma, C. McKay, and N. Ames, "Remote Raman spectroscopy for planetary exploration: A review," *Appl. Spectrosc.*, vol. 66, no. 2, pp. 137–150, 2012, doi: 10.1366/11-06535.
- [89] L. Beegle *et al.*, "SHERLOC: Scanning habitable environments with Raman & luminescence for organics & chemicals," 2015. doi: 10.1109/AERO.2015.7119105.

- [90] J. Blacksberg, E. Alerstam, Y. Maruyama, C. J. Cochrane, and G. R. Rossman, "Miniaturized time-resolved Raman spectrometer for planetary science based on a fast single photon avalanche diode detector array," *Appl. Opt.*, vol. 55, no. 4, p. 739, 2016, doi: 10.1364/AO.55.000739.
- [91] P. J. Gasda, T. E. Acosta-Maeda, P. G. Lucey, A. K. Misra, S. K. Sharma, and G. J. Taylor, "Next generation laser-based standoff spectroscopy techniques for Mars exploration," *Appl. Spectrosc.*, vol. 69, no. 2, pp. 173–192, 2015, doi: 10.1366/14-07483.
- [92] S. M. Clegg *et al.*, "Planetary geochemical investigations using raman and laser-induced breakdown spectroscopy," *Appl. Spectrosc.*, vol. 68, no. 9, pp. 925–936, 2015, doi: 10.1366/13-07386.
- [93] E. Eshelman *et al.*, "WATSON: Detecting organic material in subsurface ice using deep-UV fluorescence and Raman spectroscopy," 2017. Accessed: Dec. 15, 2018. [Online]. Available: <http://adsabs.harvard.edu/abs/2017AGUFM.B41H2070E>
- [94] J. J. Freeman, A. Wang, K. E. Kuebler, B. L. Jolliff, and L. A. Haskin, "Characterization of natural feldspars by raman spectroscopy for future planetary exploration," *Can. Mineral.*, vol. 46, no. 6, pp. 1477–1500, 2008, doi: 10.3749/canmin.46.6.1477.
- [95] M. A. Miller, D. S. Dunn, T. A. Abrajano, N. Sridhar, R. Pabalan, and K. T. Price, "Development of a Surface-Enhanced Raman Technique for Biomarker Studies on Mars," *Appl. Spectrosc.*, vol. 61, no. 1, pp. 25–31, 2007, doi: 10.1366/000370207779701424.
- [96] C. C. van den Akker, M. Schleegeer, M. Bonn, and G. H. Koenderink, "Structural Basis for the Polymorphism of β -Lactoglobulin Amyloid-Like Fibrils," in *Bio-nanoimaging*, Vladimir N. Uversky and Yuri L. Lyubchenko, Ed. Academic Press, 2014, pp. 333–343. doi: 10.1016/B978-0-12-394431-3.00031-6.
- [97] S. Rolfe, "Characteristic Raman Bands of Amino Acids and Halophiles as Biomarkers in Planetary Exploration," University of Leicester, 2016.
- [98] W. J. Abbey *et al.*, "Deep UV Raman spectroscopy for planetary exploration: The search for in situ organics," *Icarus*, vol. 290, pp. 201–214, 2017, doi: 10.1016/j.icarus.2017.01.039.
- [99] A. Kereszturi, O. Prieto-Ballesteros, M. Blanc, J. Gomez-Elvira, and F. Westall, "Evaluation of instruments for coming Europa missions to conduct research on astrobiology," 2018.
- [100] J. Blacksberg, E. Alerstam, Y. Maruyama, C. Cochrane, and G. R. Rossman, "High-speed Pulsed Raman for Mapping of Minerals and Organics on a Microscopic Scale," 2016.

List of References

- Accessed: Nov. 19, 2018. [Online]. Available:
http://minerals.gps.caltech.edu/manuscripts/2016/IWIPM_4017/IWIPM_4017.pdf
- [101] J. Blacksberg, E. Alerstam, Y. Maruyama, C. Cochrane, and G. R. Rossman, "Advances in Time-Resolved Raman Spectroscopy for in situ Characterization of Minerals and Organics," 2015. Accessed: Nov. 18, 2018. [Online]. Available:
<https://www.hou.usra.edu/meetings/lpsc2015/pdf/1304.pdf>
- [102] D. L. Dickensheets, D. D. Wynn-Williams, H. G. M. Edwards, C. Schoen, C. Crowder, and E. M. Newton, "A novel miniature confocal microscope/Raman spectrometer system for biomolecular analysis on future Mars missions after Antarctic trials," *J. Raman Spectrosc.*, vol. 31, no. 7, pp. 633–635, 2000, doi: 10.1002/1097-4555(200007)31:7<633::AID-JRS620>3.0.CO;2-R.
- [103] B. Lafuente, R. Navarro, B. Lafuente, R. Navarro, A. Sansano, and F. Rull, "Surface-enhanced Raman spectroscopy (SERS) for identifying traces of adenine in different mineral and rock samples," *European Planetary Science Congress 2012*, vol. 7, 2012. Accessed: Jan. 14, 2019. [Online]. Available: <https://www.researchgate.net/publication/258732532>
- [104] E. Eshelman, M. G. Daly, G. Slater, P. Dietrich, and J. F. Gravel, "An ultraviolet Raman wavelength for the in-situ analysis of organic compounds relevant to astrobiology," *Planet. Space Sci.*, vol. 93–94, pp. 65–70, 2014, doi: 10.1016/j.pss.2014.01.021.
- [105] T. T. Cai, D. Zhang, and D. Ben-Amotz, "Enhanced chemical classification of Raman images using multiresolution wavelet transformation," *Appl. Spectrosc.*, vol. 55, no. 9, pp. 1124–1130, 2001, doi: 10.1366/0003702011953289.
- [106] T. Hasegawa, J. Nishijo, and J. Umemura, "Separation of Raman spectra from fluorescence emission background by principal component analysis," *Chem. Phys. Lett.*, vol. 317, no. 6, pp. 642–646, 2000, doi: 10.1016/S0009-2614(99)01427-X.
- [107] C. A. Lieber and A. Mahadevan-Jansen, "Automated Method for Subtraction of Fluorescence from Biological Raman Spectra," *Appl. Spectrosc.*, vol. 57, no. 11, pp. 1363–1367, 2003, doi: 10.1366/000370203322554518.
- [108] J. B. Cooper, M. Abdelkader, and K. L. Wise, "Sequentially shifted excitation Raman spectroscopy: Novel algorithm and instrumentation for fluorescence-free Raman spectroscopy in spectral space," *Appl. Spectrosc.*, vol. 67, no. 8, pp. 973–984, 2013, doi: 10.1366/12-06852.

- [109] S. T. McCain, R. M. Willett, and D. J. Brady, "Multi-excitation Raman spectroscopy technique for fluorescence rejection," *Opt. Express*, vol. 16, no. 15, pp. 10975–10991, 2008, doi: 10.1364/oe.16.010975.
- [110] A. P. Shreve, N. J. Cherepy, and R. A. Mathies, "Effective Rejection of Fluorescence Interference in Raman Spectroscopy Using a Shifted Excitation Difference Technique," *Appl. Spectrosc.*, vol. 46, no. 4, pp. 707–711, 1992.
- [111] J. B. Cooper, S. Marshall, R. Jones, M. Abdelkader, and K. L. Wise, "Spatially compressed dual-wavelength excitation Raman spectrometer," *Appl. Opt.*, vol. 53, no. 15, pp. 3333–3340, 2014, doi: 10.1364/ao.53.003333.
- [112] B. J. Bozlee, A. K. Misra, S. K. Sharma, and M. Ingram, "Remote Raman and fluorescence studies of mineral samples," *Spectrochim. Acta - Part A Mol. Biomol. Spectrosc.*, vol. 61, no. 10, pp. 2342–2348, 2005, doi: 10.1016/j.saa.2005.02.033.
- [113] J. Blacksberg, G. R. Rossman, and A. Gleckler, "Time-resolved Raman spectroscopy for in situ planetary mineralogy," *Appl. Opt.*, vol. 49, no. 26, p. 4951, 2010, doi: 10.1364/ao.49.004951.
- [114] S. Asher and C. Johnson, "Raman Speciroscopy of a Coal Liquid Shows That Fluorescence Interference Is Minimized with Ultraviolet Excitation," *Science (80-.)*, vol. 225, no. 4659, pp. 311–313, 1984.
- [115] N. Tarcea *et al.*, "UV Raman spectroscopy-A technique for biological and mineralogical in situ planetary studies," *Spectrochim. Acta - Part A Mol. Biomol. Spectrosc.*, vol. 68, no. 4, pp. 1029–1035, 2007, doi: 10.1016/j.saa.2007.06.051.
- [116] D. Cebeci-Maltaş, P. Wang, M. A. Alam, R. Pinal, and D. Ben-Amotz, "Photobleaching profile of Raman peaks and fluorescence background," *Eur. Pharm. Rev.*, vol. 22, no. 6, pp. 18–21, 2017.
- [117] D. C. Shan Yang, Ozan Akkus, "1064-nm Raman: The Right Choice for Biological Samples?," *Spectroscopy*, vol. 32, no. 6, pp. 46–54, 2017, [Online]. Available: <http://www.spectroscopyonline.com/1064-nm-raman-right-choice-biological-samples>
- [118] L. W. Beegle *et al.*, "The SHERLOC Investigation on the Mars 2020 Rover," 2020.
- [119] Photon Systems, "DUV Raman," 2021. <https://photonsystems.com/technology/duv-raman/> (accessed Jul. 13, 2022).

List of References

- [120] J. M. Kohel, J. P. Kirby, and J. L. Lambert, "Development of a compact high-resolution spectrometer for multi-line UV Raman spectroscopy," 2010. doi: 10.1109/AERO.2010.5446978.
- [121] B. Li and A. B. Myers, "Absolute raman cross sections for cyclohexane, acetonitrile, and water in the far-ultraviolet region," *J. Phys. Chem.*, vol. 94, no. 10, pp. 4051–4054, 1990, doi: 10.1021/j100373a031.
- [122] S. A. Asher and C. R. Johnson, "UV Resonance Raman Excitation Profile through the 1B₂ State of Benzene," *J. Phys. Chem.*, vol. 89, pp. 1375–1379, 1985.
- [123] I. López-Peña, B. S. Leigh, D. E. Schlamadinger, and J. E. Kim, "Insights into Protein Structure and Dynamics by Ultraviolet and Visible Resonance Raman Spectroscopy," *Biochemistry*, vol. 54, no. 31, pp. 4770–4783, 2015, doi: 10.1007/s11065-015-9294-9.Functional.
- [124] G. R. Loppnow, L. Shoute, K. J. Schmidt, A. Savage, R. H. Hall, and J. T. Bulmer, "UV Raman spectroscopy of hydrocarbons," *Philos. Trans. R. Soc. A Math. Phys. Eng. Sci.*, vol. 362, no. 1824, pp. 2461–2476, 2004, doi: 10.1098/rsta.2004.1449.
- [125] J. L. Lambert, "Dual Wavelength Context Imaging Raman and Fluorescence Spectrometer," US Patent 10,746,600 B2, 2020
- [126] L. V. Harris, I. B. Hutchinson, R. Ingley, C. P. Marshall, A. Olcott Marshall, and H. G. M. Edwards, "Selection of portable spectrometers for planetary exploration: A comparison of 532 nm and 785 nm raman spectroscopy of reduced carbon in Archean cherts," *Astrobiology*, vol. 15, no. 6, pp. 420–429, 2015, doi: 10.1089/ast.2014.1220.
- [127] H. Yoshino, Y. Saito, Y. Kumamoto, A. Taguchi, P. Verma, and S. Kawata, "Temperature-dependent photodegradation in UV-resonance raman spectroscopy," *Anal. Sci.*, vol. 31, no. 5, pp. 451–454, 2015, doi: 10.2116/analsci.31.451.
- [128] Q. Wu, G. Balakrishnan, A. Pevsner, and T. G. Spiro, "Histidine photodegradation during UV resonance Raman spectroscopy," *J. Phys. Chem. A*, vol. 107, no. 40, pp. 8047–8051, 2003, doi: 10.1021/jp027190f.
- [129] E. Smith and G. Dent, "Chapter 4: Resonance Raman Scattering," in *Modern Raman Spectroscopy: A Practical Approach*, John Wiley & Sons Ltd., 2005, pp. 93–112. doi: 10.1002/0470011831.
- [130] E. V. Efremov, F. Ariese, and C. Gooijer, "Achievements in resonance Raman spectroscopy.

- Review of a technique with a distinct analytical chemistry potential," *Anal. Chim. Acta*, vol. 606, no. 2, pp. 119–134, 2008, doi: 10.1016/j.aca.2007.11.006.
- [131] M. Fleischmann, P. J. Hendra, and A. J. McQuillan, "Raman spectra of pyridine adsorbed at a silver electrode," *Chem. Phys. Lett.*, vol. 26, no. 2, pp. 163–166, 1974, doi: 10.1007/bf02578984.
- [132] B. Sharma, R. R. Frontiera, A. I. Henry, E. Ringe, and R. P. Van Duyne, "SERS: Materials, applications, and the future," *Mater. Today*, vol. 15, no. 1–2, pp. 16–25, 2012, doi: 10.1016/S1369-7021(12)70017-2.
- [133] E. C. Le Ru, E. Blackie, M. Meyer, and P. G. Etchegoint, "Surface enhanced raman scattering enhancement factors: A comprehensive study," *J. Phys. Chem. C*, vol. 111, no. 37, pp. 13794–13803, 2007, doi: 10.1021/jp0687908.
- [134] O. E. Eremina *et al.*, "Surface-enhanced Raman spectroscopy in modern chemical analysis: advances and prospects," *Russ. Chem. Rev.*, vol. 87, no. 8, pp. 741–770, 2018, doi: 10.1070/rcr4804.
- [135] S. Nie and S. R. Emory, "Probing single molecules and single nanoparticles by surface-enhanced Raman scattering," *Science (80-.)*, vol. 275, no. 5303, pp. 1102–1106, 1997, doi: 10.1126/science.275.5303.1102.
- [136] M. Muniz-Miranda, C. Gellini, P. R. Salvi, and M. Pagliai, "Surface-enhanced Raman microspectroscopy of DNA/RNA bases adsorbed on pyroxene rocks as a test of in situ search for life traces on Mars," *J. Raman Spectrosc.*, vol. 41, no. 1, pp. 12–15, 2010, doi: 10.1002/jrs.2398.
- [137] N. Sridhar, D. S. Dunn, K. T. Price, M. A. Miller, R. T. Pabalan, and T. A. Abrajano, "Development of a Surface Enhanced Raman Spectroscopy Technique for Identification of Biomarkers on Mars," 2005.
- [138] C. G. Atkins, K. Buckley, M. W. Blades, and R. F. B. Turner, "Raman Spectroscopy of Blood and Blood Components," *Appl. Spectrosc.*, vol. 71, no. 5, pp. 767–793, 2017, doi: 10.1177/0003702816686593.
- [139] A. Bonifacio *et al.*, "Surface-enhanced Raman spectroscopy of blood plasma and serum using Ag and Au nanoparticles: A systematic study," *Anal. Bioanal. Chem.*, vol. 406, no. 9–10, pp. 2355–2365, 2014, doi: 10.1007/s00216-014-7622-1.
- [140] L. Mikac *et al.*, "Preparation and characterization of SERS substrates: From colloids to solid

List of References

- substrates,” in *2015 38th International Convention on Information and Communication Technology, Electronics and Microelectronics, MIPRO 2015 - Proceedings*, 2015, no. May. doi: 10.1109/MIPRO.2015.7160228.
- [141] P. Mosier-Boss, “Review of SERS Substrates for Chemical Sensing,” *Nanomaterials*, vol. 7, no. 6, p. 142, 2017, doi: 10.3390/nano7060142.
- [142] I. Bruzas, W. Lum, Z. Gorunmez, and L. Sagle, “Advances in surface-enhanced Raman spectroscopy (SERS) substrates for lipid and protein characterization: Sensing and beyond,” *Analyst*, vol. 143, no. 17, pp. 3990–4008, 2018, doi: 10.1039/c8an00606g.
- [143] R. Pilot, R. Signorini, C. Durante, L. Orian, M. Bhamidipati, and L. Fabris, “A review on surface-enhanced Raman scattering,” *Biosensors*, vol. 9, no. 2, p. 57, 2019, doi: 10.3390/bios9020057.
- [144] S. K. Jha, Z. Ahmed, M. Agio, Y. Ekinci, and J. F. Löffler, “Deep-UV surface-enhanced resonance Raman scattering of adenine on aluminum nanoparticle arrays,” *J. Am. Chem. Soc.*, vol. 134, no. 4, pp. 1966–1969, 2012, doi: 10.1021/ja210446w.
- [145] A. Dubey, R. Mishra, C. W. Cheng, Y. P. Kuang, S. Gwo, and T. J. Yen, “Demonstration of a Superior Deep-UV Surface-Enhanced Resonance Raman Scattering (SERRS) Substrate and Single-Base Mutation Detection in Oligonucleotides,” *J. Am. Chem. Soc.*, vol. 143, no. 46, pp. 19282–19286, 2021, doi: 10.1021/jacs.1c09762.
- [146] A. Matikainen *et al.*, “Atmospheric oxidation and carbon contamination of silver and its effect on surface-enhanced Raman spectroscopy (SERS),” *Sci. Rep.*, vol. 6, p. 37192, 2016, doi: 10.1038/srep37192.
- [147] A. Gutés, R. Maboudian, and C. Carraro, “Gold-coated silver dendrites as SERS substrates with an improved lifetime,” *Langmuir*, vol. 28, no. 51, pp. 17846–17850, 2012, doi: 10.1021/la303421s.
- [148] L. E. Kreno, N. G. Greeneltch, O. K. Farha, J. T. Hupp, and R. P. Van Duyne, “SERS of molecules that do not adsorb on Ag surfaces: A metal-organic framework-based functionalization strategy,” *Analyst*, vol. 139, no. 16, pp. 4073–4080, 2014, doi: 10.1039/c4an00413b.
- [149] N. E. Marotta, K. R. Beavers, and L. A. Bottomley, “Limitations of surface enhanced raman scattering in sensing DNA hybridization demonstrated by label-free DNA oligos as molecular rulers of distance-dependent enhancement,” *Anal. Chem.*, vol. 85, no. 3, pp.

- 1440–1446, 2013, doi: 10.1021/ac302454j.
- [150] F. Tam, M. E. Piotti, E. Stone, and R. G. Freeman, “Molecule size-dependent SERS enhancement,” in *AIP Conference Proceedings*, 2010, vol. 1267, no. August, pp. 996–997. doi: 10.1063/1.3482934.
- [151] K. Nehra, S. K. Pandian, M. S. S. Bharati, and V. R. Soma, “Enhanced catalytic and SERS performance of shape/size controlled anisotropic gold nanostructures,” *New J. Chem.*, vol. 43, no. 9, pp. 3835–3847, 2019, doi: 10.1039/c8nj06206d.
- [152] Z.-Q. Tian, B. Ren, and D.-Y. Wu, “Surface-Enhanced Raman Scattering: From Noble to Transition Metals and from Rough Surfaces to Ordered Nanostructures,” *J. Phys. Chem. B*, vol. 106, no. 37, pp. 9463–9483, 2002, doi: 10.1177/074193258901000304.
- [153] X. Liu, Y. Shao, Y. Tang, and K. F. Yao, “Highly Uniform and Reproducible Surface Enhanced Raman Scattering on Air-stable Metallic Glassy Nanowire Array,” *Sci. Rep.*, vol. 4, p. 5835, 2014, doi: 10.1038/srep05835.
- [154] A. S. Luna, “Raman Spectroscopy, Soil Analysis Applications,” in *Encyclopedia of Spectroscopy and Spectrometry*, 3rd ed., G. E. T. and D. W. K. John C. Lindon, Ed. Academic Press, 2017, pp. 919–923. doi: 10.1016/B978-0-12-409547-2.12171-7.
- [155] S. A. Bowden, R. Wilson, J. M. Cooper, and J. Parnell, “The Use of Surface-Enhanced Raman Scattering for Detecting Molecular Evidence of Life in Rocks, Sediments, and Sedimentary Deposits,” *Astrobiology*, vol. 10, no. 6, pp. 629–641, 2010, doi: 10.1089/ast.2009.0435.
- [156] M. Namkung and J. T. Seo, “Surface-Enhanced Raman Spectroscopy for Astrobiology Exploration on Mars,” in *International Workshop on Instrumentation for Planetary Missions*, 2012, pp. 2–4.
- [157] S. Caporali, M. Pagliai, G. Pratesi, and V. Schettino, “Surface-enhanced Raman scattering investigation of nucleobases adsorbed on samples of Martian analogue material,” *Spectrosc. Lett.*, vol. 44, no. 7–8, pp. 580–584, 2011, doi: 10.1080/00387010.2011.611572.
- [158] A. Matikainen, T. Nuutinen, P. Vahimaa, and S. Honkanen, “A solution to the fabrication and tarnishing problems of surface-enhanced Raman spectroscopy (SERS) fiber probes,” *Sci. Rep.*, vol. 5, p. 8320, 2015, doi: 10.1038/srep08320.
- [159] S. J. Blanksby and G. B. Ellison, “Bond dissociation energies of organic molecules,” *Acc. Chem. Res.*, vol. 36, no. 4, pp. 255–263, 2003, doi: 10.1021/ar020230d.

List of References

- [160] Y. Kumamoto, A. Taguchi, N. I. Smith, and S. Kawata, "Deep UV resonant Raman spectroscopy for photodamage characterization in cells," *Biomed. Opt. Express*, vol. 2, no. 4, p. 927, 2011, doi: 10.1364/boe.2.000927.
- [161] G. Tahu and M. Schulte, "Mars 2020 Project Update." 2014.
- [162] X. Sun, B. Hu, C. Zou, Q. Bai, and L. Wang, "The research of relay lens coupling in image intensified camera," in *International Symposium on Photoelectronic Detection and Imaging 2013: Low-Light-Level Technology and Applications*, 2013, vol. 8912, no. August 2013, p. 89121E. doi: 10.1117/12.2034709.
- [163] R. C. Wiens *et al.*, "The SuperCam Instrument Suite on the NASA Mars 2020 Rover: Body Unit and Combined System Tests," *Space Sci. Rev.*, vol. 217, no. 4, 2021, doi: 10.1007/s11214-020-00777-5.
- [164] Y. Cho *et al.*, "In situ science on Phobos with the Raman spectrometer for MMX (RAX): preliminary design and feasibility of Raman measurements," *Earth, Planets Sp.*, vol. 73, p. 232, 2021, doi: 10.1186/s40623-021-01496-z.
- [165] R. Hibbert, M. C. Price, T. M. Kinnear, M. J. Cole, and M. J. Burchell, "The effects of temperature on the Raman spectrum of high purity quartz crystals," 2015.
- [166] M. Le Tacon *et al.*, "Two energy scales and two distinct quasiparticle dynamics in the superconducting state of underdoped cuprates," *Nat. Phys.*, vol. 2, no. 8, pp. 537–543, 2006, doi: 10.1038/nphys362.
- [167] L. J. Sandilands, Y. Tian, K. W. Plumb, Y. J. Kim, and K. S. Burch, "Scattering Continuum and Possible Fractionalized Excitations in α -RuCl₃," *Phys. Rev. Lett.*, vol. 114, no. 14, pp. 1–7, 2015, doi: 10.1103/PhysRevLett.114.147201.
- [168] C. Girardot, J. Kreisel, S. Pignard, N. Caillault, and F. Weiss, "Raman scattering investigation across the magnetic and metal-insulator transition in rare earth nickelate R NiO₃ (R=Sm, Nd) thin films," *Phys. Rev. B - Condens. Matter Mater. Phys.*, vol. 78, p. 104101, 2008, doi: 10.1103/PhysRevB.78.104101.
- [169] J. Haines, J. Rouquette, V. Bornand, M. Pintard, P. Papet, and F. A. Gorelli, "Raman scattering studies at high pressure and low temperature: Technique and application to the piezoelectric material PbZr_{0.52}Ti_{0.48}O₃," *J. Raman Spectrosc.*, vol. 34, no. 7–8, pp. 519–523, 2003, doi: 10.1002/jrs.1009.
- [170] P. Sobron and A. Wang, "Low-temperature Raman Spectroscopy of Materials Relevant for

- Planetary Exploration,” 2011.
- [171] R. W. Berg, “Raman detection of hydrohalite formation: Avoiding accidents on icy roads by deicing where salt will not work,” *Appl. Spectrosc. Rev.*, vol. 53, no. 6, pp. 503–515, 2018, doi: 10.1080/05704928.2017.1396540.
- [172] J. F. D. Liljeblad, I. Furó, and E. C. Tyrode, “The premolten layer of ice next to a hydrophilic solid surface: correlating adhesion with molecular properties,” *Phys. Chem. Chem. Phys.*, vol. 19, no. 1, pp. 305–317, 2017, doi: 10.1039/c6cp05303c.
- [173] S. M. Pershin, V. N. Lednev, R. N. Yulmetov, V. K. Klinkov, and A. F. Bunkin, “Transparent material thickness measurements by Raman scattering,” *Appl. Opt.*, vol. 54, no. 19, p. 5943, 2015, doi: 10.1364/ao.54.005943.
- [174] J. Jehlicka, H. G. M. Edwards, and A. Culka, “Using portable Raman spectrometers for the identification of organic compounds at low temperatures and high altitudes: Exobiological applications,” *Philos. Trans. R. Soc. A Math. Phys. Eng. Sci.*, vol. 368, no. 1922, pp. 3109–3125, 2010, doi: 10.1098/rsta.2010.0075.
- [175] F. Kenig *et al.*, “Branched aliphatic alkanes with quaternary substituted carbon atoms in modern and ancient geologic samples,” *Proc. Natl. Acad. Sci.*, vol. 100, no. 22, pp. 12554–12558, 2003, doi: 10.1073/pnas.1735581100.
- [176] C. Hallman, “Reconstructing Deep-Time Biology with Molecular Fossils,” in *Quantifying the Evolution of Early Life: Numerical Approaches to the Evaluation of Fossils and Ancient Ecosystems*, M. Laflamme, J. D. Schiffbauer, and S. Q. Dornbos, Eds. New York, 2011, p. 386.
- [177] Helga Stan-Lotter and S. Fendrihan, *Adaption of Microbial Life to Environmental Extremes: Novel Research Results and Application*. Springer-Verlag Wien, 2012. doi: 10.1007/978-3-211-99691-1.
- [178] A. Yamagishi, T. Kakegawa, and T. Usui, Eds., *Astrobiology: From the Origins of Life to the Search for Extraterrestrial Intelligence*. Springer Singapore, 2019. doi: 10.1007/978-981-13-3639-3.
- [179] H. G. M. Edwards, B. Herschy, K. Page, T. Munshi, and I. J. Scowen, “Raman spectra of biomarkers of relevance to analytical astrobiological exploration: Hopanoids, sterols and steranes,” *Spectrochim. Acta - Part A Mol. Biomol. Spectrosc.*, vol. 78, no. 1, pp. 191–195, 2011, doi: 10.1016/j.saa.2010.09.020.

List of References

- [180] J. Jehlička *et al.*, “Potential and limits of Raman spectroscopy for carotenoid detection in microorganisms: Implications for astrobiology,” *Philos. Trans. R. Soc. A Math. Phys. Eng. Sci.*, vol. 372, no. 2030, 2014, doi: 10.1098/rsta.2014.0199.
- [181] T. Soule, V. Stout, W. D. Swingley, J. C. Meeks, and F. Garcia-Pichel, “Molecular Genetics and Genomic Analysis of Scytonemin Biosynthesis in *Nostoc punctiforme* ATCC 29133,” *J. Phycol.*, vol. 189, no. 12, pp. 4465–4472, 2007, doi: 10.1128/JB.01816-06.
- [182] J. Pathak, H. Ahmed, P. R. Singh, S. P. Singh, and D. Häder, “Mechanisms of Photoprotection in Cyanobacteria,” in *Cyanobacteria*, Elsevier Inc., 2019, pp. 145–171. doi: 10.1016/B978-0-12-814667-5.00007-6.
- [183] B. Tian and Y. Hua, “Carotenoid biosynthesis in extremophilic *Deinococcus* – *Thermus* bacteria,” *Trends Microbiol.*, vol. 18, no. 11, pp. 512–520, 2010, doi: 10.1016/j.tim.2010.07.007.
- [184] R. B. Hoover, E. V. Pikuta, N. C. Wickramasinghe, M. K. Wallis, and R. B. Sheldon, “Astrobiology of comets,” in *Proceedings of SPIE*, 2004, vol. 5555, pp. 93–106. doi: 10.1117/12.566496.
- [185] G. Multhoff, “Heat shock protein 70 (Hsp70): Membrane location, export and immunological relevance,” *Methods*, vol. 43, no. 3, pp. 229–237, 2007, doi: 10.1016/j.ymeth.2007.06.006.
- [186] M. L. Deegenars and K. Watson, “Heat shock response in psychrophilic and psychrotrophic yeast from Antarctica,” *Extremophiles*, vol. 2, no. 1, pp. 41–49, 1998, doi: 10.1007/s007920050041.
- [187] I. Callebaut, M. G. Catelli, D. Portetelle, A. Burny, E. E. Baulieu, and J. P. Mornon, “Structural similarities between chaperone molecules of the HSP60 and HSP70 families deduced from hydrophobic cluster analysis,” *FEBS Lett.*, vol. 342, no. 3, pp. 242–248, 1994, doi: 10.1016/0014-5793(94)80510-5.
- [188] M. Höhl, C. Zeilinger, B. Roth, M. Meinhardt-Wollweber, and U. Morgner, “Multivariate discrimination of heat shock proteins using a fiber optic Raman setup for in situ analysis of human perilymph,” *Rev. Sci. Instrum.*, vol. 90, no. 4, 2019, doi: 10.1063/1.5030301.
- [189] J. S. Creamer, M. F. Mora, and P. A. Willis, “Enhanced Resolution of Chiral Amino Acids with Capillary Electrophoresis for Biosignature Detection in Extraterrestrial Samples,” *Anal. Chem.*, vol. 89, no. 2, pp. 1329–1337, 2017, doi: 10.1021/acs.analchem.6b04338.

- [190] P. De Maayer, D. Anderson, C. Cary, and D. A. Cowan, "Some like it cold : understanding the survival strategies of psychrophiles," *EMBO Rep.*, vol. 15, no. 5, pp. 508–517, 2014.
- [191] A. Casanueva, M. Tuffin, C. Cary, and D. A. Cowan, "Molecular adaptations to psychrophily : the impact of 'omic' technologies," *Trends Microbiol.*, vol. 18, no. 8, pp. 374–381, 2010, doi: 10.1016/j.tim.2010.05.002.
- [192] J. E. Elsila, D. P. Glavin, M. P. Callahan, J. P. Dworkin, and H. Brückner, "Distribution and Stable Isotopic Composition of Amino Acids from Fungal Peptaibiotics : Assessing the Potential for Meteoritic Contamination," *Astrobiology*, vol. 11, no. 2, pp. 123–133, 2011, doi: 10.1089/ast.2010.0505.
- [193] M. Gargaud *et al.*, Eds., *Encyclopedia of Astrobiology*. Springer-Verlag Berlin Heidelberg, 2011.
- [194] J. L. Harwood and N. J. Russell, *Lipids in Plants and Microbes*. London: George Allen and Unwin, 1984.
- [195] D. V. Dibrova, M. Y. Galperin, and A. Y. Mulkidjanian, "Phylogenomic reconstruction of archaeal fatty acid metabolism," *Env. Microbiol.*, vol. 16, no. 4, pp. 907–918, 2014.
- [196] J. Lai, B. K. D. Pearce, R. E. Pudritz, and D. Lee, "Meteoritic Abundances of Fatty Acids and Potential Reaction Pathways in Planetesimals," *Icarus*, vol. 319, pp. 685–700, 2019.
- [197] G. Ourisson, P. Albrecht, and M. Rohmer, "Predictive microbial biochemistry — from molecular fossils to procaryotic membranes," *Trends Biochem. Sci.*, vol. 7, no. 7, pp. 236–239, 1982.
- [198] B. Cavalazzi and F. Westall, Eds., *Biosignatures for Astrobiology*. Springer, 2019. doi: 10.1007/978-3-319-96175-0.
- [199] W. M. O'Leary, "The fatty acids of bacteria," *Bacteriol. Rev.*, vol. 26, no. 4, pp. 421–447, 1962.
- [200] J. R. Vestal and D. C. White, "Lipid Analysis in Microbial Ecology: Quantitative approaches to the study of microbial communities," *Bioscience*, vol. 39, no. 8, pp. 535–541, 1989.
- [201] M. Nishikiori, M. H. Kimitaka Kawamura, and Y. Fujii, "Mono- and di-carboxylic acids and mid-chain oxocarboxylic acids in the Antarctic aerosols," *Chikyukagaku (Geochemistry)*, vol. 30, no. 1, pp. 27–34, 1996, doi: 10.14934/chikyukagaku.30.27.
- [202] M. A. Y. Chan, R. H. Himes, and J. M. Akagi, "Fatty Acid Composition of Thermophilic ,

List of References

- Mesophilic , and Psychrophilic Clostridia," *J. Bacteriol.*, vol. 106, no. 3, pp. 876–881, 1971.
- [203] K. R. Rotert, A. P. Toste, and J. G. Steiert, "Membrane fatty acid analysis of Antarctic bacteria," *FEMS Microbiol. Lett.*, vol. 114, no. 3, pp. 253–257, 1993.
- [204] T. Hamamoto, N. Takata, T. Kudo, and K. Horikoshi, "Characteristic presence of polyunsaturated fatty acids in marine psychrophilic vibrios," *FEMS Microbiol. Lett.*, vol. 129, no. 1, pp. 51–56, 1995.
- [205] S. D. Amico, T. Collins, J. Marx, G. Feller, and C. Gerday, "Psychrophilic microorganisms: challenges for life," *EMBO*, vol. 7, no. 4, pp. 385–389, 2006, doi: 10.1038/sj.embor.7400662.
- [206] C. D. Powers, D. C. S. Maya R. Sternberg, Shahzad S. Momin, Elizabeth C. Pendergrast, and R. L. Schleicher, "Stability of 30 Fatty Acids in Serum Stored at – 20 ° C for up to 5 Years TO THE EDITOR ;," *J. Appl. Lab. Med.*, vol. 2, no. 1, pp. 125–127, 2017, doi: 10.1373/jalm.2017.023234.
- [207] L. Czech *et al.*, "Role of the Extremolytes Ectoine and Hydroxyectoine as Stress Protectants and Nutrients: Genetics, Phylogenomics, Biochemistry, and Structural Analysis," *Genes (Basel)*, vol. 9, no. 4, p. 177, 2018, doi: 10.3390/genes9040177.
- [208] M. A. Schröter, S. Meyer, M. B. Hahn, T. Solomun, H. Sturm, and H. J. Kunte, "Ectoine protects DNA from damage by ionizing radiation," *Sci. Rep.*, vol. 7, p. 15272, 2017, doi: 10.1038/s41598-017-15512-4.
- [209] K. Lippert and E. A. Galinski, "Enzyme stabilization by ectoine-type compatible solutes: protection against heating, freezing and drying," *Appl. Microbiol. Biotechnol.*, vol. 37, no. 1, pp. 61–65, 1992.
- [210] R. B. Hoover, "Microfossils, Biominerals and Chemical Biomarkers in Meteorites," in *Perspectives in Astrobiology*, IOS Press, 2005, pp. 43–65.
- [211] J. D. Brooks, K. Gould, and J. W. Smith, "Isoprenoid Hydrocarbons in Coal and Petroleum," *Nature*, vol. 222, pp. 257–259, 1969.
- [212] M. D. Larrañaga, R. J. Lewis, and R. A. Lewis, *Hawley's Condensed Chemical Dictionary*, 16th ed. John Wiley & Sons, 2016.
- [213] A. Hammerbacher, B. Raguschke, D. González-Cabanelas, J. Gershenzon, and L. P. Wright, "Quantifying the Metabolites of the Methylerythritol 4-Phosphate (MEP) Pathway in

- Plants and Bacteria by Liquid Chromatography – Triple Quadrupole Mass Spectrometry,” in *Methods in Enzymology*, vol. 576, 2016, pp. 225–249. doi: 10.1016/bs.mie.2016.02.025.
- [214] M. Blumer, M. M. Mullin, and D. W. Thomas, “Pristane in the marine environment,” *Helgol. Mar. Res.*, vol. 10, no. 1–4, pp. 187–201, 1964.
- [215] H. Schaller, “Sterol and Steroid Biosynthesis and Metabolism in Plants and Microorganisms,” in *Comprehensive Natural Products II Volume 1*, Elsevier, 2010, pp. 755–787.
- [216] K. E. Peters, C. C. Walters, and J. M. Moldowan, *Biomarker Guide Volume 1 -Biomarkers and Isotopes in the Environment and Human History*. Cambridge University Press, 2005.
- [217] K. E. Peters, C. C. Walters, and J. M. Moldowan, *Biomarker Guide Volume 2 - Biomarkers and Isotopes in Petroleum Systems and Earth History*. Cambridge University Press, 2005.
- [218] N. E. Archer, Y. Charles, J. A. Elliott, and S. Jickells, “Changes in the lipid composition of latent fingerprint residue with time after deposition on a surface \$,” *Forensic Sci. Int.*, vol. 154, no. 2–3, pp. 224–239, 2005, doi: 10.1016/j.forsciint.2004.09.120.
- [219] J. J. Brocks, G. A. Logan, R. Buick, and R. E. Summons, “Archean Molecular Fossils and the Early Rise of Eukaryotes,” *Science (80-.)*, vol. 285, no. 5430, pp. 1033–1037, 1999.
- [220] S. M. El-sabagh, A. Y. El-naggar, M. M. El Nady, M. A. Ebiad, A. M. Rashad, and E. S. Abdullah, “Distribution of triterpanes and steranes biomarkers as indication of organic matters input and depositional environments of crude oils of oilfields in Gulf of Suez , Egypt,” *Egypt. J. Pet.*, vol. 27, no. 4, pp. 969–977, 2018, doi: 10.1016/j.ejpe.2018.02.005.
- [221] C. Galasso, C. Corinaldesi, and C. Sansone, “Carotenoids from Marine Organisms : Biological Functions and Industrial Applications,” *Antioxidants*, vol. 6, no. 4, p. 96, 2017, doi: 10.3390/antiox6040096.
- [222] H. A. Frank, V. Chynwat, R. Z. B. Desamero, and R. Farhoosh, “On the photophysics and photochemical properties of carotenoids and their role as light-harvesting pigments in photosynthesis,” *Pure Appl. Chem.*, vol. 69, no. 10, pp. 2117–2124, 1997.
- [223] A. Koutsaviti, E. Ioannou, and V. Roussis, “Bioactive Seaweed Substances,” in *Bioactive Seaweeds for Food Applications*, Elsevier Inc., 2018, pp. 25–52. doi: 10.1016/B978-0-12-813312-5.00002-9.
- [224] M. V Jagannadham *et al.*, “Carotenoids of an Antarctic psychrotolerant bacterium ,

List of References

- Sphingobacterium antarcticus , and a mesophilic bacterium , Sphingobacterium multivorum,” *Arch. Microbiol.*, vol. 173, pp. 418–424, 2000.
- [225] J. Kumar, D. Singh, M. B. Tyagi, and A. Kumar, “Cyanobacteria : Applications in Biotechnology,” in *Cyanobacteria*, Elsevier Inc., 2019, pp. 327–346. doi: 10.1016/B978-0-12-814667-5.00016-7.
- [226] F. A. Rainey and A. Oren, “Extremophile Microorganisms and the Methods to Handle Them,” in *Methods in Microbiology*, vol. 35, 2006, pp. 1–25. doi: 10.1016/S0580-9517(05)35001-X.
- [227] R. A. Baraúna, D. Y. Freitas, J. C. Pinheiro, A. R. C. Folador, and A. Silva, “A Proteomic Perspective on the Bacterial Adaptation to Cold: Integrating OMICs Data of the Psychrotrophic Bacterium Exiguobacterium antarcticum B7,” *Proteomes*, vol. 5, no. 1, p. 9, 2017, doi: 10.3390/proteomes5010009.
- [228] M. Dsouza, M. W. Taylor, S. J. Turner, and J. Aislabie, “Genomic and phenotypic insights into the ecology of Arthrobacter from Antarctic soils,” *BMC Genomics*, vol. 16, no. 36, 2015, doi: 10.1186/s12864-015-1220-2.
- [229] J. J. Brocks, G. D. Love, R. E. Summons, A. H. Knoll, G. A. Logan, and S. A. Bowden, “Biomarker evidence for green and purple sulphur bacteria in a stratified Palaeoproterozoic sea,” *Nature*, vol. 437, no. October 6, pp. 866–870, 2005, doi: 10.1038/nature04068.
- [230] C. P. Marshall and A. O. Marshall, “The potential of Raman spectroscopy for the analysis of diagenetically transformed carotenoids,” *Philos. Trans. R. Soc. A*, vol. 368, no. 1922, pp. 3137–3144, 2010, doi: 10.1098/rsta.2010.0016.
- [231] J. S. S. Damst and M. P. Koopmans, “The fate of carotenoids in sediments : An overview,” *Pure Appl. Chem.*, vol. 69, no. 10, pp. 2067–2074, 1997.
- [232] H. Huang, “The effect of biodegradation on gammacerane in crude oils,” *Biodegradation*, vol. 28, pp. 313–326, 2017, doi: 10.1007/s10532-017-9798-5.
- [233] Y. Hoshino *et al.*, “Cryogenian evolution of stigmasteroid biosynthesis,” *Sci. Adv.*, vol. 3, no. 9, p. e1700887, 2017.
- [234] R. E. Johnson, A. V. Oza, F. Leblanc, C. Schmidt, T. A. Nordheim, and T. A. Cassidy, “The Origin and Fate of O₂ in Europa’s Ice: An Atmospheric Perspective,” *Space Sci. Rev.*, vol. 215, no. 20, 2019.

- [235] J. Volkman, "Sterols in microorganisms," *Appl. Microbiol. Biotechnol.*, vol. 60, pp. 495–506, 2003, doi: 10.1007/s00253-002-1172-8.
- [236] J. Tritz, D. Herrmann, P. Bissere, J. Connan, and M. Rohmer, "Abiotic and biological hopanoid transformation : towards the formation of molecular fossils of the hopane series," *Org. Geochem.*, vol. 30, pp. 499–514, 1999.
- [237] H. Croft and J. M. Chen, "Leaf Pigment Content," in *Comprehensive Remote Sensing*, Elsevier, 2018, pp. 117–142. doi: 10.1016/B978-0-12-409548-9.10547-0.
- [238] R. E. Blankenship, "Future Perspectives in Plant Biology: Early Evolution of Photosynthesis," *Plant Physiol.*, vol. 154, no. 2, pp. 434–438, 2010, doi: 10.1104/pp.110.161687.
- [239] N. T. Eriksen, "Production of phycocyanin — a pigment with applications in biology, biotechnology, foods and medicine," *Appl. Microbiol. Biotechnol.*, vol. 80, no. 10, pp. 1–14, 2008, doi: 10.1007/s00253-008-1542-y.
- [240] W. F. M. Roling, J. W. Aerts, P. C. H. Lucas, I. L. ten Kate, P. Ehrenfreund, and S. O. L. Direito, "The Significance of Microbe-Mineral-Biomarker Interactions in the Detection of Life on Mars and Beyond," *Astrobiology*, vol. 15, no. 6, pp. 492–507, 2015, doi: 10.1089/ast.2014.1276.
- [241] Z. Martins *et al.*, "Extraterrestrial nucleobases in the Murchison meteorite," *Earth Planet. Sci. Lett.*, vol. 270, no. 1–2, pp. 130–136, 2008, doi: 10.1016/j.epsl.2008.03.026.
- [242] M. P. Callahan *et al.*, "Carbonaceous meteorites contain a wide range of extraterrestrial nucleobases," *Proc. Natl. Acad. Sci.*, vol. 108, no. 34, pp. 13995–13998, 2011, doi: 10.1073/pnas.1106493108.
- [243] T. Lindahl, "Facts and Artifacts of Ancient DNA," *Cell*, vol. 90, no. 1, pp. 1–3, 1997.
- [244] E. Willerslev *et al.*, "Ancient Biomolecules from Deep Ice Cores Reveal a Forested," *Science (80-.)*, vol. 317, no. 5834, pp. 111–114, 2007.
- [245] G. Panieri *et al.*, "Ribosomal RNA gene fragments from fossilized cyanobacteria identified in primary gypsum from the late Miocene , Italy," *Geobiology*, vol. 8, pp. 101–111, 2010, doi: 10.1111/j.1472-4669.2009.00230.x.
- [246] R. H. Vreeland and William D. Rosenzweig Dennis W. Powers, "Isolation of a 250 million-year-old halotolerant bacterium from a primary salt crystal," *Nature*, vol. 407, pp. 897–900, 2000.

List of References

- [247] G. Feller, "Cryosphere and Psychrophiles : Insights into a Cold Origin of Life ?," *Life*, vol. 7, no. 25, 2017, doi: 10.3390/life7020025.
- [248] S. S. Johnson *et al.*, "Ancient bacteria show evidence of DNA repair," *Proc. Natl. Acad. Sci.*, vol. 104, no. 36, pp. 14401–14405, 2007.
- [249] L. R. Gurley, J. G. Valdez, W. D. Spall, B. F. Smith, and D. D. Gillette, "Proteins in the Fossil Bone of the Dinosaur, *Seismosaurus*," *J. Protein Chem.*, vol. 10, no. 1, pp. 75–90, 1991.
- [250] B. Demarchi *et al.*, "Protein sequences bound to mineral surfaces persist into deep time," *Elife*, vol. 5, p. e17092, 2016, doi: 10.7554/eLife.17092.
- [251] J. Sarfati, "Design in Living Organisms : Motors," *J. Creat.*, vol. 12, no. 1, pp. 3–5, 1998.
- [252] T. Elliott, "Stress Proteins," in *Encyclopedia of Immunology*, Second., Elsevier, 1998, pp. 2228–2232.
- [253] O. Kozlova, A. Cherkasov, A. Przhiboro, and E. Shagimardanova, "Complexity of Expression Control of HSP70 Genes in Extremophilic Midges," *Bionanoscience*, vol. 6, pp. 388–391, 2016, doi: 10.1007/s12668-016-0256-3.
- [254] E. Kuhn, "Toward Understanding Life Under Subzero Conditions: The Significance of Exploring Psychrophilic 'Cold-Shock' Proteins," *Astrobiology*, vol. 12, no. 11, pp. 1078–1086, 2014, doi: 10.1089/ast.2012.0858.
- [255] J. Goldstein, N. S. Pollitt, and M. Inouyet, "Major cold shock protein of *Escherichia coli*," *Proc. Natl. Acad. Sci.*, vol. 87, no. 1, pp. 283–287, 1990.
- [256] B. Xia, H. Ke, and M. Inouye, "Acquirement of cold sensitivity by quadruple deletion of the *cspA* family and its suppression by PNPase S1 domain in *Escherichia coli*," *Mol. Microbiol.*, vol. 40, no. 1, pp. 179–188, 2001.
- [257] W. Bae, S. Phadtare, K. Severinov, and M. Inouye, "Characterization of *Escherichia coli* *cspE*, whose product negatively regulates transcription of *cspA*, the gene for the major cold shock protein," *Mol. Microbiol.*, vol. 31, no. 5, pp. 1429–1441, 1999.
- [258] M. Juen *et al.*, "RNA binding and chaperone activity of the *E. coli* cold-shock protein CspA," *Nucleic Acids Res.*, vol. 45, no. 7, pp. 4255–4268, 2017, doi: 10.1093/nar/gkx044.
- [259] S. Phadtare and K. Severinov, "RNA remodeling and gene regulation by cold shock proteins," *RNA Biol.*, vol. 7, no. 6, pp. 788–795, 2010.

- [260] R. Keto-timonen, N. Hietala, E. Palonen, A. Hakakorpi, and M. Lindström, "Cold Shock Proteins : A Minireview with Special Emphasis on Csp-family of Enteropathogenic Yersinia," *Front. Microbiol.*, vol. 7, p. 1151, 2016, doi: 10.3389/fmicb.2016.01151.
- [261] R. V. Stick and S. J. Williams, "Modifications of Glycans and Glycoconjugates," in *Carbohydrates: The Essential Molecules of Life*, Second., Elsevier Science, 2009, pp. 343–367. doi: 10.1016/B978-0-240-52118-3.00010-7.
- [262] J. G. Swoboda, J. Campbell, T. C. Meredith, and S. Walker, "Wall Teichoic Acid Function, Biosynthesis, and Inhibition," *ChemBiochem*, vol. 11, no. 1, pp. 35–45, 2010, doi: 10.1002/cbic.200900557.Wall.
- [263] I. B. N. Y *et al.*, "Cell wall teichoic acids : structural diversity, species specificity in the genus Nocardiosis and chemotaxonomic perspective," *FEMS Microbiol. Rev.*, vol. 25, no. 3, pp. 269–283, 2001.
- [264] S. Phadtare and M. Inouye, "Cold-Shock Proteins," in *Psychrophiles: From Biodiversity to Biotechnology*, R. Margesin, F. Schinner, J.-C. Marx, and C. Gerday, Eds. Springer, 2008, pp. 191–209.
- [265] S. Ohtake and Y. J. Wang, "Trehalose : Current Use and Future Applications," *J. Pharm. Sci.*, vol. 100, no. 6, pp. 2020–2053, 2020, doi: 10.1002/jps.
- [266] L. Sorci, O. Kurnasov, D. A. Rodionov, and A. L. Osterman, "Genomics and Enzymology of NAD Biosynthesis," in *Comprehensive Natural Products II Volume 7*, Elsevier, 2010, pp. 213–257.
- [267] T. E. Crowley and J. Kyte, "Introduction to Enzymes Catalyzing Oxidation- Reductions with the Coenzyme NAD (P)," in *Experiments in the Purification and Characterization of Enzymes*, Academic Press, 2012, pp. 1–9. doi: 10.1016/B978-0-12-409544-1.02002-6.
- [268] M. C. Storrie-Lombardi, J.-P. Muller, M. R. Fisk, A. D. Griffiths, A. J. Coates, and R. B. Hoover, "Epifluorescence Surveys of Extreme Environments Using PanCam Imaging Systems : Antarctica and the Mars Regolith," in *Proceedings of SPIE - The International Society for Optical Engineering*, 2008, p. 7097. doi: 10.1117/12.800924.
- [269] S. A. Sañudo-Wilhelmy, D. R. Monteverde, L. Gómez-Consarnau, and C. Suffridge, "Life's utilization of B vitamins on early Earth," *Geobiology*, vol. 15, pp. 3–18, 2017, doi: 10.1111/gbi.12202.
- [270] T. Baj and E. Sieniawska, "Vitamins," in *Pharmacognosy*, Elsevier Inc., 2017, pp. 281–292.

List of References

doi: 10.1016/B978-0-12-802104-0.00013-5.

- [271] C. Brenner, "Evolution of NAD Biosynthetic Enzymes," *Structure*, vol. 13, no. 9, pp. 1239–1240, 2005, doi: 10.1016/j.str.2005.08.004.
- [272] F. Gazzaniga, R. Stebbins, S. Z. Chang, M. A. Mcpeek, and C. Brenner, "Microbial NAD Metabolism : Lessons from Comparative Genomics," *Microbiol. Mol. Biol. Rev.*, vol. 73, no. 3, pp. 529–541, 2009, doi: 10.1128/MMBR.00042-08.
- [273] A. Gutiérrez-Preciado, A. G. Torres, E. Merino, H. R. Bonomi, F. A. Goldbaum, and V. A. García-Angulo, "Extensive Identification of Bacterial Riboflavin Transporters and Their Distribution across Bacterial Species," *PLoS One*, vol. 10, no. 5, pp. 1–17, 2015, doi: 10.1371/journal.pone.0126124.
- [274] M. Schrenk, S. Seager, and W. Bains, "An Astrophysical View of Earth-Based Metabolic Biosignature Gases," *Astrobiology*, vol. 12, no. 1, pp. 61–82, 2019, doi: 10.1089/ast.2010.0489.
- [275] H. Rauer *et al.*, "Potential Biosignatures in Super-Earth Atmospheres II. Photochemical Responses," *Astrobiology*, vol. 13, no. 5, pp. 415–438, 2013, doi: 10.1089/ast.2012.0926.
- [276] D. C. Catling *et al.*, "Exoplanet Biosignatures: A Framework for Their Assessment," *Astrobiology*, vol. 18, no. 6, pp. 709–738, 2018, doi: 10.1089/ast.2017.1737.
- [277] F. Selsis, A. Leger, and M. Ollivier, "Spectroscopic Signatures of Life on Exoplanets – The Darwin and TPF Missions," in *Lectures in Astrobiology*, M. Gargaud, B. Barbier, H. Martin, and J. Reisse, Eds. Springer, 2005, pp. 385–423.
- [278] S. I. Walker *et al.*, "Exoplanet Biosignatures: Future Directions," *Astrobiology*, vol. 18, no. 6, pp. 779–824, 2018, doi: 10.1089/ast.2017.1738.
- [279] C. S. Cockell, "Exoplanets: The Search for Other Habitable Worlds," in *Astrobiology: Understanding Life in the Universe*, 2015, pp. 363–382.
- [280] Ö. Eyice *et al.*, "Bacterial SBP56 identified as a Cu-dependent methanethiol oxidase widely distributed in the biosphere," *Multidiscip. J. Microb. Ecol.*, vol. 12, pp. 145–160, 2018, doi: 10.1038/ismej.2017.148.
- [281] P. D. Nightingale and P. S. Liss, "Gases in Seawater," in *Treatise on Geochemistry Volume 6*, 2003, pp. 1–33.
- [282] R. Avci, M. H. Schweitzer, Z. Suo, and M. Deliorman, "Porphyrin as an Ideal Biomarker in

- the Search for Extraterrestrial Life,” *Astrobiology*, vol. 7, no. 4, pp. 605–615, 2007, doi: 10.1089/ast.2006.0120.
- [283] G. . Hodgson, B. Hitchon, K. Taguchi, B. L. Baker, and E. Peake, “Geochemistry of porphyrins, chlorins and polycyclic aromatics in soils, sediments and sedimentary rocks,” *Geochim. Cosmochim. Acta*, vol. 32, no. 7, pp. 737–772, 1968.
- [284] R. S. Czernuszewicz, “Geochemistry of porphyrins: biological, industrial and environmental aspects,” *J. Porphyr. Phthalocyanines*, vol. 4, no. 4, pp. 426–431, 2000.
- [285] J. S. Lindsey, M. Ptaszek, and M. Taniguchi, “Simple Formation of an Abiotic Porphyrinogen in Aqueous Solution,” *Orig. Life Evol. Biosph.*, vol. 39, no. 6, pp. 495–515, 2009, doi: 10.1007/s11084-009-9168-3.
- [286] S. Fox and H. Strasdeit, “Abiotic synthesis of porphyrins and other oligopyrroles on the early Earth and Earth-like planets,” in *European Planetary Science Congress*, 2013, vol. 8.
- [287] C. S. Cockell, “Energy for Life,” in *Astrobiology: Understanding Life in the Universe*, Wiley-Blackwell, 2015, pp. 77–103.
- [288] L. A. Cole, “Adenosine Triphosphate Energetics,” in *Biology of Life*, Academic Press, 2016, pp. 65–77. doi: 10.1016/B978-0-12-809685-7.00010-1.
- [289] C. M. Furdui and K. S. Anderson, “Detection of Novel Enzyme Intermediates,” in *Comprehensive Natural Products II Volume 8*, Elsevier, 2010, pp. 663–688.
- [290] D. M. Karl and K. M. Björkman, “Dynamics of Dissolved Organic Phosphorus,” in *Biogeochemistry of Marine Dissolved Organic Matter*, Second., Elsevier Inc., 2015, pp. 233–334. doi: 10.1016/B978-0-12-405940-5.00005-4.
- [291] T. R. Sandrin, D. C. Herman, and R. M. Maier, “Physiological Methods,” in *Environmental Microbiology*, Second., Elsevier, 2009, pp. 191–223.
- [292] J. Engel, *A Critical Survey of Biomineralization Control, Mechanisms, Functions and Material Properties*. Springer, 2016.
- [293] E. J. Baran and P. V. Monje, “Oxalate Biominerals,” in *Biomineralization: From Nature to Application*, vol. 4, A. Sigel, H. Sigel, and R. K. O. Sigel, Eds. John Wiley & Sons Ltd., 2008, pp. 219–254.
- [294] T. Echigo and M. Kimata, “Crystal chemistry and genesis of organic minerals: a review of oxalate and polycyclic aromatic hydrocarbon minerals,” *Can. Mineral.*, vol. 48, no. 6, pp.

List of References

- 1329–1357, 2010.
- [295] E. Ruiz-agudo, A. Burgos-Cara, H. Cölfen, C. Rodriguez-Navarro, C. Ruiz-Agudo, and A. Ibañez-Velasco, “A non-classical view on calcium oxalate precipitation and the role of citrate,” *Nat. Commun.*, vol. 8, p. 768, 2017, doi: 10.1038/s41467-017-00756-5.
- [296] M. Hajir, R. Graf, and W. Tremel, “Stable amorphous calcium oxalate: synthesis and potential intermediate in biomineralization,” *Chem. Commun.*, no. 50, pp. 6534–6536, 2014, doi: 10.1039/c4cc02146k.
- [297] U. Böttger *et al.*, “Raman spectroscopic analysis of the calcium oxalate producing extremotolerant lichen *Circinaria gyrosa*,” *Int. J. Astrobiol.*, vol. 13, no. 1, pp. 19–27, 2014, doi: 10.1017/S1473550413000293.
- [298] J. Jehlicka, H. G. M. Edwards, and S. E. J. Villar, “Raman spectroscopic study of mellite — A naturally occurring aluminium benzenehexacarboxylate from lignite — Claystone series of the tertiary age,” *Spectrochim. Acta Part A Mol. Biomol. Spectrosc.*, vol. 65, no. 1, pp. 229–234, 2006, doi: 10.1016/j.saa.2005.10.036.
- [299] J. W. Anthony, *Handbook of Mineralogy: Volume II*. Mineral Data Publishing, 1995.
- [300] W. R. Martin and F. L. Sayles, “The Recycling of Biogenic Material at the Seafloor,” in *Treatise on Geochemistry Volume 7*, 2003, pp. 37–65.
- [301] H. Ehrlich, K. D. Demadis, O. S. Pokrovsky, and P. G. Koutsoukos, “Modern Views on Desilicification : Biosilica and Abiotic Silica Dissolution in Natural and Artificial Environments,” *Chem. Rev.*, vol. 110, no. 8, pp. 4656–4689, 2010.
- [302] K. Sato, “Origin of Organism-Dependent Biogenic Silica Quartz Formation,” *J. Phys. Chem.*, vol. 115, no. 49, pp. 14874–14877, 2011, doi: 10.1021/jp208720c.
- [303] J. Schieber, “Sedimentary Pyrite : A Window into the Microbial Past,” *Geology*, vol. 30, no. 6, 2002.
- [304] J. A. Saunders, M. A. Pritchett, and R. B. Cook, “Geochemistry of biogenic pyrite and ferromanganese coatings from a small watershed : A bacterial connection?,” *Geomicrobiol. J.*, vol. 14, no. 3, pp. 203–217, 2009, doi: 10.1080/01490459709378044.
- [305] S. R. Chang and J. L. Kirschvink, “Magnetofossils, the Magnetization of Sediments, and the Evolution of Magnetite Biomineralization,” *Annu. Rev. Earth Planet. Sci.*, vol. 17, pp. 169–195, 1989.

- [306] J. L. Kirschvink and J. L. Gould, "Biogenic magnetite as a basis for magnetic field detection in animals," *Biosystems*, vol. 13, no. 3, pp. 181–201, 1981.
- [307] Y. Li and J. E. Schoonmaker, "Chemical Composition and Mineralogy of Marine Sediments," in *Treatise on Geochemistry Volume 7*, 2003, pp. 1–35.
- [308] M. A. Chan *et al.*, "Exploring, Mapping, and Data Management Integration of Habitable Environments in Astrobiology," *Front. Microbiology*, vol. 10, no. 147, 2019, doi: 10.3389/fmicb.2019.00147.
- [309] A. Blanco, M. D. Elia, D. Licchelli, V. Orofino, and S. Fonti, "Studies of Biominerals Relevant to the Search for Life on Mars," *Orig. Life Evol. Biosph.*, vol. 36, no. 5–6, pp. 621–622, 2006, doi: 10.1007/s11084-006-9045-2.
- [310] A. Vitkova, S. J. I. Walker, and H. Sykulska-Lawrence, "The Impact of Extreme Low Temperatures on Raman Spectra of Amino Acids Relevant," *Astrobiology*, vol. 22, no. 11, 2022, doi: 10.1089/ast.2021.0136.
- [311] A. Vitkova, S. J. I. Walker, and H. Sykulska-Lawrence, "Cryogenically induced signal enhancement of Raman spectra of porphyrin molecules," *Anal. Methods*, vol. 14, no. 34, pp. 3307–3314, 2022, doi: 10.1039/d2ay00538g.
- [312] M. T. Rosado, M. L. T. S. Duarte, and R. Fausto, "Vibrational spectra of acid and alkaline glycine salts," *Vib. Spectrosc.*, vol. 16, pp. 35–54, 1998, doi: 10.1016/S0924-2031(97)00050-7.
- [313] H. Stenback, "On the Raman spectra of solid natural alpha-glycine and solid 15N-substituted alpha-glycine," *J. Raman Spectrosc.*, vol. 5, pp. 49–55, 1976.
- [314] S. M. Rolfe, M. R. Patel, I. Gilmour, K. Olsson-Francis, and T. J. Ringrose, "Defining Multiple Characteristic Raman Bands of α -Amino Acids as Biomarkers for Planetary Missions Using a Statistical Method," *Orig. Life Evol. Biosph.*, vol. 46, pp. 323–346, 2016, doi: 10.1007/s11084-015-9477-7.
- [315] M. T. S. Rosado, M. L. R. S. Duarte, and R. Fausto, "Vibrational spectra (FT-IR, Raman and MI-IR) of α - and β -alanine," *J. Mol. Struct.*, vol. 410–411, pp. 343–348, 1997, doi: 10.1016/S0022-2860(96)09695-0.
- [316] K. J. Jalkanen *et al.*, "A comparison of aqueous solvent models used in the calculation of the Raman and ROA spectra of L-alanine," *Chem. Phys.*, vol. 265, pp. 125–151, 2001, doi: 10.1016/S0301-0104(01)00267-1.

List of References

- [317] E. Tajkhorshid, K. J. Jalkanen, and S. Suhai, "Structure and Vibrational Spectra of the Zwitterion L-Alanine in the Presence of Explicit Water Molecules: A Density Functional Analysis," *J. Phys. Chem. B*, vol. 102, no. 30, pp. 5899–5913, 1998, doi: 10.1016/S0022-2860(02)00680-4.
- [318] P. T. C. Freire, F. M. Barboza, J. A. Lima, F. E. A. Melo, and J. M. Filho, "Raman Spectroscopy of Amino Acid Crystals," in *Raman Spectroscopy and Applications*, INTECH, 2017. doi: 10.5772/65480.
- [319] K. Fukushima, T. Onishi, T. Shimanouchi, and S. ichiro Mizushima, "Assignment of vibration bands of DL-alanine," *Spectrochim. Acta*, vol. 15, pp. 236–241, 1959, doi: 10.1016/s0371-1951(59)80312-x.
- [320] S. Kumar, A. Kumar Rai, S. B. Rai, D. K. Rai, A. N. Singh, and V. B. Singh, "Infrared, Raman and electronic spectra of alanine: A comparison with ab initio calculation," *J. Mol. Struct.*, vol. 791, pp. 23–29, 2006, doi: 10.1016/j.molstruc.2006.01.004.
- [321] S. Martusevičius, G. Niaura, Z. Talaikyte, and V. Razumas, "Adsorption of L-histidine on copper surface as evidenced by surface-enhanced Raman scattering spectroscopy," *Vib. Spectrosc.*, vol. 10, no. 2, pp. 271–280, 1996, doi: 10.1016/0924-2031(95)00025-9.
- [322] S. Kumar, A. K. Rai, S. B. Rai, and D. K. Rai, "Infrared and Raman spectra of Histidine: an ab initio DFT calculations of Histidine molecule and its different protonated forms," *Indian J. Phys.*, vol. 84, no. 5, pp. 563–573, 2010.
- [323] J. G. Mesu, T. Visser, F. Soulimani, and B. M. Weckhuysen, "Infrared and Raman spectroscopic study of pH-induced structural changes of L-histidine in aqueous environment," *Vib. Spectrosc.*, vol. 39, no. 1, pp. 114–125, 2005, doi: 10.1016/j.vibspec.2005.01.003.
- [324] T. Deckert-Gaudig and V. Deckert, "Tip-enhanced Raman scattering studies of histidine on novel silver substrates," *J. Raman Spectrosc.*, vol. 40, no. 10, pp. 1446–1451, 2009, doi: 10.1002/jrs.2359.
- [325] G. Zhu, X. Zhu, Q. Fan, and X. Wan, "Raman spectra of amino acids and their aqueous solutions," *Spectrochim. Acta - Part A Mol. Biomol. Spectrosc.*, vol. 78, no. 3, pp. 1187–1195, 2011, doi: 10.1016/j.saa.2010.12.079.
- [326] C. H. Chuang and Y. T. Chen, "Raman scattering of L-tryptophan enhanced by surface plasmon of silver nanoparticles: Vibrational assignment and structural determination," *J.*

- Raman Spectrosc.*, vol. 40, no. 2, pp. 150–156, 2009, doi: 10.1002/jrs.2097.
- [327] K. A. Wilk *et al.*, “Cryolava Dome growth resulting from active eruptions on Jupiter’s moon Europa,” *Icarus*, vol. 387, no. November, p. 115185, 2022, doi: 10.1016/j.icarus.2022.115185.
- [328] F. Hawthorne, M. H. Hazen, R. M. Hazen, R. Lavinsky, E. Sokolova, and W. Larson, “RRUFF.” <http://rruff.info/>
- [329] B. Lafuente, R. T. Downs, H. Yang, and N. Stone, “The power of databases: The RRUFF project,” in *Highlights in Mineralogical Crystallography*, T. Armbruster and R. M. Danisi, Eds. Berlin: De Gruyter, 2015, pp. 1–30. doi: 10.1515/9783110417104-003.
- [330] K. Dziejcz-Kocurek, H. J. Byrne, A. Świdorski, and J. Stanek, “Spectroscopic study of the dimerization process of iron protoporphyrin IX,” *Acta Phys. Pol. A*, vol. 115, no. 2, pp. 552–555, 2009, doi: 10.12693/APhysPolA.115.552.
- [331] A. Vitkova, H. Sykulska-Lawrence, and S. Walker, “The Impact of Extreme Low Temperatures Analogous to Europa’s Surface and Sub-surface on Raman Spectra of Amino Acids,” in *AGU Fall Meeting 2021: 13-17 December*, 2021, pp. P22A-06.
- [332] R. Bhartia *et al.*, *Perseverance’s Scanning Habitable Environments with Raman and Luminescence for Organics and Chemicals (SHERLOC) Investigation*, vol. 217. The Author(s), 2021. doi: 10.1007/s11214-021-00812-z.
- [333] N. Lamsal and S. M. Angel, “Deep-ultraviolet Raman measurements using a spatial heterodyne Raman spectrometer (SHRS),” *Appl. Spectrosc.*, vol. 69, no. 5, pp. 525–534, 2015, doi: 10.1366/14-07844.
- [334] A. Wang *et al.*, “Development of the Mars microbeam Raman spectrometer (MMRS),” *J. Geophys. Res. E Planets*, vol. 108, no. E1, p. 5005, 2003, doi: 10.1029/2002je001902.
- [335] J. L. Lambert, “Context imaging raman spectrometer,” US Patent 10,048,130 B2, 2018
- [336] A. Boffi, T. K. Das, S. Della Longa, C. Spagnuolo, and D. L. Rousseau, “Pentacoordinate heme derivatives in sodium dodecyl sulfate micelles: Model systems for the assignment of the fifth ligand in ferric heme proteins,” *Biophys. J.*, vol. 77, no. 2, pp. 1143–1149, 1999, doi: 10.1016/S0006-3495(99)76965-1.
- [337] T. Kitagawa, Y. Ozaki, and Y. Kyōgoku, “Resonance Raman studies on the ligand-iron interactions in hemoproteins and metallo-porphyrins,” *Adv. Biophys.*, vol. 11, pp. 153–196,

List of References

1978.

- [338] A. Pilinkienė *et al.*, "Resonance Raman spectroscopic study of interaction of hemin chloride with polyclonal antibodies," *Acta medica Litu.*, vol. 12, no. 3, pp. 47–53, 2005.
- [339] B. R. Wood, L. Hammer, L. Davis, and D. McNaughton, "Raman microspectroscopy and imaging provides insights into heme aggregation and denaturation within human erythrocytes," *J. Biomed. Opt.*, vol. 10, no. 1, p. 014005, 2005, doi: 10.1117/1.1854678.
- [340] B. R. Wood, P. Caspers, G. J. Puppels, S. Pandiancherri, and D. McNaughton, "Resonance Raman spectroscopy of red blood cells using near-infrared laser excitation," *Anal. Bioanal. Chem.*, vol. 387, no. 5, pp. 1691–1703, 2007, doi: 10.1007/s00216-006-0881-8.
- [341] H. Sato, H. Chiba, H. Tashiro, and Y. Ozaki, "Excitation wavelength-dependent changes in Raman spectra of whole blood and hemoglobin: comparison of the spectra with 514.5-, 720-, and 1064-nm excitation," *J. Biomed. Opt.*, vol. 6, no. 3, pp. 366–370, 2001, doi: 10.1117/1.1380668.
- [342] B. Venkatesh, S. Ramasamy, M. Mylrajan, R. Asokan, P. T. Manoharan, and J. M. Rifkind, "Fourier transform Raman approach to structural correlation in hemoglobin derivatives," *Spectrochim. Acta - Part A Mol. Biomol. Spectrosc.*, vol. 55, no. 7–8, pp. 1691–1697, 1999, doi: 10.1016/S1386-1425(99)00008-6.
- [343] T. G. Spiro and T. C. Strekas, "Resonance Raman Spectra of Heme Proteins. Effects of Oxidation and Spin State," *J. Am. Chem. Soc.*, vol. 96, no. 2, pp. 338–345, 1974, doi: 10.1021/ja00809a004.
- [344] D. McNaughton and B. Wood, "Raman Spectroscopy and Imaging of Hemes in Healthy and diseased live red blood cells," in *Proceedings of the XIXth International Conference on Raman Spectroscopy*, 2004, pp. 42–47.
- [345] C. Tempera *et al.*, "Characterization and optimization of the haemozoin-like crystal (HLC) assay to determine Hz inhibiting effects of anti-malarial compounds," *Malar. J.*, vol. 14, p. 403, 2015, doi: 10.1186/s12936-015-0913-y.
- [346] B. R. Wood *et al.*, "Resonance raman spectroscopy reveals new insight into the electronic structure of β -hematin and malaria pigment," *J. Am. Chem. Soc.*, vol. 126, no. 30, pp. 9233–9239, 2004, doi: 10.1021/ja038691x.
- [347] A. J. Hobro, A. Konishi, C. Coban, and N. I. Smith, "Raman spectroscopic analysis of malaria disease progression via blood and plasma samples," *Analyst*, vol. 138, no. 14, pp. 3927–

- 3933, 2013, doi: 10.1039/c3an00255a.
- [348] T. Frosch *et al.*, "In situ localization and structural analysis of the malaria pigment hemozoin," *J. Phys. Chem. B*, vol. 111, no. 37, pp. 11047–11056, 2007, doi: 10.1021/jp071788b.
- [349] R. Dasgupta, S. Ahlawat, R. S. Verma, A. Uppal, and P. K. Gupta, "Hemoglobin degradation in human erythrocytes with long-duration near-infrared laser exposure in Raman optical tweezers," *J. Biomed. Opt.*, vol. 15, no. 5, pp. 055009–10, 2010, doi: 10.1117/1.3497048.
- [350] K. Ramser, K. Logg, M. Goksör, J. Enger, M. Käll, and D. Hanstorp, "Resonance Raman spectroscopy of optically trapped functional erythrocytes," *J. Biomed. Opt.*, vol. 9, no. 3, p. 593, 2004, doi: 10.1117/1.1689336.
- [351] Y. Ozaki, A. Mizuno, H. Sato, K. Kawauchi, and S. Muraishi, "Biomedical Application of Near-Infrared Fourier Transform Raman Spectroscopy. Part I: The 1064-nm Excited Raman Spectra of Blood and Met Hemoglobin," *Appl. Spectrosc.*, vol. 46, no. 3, pp. 533–536, 1992, doi: 10.1366/0003702924125131.
- [352] F. Madzharova, Z. Heiner, M. Gühlke, and J. Kneipp, "Surface-Enhanced Hyper-Raman Spectra of Adenine, Guanine, Cytosine, Thymine, and Uracil," *J. Phys. Chem. C*, vol. 120, no. 28, pp. 15415–15423, 2016, doi: 10.1021/acs.jpcc.6b02753.
- [353] J. S. Singh, "FTIR and Raman spectra and fundamental frequencies of biomolecule: 5-Methyluracil (thymine)," *J. Mol. Struct.*, vol. 876, no. 1–3, pp. 127–133, 2008, doi: 10.1016/j.molstruc.2007.06.014.
- [354] D. D. Wynn-Williams, H. G. M. Edwards, E. M. Newton, and J. M. Holder, "Pigmentation as a survival strategy for ancient and modern photosynthetic microbes under high ultraviolet stress on planetary surfaces," *Int. J. Astrobiol.*, vol. 1, no. 1, pp. 39–49, 2002, doi: 10.1017/S1473550402001039.
- [355] A. Ellery and D. Wynn-Williams, "Why Raman spectroscopy on Mars?—A case of the right tool for the right job," *Astrobiology*, vol. 3, no. 3, pp. 565–579, 2003.
- [356] E. Janik-Zabrotowicz *et al.*, "Cremophor EL nano-emulsion monomerizes chlorophyll a in water medium," *Biomolecules*, vol. 9, no. 12, pp. 1–18, 2019, doi: 10.3390/biom9120881.
- [357] V. Vaverkova, O. Vrana, V. Adam, T. Pekarek, J. Jampilek, and P. Babula, "The study of naphthoquinones and their complexes with DNA by using Raman spectroscopy and surface enhanced Raman spectroscopy: New insight into interactions of DNA with plant secondary

List of References

- metabolites," *Biomed Res. Int.*, vol. 11, p. 461393, 2014, doi: 10.1155/2014/461393.
- [358] K. A. Okotrub, N. V. Surovtsev, V. F. Semeshin, and L. V. Omelyanchuk, "Raman spectroscopy for DNA quantification in cell nucleus," *Cytom. Part A*, vol. 87, no. 1, pp. 68–73, 2015, doi: 10.1002/cyto.a.22585.
- [359] S. Nasir *et al.*, "Surface enhanced Raman spectroscopy of RNA samples extracted from blood of hepatitis C patients for quantification of viral loads," *Photodiagnosis Photodyn. Ther.*, vol. 33, p. 102152, 2021, doi: 10.1016/j.pdpdt.2020.102152.
- [360] R. V. Kruzelecky *et al.*, "Inukshuk Landed Robotic Canadian Mission to Mars using a Miniature Sample Analysis Lab for Planetary Mineralogy and Microbiology," *SAE Tech. Pap. Ser.*, 2007, doi: 10.4271/2007-01-3104.
- [361] P. Pal *et al.*, "A generalized exponential relationship between the surface-enhanced Raman scattering (SERS) efficiency of gold/silver nanoisland arrangements and their non-dimensional interparticle distance/particle diameter ratio," *Sensors Actuators, A Phys.*, vol. 314, p. 112225, 2020, doi: 10.1016/j.sna.2020.112225.
- [362] K. Mohamed and M. M. Alkaiji, "The Fabrication of High Aspect Ratio Nanostructures on Quartz Substrate," in *Updates in Advanced Lithography*, S. Hosaka, Ed. London, 2013. doi: 10.5772/56315.
- [363] M. Volkan, D. L. Stokes, and T. Vo-Dinh, "A sol-gel derived AgCl photochromic coating on glass for SERS chemical sensor application," *Sensors Actuators, B Chem.*, vol. 106, no. 2, pp. 660–667, 2005, doi: 10.1016/j.snb.2004.09.019.
- [364] J. Lambert, M. ; Anderson, N. ; Tallarida, T. Vu, M. ; Wallace, and A. Fisher, "Low-Level Organic Detection using the Compact Integrated Raman Spectrometer (CIRS)," in *AGU Fall Meeting 2021: 13-17 December, 2021*, pp. P22A-05.
- [365] A. Zettner, A. B. Gojani, T. Schmid, and I. B. Gornushkin, "Evaluation of a spatial heterodyne spectrometer for raman spectroscopy of minerals," *Minerals*, vol. 10, no. 202, 2020, doi: 10.3390/min10020202.
- [366] G. Hu, W. Xiong, H. Shi, Z. Li, J. Shen, and X. Fang, "Raman spectroscopic detection using a two-dimensional spatial heterodyne spectrometer," *Opt. Eng.*, vol. 54, no. 11, p. 114101, 2015, doi: 10.1117/1.oe.54.11.114101.
- [367] W. Harris *et al.*, "Applications of spatial heterodyne spectroscopy for remote sensing of diffuse UV-vis emission line sources in the solar system," *J. Electron Spectros. Relat.*

- Phenomena*, vol. 144–147, pp. 973–977, 2005, doi: 10.1016/j.elspec.2005.01.223.
- [368] J. M. Ottaway, A. Allen, A. Waldron, P. H. Paul, S. M. Angel, and J. C. Carter, “Spatial Heterodyne Raman Spectrometer (SHRS) for In Situ Chemical Sensing Using Sapphire and Silica Optical Fiber Raman Probes,” *Appl. Spectrosc.*, vol. 73, no. 10, pp. 1160–1171, 2019, doi: 10.1177/0003702819868237.
- [369] J. M. Harlander, F. L. Roesler, and S. Chakrabarti, “Spatial heterodyne spectroscopy: a novel interferometric technique for the FUV,” *SPIE EUV, X-Ray, Gamma-Ray Instrum. Astron.*, vol. 1344, no. November, 1990, doi: 10.1117/12.23275.
- [370] N. Lamsal, “The Development Of A High Resolution Deep- UV Spatial Heterodyne Raman Spectrometer,” 2016.
- [371] S. J. Kim, J. S. Hwang, J. E. Park, M. Yang, and S. Kim, “Exploring SERS from complex patterns fabricated by multi-exposure laser interference lithography,” *Nanotechnology*, vol. 32, p. 315303, 2021, doi: 10.1088/1361-6528/abfb32.
- [372] J. Langer *et al.*, “Present and future of surface-enhanced Raman scattering,” *ACS Nano*, vol. 14, pp. 28–117, 2020, doi: 10.1021/acsnano.9b04224.
- [373] “Jupiter’s Moon Europa,” *Graphic News*, Nov. 11, 2011. [Online]. Available: <https://www.graphicnews.com/en/pages/28624/SPACE-Jupiter’s-moon-Europa>

